Electromagnetic modeling and simulation of fiber-reinforced periodically-structured planar laminates

Changyou Li

UNIVERSITÉ PARIS SUD
Comprendre le monde, construire l'avenir®

STITS ECOLE DOCTORALE

UNIVERSITÉ PARIS-SUD

ECOLE DOCTORALE No. 422 :
STITS-SCIENCES ET TECHNOLOGIES DE L'INFORMATION DES TÉLÉCOMMUNICATIONS ET DES SYSTÈMES

LABORATOIRE DES SIGNAUX ET SYSTÈMES, UMR8506
(CNRS-CENTRALESUPÉLEC-UNIVERSITÉ PARIS-SUD)

DISCIPLINE : PHYSIQUE

THÈSE DE DOCTORAT

Soutenue le 28 Septembre 2015 par

Changyou Li

Modélisation et simulation de la diffraction électromagnétique par des laminés plans renforcés par des fibres cylindriques arrangées périodiquement

Directeur de thèse :	Dominique Lesselier	Directeur de recherche CNRS
Composition du jury :		
Président du jury :	Jean-Jacques Greffet	Professeur, Université Paris Sud
Rapporteurs :	Olivier Dazel	Professeur, Université du Maine
	André Nicolet	Professeur, Aix-Marseille Université
Examinateurs :	Jean-Jacques Greffet	Professeur, Université Paris Sud
	Patrick Joly	Directeur de recherche INRIA
	Christophe Reboud	Ingénieur Chercheur CEA

UNIVERSITÉ PARIS SUD

Comprendre le monde, construire l'avenir®

STITS ECOLE DOCTORALE

UNIVERSITÉ PARIS-SUD

ECOLE DOCTORALE NO. 422:

STITS-SCIENCES ET TECHNOLOGIES DE L'INFORMATION DES TÉLÉCOMMUNICATIONS ET DES SYSTÈMES

LABORATOIRE DES SIGNAUX ET SYSTÈMES, UMR8506

(CNRS-CENTRALESUPÉLEC-UNIVERSITÉ PARIS-SUD)

DISCIPLINE: PHYSICS

THESIS OF DOCTORATE

Defended September 28, 2015 by

Changyou Li

Electromagnetic modeling and simulation of fiber-reinforced periodically-structured planar laminates

Director of the thesis:	Dominique Lesselier	Directeur de recherche CNRS
Composition of jury:		
President of jury:	Jean-Jacques Greffet	Professeur, Université Paris Sud
Reporters:	Olivier Dazel	Professeur, Université du Maine
	André Nicolet	Professeur, Aix-Marseille Université
Examiners:	Jean-Jacques Greffet	Professeur, Université Paris Sud
	Patrick Joly	Directeur de recherche INRIA
	Christophe Reboud	Ingénieur Chercheur CEA

Acknowledgements

Sincere thanks and gratitude are first given to my supervisor Dr. Dominique Lesselier, Directeur de Recherche, Centre National de la Recherche Scientifique (CNRS), for providing me this great opportunity to study the theory of electromagnetic waves and fields, for sharing his expertise and for giving his valuable guidance during the three years.

I wish also to express my warm thanks to Dr. Yu Zhong, who is now working in the Institute of High Performance in Singapore, for the helpful discussions and for carefully reviewing various manuscripts. My appreciation also goes to Dr. Vincent Lescarret, who is working in Laboratoire des Signaux et Systèmes (L2S), for helping me in my work on homogenization of the structure. Many thanks are also given to Dr. Marc Lambert, Chargé de Recherche CNRS, for providing me good advices whenever needed.

This three-year life in L2S offered me a valuable opportunity to encounter many friends and nice colleagues. I express my warm thanks to Giacomo Rodeghiero, Panagiotis Piteros and Henri Vallon for helping me from the very beginning and sharing with me their happiness. I am grateful to Christophe Conessa for explaining so many interesting things to me during the three years, from the name of a special fruits to the cultural background of monuments and places.

I also wish to express my thanks to my Chinese friends Fan Huang, Xi Cheng, Pingping Ding and Zicheng Liu in L2S, Xusheng Wang in Université Paris-Sud, Ming Xu in Génie électrique et électronique de Paris (GEPS), and Yan Tang in Université Pierre et Marie CURIE. They helped and accompanied me through the three years.

I would also like to thank my jury members, Professor Olivier Dazel, Professor André Nicolet, Professor Jean-Jacques Greffet, Professor Patrick Joly, and Dr. Christophe Reboud for serving as my jury members of the thesis defense and referees for the first two.

I am very grateful to my parents for their great support and confidence. I am also deeply indebted to my adorable wife Jinxiu Wang. Her great support, warm encouragements and firm confidence are the key of the success of this adventure. Gratitude is also given to my brothers and sisters for carefully looking after our parents and supporting me all these years with never-ending loves. Thanks to all the people who has helped me in the work and has brought me the colorful life in the three years.

Summary

English: The contribution corresponds to the electromagnetic modeling of fiber-reinforced periodically organized composites. The final goal is to gain a good understanding of their electromagnetic behavior as well as to acquire images that should exhibit the location of possibly damaged zones, and provide some quantification of these zones. The thesis focuses on the scattering of well-organized periodic structures and building up an efficient full-wave computational model for multilayered composites, wherein each layer is reinforced by a periodic array of fibers, which is the first step for further study of the disorganized one.

The work firstly considered the scattering problem of a slab in which infinite circular fibers, with the same radius, are periodically embedded with the same orientation of their axes and the same center-to-center distance. A 2-dimensional problem with normally and obliquely incident E- and H-polarized plane waves as well as Gaussian beams is firstly considered for understanding the principles and philosophies of the used mode-matching method and multipole expansion. Then the work is extended to the investigation of the scattering of the slab to a conically incident 3-dimensional electromagnetic wave, which shows the potential of the work for obtaining the response of the structure to a point source.

A more practical but complicated multilayered composite, constructed by stacking up the slabs one over the other, is further investigated. Two different composites are taken into account. To study the first composite, with fibers in different layers having the same orientations, T-matrix- and S-matrix-based methods are introduced into the work for solving the linear system produced by mode-matching at the boundaries between two adjacent layers. Then, further investigation of the second kind of composite, wherein the fibers within different layers are orientated into different directions, is carried out by extending the approach properly. Some attention is also given to homogenization issues, so as to link small-scale approaches as developed in the thesis with large-scale ones as often considered in non-destructive testing of composite laminates.

Extensive numerical simulations are proposed, validated with results existing in the literature (notably the ones of photonic crystals) and by using brute-force solvers. Emphasis is also on special cases of composites (glass-fiber- and graphite-fiber-based ones) as most often faced in practical applications, with appropriate frequency bands chosen in harmony with the dielectric or conductive aspect of the reinforcing fibers.

Français: La thèse porte sur la modélisation électromagnétique et la simulation de composites stratifiés plans (laminés), renforcés par des fibres organisées périodiquement. L'objectif est d'acquérir une bonne compréhension du comportement électromagnétique de telles structures, en première et étape de ce que pourrait ultérieurement être la production d'images mettant en évidence la localisation de zones éventuellement endommagées, et fournissant une certaine quantification de celles-ci.

La thèse proprement dite se concentre donc sur la construction et l'évaluation de modèles de la diffraction électromagnétique par des composites multicouches tels que chaque couche est renforcée par des fibres disposées périodiquement. Est d'abord investiguée la diffraction par une plaque diélectrique (mono-couche) au sein de laquelle des fibres cylindriques de section circulaire de même rayon sont incorporées périodiquement, ces fibres ayant la même orientation de leurs axes et la même distance de centre à centre.

Un cas bidimensionnel impliquant des ondes planes E ou H-polarisées, ainsi que des faisceaux gaussiens, normalement ou obliquement incidents, est d'abord pris en considération afin de mieux comprendre principes et philosophies des méthodes de choix, le couplage de mode et l'expansion multipolaire. Puis le travail est étendu, la diffraction de la plaque sous un éclairement tridimensionnel (conique) étant alors traitée en détail, ce qui montre aussi le potentiel de la méthodologie mise en œuvre si l'on souhaite obtenir la réponse électromagnétique de la structure à une source ponctuelle.

Un composite multicouche, plus courant, mais plus complexe, qui est fait d'un empilement de plaques l'une sur l'autre, est alors étudié. Deux différentes espèces de composites sont ici prises en compte. Pour étudier la première, dont les fibres dans les différentes couches possèdent les mêmes orientations, des méthodes à base de matrices dites S ou dites T sont introduites, impliquant entre autre de s'intéresser à une résolution convenable du système linéaire produit selon le couplage de mode à la transition entre deux couches adjacentes. Une investigation de la deuxième espèce de composites suit alors, pour lequel les fibres au sein des différentes couches sont orientées dans des directions différentes quelconques, ce que permet une extension précautionneuse des approches précédentes.

Une certaine attention est également portée au problème de l'homogénéisation des composites, de manière à lier les démarches à petite échelle telles que développées dans la thèse à celles à grande échelle souvent les seules prises en compte dans le contrôle non destructif et l'imagerie des composites stratifiés.

De nombreux résultats de simulations numériques sont proposés et validés autant que possible par des résultats de référence de la littérature (notamment dans le cas de cristaux photoniques) et l'utilisation de solveurs «brute-force». L'accent est aussi mis sur des cas particuliers de matériaux composites (ceux à base de fibres de verre et ceux à base de

fibres de carbone) qui sont le plus souvent rencontrés dans les applications pratiques, avec des bandes de fréquences appropriées choisies en accord avec le comportement des fibres, principalement diélectrique ou principalement conducteur.

Table of contents

List of figures

List of tables

Chapter 1

Introduction

1.1 Background

Laminated composite materials are increasingly used in aerospace, naval and automotive industries as a replacement of traditional metal materials due to their light weight, high stiffness and good corrosion resistance properties, etc. For fabrication, two or more constituent materials are always combined together to produce desired characteristics which cannot be easily provided by either of the individual materials.

An example of the laminated composite material is composed of two parts, the matrix and the reinforcement. The reinforcements are embedded inside the background matrix and periodically arranged to provide strength and stiffness while the matrix is used to bind the reinforcements together. Taking one epoxy or polyester slab, reinforced by embedding a periodic array of infinite glass or carbon fibers orientated to the same direction, as a building block, a stack can be fabricated by piling up the slabs one over the other with the fibers in different slabs orientated into different directions, hence providing the stack strength and stiffness in all directions. Piling up the resulting stacks produces a periodically laminated composite [5, 6].

For the aforementioned composite laminates, damages caused by impact, fiber rupture and cracks, etc., might appear during manufacturing and/or in-service time, which impacts mechanical properties or shortens the service life, and especially in the area of aerospace, these subsurface defects might have catastrophic consequences. The damages as micro-cracks and small delaminations buried inside the composites are generally invisible for visual inspection. Hence, non-destructive testing methods are needed for effective inspection.

Ultrasonic methods are the most widely used non-destructive testing (NdT) method in industry, though mainly for characterization of metals and alloys, and it remains challeng-

ing to apply them to this kind of complex-structured composite with ensuring good resolution [7]. However, ultrasonic waves are significantly attenuated when the measurement is made in near field [8] or with relative high frequency [9], which can cause faulty detection of the damaged area. Infrared thermography is another method, but detection can be impaired by low conductivity of the fibers [10]. Using other traditional NdT methods to detect these damages remains challenging or high-cost, too. All the mentioned traditional non-destructive methods have also some other difficulties to be applied to fiber-reinforced components [11], hence development of novel non-destructive testing methods becomes important [12, 13]. Testing with electromagnetic waves is one of the alternative methods, which already shows good potential for inspecting low-energy impact damages [14] at eddy-current [11] and microwave [15, 16] frequencies for dielectric and conductive fibers.

But effective imaging requires good understanding of electromagnetic behavior, the one of the undamaged laminates in the first step. For a low-frequency range with assumption of time-harmonic inspection, when the center-to-center distance between fibers is much smaller than the electrical wavelength for dielectric cases or skin-depth for conductive cases, uniaxial anisotropic homogeneous layers are usually hypothesized with equivalent-layer model [17], involving effective permittivity or conductivity tensors, the laminate simply being a superposition of such layers [18–20]. Reflection/transmission coefficients of the laminate can be computed with classical approaches for planarly-layered media, general scattering situations possibly requiring more sophisticated approaches, refer to [21]. Asymptotic model has also been proposed for periodic structures, refer to [22, 23].

For a high-frequency range, when the distance between fibers is of the order of the wavelength or skin-depth, the above homogenization usually fails. The investigation can be carried out with periodic surface integral formulation [24, 25] which represents the unknown electric and magnetic fields with related equivalent currents on the boundary interfaces and handles the needed Green's function by applying the Poisson summation formula and the periodicity of the structure. The surface integral equation is formulated over one unit cell and solved with method of moments [26].

However, existing investigations appear to be limited to two-dimensional (2D) scattering cases involving TE- or TM-polarized plane or beam waves and one-dimensional (1D) periodicity. For the more practical 2.5D case, in which the incident wave impinges conically onto the structure of 1D periodicity with non-zero azimuth and elevation angles for the wave vector in the defined coordinate system, or the more complicated 3D case, conically incident waves on a composite with several directions of periodicity of the embedded fibers, the field of investigation is wide open. Although FDTD [27] or FEM

[28] could deal with composites with complex cross-section profile of the fibers, but these brute-force methods could only manage 3D scattering situations with a limited level of structural complexities, such as the so-called woodpile structure [4, 29–31] constructed with a 2-layer stack in which fibers in the two layers are orientated into two orthogonal directions [32]. But these numerical methods, in addition to be computationally demanding, might fail to model complex laminates with arbitrary orientations between fibers in different layers. Meanwhile, most of the imaging algorithms require full availability of dyadic Green's functions associated to the structure investigated, which brute-force numerical or analytical-numerical methods do not easily provide.

In the past few decades, many efficient and accurate electromagnetic theoretical methods have been effectively applied for modeling photonic crystals with similar arrangement of the fibers as the one inside the composite materials. In the studies, wide attention has been given to Rayleigh methods [33] and plane wave expansions [34, 35] for their computational efficiency and accuracy as well as their analytic tractability. A typical investigation on photonic crystals has been carried out by Yasumoto *et al.* [3]. The cylindrical harmonic expansion method is brought to a simple and tractable formulation with transition matrix for modeling the electromagnetic scattering of the periodically arranged dielectric cylinders standing in air. The way of arranging the cylinders is similar to the one of the cases considered in this thesis, hence this work provided good examples to compare with and to be used to validate the approach. Multipole method and plane wave expansion are combined together by Botten and coworkers [36–38] for studying photonic devices. Focus was mainly on scattering of microstructured optical fibers or the Bloch mode analysis of optical devices, thus a bit differing from the problems considered here. But the way of combining the multipole method and plane wave expansion is quite interesting for investigating the scattering characteristics of the composite laminates. Most of the reported works concentrate on the widely studied woodpile structure [3, 38, 39] standing in air for the attractive optical gaps. But this kind of structure, even though structurally similar with laminated composites, actually does not exist for real composite materials since, with only two fiber orientations, it cannot provide sufficient strength and stiffness along all directions to fit practical requirements.

In addition, the presence of the isotropic homogeneous background material in the composites results in strong interactions between the waves reflected by the fiber arrays and the slab interfaces, hence leading to much more complicated electromagnetic behavior. This interaction becomes stronger with higher permittivity contrast. Arbitrary orientations of the fibers in different layers bring another degree of complexity, especially in the case involving tens of hundreds of layers. The dispersion brought into the system by differ-

ently orientated fibers needs to be considered carefully with a proper decomposition of the modes of plane-wave expansions. Some of the modes are propagating one, but some of them become evanescent. In the calculation, all the propagating modes and a limited number of the evanescent modes need to be considered to achieve a good convergence of the field. Too many evanescent modes will slow down the speed of the calculation. Arbitrarily orientating the fibers also complicates the procedure of separating propagating modes from the evanescent ones, so a proper number of evanescent modes need to be chosen for balancing efficiency of the calculation and the speed of convergence. This choosing procedure becomes tedious when more than three orientations of the fibers exist in the structure. At the same time, mode-matching at the boundary between two adjacent layers is necessary to produce a linear system for obtaining the reflection and transmission coefficients, which must be done in the same reference system. Thus the corresponding field expansions or matrices of the modes in the layers where the fibers are orientated into different directions need to be carefully arranged and transformed into the same coordinate system before mode-matching at the boundaries. Combining these complexities with the conically incident waves produces a complicated electromagnetic scattering problem which must be solved for obtaining the dyadic Green's function by investigating the electromagnetic response of elementary sources.

The studies in this thesis give the fundamentals of investigating the electromagnetic response of complex composite materials. Meanwhile, these investigations provide some good techniques which can be applied straightforwardly to the case of disorganized periodic structures. This disorganization can be caused by either missing and displacing some fibers in the composites or by changing their physical parameters and shapes. All these contributions are necessary for further researches corresponding to non-destructive testing of damages with electromagnetic waves, being underlined that emphasis of this thesis is on the above mentioned electromagnetic problem corresponding to several kinds of composite materials. The final goal is to develop an efficient full-wave computational model of multilayered composites.

As the first step, multipole method and plane-wave expansion, borrowing a good part from earlier analyses [2, 40–42] and photonic ones [43], are applied together to study the most simple composite structure which is produced by embedding a periodic array of infinitely long circular cylindrical fibers into a dielectric slab. The focus is mainly on carbon- or glass-fiber reinforced epoxy slabs illuminated by time harmonic waves. E- (TM) and H-polarized (TE) incident waves are considered with the plane of incidence in the plane of the common cross-section of the fibers. In this thesis, this case is called 2D case, a 2D structure and 2D incident waves being involved. The field near each cylinder is natu-

rally expanded into cylindrical harmonics involving Bessel functions. Then the cylindrical functions are combined with the so-called lattice sums [44, 45] which renders their superposition periodic to satisfy the required periodic boundary conditions along the line connecting the center of the cylinders and also orthogonal to their axes. Integration along the boundary of one periodic cell and the one of the cylinder included inside relates the field in the vicinity of the central cylinder to the one above and below the grating, where plane-wave expansion of the fields is involved to calculate the field in the upper or lower half-space.

At the same time, mode-matching at the boundaries of circular cylinders reveals the fine details of the structure and allows further calculating the field distribution within them. Investigation of this case allows one to understand the preliminaries and basic principles of the approaches, as well as to build a solid fundamental for further studies. Gaussian beam is also considered by decomposing the beam into plane waves. The scattered field of the beam is obtained by overlapping the one of all the plane waves. Besides, the homogenization theory is also considered and developed as a connection between the present full-wave model and the one for low-frequency investigations.

Keeping the same 2D structure, the approaches applied to the 2D case are then extended for the scattering of a conically incident wave where the plane of incidence is out of the plane of the cross-section of the fibers. This case is called 2.5D case. Since the wave vector of the incident wave has longitudinal components, the electric and magnetic fields are coupled together. This complicates the relations between the transverse and longitudinal field components, which then leads to a more complicated field representation of the transverse field components, hence to a more complicated relationship between the expansion coefficients. Because of the simplicity of the single-layer composite structure, the field expansion coefficients can still be obtained explicitly to avoid matrix inversions.

Once, based on a single-layer fiber-reinforced composite, the approach for the 2D and 2.5D scattering problems is well developed and understood, extension of the method is carried out for investigating the scattering of a multilayered fiber-based composite. It is constructed by stacking up the single-layer composite laminates one over the other, but all the circular cylindrical fiber arrays in different layers are still orientated into the same direction. Carbon and glass fibers are under consideration with their radii being the same in the same layer but maybe different from layer to layer, keeping the same center-to-center distances for every layer of the structure. The background materials and thicknesses of different layers can also vary from one to the other.

Time-harmonic incident plane waves with plane of incidence differing from the cross-section of the fibers, and Gaussian beam waves, via corresponding plane wave expansions,

are considered here. Following the treatment for a single-layer composite, electric and magnetic fields in regions of interest are first plane-wave expanded in view of the periodicity of the fibers. Mode-matching at the boundary between any two layers yields the matrix that links the field expansion coefficients at the two sides of the boundary. Rayleigh's identity is established around the fibers to relate the fields within the same layer above and below the fibers. Scattering matrices (S-matrices) or transfer matrices (T-matrix) for each single layer easily follow. Cascading them layer by layer down to the one of the bottom layer produces an S-matrix or a T-matrix which relates the reflection and transmission coefficients to the incident field, both for planar ones and Gaussian beams. For Gaussian beam, the S-matrix is built for each of the plane waves on which the beam is expanded.

The schemes based on S-matrix and T-matrix are implemented individually. Numerical instability is then exhibited in the two schemes at different levels because of the ill-conditioning of the matrices. This property brings some difficulties to invert the corresponding matrices. Because of this limitation, the T-matrix method can only be applied to investigate the characteristics of propagating modes. Once evanescent modes are involved in the calculation, the method becomes quite unstable. This instability of the T-matrices is heavily influenced by their exponentially increasing elements. Comparatively, the S-matrix based scheme is much more stable. It exhibit instability for calculating field distribution inside the structure, but that can be solved by rearranging the matrices so as to link the field expansion coefficients in every layer to the incident field.

So far, all the basic techniques for characterizing complicated composite structures has been made available. Hence one quite practical multilayered composite is taken into account. To fabricate these composites, a 4-layer stack is firstly constructed by piling up single-layer composites, with the fibers in different layers orientated into different directions to provide the required strength and stiffness. Then, tens of the stacks are overlapped to produce the multilayered composite. Before building the modeling for 4-layer stack, one 2-layer stack is used to explain and demonstrate the basic ideas. The S-matrix based approach is then further developed to investigate the scattering of this kind of composites. A full-wave computational model of the practically used laminated composites is finally given.

1.2 Overview of the manuscript

This thesis is divided into six chapters. Chapter 1 introduces the research background and the contributions of the thesis. Chapter 2 and Chapter 3 introduce the basic principles of the investigation by considering the electromagnetic behavior of single-layer composite

reinforced by a periodic array of fibers, under illumination of plane waves or Gaussian beams. These techniques are then extended in Chapter 4 for further studying the response of multilayered composites where the fibers in different layers are all parallel to each other. These investigations allow to understand the performance of the S-matrix and T-matrix based approaches as well as giving the some knowledge about the behavior of the multilayered structures. Then the S-matrix based recursive approach is extended in Chapter 5 to exhibit the electromagnetic characteristics of multilayered structures where fibers in different layers are now orientated into different directions. Chapter 6 presents the conclusions and perspectives. Several appendices follow with corresponding material.

Chapter 2

Scattering of TM and TE wave by a fiber-based slab

The first step in developing the full-wave computational model of multilayered composite is made in this chapter. Multipole method and plane wave expansion are combined together via evaluating the Green's second identity with periodic Green's functions. The scattering of a single-layer composite is studied with illumination of an in-plane E-polarized (TM) or H-polarized (TE) wave. The investigation of this scattering problem allows one to understand the preliminaries and basic principles of the approaches, hence it provides a solid fundamental for further building the more complicated model. The contribution also allows to calculate scattering of a line source or beam wave in an easy way. To illustrate, scattering of Gaussian beam is calculated by expanding the beam into plane waves. The scattered field of a Gaussian beam is then produced by overlapping all the scattered fields of the plane waves.

2.1 Wave propagation and preliminary formulation

The single-layer composite considered here is shown in Fig. 2.1, and a Cartesian coordinate system xyz is introduced with $\hat{x}$, $\hat{y}$ and $\hat{z}$ as unit vectors along the corresponding axes. The structure consists of a horizontal slab of thickness $L = a - b$ sandwiched between two homogeneous half-spaces with corresponding interfaces Γ_a ($z = a$) and Γ_b ($z = b$). A set of circular fibers, which parallel with each other and directed into the y direction, is embedded in the slab, which is infinite along both x and y axes. All fibers are arranged periodically along the x direction with a center-to-center distance d. Their radii are all the same and indicated as c. The structure divides the whole space into four regions named as

Ω_j, $j = 0, 1, 2, 3$, where Ω_0 and Ω_3 denote the upper and lower half-spaces respectively. The upper half-space is filled with air. The materials in all other regions are homogeneous and isotropic, with their permittivities and permeabilities given as $\epsilon_j = \epsilon_r^{(j)}\epsilon_0$ and $\mu_j = \mu_r^{(j)}\mu_0$, $j = 1, 2, 3$, where ϵ_0 and μ_0 are the ones for air.

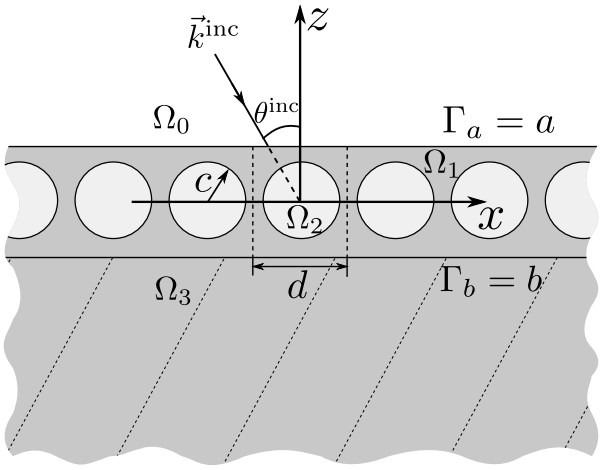

Fig. 2.1 Sketch for the single layer composite structure with TM or TE polarized waves impinging upon it obliquely.

Assuming an implicit time dependence $e^{-i\omega t}$, the electric field $\boldsymbol{\mathcal{E}}_j(x, y, z)$ and the magnetic field $\boldsymbol{\mathcal{H}}_j(x, y, z)$ are therefore the solution of the time-harmonic Maxwell-equations,

$$\nabla \times \boldsymbol{\mathcal{E}} = i\sqrt{\frac{\mu_0}{\epsilon_0}}k\mu_r\boldsymbol{\mathcal{H}}, \tag{2.1a}$$

$$\nabla \times \boldsymbol{\mathcal{H}} = -i\sqrt{\frac{\epsilon_0}{\mu_0}}k\epsilon_r\boldsymbol{\mathcal{E}}, \tag{2.1b}$$

$$\nabla \cdot \boldsymbol{\mathcal{E}} = 0, \tag{2.1c}$$

$$\nabla \cdot \boldsymbol{\mathcal{H}} = 0. \tag{2.1d}$$

Here the index j is neglected since the equation is established in all regions. $\boldsymbol{\mathcal{E}} = E_x\hat{x} + E_y\hat{y} + E_z\hat{z}$, and $\boldsymbol{\mathcal{H}} = H_x\hat{x} + H_y\hat{y} + H_z\hat{z}$.

2.1.1 TM and TE wave illumination

Considering a plane wave incident from the upper space upon the slab with its plane of incidence parallel with the x-z plane, field vectors will thus be independent of y, which

leads to the wave equations for TM and TE waves

$$H_x = -\frac{1}{i\omega\mu_0\mu_r}\frac{\partial E_y}{\partial z}, \tag{2.2a}$$

$$\left(\frac{\partial^2}{\partial x^2} + \frac{\partial^2}{\partial z^2} + \omega^2\mu_0\mu_r\epsilon_0\epsilon_r\right)E_y = 0, \tag{2.2b}$$

$$E_x = \frac{1}{i\omega\epsilon_0\epsilon_r}\frac{\partial H_y}{\partial z}, \tag{2.2c}$$

$$\left(\frac{\partial^2}{\partial x^2} + \frac{\partial^2}{\partial z^2} + \omega^2\mu_0\mu_r\epsilon_0\epsilon_r\right)H_y = 0, \tag{2.2d}$$

Allowing the wave vector of the TM or TE incident wave as $\vec{k}^{\text{inc}} = k_x^{\text{inc}}\hat{x} - k_z^{\text{inc}}\hat{z}$ with k_x^{inc} and k_z^{inc} being x- and z-components of $\vec{k}^{\text{inc}}$, then $k_x^{\text{inc}} = k^{\text{inc}}\sin\theta^{\text{inc}}$, $k_z^{\text{inc}} = k^{\text{inc}}\cos\theta^{\text{inc}}$, where θ^{inc} is the angle of incidence. Thus the incident wave can be written as

$$\mathbf{V}_y^{\text{inc}}(x,z) = \hat{y}V_y^{\text{inc}}e^{i[k_x^{\text{inc}}x - k_z^{\text{inc}}(z-a)]}, \tag{2.3}$$

where $\mathbf{V}_y^{\text{inc}}$ denotes $\mathbf{E}_y^{\text{inc}}$ for the TM polarized wave or $\mathbf{H}_y^{\text{inc}}$ for the TE polarized wave, with V_y^{inc} being the corresponding amplitude.

With wave numbers k_j corresponding to regions Ω_j, then $k_j = \omega\sqrt{\epsilon_j\mu_j}$, $j = 0,1,2,3$. The related wave vector $\vec{k}_j$ is defined as $\vec{k}_j = \alpha_j\hat{x} - \beta_j\hat{z}$ with α_j and β_j indicating the x and z components of $\vec{k}_j$, so $\alpha_0 = k_x^{\text{inc}}$. A particular feature of the problem is the transverse periodicity of these inclusions in the slab. According to the Floquet theorem, this periodicity and the plane wave nature force the fields to satisfy

$$V_{jy}(x+d,z) = V_{jy}(x,z)e^{i\alpha_0 d}, \tag{2.4}$$

where V_{jy} denotes either E_{jy} for the TM case or H_{jy} for the TE case in regions Ω_j. Allowing $U_j(x,z) = V_{jy}(x,z)e^{-i\alpha_0 x}$ produces a periodic function $U_j(x,z)$ with the same period d as the structure. Hence $U_j(x,z)$ can be expanded into a Fourier series

$$U_j(x,z) = \sum_{p\in\mathbb{Z}} v_p(z)e^{i\frac{2\pi p}{d}x} \tag{2.5}$$

where $\mathbb{Z}$ is the set of all integers, $p \in \mathbb{Z}$. Then the field $V_{jy}(x,z)$ can be written as

$$V_{jy}(x,z) = \sum_{p\in\mathbb{Z}} v_p(z)e^{i\alpha_p x} \tag{2.6}$$

with $\alpha_p = \alpha_0 + \frac{2\pi p}{d}$ and $v_p(z)$ as the expansion coefficients.

2.1.2 Scattering of TM and TE wave by single cylinder

First, TM or TE incident wave is considered. The relation between V_y and V_θ in the cylindrical coordinate system can be obtained from equation (2.1), which is given as

$$H_\theta = \frac{1}{i\omega\mu}\frac{\partial E_y}{\partial r}, \qquad \text{TM wave} \tag{2.7a}$$

$$E_\theta = -\frac{1}{i\omega\epsilon}\frac{\partial H_y}{\partial r}, \qquad \text{TE wave.} \tag{2.7b}$$

Here, $\mu = \mu_r\mu_0$, $\epsilon = \epsilon_r\epsilon_0$. Index j is not introduced since they establish in the whole space.

Considering a circular cylinder as sketched in Fig. 2.2, the field outside the cylinder can be expanded into cylindrical harmonics [46], and it reads as

$$V_{1y} = \sum_{n\in\mathbb{Z}} \left[B_n H_n^{(1)}(k_1 c) + A_n J_n(k_1 c)\right] e^{in\theta} \tag{2.8}$$

where J_n is the first kind Bessel function of the n-th order, and $H_n^{(1)}$ is the first kind Hankel function of the n-th order. c is the radius of the cylinder, k_1 is the wave number in the space excluding the cylinder. If the cylinder is filled with isotropic dielectric material, then the field inside the cylinder is

$$V_{2y} = \sum_{n\in\mathbb{Z}} C_n J_n(k_2 r) e^{in\theta}, \tag{2.9}$$

where C_n are the expansion coefficients. The corresponding field components $V_{j\theta}$ are easily obtained with (2.7a) and (2.7b). Matching the field at the boundary of the cylinder produces the relation between B_n and A_n, which is written as

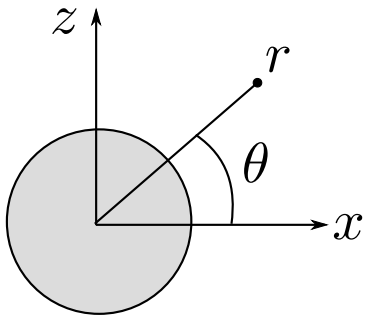

Fig. 2.2 Sketch of single cylinder

$$B_n = L_n A_n, \tag{2.10}$$

where

$$L_n = \begin{cases} \dfrac{\eta_1 \dot{J}_n(k_2c)J_n(k_1c) - \eta_2 J_n(k_2c)\dot{J}_n(k_1c)}{\eta_2 \dot{H}_n^{(1)}(k_1c)J_n(k_2c) - \eta_1 \dot{J}_n(k_2c)H_n^{(1)}(k_1c)} & \text{for TM} \\ \dfrac{\eta_2 \dot{J}_n(k_2c)J_n(k_1c) - \eta_1 J_n(k_2c)\dot{J}_n(k_1c)}{\eta_1 \dot{H}_n^{(1)}(k_1c)J_n(k_2c) - \eta_2 \dot{J}_n(k_2c)H_n^{(1)}(k_1c)} & \text{for TE.} \end{cases} \tag{2.11}$$

Here, an isotropic dielectric material for the cylinder is assumed. $\eta_j = \sqrt{\frac{\mu_j}{\epsilon_j}}$, $j = 1, 2$. $\dot{J}_n(x)$ and $\dot{H}_n^{(1)}(x)$ are the first order derivative of $J_n(x)$ and $H_n^{(1)}(x)$ with respect to x. When a metal (perfect conducting) cylinder is considered, then the relation (2.10) simply becomes

$$L_n = \begin{cases} -\dfrac{J_n(k_1c)}{H_n^{(1)}(k_1c)} & \text{for TM} \\ -\dfrac{\dot{J}_n(k_1c)}{\dot{H}_n^{(1)}(k_1c)} & \text{for TE.} \end{cases} \tag{2.12}$$

2.2 Scattering of TM or TE wave

Now, scattering of TM or TE polarized incident wave by a single layer slab reinforced by an infinite number of fibers arranged periodically is investigated. Plane-wave field expansion in regions Ω_0 and Ω_3 are easily obtained with equation (2.6), but to obtain the one in regions Ω_1 and Ω_2, periodic Green's functions defined in both Cartesian and cylindrical coordinates are needed. Then the integration along the boundary of one periodic cell and the one of the central cylinder is performed to combine the plane-wave and multipole expansion coefficients. Mode-matching at boundaries Γ_a and Γ_b produces the relation between reflection/transmission coefficients and multiple expansion coefficients which is achieved by establishing Rayleigh's identity at the boundary of the central cylinder. The power reflection/transmission coefficients follow with application of Poynting theorem.

2.2.1 Fields representations in Ω_0 and Ω_3

In the upper half-space, both incident and reflected fields exist. Expanding the reflected field with (2.6) and adding it to the incident field produce the total field in Ω_0,

$$V_{0y}(x,z) = \sum_{p\in\mathbb{Z}} (V^{\text{inc}} e^{-i\beta_{0p}(z-a)}\delta_{p0} + R_p e^{i\beta_{0p}(z-a)})e^{i\alpha_p x}, \tag{2.13}$$

where R_p, depending on $V_{0y}(x,z)$ for $E_{0y}(x,z)$ and $H_{0y}(x,z)$, stands for the reflection coefficients of the plane wave indexed by p, and R_p^e for TM wave or R_p^h for TE wave. δ_{p0}

is the Kronecker symbol which is required to generate a matrix. $\alpha_p = \alpha_0 + 2p\pi/d$, since the tangential components of $\vec{k}_j$ cross the boundaries Γ_a and Γ_b continuously, α_p is used in the equations instead of α_{jp}. Meanwhile β_{jp} is defined as $\beta_{jp} = \sqrt{k_j^2 - \alpha_p^2}, \quad j = 0,1,2,3$. Since $p \in \mathbb{Z}$ and varies from $-\infty$ to $+\infty$, α_p varies dramatically between $-\infty$ and $+\infty$. So β_{jp} is properly defined as

$$\beta_{jp} = \begin{cases} \sqrt{k_j^2 - \alpha_p^2}, & k_j^2 > \alpha_p \\ i\sqrt{\alpha_p^2 - k_j^2}, & k_j^2 < \alpha_p \end{cases}, \tag{2.14}$$

where the modes for $\beta_{jp}^2 > 0$ are propagating modes, and the ones for $\beta_{jp}^2 < 0$ are evanescent modes. The propagating modes carry all the energy of the wave. But, enough evanescent modes are needed in the calculation for good convergence of the field expansions.

In the lower half-space, only transmitted field exists. The field is expanded with (2.6), which reads as

$$V_{3y}(x,z) = \sum_{p\in\mathbb{Z}} T_p e^{i(\alpha_p x - \beta_{3p}(z-b))} \tag{2.15}$$

where T_p represents the transmission coefficients of the plane wave indexed by p, T_p^e for the TM wave or T_p^h for the TE wave.

2.2.2 Fields representations in Ω_1 and Ω_2

In order to get the field representation in region Ω_1 and Ω_2, the corresponding periodic Green's functions which satisfy

$$(\nabla^2 + k^2)G(\vec{r}) = \sum_{n=-\infty}^{+\infty} \delta(\vec{r} - nd\hat{x}) e^{i\alpha_0 nd} \tag{2.16}$$

are first introduced within both Cartesian and cylindrical coordinate systems. In cylindrical form, $\vec{r} = (r,\theta)$, one has

$$G(\vec{r}) = -\frac{i}{4} \sum_{n=-\infty}^{+\infty} e^{i\alpha_0 nd} H_0^{(1)}(k_1|\vec{r} - nd\hat{x}|). \tag{2.17}$$

Applying Graf's addition theorem [47], as detailed in appendix A, to the right hand side of equation (2.17) produces a second form of the periodic Green's function

$$G(\vec{r}) = -\frac{i}{4} H_0^{(1)}(k_1 r) - \frac{i}{4} \sum_{l=-\infty}^{+\infty} S_l J_l(k_1 r) e^{il\theta} \tag{2.18}$$

with the hypothesis that $r < d$. J_m is the first kind Bessel function of the m-th order. The first term in equation (2.18) refers to outgoing waves, and the second one represents in-going waves. S_l is called lattice sums which is defined as

$$S_l = \sum_{n=1}^{+\infty} H_l^{(1)}(k_1 nd)[e^{i\alpha_0 nd} + (-1)^l e^{-i\alpha_0 nd}]. \tag{2.19}$$

Lattice sums arise naturally for investigating the scattering of periodic structures. They actually superpose the contribution of the cylindrical wave functions in a way satisfying the periodic conditions along the x axis. But the lattice sums have a problem of bad convergence, and further discussion will be given in section 2.2.6.

The plane wave form of the periodic Green's function (2.18) is given as

$$G(x,z) = \frac{1}{2id} \sum_{p=-\infty}^{+\infty} \frac{1}{\beta_p} e^{i(\alpha_p x + \beta_p |z|)}. \tag{2.20}$$

It can be proven by using Fourier transformation that the two forms of periodic Green's function (2.18) and (2.20) are equivalent to each other.

Define a primary cell as shown in Fig. 2.3, which includes only one circular cylinder inside and has a width d and height L. Two paths, C and D, are defined here. C denotes the boundary of the central cylinder, and D denotes the outside boundary of the primary cell. Meanwhile, the surface of the area between C and D is denoted as S. To obtain the

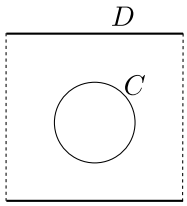

Fig. 2.3 Integration path

field within region Ω_1, Green's second identity is necessary, which reads as

$$\int_S V_{1y}(\vec{r}_1)\nabla^2 G(\vec{r}-\vec{r}_1) - G(\vec{r}-\vec{r}_1)\nabla^2 V_{1y}(\vec{r}_1) ds = \oint_{C+D} V_{1y}(\vec{r}_1)\nabla G(\vec{r}-\vec{r}_1) - G(\vec{r}-\vec{r}_1)\nabla V_{1y}(\vec{r}_1) d\vec{r}_1. \tag{2.21}$$

Here, the vector $\vec{r}$ is a field point located in the vicinity of the cylinder, $|\vec{r}| > c$ but stays in the region Ω_1. Similarly, the source point associated with contributions from the central

cylinder is written as $\vec{r}_1$. The fields in any region should satisfy the Helmholtz equation

$$(\nabla^2 + k_j^2)V_{jy} = 0. \tag{2.22}$$

Substituting equations (2.16) and (2.22) into the left hand side of equation (2.21) produces

$$\begin{aligned}
&\int_S V_{1y}(\vec{r}_1)\nabla^2 G(\vec{r}-\vec{r}_1) - G(\vec{r}-\vec{r}_1)\nabla^2 V_{1y}(\vec{r}_1)ds \\
&= \int_S \Big[V_{1y}(\vec{r}_1)[\sum_{n=-\infty}^{+\infty} \delta(\vec{r}-\vec{r}_1-nd\hat{x})e^{i\alpha_0 nd} - k^2 G(\vec{r}-\vec{r}_1)] + G(\vec{r}-\vec{r}_1)k^2 V_{1y}(\vec{r}_1)\Big]ds \\
&= V_{1y}(\vec{r}).
\end{aligned} \tag{2.23}$$

then, the Green's second identity (2.21) can be simplified as $V_{1y}(\vec{r}) = I_C + I_D$ where

$$I_C = \oint_C \Big[G(\vec{r}-\vec{r}_1)\frac{\partial V_{1y}(\vec{r}_1)}{\partial \vec{n}_1} - V_{1y}(\vec{r}_1)\frac{\partial G(\vec{r}-\vec{r}_1)}{\partial \vec{n}_1}\Big]d\vec{r}_1, \tag{2.24a}$$

$$I_D = \oint_D \Big[V_{1y}(\vec{r}_1)\frac{\partial G(\vec{r}-\vec{r}_1)}{\partial \vec{n}_1} - G(\vec{r}-\vec{r}_1)\frac{\partial V_{1y}(\vec{r}_1)}{\partial \vec{n}_1}\Big]d\vec{r}_1. \tag{2.24b}$$

Here I_C and I_D represent the field scattered by the embedded circular cylinders and the slab. The expression for $G(\vec{r}-\vec{r}_1)$ is directly obtained from equation (2.18), it reads as

$$G(\vec{r}-\vec{r}_1) = -\frac{i}{4}H_0^{(1)}(k_1|\vec{r}-\vec{r}_1|) - \frac{i}{4}\sum_{l=-\infty}^{+\infty} S_l J_l(k_1|\vec{r}-\vec{r}_1|)e^{il\theta'}, \tag{2.25}$$

where $\vec{r} = (r,\theta)$, $\vec{r}_1 = (r_1,\theta_1)$ and $\vec{r}-\vec{r}_1 = (|\vec{r}-\vec{r}_1|,\theta')$. According to Graf's addition,

$$H_0^{(1)}(k_1|\vec{r}-\vec{r}_1|) = \sum_{m\in\mathbb{Z}} H_m(k_1 r)J_m(k_1 r_1)e^{im(\theta-\theta_1)}, \tag{2.26a}$$

$$J_l(k_1|\vec{r}-\vec{r}_1|)e^{il\theta'} = \sum_{m\in\mathbb{Z}} J_m(k_1 r_1)J_{m+l}(k_1 r)e^{i(m+l)\theta - im\theta_1}. \tag{2.26b}$$

Refer to appendix A for details. Applying equations (2.26) to (2.25) yields

$$\begin{aligned}
G(\vec{r}-\vec{r}_1) = &-\frac{i}{4}\sum_{m\in\mathbb{Z}} J_m(k_1 r_1)H_m^{(1)}(k_1 r)e^{im(\theta-\theta_1)} \\
&-\frac{i}{4}\sum_{m\in\mathbb{Z}} S_m \sum_{n\in\mathbb{Z}} J_{n+m}(k_1 r)J_n(k_1 r_1)e^{i(n+m)\theta - in\theta_1},
\end{aligned} \tag{2.27}$$

which is rearranged as

$$G(\vec{r}-\vec{r}_1) = -\frac{i}{4}\sum_{m\in\mathbb{Z}} J_m(k_1 r_1)H_m^{(1)}(k_1 r)e^{im(\theta-\theta_1)} \\ -\frac{i}{4}\sum_{m\in\mathbb{Z}} J_m(k_1 r)e^{im\theta}\sum_{n\in\mathbb{Z}} S_{m-n}J_n(k_1 r_1)e^{-in\theta_1}. \tag{2.28}$$

Substituting equation (2.28) and $V_{1y}(\vec{r}_1)$ into equation (2.24a) produces

$$\begin{aligned} I_C &= \oint_C \Big[G(\vec{r}-\vec{r}_1)\frac{\partial V_{1y}(\vec{r}_1)}{\partial \vec{n}_1} - V_{1y}(\vec{r}_1)\frac{\partial G(\vec{r}-\vec{r}_1)}{\partial \vec{n}_1}\Big]d\vec{r}_1, \\ &= \sum_{m\in\mathbb{Z}} B_m H_m^{(1)}(k_1 r)e^{im\theta} + \sum_{m\in\mathbb{Z}} J_m(k_1 r)e^{im\theta}\sum_{n\in\mathbb{Z}} S_{m-n}B_n, \end{aligned} \tag{2.29}$$

which represents the field diffracted by the central cylinder. The coefficients B_m are

$$B_m = -\frac{i}{4}\oint_C \Big[J_m(k_1 r_1)e^{-im\theta_1}\frac{\partial V_{1y}(\vec{r}_1)}{\partial \vec{n}_1} - V_{1y}(\vec{r}_1)\frac{\partial}{\partial \vec{n}_1}(J_m(k_1 r_1)e^{-im\theta_1})\Big]d\vec{r}_1. \tag{2.30}$$

Hence, the cylindrical form of I_C is finally obtained, but in the analysis the expression of I_C in Cartesian coordinate system is also needed, which is derived from the plane wave form of the periodic Green's function (2.20). In the Cartesian coordinate system, $G(\vec{r}-\vec{r}_1)$ reads as

$$G(\vec{r}-\vec{r}_1) = \frac{1}{2id}\sum_{p=-\infty}^{+\infty}\frac{1}{\beta_{1p}}e^{i(\alpha_p(x-x_1)+\beta_p|z-z_1|)}, \tag{2.31}$$

which is further written as

$$G(\vec{r}-\vec{r}_1) = \begin{cases} \dfrac{1}{2id}\displaystyle\sum_{p=-\infty}^{+\infty}\frac{1}{\beta_{1p}}e^{i(\alpha_p x-\beta_p z)}e^{-ik_1 r_1\cos(-\theta_1-\theta_p)}, & z-z_1<0, \\ \dfrac{1}{2id}\displaystyle\sum_{p=-\infty}^{+\infty}\frac{1}{\beta_{1p}}e^{i(\alpha_p x+\beta_p z)}e^{-ik_1 r_1 cos(\theta_p-\theta_1)}, & z-z_1>0. \end{cases} \tag{2.32}$$

Here, θ_p satisfy $k_1 e^{i\theta_p} = \alpha_p + i\beta_{1p}$. Careful computation of θ_p is required here to make sure that their real part $\Re(\theta_p) > 0$ for the propagating modes and the imaginary part $\Im(\theta_p) > 0$ for the evanescent modes which attenuate as they propagate in the $+z$ direction. Following the discussion in [1], if $|\alpha_p/k_1| < 1$, then $0 < \theta_p < \pi$ and $\sin\theta_p = \sqrt{1-\alpha_p^2/k_1^2} > 0$. When $|\alpha_p/k_1| > 1$, then θ_p is no longer real and has two possible values corresponding to $\alpha_p/k_1 > 1$ and $\alpha_p/k_1 < -1$. For $\alpha_p/k_1 > 1$, $\theta_p = i\text{arccosh}(|\alpha_p/k_1|)$, where $\text{arccosh}x = \ln(x+\sqrt{x^2-1})$. If $\alpha_p/k_1 < -1$, then $\theta_p = \pi - i\text{arccosh}(|\alpha_p/k_1|)$.

Here, $e^{ik_1 r_1 \cos(\theta)}$ can be expanded into cylindrical harmonics as

$$e^{-ik_1 r_1 \cos(\theta)} = \sum_{m=-\infty}^{\infty} i^m J_m(-k_1 r_1) e^{im\theta} = \sum_{m=-\infty}^{\infty} (-i)^m J_m(k_1 r_1) e^{im\theta} \tag{2.33}$$

with the property of Bessel function $J_m(-x) = (-1)^m J_m(x)$. Keeping the field dependence of $\vec{r} = (x, z)$ in equation (2.32) in Cartesian exponential form and transforming the terms corresponding to source point $\vec{r}_1 = (x_1, z_1)$ into cylindrical harmonics with (2.33) yields

$$G(\vec{r}-\vec{r}_1) = \begin{cases} \dfrac{1}{2id} \displaystyle\sum_{p=-\infty}^{+\infty} \frac{1}{\beta_{1p}} e^{i(\alpha_p x - \beta_{1p} z)} \sum_{m=-\infty}^{\infty} (-i)^m J_m(k_1 r_1) e^{im(-\theta_1-\theta_p)}, & z - z_1 < 0, \\ \dfrac{1}{2id} \displaystyle\sum_{p=-\infty}^{+\infty} \frac{1}{\beta_{1p}} e^{i(\alpha_p x + \beta_{1p} z)} \sum_{m=-\infty}^{\infty} (-i)^m J_m(k_1 r_1) e^{im(\theta_p-\theta_1)}, & z - z_1 > 0. \end{cases} \tag{2.34}$$

Substituting (2.33) and $V_{1y}(\vec{r}_1)$ into (2.24a) produces

$$\begin{aligned} I_C = & \frac{1}{2id} \sum_{p=-\infty}^{+\infty} \frac{1}{\beta_{1p}} e^{i(\alpha_p x - \beta_{1p} z)} \\ & \times \sum_{m=-\infty}^{\infty} (-i)^m e^{-im\theta_p} \oint_C \left[J_m(k_1 r_1) e^{-im\theta_1} \frac{\partial V_{1y}(\vec{r}_1)}{\partial \vec{n}_1} - V_1(\vec{r}_1) \frac{\partial}{\partial \vec{n}_1} (J_m(k_1 r_1) e^{-im\theta_1}) \right] d\vec{r}_1 \end{aligned} \tag{2.35}$$

for $z - z_1 < 0$, and

$$\begin{aligned} I_C = & \frac{1}{2id} \sum_{p=-\infty}^{+\infty} \frac{1}{\beta_{1p}} e^{i(\alpha_p x + \beta_{1p} z)} \\ & \times \sum_{m=-\infty}^{\infty} (-i)^m e^{im\theta_p} \oint_C \left[J_m(k_1 r_1) e^{-im\theta_1} \frac{\partial V_{1y}(\vec{r}_1)}{\partial \vec{n}_1} - V_1(\vec{r}_1) \frac{\partial}{\partial \vec{n}_1} (J_m(k_1 r_1) e^{-im\theta_1}) \right] d\vec{r}_1 \end{aligned} \tag{2.36}$$

for $z - z_1 > 0$. Allowing $Q_{pm}^{\pm} = \frac{2(-i)^m e^{\pm im\theta_p}}{d\beta_{1p}}$, equations (2.35) and (2.36) are combined together into a unified form

$$I_C = \sum_{p\in\mathbb{Z}} \sum_{m\in\mathbb{Z}} B_m Q_{pm}^{\pm} e^{i(\alpha_p x \pm \beta_{1p} z)}, \tag{2.37}$$

where $+$ corresponds to $z - z_1 > 0$ and $-$ relates to $z - z_1 < 0$. As it will be illustrated, B_m are the field expansion coefficients of cylindrical harmonics around the central cylinder.

The field in the region Ω_1 but above and below the cylinders are immediately plane-wave expanded as

$$V_{1y}^{\pm} = \sum_{p\in\mathbb{Z}} (f_p^{\pm} e^{-i\beta_{1p}z} + g_p^{\pm} e^{i\beta_{1p}z}) e^{i\alpha_p x} \tag{2.38}$$

where the expansion coefficients $f_p^{\pm}$ and $g_p^{\pm}$ depending on V_{1y} for E_{1y} and H_{1y} represent $f_{ep}^{\pm}$ and $g_{ep}^{\pm}$ for TM wave or $f_{hp}^{\pm}$ and $g_{hp}^{\pm}$ for TE wave. $+$ signifies $c < z < a$ which is above the cylinders, and $-$ corresponds to $b < z < c$ for the region below. Evaluating the integral (2.24a) over D with equation (2.38) produces

$$I_D = \sum_{p\in\mathbb{Z}} (f_p^{+} e^{-i\beta_{1p}z} + g_p^{-} e^{i\beta_{1p}z}) e^{i\alpha_p x} \tag{2.39}$$

So the field in region Ω_1 is given as

$$V_{1y}^{\pm}(x,z) = I_C + I_D = \sum_{p\in\mathbb{Z}} (f_p^{+} e^{-i\beta_{1p}z} + g_p^{-} e^{i\beta_{1p}z}) e^{i\alpha_p x} + \sum_{p\in\mathbb{Z}} \sum_{m\in\mathbb{Z}} B_m Q_{pm}^{\pm} e^{i(\alpha_p x \pm \beta_{1p} z)}. \tag{2.40}$$

Comparing it with equation (2.38) produces

$$f_p^{-} = f_p^{+} + \sum_{m\in\mathbb{Z}} B_m Q_{pm}^{-}, \tag{2.41a}$$

$$g_p^{+} = g_p^{-} + \sum_{m\in\mathbb{Z}} B_m Q_{pm}^{+}, \tag{2.41b}$$

which is a rather important relation and will be used in the whole thesis. The field V_{jx} are obtained by applying equations (2.2a) and (2.2c) to the field representations of V_{jy}.

2.2.3 Mode-matching at the boundary Γ_a and Γ_b

Matching the modes at boundaries is necessary to produce a linear system taking R_p, T_p, f_p^{+} and g_p^{-} as unknowns. These unknowns will be expressed as a function of B_m which is finally solved by building Rayleigh's identity on the boundary of the central fiber. Mode-matching at the boundaries Γ_a and Γ_b with equations (2.13), (2.15), (2.40) and the corresponding x components of the fields produces a linear system, and applying the property $\int_{-d/2}^{d/2} e^{i(\alpha_m - \alpha_n)x} dx = d\delta_{mn}$, $m, n \in \mathbb{Z}$, to the linear system yields

$$V^{\text{inc}}\delta_{p0} + R_p - f_p^{-} e^{-i\beta_{1p}a} - g_p^{-} e^{i\beta_{1p}a} - \sum_{m\in\mathbb{Z}} B_m Q_{pm}^{+} e^{i\beta_{1p}a} = 0, \tag{2.42a}$$

$$\chi_{0p}(V^{\text{inc}}\delta_{p0} - R_p) - \chi_{1p}\Big[(f_p^{+} e^{-i\beta_{1p}a} - g_p^{-} e^{i\beta_{1p}a}) - \sum_{m\in\mathbb{Z}} B_m Q_{pm}^{+} e^{i\beta_{1p}a}\Big] = 0, \tag{2.42b}$$

$$T_p - f_p^+ e^{-i\beta_{1p}b} - g_p^- e^{i\beta_{1p}b} - \sum_{m\in\mathbb{Z}} B_m Q_{pm}^- e^{-i\beta_{1p}b} = 0, \tag{2.42c}$$

$$\chi_{3p} T_p - \chi_{1p}\Big[(f_p^+ e^{-i\beta_{1p}b} - g_p^- e^{i\beta_{1p}b}) + \sum_{m\in\mathbb{Z}} B_m Q_{pm}^- e^{-i\beta_{1p}b}\Big] = 0, \tag{2.42d}$$

where $\chi_{jp} = \beta_{jp}/\mu_j$ for TM polarization and $\chi_{jp} = \beta_{jp}/\epsilon_j$ for TE polarization, $j = 0, 1, 2, 3$. Solving this linear system yields R_p, T_p, f_p^+ and g_p^-, which read as

$$\begin{aligned} T_p = -\frac{1}{D_p}\Bigg[& 4\chi_{1p}\chi_{0p} V^{\mathrm{inc}} \delta_{0p} \\ & + \sum_{m\in\mathbb{Z}} \frac{8(-i)^m \chi_{1p} B_m}{d\beta_{1p}} [\chi_{1p}\cos(\beta_{1p}a + m\theta_p) - i\chi_{0p}\sin(\beta_{1p}a + m\theta_p)]\Bigg], \end{aligned} \tag{2.43a}$$

$$\begin{aligned} R_p = -\frac{1}{D_p}\Bigg[& \big[2(\chi_{1p}\chi_{0p} - \chi_{1p}\chi_{3p})\cos(\beta_{1p}L) + 2i(\chi_{1p}^2 - \chi_{0p}\chi_{3p})\sin(\beta_{1p}L)\big] V^{\mathrm{inc}} \delta_{0p} \\ & + \sum_{m\in\mathbb{Z}} \frac{8(-i)^m \chi_{1p} B_m}{d\beta_{1p}} [\chi_{1p}\cos(m\theta_p + \beta_{1p}b) + i\chi_{3p}\sin(m\theta_p + \beta_{1p}b)]\Bigg], \end{aligned} \tag{2.43b}$$

and

$$\begin{aligned} f_p^+ = -\frac{1}{D_p}\Big[& 2V^{\mathrm{inc}}\delta_{0p}\chi_{0p}(\chi_{1p} + \chi_{3p}) e^{i\beta_{1p}b} \\ & + (\chi_{1p} - \chi_{0p})(\chi_{1p} + \chi_{3p}) \sum_{m\in\mathbb{Z}} B_m K_{pm}^+ e^{i\beta_{1p}(a+b)} \\ & + (\chi_{1p} - \chi_{0p})(\chi_{1p} - \chi_{3p}) \sum_{m\in\mathbb{Z}} B_m K_{pm}^- e^{i\beta_{1p}(a-b)}\Big], \end{aligned} \tag{2.44a}$$

$$\begin{aligned} g_p^- = -\frac{1}{D_p}\Big[& 2V^{\mathrm{inc}}\delta_{0p}\chi_{0p}(\chi_{1p} - \chi_{3p}) e^{-i\beta_{1p}b} \\ & + (\chi_{1p} - \chi_{0p})(\chi_{1p} - \chi_{3p}) \sum_{m\in\mathbb{Z}} B_m K_{pm}^+ e^{i\beta_{1p}(a-b)} \\ & + (\chi_{1p} + \chi_{0p})(\chi_{1p} - \chi_{3p}) \sum_{m\in\mathbb{Z}} B_m K_{pm}^- e^{-i\beta_{1p}(a+b)}\Big], \end{aligned} \tag{2.44b}$$

where $D_p = 2i(\chi_{0p}\chi_{3p} + \chi_{1p}^2)\sin(\beta_{1p}L) - 2(\chi_{1p}\chi_{3p} + \chi_{1p}\chi_{0p})\cos(\beta_{1p}L)$ and $L = a - b$.

2.2.4 Rayleigh's identity

Substituting equation (2.44) into (2.39) produces a Cartesian form of I_D, which is transformed into cylindrical harmonic form with $x = r\cos\theta$, $z = r\sin\theta$, $\alpha_{1p} = k_1\cos\theta_p$, $\beta_{1p} = k_1\sin\theta_p$ and $e^{ikr\cos\theta} = \sum_{m\in\mathbb{Z}} i^m J_m(kr) e^{im\theta}$, then the cylindrical form of I_D is ob-

tained. Combining it with the cylindrical form of I_C yields

$$V_{1y}(x,z)=\sum_{n\in\mathbb{Z}}\left[B_nH_n^{(1)}(k_1r)+\left(\sum_{m\in\mathbb{Z}}M_{nm}B_m+F_n\right)J_n(k_1r)\right]e^{in\theta}, \tag{2.45}$$

where $M_{nm}=Q_{nm}+P_{nm}+S_{n-m}$ with Q_{nm}, P_{nm} and F_n being defined as

$$\begin{aligned}Q_{nm}=\sum_{p\in\mathbb{Z}}-\frac{4(-i)^{m-n}}{d\beta_{1p}D_p}\Big[&i\chi_{1p}(\chi_{3p}-\chi_{0p})\sin(\beta_{1p}(a+b)+(m+n)\theta_p)\\&+(\chi_{1p}^2-\chi_{0p}\chi_{3p})\cos(\beta_{1p}(a+b)+(n+m)\theta_p)\Big]\end{aligned} \tag{2.46a}$$

$$P_{nm}=\sum_{p\in\mathbb{Z}}-\frac{4(-i)^{m-n}(\chi_{1p}-\chi_{0p})(\chi_{1p}-\chi_{3p})}{d\beta_{1p}D_p}e^{i\beta_{1p}L}\cos((n-m)\theta_p) \tag{2.46b}$$

$$F_n=\sum_{p\in\mathbb{Z}}-\frac{2i^nV^{\text{inc}}\delta_{p0}\chi_{0p}}{D_p}\Big[(\chi_{1p}+\chi_{3p})e^{i(\beta_{1p}b+n\theta_p)}+(\chi_{1p}-\chi_{3p})e^{-i(\beta_{1p}b+n\theta_p)}\Big], \tag{2.46c}$$

At the same time, S_{n-m} is a lattice sum. As been discussed in section 2.1.2, in the annular region around the central cylinder of the primary cell but excluding all other fibers, the field is expanded into the form of (2.8), and comparing it with (2.45) yields $A_n=\sum_{m\in\mathbb{Z}}M_{nm}B_m+F_n$ which is combined with equation (2.10) to produce the Rayleigh's identity. One has

$$B_n=\sum_{m\in\mathbb{Z}}L_nM_{nm}B_m+L_nF_n. \tag{2.47}$$

Solving it produces the value of B_n which is then introduced into (2.43) and (2.44) to obtain the coefficients R_p, T_p, f_p^+ and g_p^-. With these coefficients, the field distribution within or without the slab is easily obtained via the field representations.

2.2.5 The power reflection and transmission coefficients

The time-average Poynting vector power density indicates the power density of the wave with units of $\mathrm{W\,m^{-2}}$. It is

$$\langle\vec{S}\rangle=\frac{1}{2}\Re\left\{\vec{E}\times\vec{H}^*\right\}, \tag{2.48}$$

where $\vec{S}=\vec{E}\times\vec{H}^*$ is the complex Poynting vector, and $\vec{H}^*$ denotes the complex conjugate of $\vec{H}$ field. With an incident TM wave, the reflected field in the upper half-space is

$$\vec{E}^r(x,z)=\hat{y}\sum_{p\in\mathbb{Z}}R_pe^{i\beta_{0p}(z-a)}e^{i\alpha_px}, \tag{2.49}$$

of which the p-th mode is

$$\vec{E}_p^r(x,z) = R_p e^{i\beta_{0p}(z-a)} e^{i\alpha_p x}. \tag{2.50}$$

Then, the H_x and H_z components of the p-th mode are written as

$$H_{px}^r(x,z) = -\frac{\beta_{0p} R_p}{\omega\mu_0} e^{i\beta_{0p}(z-a)}, \tag{2.51a}$$

$$H_{pz}^r(x,z) = \frac{\alpha_p R_p}{\omega\mu_0} e^{i\beta_{0p}(z-a)}. \tag{2.51b}$$

With the magnetic field defined as $\vec{H}_p^r = \hat{x}H_{px}^r + \hat{z}H_{pz}^r$, the complex Poynting vector of the p-th mode of the reflected field is obtained,

$$\begin{aligned} \vec{S}_p^r =& \vec{E}_p^r \times \vec{H}_p^{r*} \\ =& \hat{x} E_{py}^r H_{pz}^{r*} - \hat{z} E_{py}^r H_{px}^{r*} \\ =& \hat{x} \frac{\alpha_p^* R_p^* R_p}{\omega\mu_0} + \hat{z} \frac{\beta_{0p}^* R_p^* R_p}{\omega\mu_0}. \end{aligned} \tag{2.52}$$

The complex Poynting vectors of the incident and the p-th mode of transmitted field are

$$\vec{S}^i = \hat{x} \frac{\alpha_0 E^{\text{inc}2}}{\omega\mu_0} - \hat{z} \frac{\beta_0 E^{\text{inc}2}}{\omega\mu_0}, \tag{2.53a}$$

$$\vec{S}_p^t = \hat{x} \frac{\alpha_p^* T_p^* T_p}{\omega\mu_3} - \hat{z} \frac{\beta_{3p}^* T_p^* T_p}{\omega\mu_3}, \tag{2.53b}$$

The power reflection and transmission coefficients of each mode are then given as

$$r_p = \Re\left\{ \frac{\hat{z} \cdot \langle \vec{S}_p^r \rangle}{-\hat{z} \cdot \langle \vec{S}^i \rangle} \right\} = \Re\left\{ \frac{\beta_{0p}^* R_p^* R_p}{\beta_0 E^{\text{inc}2}} \right\}, \tag{2.54a}$$

$$t_p = \Re\left\{ \frac{-\hat{z} \cdot \langle \vec{S}_p^t \rangle}{-\hat{z} \cdot \langle \vec{S}^i \rangle} \right\} = \Re\left\{ \frac{\mu_0 \beta_{3p}^* T_p^* T_p}{\mu_3 \beta_0 E^{\text{inc}2}} \right\}. \tag{2.54b}$$

Allowing

$$\xi = \frac{\beta_{0p}^*}{\beta_0 E^{\text{inc}2}} \qquad \zeta = \frac{\mu_0 \beta_{3p}^*}{\mu_3 \beta_0 E^{\text{inc}2}}, \tag{2.55}$$

then r_p and t_p are written as

$$r_p = \Re\left\{ \xi R_p^* R_p \right\}, \quad t_p = \Re\left\{ \zeta T_p^* T_p \right\}. \tag{2.56a}$$

Therefore, the power reflection, transmission and absorption coefficients are defined as

$$\mathcal{R} = \sum_{p\in\mathbb{Z}} r_p, \tag{2.57a}$$

$$\mathcal{T} = \sum_{p\in\mathbb{Z}} t_p, \tag{2.57b}$$

Hence, the absorption coefficients for lossy materials can be defined as $\mathcal{A} = 1-\mathcal{R}-\mathcal{T}$. The power reflection and transmission coefficients of TE waves are derived in a similar manner. One obtains the power reflection and transmission coefficients for TE waves having the same form of (2.57) with ξ and ζ in (2.56) being replaced by

$$\xi = \frac{\beta_{0p}}{\beta_0 H^{\text{inc}2}} \qquad \zeta = \frac{\epsilon_0\beta_{3p}}{\epsilon_3\beta_0 H^{\text{inc}2}}, \tag{2.58}$$

2.2.6 Numerical investigation

Lattice sums

Lattice sums are a class of Schlömilch series which arise naturally in the investigation of the scattering problems involving periodic structures. For 1D periodicity, 2D scattering case, they are defined as

$$S_m = \sum_{n=1}^{\infty} \mathrm{H}_m^{(1)}(knd)[e^{i\alpha_0 nd} + (-1)^m e^{-i\alpha_0 nd}]. \tag{2.59}$$

where $\mathrm{H}_m^{(1)}(x)$ is the first-kind Hankel function of m-th order. k is the wave number of the media where the sums are evaluated. $\alpha_0 = k_0 \sin\theta^{\text{inc}}$ with k_0 and θ^{inc} being the wave number and incident angle of the incident wave. d is the period of the structure.

Lattice sums play the role of superposing the contribution of the cylindrical wave functions in a proper way which satisfies the required periodic conditions. The sums suffers from a problem of bad convergence, which can not be easily overcome. Meanwhile the lattice sums cannot be simply avoided in the problems involving periodic structures. Computation of lattice sums seriously influences the speed of calculating the field and also the accuracy of the results.

As seen from (2.59), lattice sums S_m can be written into a function of wave vector k, incident angle θ and period of the structure d. Hence, the convergence of lattice sums is mainly influenced by the frequency of the incident wave, the considered material, the observation points and the period of the structure. Much literature exists for accelerating the

corresponding calculations [1, 45, 48–51]. In this thesis, one of the most recent method, presented in [1], is used for the calculation. This method actually combined the new results [50–52] derived from integral representations and the Poisson summation formula and then introduced some new expressions in terms of some elementary functions which enable the series to be computed accurately and efficiently.

With definition of partial sums $S_m^{\pm} = \sum_{n=1}^{\infty} \mathrm{H}_m^{(1)}(k_1 nd) e^{\pm i\alpha_0 nd}$, the numerical results shown in [1] are reproduced by implementing the approach, which illustrates that the present implementation works well, as shown in figure 2.4 and 2.5.

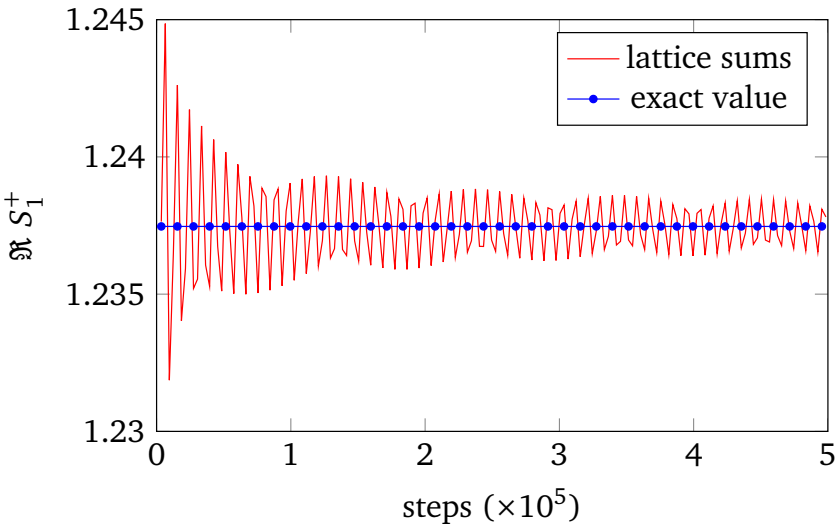

Fig. 2.4 Computed values of $\Re\ S_1^+$ with $k_1 d = 0.7$, $\alpha_0/k_1 = 0.5$. The horizontal line represents the exact value 1.23746 calculated with the approach given in [1]. The partial sums of S_m^+ are computed in steps of 1000, up to 10^6.

Considering an incident wave with low frequency $f = 5\,\mathrm{MHz}$, which normally impinges upon a glass-fiber-reinforced epoxy composite (epoxy $\epsilon_r = 3.6$), letting $L = d = 0.1\,\mathrm{mm}$, the exact values of corresponding lattice sums are computed with the approach given in [1]. Numerical results with relative error below 10^{-6} are achieved in only 0.0286s on a computer with 4 CPU cores, 2.0 GHz each, and 8 G memories. Direct calculation with the definition of lattice sums is carried out for comparison, and the convergence is much slower. At the higher frequency 5 GHz, the convergence is also not good, and the results keep oscillating around the exact value. Hence, the calculation with the definition of lattice sums is too slow to satisfy the requirement of efficient calculation. Results for 5 MHz and 5 GHz are shown in Fig. 2.6 and Fig. 2.7.

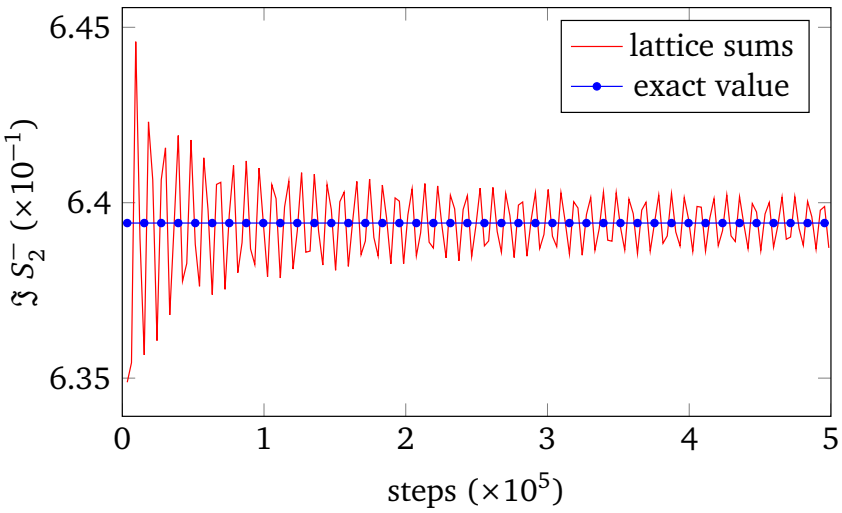

Fig. 2.5 Computed values of $\Im\, S_2^-$ with $kd = 1.7$, $\alpha_0/d = 1.5$. The horizontal line represents the exact value 0.639421 calculated with the approach presented in [1]. The partial sums of S_m^- are computed in steps of 1000, up to 10^6.

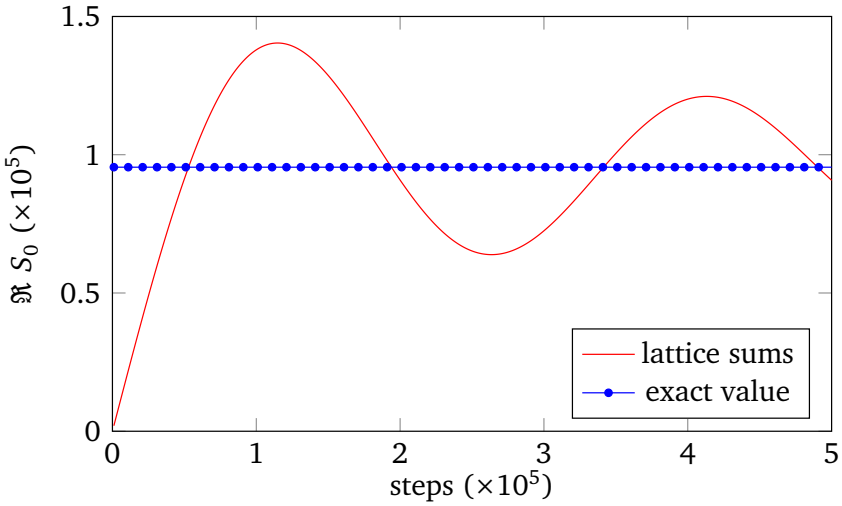

Fig. 2.6 Computed values of the real part of S_0 for $f = 5\,\text{MHz}$, $\theta_i = 0$, $L = d = 0.1\,\text{mm}$. Slow convergence is observed.

Scattering by fiber-array-based slab

The infinite sums $\sum_{p\in\mathbb{Z}}$ for plane-wave expansions and $\sum_{m\in\mathbb{Z}}$ for multipole expansions are truncated as $\sum_{p=-P}^{P}$ and $\sum_{m=-M}^{M}$ in the calculation with $P = \text{Int}\,(d/2\pi(3\Re(k_1) - \alpha_0))$ and $M = \text{Int}\left(\Re(4.05 \times (k_1 c)^{1/3}) + k_1 c\right)$. With the definition of relative error $|\boldsymbol{\mathcal{R}}^{n+1} - \boldsymbol{\mathcal{R}}^n|$, n the truncation order P or M, convergence of the results is shown in Fig. 2.8 for increasing values of M and P. It is observed that the results converge quickly with increase of P or

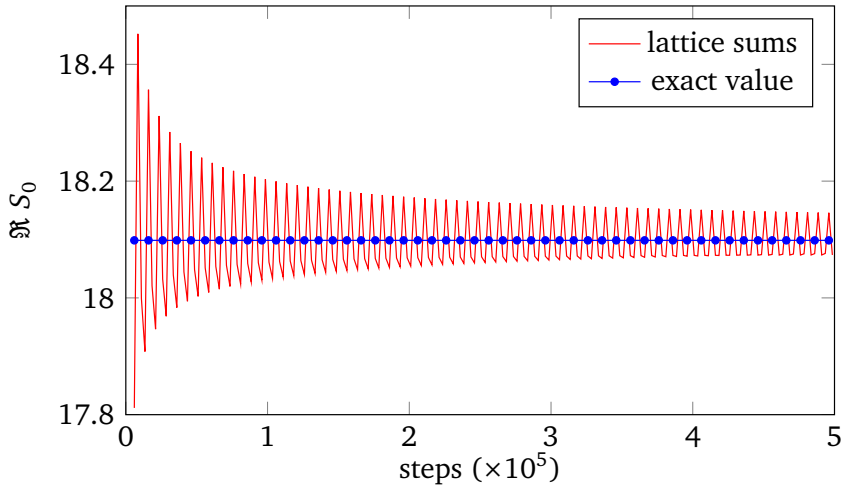

Fig. 2.7 Computed values of the real part of S_0 for $f = 5\,\text{GHz}$, $\theta_i = 0$, $L = d = 0.1\,\text{mm}$. Fast oscillation show up, but it converges slowly.

M. In the following calculation, the sums are truncated at $M = 11$ and $P = 5$ to obtain a relative error less than 10^{-6}.

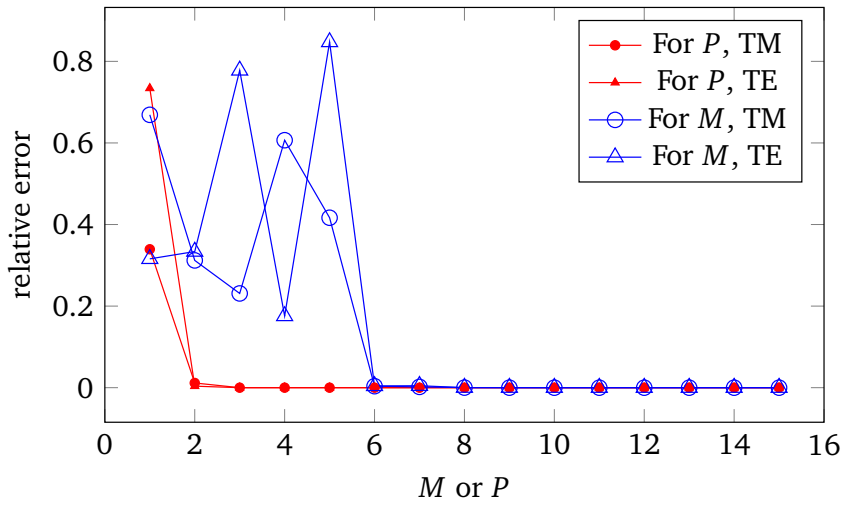

Fig. 2.8 Relative error versus M or P for glass fibers ($\epsilon_r^{(2)} = 6.0$) embedded in an epoxy matrix ($\epsilon_r^{(1)} = 3.6$). $d = \lambda_i = 0.1\,\text{mm}$, $L = 2d$, $c = 0.4d$.

In order to verify the approach, the results of power reflection coefficients for an incident plane wave are compared with those given in reference [2] and [53]. In the calculation, the structure has a period of $d = 0.2\,\mu\text{m}$ and a height of $L = 0.95d$.

The numerical results for an array of cylinders standing in air is first carried out with both TM and TE incident waves, as shown in Fig. 2.9. The radius of each cylinder $c = 0.25d$ for TM case and $c = 0.375d$ for TE case. Cylinders are filled with a material with

relative permittivity $\epsilon_r^{(2)} = 2$. As seen in Fig. 2.9, good matches are observed in both TM and TE cases.

Then, power reflection coefficients are calculated for a periodic array of cylinders ($\epsilon_r^{(2)} = 2$) embedded in a single-layer slab ($\epsilon_r^{(1)} = 4$). A TE wave is incident upon the slab normally. Results are shown in Fig. 2.10, and good matches are observed.

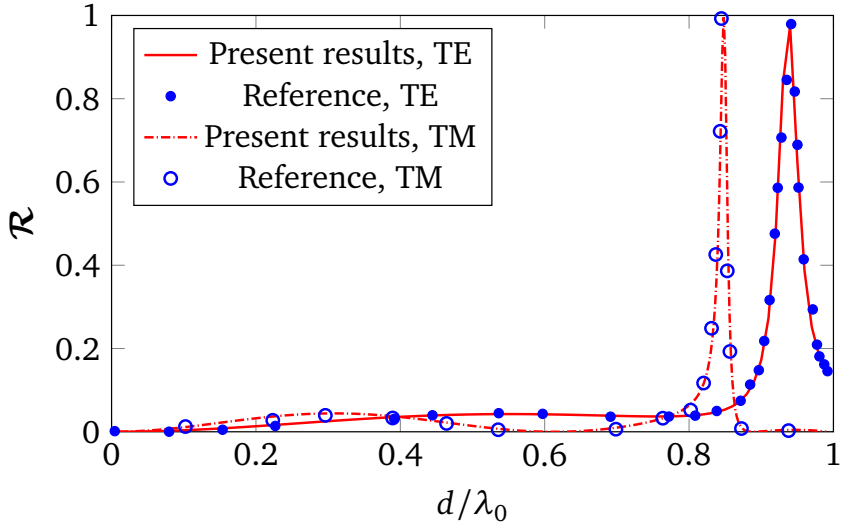

Fig. 2.9 Comparing the present results to the ones of reference [2] for TM wave with $c = 0.25d$ and TE wave with $c = 0.375d$. $d = 0.2\mu m$, $L = 0.95d$, $\epsilon_r^{(1)} = 1$, and $\epsilon_r^{(2)} = 2$.

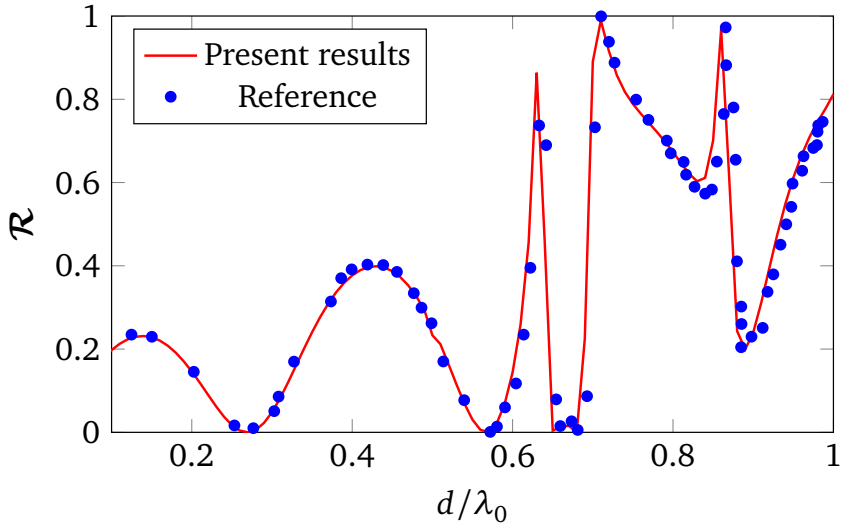

Fig. 2.10 Comparing the present results to the ones of [2] for TM wave with $c = 0.375d$, and fibers ($\epsilon_r^{(2)} = 2$) are embedded into a slab ($\epsilon_r^{(1)} = 4$) with $d = 0.2\mu m$ and $L = 0.95d$.

For lossy fibers within a dielectric matrix, an epoxy slab including an array of carbon fibers is considered with $d = \lambda^{\text{inc}} = 0.1\,\text{mm}$, $L = 2d$ and $c = 0.4d$. The power reflection

coefficients for both TM and TE waves are computed with $P = 0$, which is the 0-th mode. Results are compared with the one obtained with COMSOL FEM code, which is shown in Fig. 2.11. A good match is observed for incident angle varying from 0° to 90°. Slight difference appears when the incident angle is close to 90° because the absorption efficiency of the employed Perfectly Matched Layer in COMSOL FEM code is not very good at large incident angle close to 90°.

At the same time, the reflection of the periodically arranged conductive fiber array with several different conductivities of fibers is calculated, and numerical results of power reflection coefficients are given in Fig. 2.12. Obviously, increasing the conductivity of the fibers make the behavior of the structure becomes close to the one of a periodic fiber array with perfectly conducting fibers, and the power reflection coefficients of the array with higher conductive fibers is closer to the one of the array with metal fibers. The results of perfectly conducting metal fibers are obtained from reference [53] for comparison. As seen in Fig. 2.12, power reflection coefficients of high conductive fibers smoothly vary with frequency, and higher transmission coefficients are observed at higher frequency points.

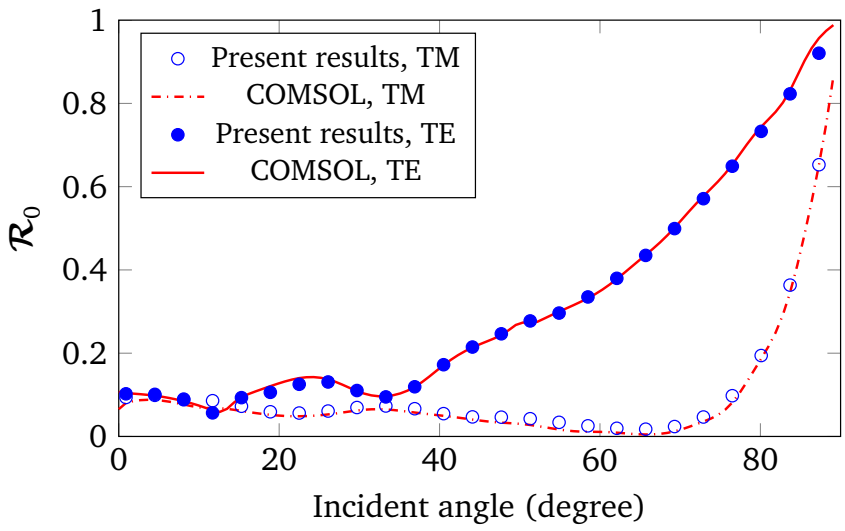

Fig. 2.11 Comparing the present results to the one from COMSOL for TM and TE cases, only the 0-th mode being under consideration. $d = \lambda_i = 0.1\,\text{mm}$, $L = 2d$ and $c = 0.4d$. $\epsilon_r^{(1)} = 3.6$, $\epsilon_r^{(2)} = 12$, $\sigma_2 = 3.3 \times 10^2\,\text{S/m}$.

The proposed approach is now focused onto power reflection and transmission properties of carbon or glass-fiber-reinforced polymers. Epoxy resin is the most common matrix material, its relative permittivity being taken as 3.6 and its conductivity as zero (below $10^{-10}\,\text{S/m}$ in practice). For glass fiber, relative permittivity ranges between ≈ 3.7 and 10, and its conductivity is close to zero. For carbon fiber, its relative permittivity ranges between ≈ 10 and 15, and its conductivity is high along its axial direction ($\approx$

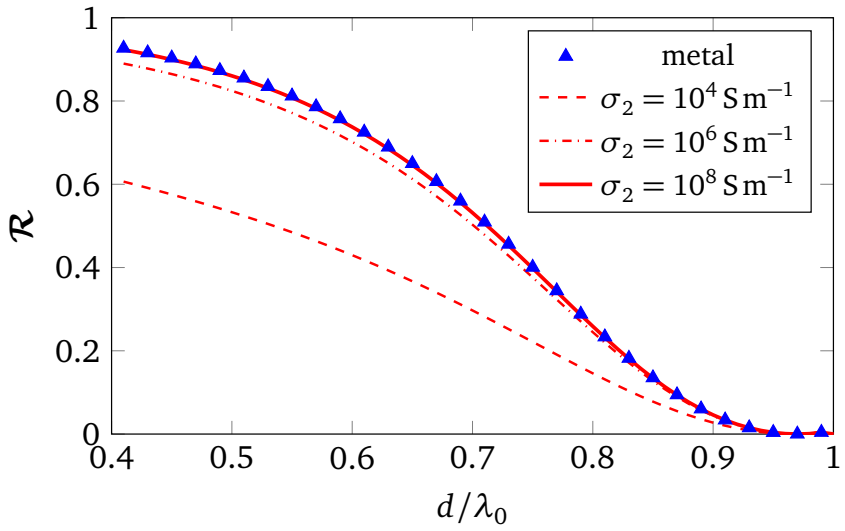

Fig. 2.12 Power reflection coefficients of a periodic array of carbon fibers with multiple conductivities. $\epsilon_r^{(1)} = 1$, $\epsilon_r^{(2)} = 12$, $c = 0.15d$. $d = 0.2\mu m$, $L = 0.95d$, TM incident wave.

2.5×10^6 S/m) [54–56], yet in the plane of its cross-section, the conductivity is much lower ($\approx 3.3 \times 10^2$ S/m) [57, 58], as now considered. In this chapter, a fiber-reinforced slab will be considered with $d = 0.1$ mm, $L = d$ and $c = 0.25d$. Epoxy ($\epsilon_r^{(1)} = 3.6$) is taken for the material of the slab. The fibers inside could be filled with either glass ($\epsilon_r^{(2)} = 6$) or graphite ($\epsilon_r^{(2)} = 12$, $\sigma = 3.3 \times 10^2$ S/m).

Power reflection and transmission coefficients of a glass-fiber reinforced slab is first computed with the proposed approach. Results are given in Fig. 2.13 for TM wave and Fig. 2.14 for TE wave. The angle of incidence is $\theta^{\mathrm{inc}} = 45°$. As can be seen, the variation of $\mathcal{R}$ is quite smooth at low frequency since only one or several propagating modes exist at low frequency and the 0-th mode dominates the electromagnetic behavior of the structure. On the other hand, the incident low-frequency TE wave can transmit the structure easier than TM wave. So higher reflection is observed with incident TM wave for $0 < d/\lambda^{\mathrm{inc}} < 0.3$.

Several peaks, some of which corresponding to total reflection, are observed at relative higher frequency, which is mainly caused by the strong interaction between the scattered field of the slab and the cylinder array, and multiple propagating modes are involved in these interactions. As seen from Fig. 2.13 and Fig. 2.14 that, the interaction appears to be stronger for TM incident wave.

Scattering by a carbon-fiber reinforced slab is also calculated for both TM and TE waves illuminating the slab with $\theta^{\mathrm{inc}} = 45°$. Power reflection, transmission and absorption coefficients are shown in Fig. 2.15 for TM wave and the one in Fig. 2.16 for TE wave. Because of carbon fibers are lossy, strong absorption is observed at high frequency. At the same time, the total reflecting phenomenon disappears. Comparing the absorption coefficients

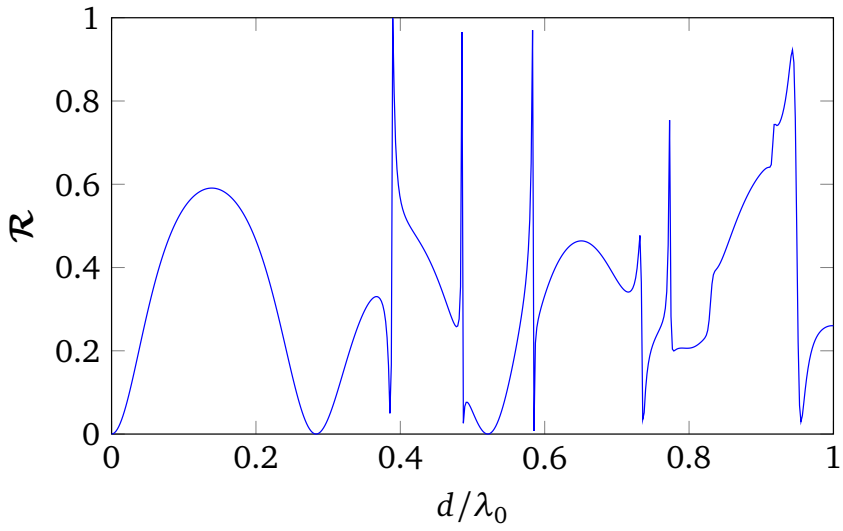

Fig. 2.13 Reflection of glass-fiber reinforced slab under TM wave illumination. $\epsilon_r^{(1)} = 3.6$, $\epsilon_r^{(2)} = 6$, $c = 0.25d$. $d = 0.1\,\text{mm}$, $L = d$.

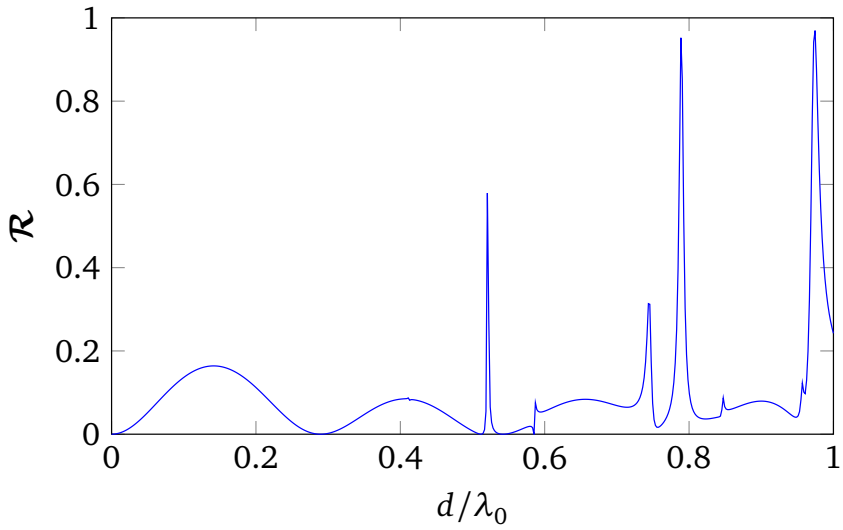

Fig. 2.14 Reflection of glass-fiber reinforced slab under TE wave illumination. $\epsilon_r^{(1)} = 3.6$, $\epsilon_r^{(2)} = 6$, $c = 0.25d$. $d = 0.1\,\text{mm}$, $L = d$.

for TE and TM waves, it is observed that the structure has stronger absorption to incident TE wave than TM wave at high frequency. Meanwhile, low frequency TE wave can transmit the structure more freely than TM wave. Especially in the microwave frequency band $10\,\text{GHz} < f < 60\,\text{GHz}$, quite strong transmission is observed for incident TE wave.

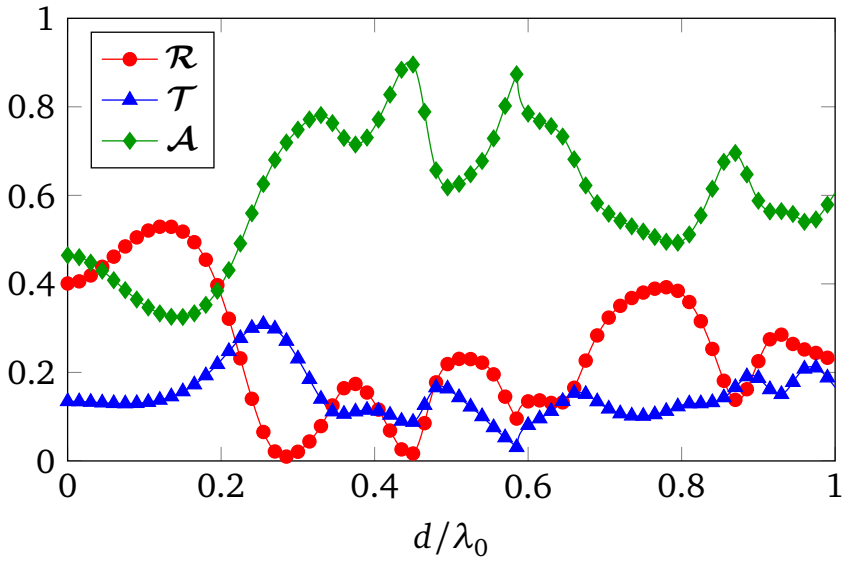

Fig. 2.15 Reflection, transmission and absorption of carbon-fiber based slab under illumination of TM wave. $\epsilon_r^{(1)} = 3.6$, $\epsilon_r^{(2)} = 12$, $\sigma = 3.3 \times 10^2$ S/m, $c = 0.25d$. $L = d = 0.1$ mm.

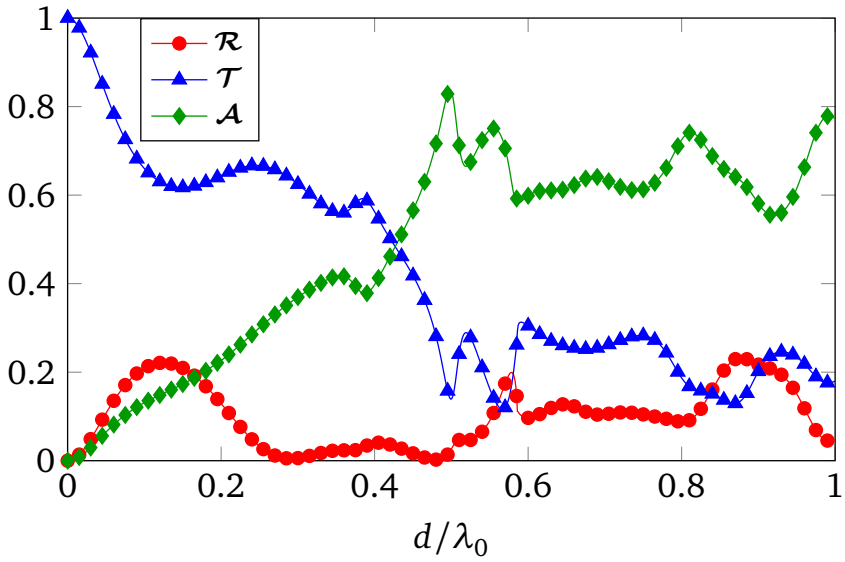

Fig. 2.16 Reflection, transmission and absorption of carbon-fiber based slab under illumination of TE wave. $\epsilon_r^{(1)} = 3.6$, $\epsilon_r^{(2)} = 12$, $\sigma = 3.3 \times 10^2$ S/m, $c = 0.25d$. $L = d = 0.1$ mm.

2.3 Scattering of Gaussian beam

Plane wave expansion of Gaussian beam is first obtained by the technique of Fourier transform. Then the expansion is discretized with quadrature scheme into a combination of multiple plane waves with different amplitude and different wave vectors. These plane waves are then taken as the wave incident upon the structure to produce the correspond-

ing scattered fields with the approach introduced above. The scattering of the beam can be obtained by superposing the scattered field of the corresponding plane waves. Enough plane waves are need to obtain a good convergence of both of the incident and scattered fields. Although the quadrature scheme used in this thesis is not the most efficient one, but it is applied since it is simple and sufficient for considered calculation. If necessary, Gaussian quadrature scheme is a good replacement for obtaining fast convergence of the fields with small number of plane waves.

2.3.1 Plane-wave expansion of Gaussian beam

Without loss of generality, the scattering of a Gaussian beam with its plane of incidence parallel with the x-z plane is considered in the thesis, which needs the two dimensions (2D) Fourier transforms to calculate the plane wave expansion. Following the discussion in Chapter 3 of [59], if the complex field distribution of a monochromatic disturbance is Fourier-analyzed across any plane, the various spatial Fourier components can be identified as plane waves traveling in different directions away from that plane, and the field amplitude at any other point (or across any other parallel plane) can be calculated by adding the contributions of these plane waves, taking due account of the phase shifts they have undergone during propagation.

Assuming that a plane wave $E(x,y,z)$ incident upon a transverse (x,y) plane traveling with a component of propagation in the positive z direction. Therefore, on the $z=0$ plane, the field can be represented with $E(x,y,0)$ which has a 2D Fourier transform given by

$$\widetilde{E}(f_x,f_y,0)=\iint_{-\infty}^{+\infty}E(x,y,0)\exp\big(-i2\pi(f_x x+f_y y)\big)dxdy. \tag{2.60}$$

With (2.60), $E(x,y,0)$ is written as

$$E(x,y,0)=\iint_{-\infty}^{+\infty}\widetilde{E}(f_x,f_y,0)\exp\big(i2\pi(f_x x+f_y y)\big)df_x df_y, \tag{2.61}$$

which is actually the inverse Fourier transform corresponding to equation (2.60). The field $E(x,y,z)$ at any point could be expressed as [59]

$$E(x,y,z)=\iint_{-\infty}^{+\infty}\widetilde{E}(f_x,f_y,0)\exp(i2\pi f_z z)\exp\big(i2\pi(f_x x+f_y y)\big)df_x df_y, \tag{2.62}$$

which is the relation between $E(x,y,z)$ and $E(x,y,0)$. This will be used for expanding Gaussian beams shown in Fig. 2.17, where a 2D Gaussian beam impinges upon a plane

obliquely with an incident angle ϕ^{inc}. Local and global coordinate system $x'y'z'$ and xyz are used. In the global coordinate system, the center of the beam is located at (x_0, z_0), which is also the origin of the local coordinate system for describing the beam.

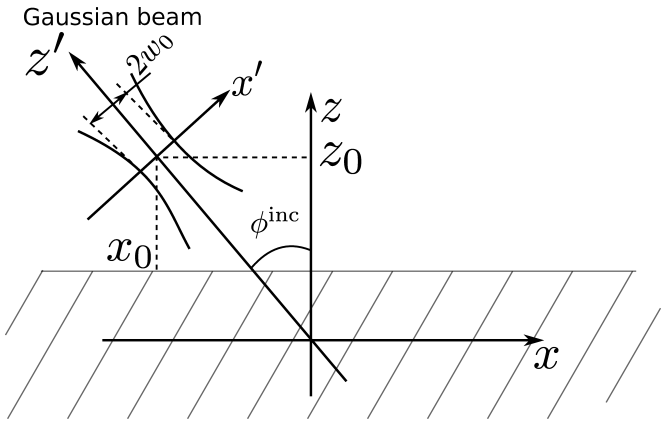

Fig. 2.17 A Gaussian beam incident upon a plane obliquely.

The beam is expressed in the following form in the local coordinate system $x'y'z'$,

$$E_{y'}(x',z') = E_0 \frac{w_0}{w(z')} \exp\left(-\frac{x^2}{w^2(z')} - i\frac{kx'^2}{2R(z')} - ikz' + i\arctan\frac{z'}{z'_0}\right), \tag{2.63}$$

where z' is the distance propagated from the plane where the wave-front is flat (the beam waist at $z'=0$), w_0 is the radius of the $1/e^2$ irradiance contour at the beam waist (the spot size at $z'=0$), $z'_0 = \pi w_0^2/\lambda$. $R(z)$ and $w(z)$ are the wave front radius of curvature and the spot size after the beam propagating a distance z', they are defined as

$$w(z') = w_0\left[1+\left(\frac{z'}{z'_0}\right)^2\right]^{\frac{1}{2}}, \qquad R(z') = z'\left[1+\left(\frac{z'_0}{z'}\right)^2\right]. \tag{2.64}$$

In the $z'=0$ plane,

$$E_{y'}(x',0) = E_0 \exp\left(-\frac{x'^2}{w_0^2}\right). \tag{2.65}$$

Applying the Fourier transform (2.60) to both sides of eq.(2.65) yields

$$\widetilde{E}_{y'}(f_{x'},0) = \int_{-\infty}^{+\infty} E_0 \exp\left(-\frac{x'^2}{w_0^2}\right)\exp\left(-2\pi i f_{x'}x'\right)df_{x'}. \tag{2.66}$$

According to the Gaussian function integral formula

$$\int_{-\infty}^{+\infty} \exp\left(-ax^2-2bx\right)dx = \sqrt{\frac{\pi}{a}}\exp\left(\frac{b^2}{a}\right), \quad a>0, \tag{2.67}$$

the integral result of equation (2.66) is easily obtained. It is read as

$$\widetilde{E}_{y'}(f_{x'},0) = \sqrt{\pi}w_0E_0\exp\left(-\pi^2 f_{x'}^2 w_0^2\right). \tag{2.68}$$

Hence, the field $E_{y'}(x',z')$ can be written into the following expression by using equation (2.62),

$$E_{y'}(x',z') = \sqrt{\pi}w_0E_0\int_{-\infty}^{+\infty}\exp\left(-\pi^2 f_{x'}^2 w_0^2\right)\exp\left[2\pi i\left(f_{z'}z'+f_{x'}x'\right)\right]df_{x'}. \tag{2.69}$$

If $\mathbf{f} = f_{x'}\hat{x}+f_{z'}\hat{z}$, and the wave vector $\mathbf{k}$ is defined as $2\pi\mathbf{f}=\mathbf{k}=k_{x'}\hat{x}+k_{z'}\hat{z}=k(\sin\vartheta\hat{x}+\cos\vartheta\hat{y})$, where $k=|\mathbf{k}|$ and ϑ is the angle between $\mathbf{k}$ and the z' axis, then equation (2.69) takes the form

$$\begin{aligned} E_{y'}(x',z') =& \frac{w_0E_0}{2\sqrt{\pi}}\int_{-k}^{k}\exp\left(-\frac{k_{x'}^2w_0^2}{4}\right)\exp\left[i\left(k_{x'}x'+k_{z'}z'\right)\right]dk_{x'} \\ =& \frac{kw_0E_0}{2\sqrt{\pi}}\int_{-\pi/2}^{\pi/2}\exp\left(-\frac{k^2w_0^2\sin^2\vartheta}{4}\right)\exp\left[ik\left(\sin\vartheta x'+\cos\vartheta z'\right)\right]\cos\vartheta d\vartheta \end{aligned} \tag{2.70}$$

In equation (2.70) the limits of integration have been modified with respect to eq.(2.69) to only account for the nonevanescent uniform plane waves, since evanescent plane waves carry no energy away [59]. Applying the Gaussian quadrature scheme to equation (2.70), then it is written into a discrete elementary plane wave spectrum [60], which reads as

$$\begin{aligned} E_{y'}(x',z') =& \frac{kw_0E_0}{2\sqrt{\pi}}\sum_{n=1}^{N}\exp\left(-\frac{k^2w_0^2\sin^2\vartheta_n}{4}\right)\exp\left[ik\left(\sin\vartheta_n x'+\cos\vartheta_n z'\right)\right]\cos\vartheta_n\Delta\vartheta \\ =& \sum_{n=1}^{N}A'(\vartheta_n)\exp\left[ik\left(\sin\vartheta_n x'+\cos\vartheta_n z'\right)\right], \end{aligned} \tag{2.71}$$

where

$$A'(\vartheta_n) = \frac{kw_0E_0}{2\sqrt{\pi}}\exp\left(-\frac{k^2w_0^2\sin^2\vartheta_n}{4}\right)\cos\vartheta_n\Delta\vartheta. \tag{2.72}$$

The expression (2.71), which is valid in the local coordinate system $x'y'z'$, is then transformed into the global coordinate system xyz through the relation [61]

$$\begin{aligned} x' =& (x - x_0)\cos\phi^{\text{inc}} + (z - a - z_0)\sin\phi^{\text{inc}} \\ z' =& (x - x_0)\sin\phi^{\text{inc}} - (z - a - z_0)\cos\phi^{\text{inc}}, \end{aligned} \tag{2.73}$$

where ϕ^{inc} is the incident angle of the Gaussian beam wave as shown in Figure 2.17. So the plane-wave expansion of Gaussian beam in the global coordinate system is

$$E_y(x,z) = \sum_{n=1}^{N} A(\vartheta_n)\exp\left[ik\left[x\sin(\vartheta_n + \phi^{\text{inc}}) - (z-a)\cos(\vartheta_n + \phi^{\text{inc}})\right]\right], \tag{2.74}$$

with $A(\vartheta_n)$ being defined as

$$\begin{aligned} A(\vartheta_n) =& \frac{kw_0E_0}{2\sqrt{\pi}}\exp\left(\frac{-k^2w_0^2\sin^2\vartheta_n}{4}\right) \\ & \times\exp\left[-ik\left[x_0\sin(\vartheta_n + \phi^{\text{inc}}) - z_0\cos(\vartheta_n + \phi^{\text{inc}})\right]\right]\cos\vartheta_n\Delta\vartheta. \end{aligned} \tag{2.75}$$

With the plane-wave expansion of the Gaussian beam given in equation (2.74), the n-th plane wave component can be treated as an incident wave, and it is written as

$$E_{y,n}(x,z) = A(\vartheta_n)e^{i\left(\alpha_n^0 x - \beta_n^0(z-a)\right)}, \tag{2.76}$$

with $\alpha_n^0 = k\sin(\vartheta_n + \phi^{\text{inc}})$ and $\beta_n^0 = \sqrt{k^2 - \alpha_n^{0\,2}}$. The superscript 0 indicates that they are the components of the wave vector in region Ω_0.

Combining expansion (2.6) with the incident wave (2.76), the field representation in region 0 is written as

$$E_{0y}^{+}(x,z) = \sum_{p\in\mathbb{Z}}\left(A(\vartheta_n)e^{-i\beta_{0p}(z-a)}\delta_{0p} + R_p e^{i\beta_{0p}(z-a)}\right)e^{i\alpha_p x}, \tag{2.77}$$

where R_p is the reflection coefficient of the plane wave indexed by p, δ_{0p} is the Kronecker symbol which is introduced to generate necessary matrices. α_p and β_{0p} are the components of the wave vector $\mathbf{k}$ in the x and z directions respectively, $\alpha_p = \alpha_n^0 + 2p\pi/d$, $\beta_{0p} = \sqrt{k^2 - \alpha_p^2}$.

With equation (2.77), the scattered field of each elementary plane wave in equation (2.74) could be obtained by the method presented in section 2.2. The scattered field of the incident Gaussian beam follows by superposing the scattered fields of all the elementary plane waves [61].

2.3.2 Numerical investigation

To accurately model a Gaussian beam, N in (2.74) must be properly chosen. One defines a relative error

$$Error = \frac{1}{N_p} \sum_{1}^{N_p} \frac{|\tilde{E}_{y'} - E_{y'}|^2}{|E_{y'}|^2} \tag{2.78}$$

taking $\tilde{E}_{y'}$ as the approximate value of the plane wave expansion and $E_{y'}$ referring to the exact value from (2.63). N_p is the total number of field points computed. Fig. 2.18

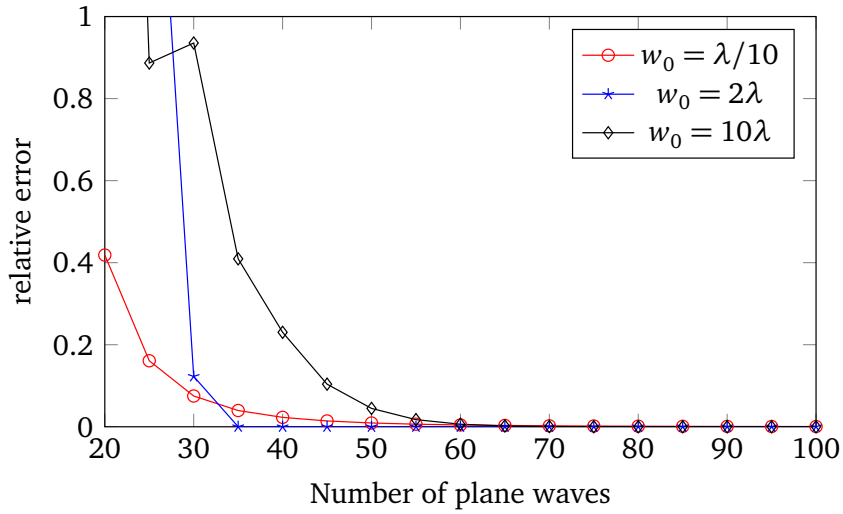

Fig. 2.18 Convergence of incident field with different values of N which is the number of plane waves. $\lambda = 0.1mm$.

shows the relative error for region $-4\lambda_0 < x' < 4\lambda_0$ and $-3\lambda_0 < z' < 3\lambda_0$, meshed into $N_p = 200 \times 200$, λ_0 as the wavelength of the beam. When $N > 60$, in all cases shown, the approximation works well, the largest error being below 10^{-6}. Expanding the Gaussian beam into 80 plane waves enables to achieve a relative error less than 10^{-6}.

To verify the convergence of the scattered field, a glass-fiber ($\epsilon_r^{(2)} = 6$) based epoxy ($\epsilon_r^{(1)} = 3.6$) slab is considered with $d = \lambda^{\text{inc}} = 0.1mm$, $c = 0.25d$, $L = d$. The beam is incident upon the structure obliquely with $\theta^{\text{inc}} = 45°$ and $\omega_0 = 2\lambda^{\text{inc}}$. A region of $-10\lambda^{\text{inc}} < x < 10\lambda^{\text{inc}}$ and $-5\lambda^{\text{inc}} < z < 5\lambda^{\text{inc}}$ is divided into $N_p = 200 \times 100$ grids. The total and scattered field in this region are computed with different number of plane waves, which is the value of N. The relative error is given in Fig. 2.19. It is observed that the relative error decreases quickly with the increase of N. With $N = 200$, a good accuracy with relative error less than 1×10^{-6} is achieved. In the following calculations, 250 plane waves are used to expand the beam which produces a relative error less than 1×10^{-7}.

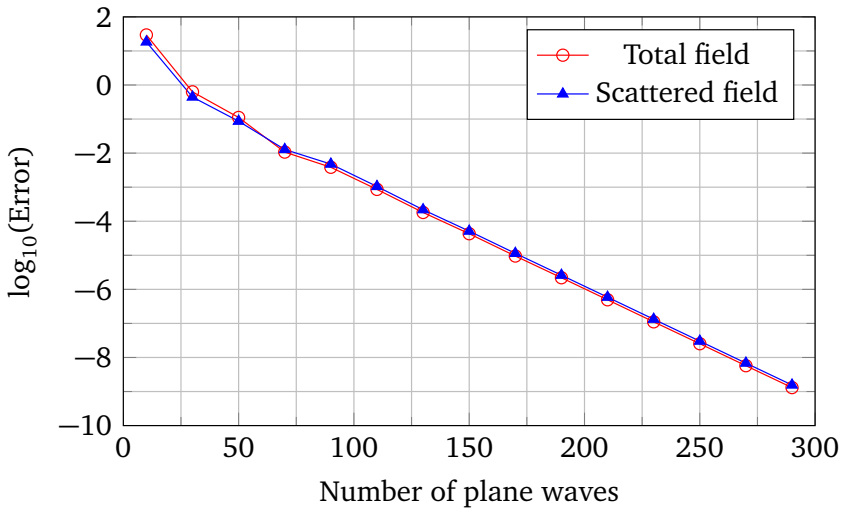

Fig. 2.19 Convergence of scattered field with different values of N as the number of plane-wave components. $\lambda = 0.1mm$.

The above structure is used here to carry out the numerical examples, wherein carbon ($\epsilon_r^{(2)} = 12$, $\sigma = 3.3 \times 10^2$ S/m), glass and perfectly conducting metal fibers are considered. The background materials are all epoxy ($\epsilon_r^{(2)} = 3.6$). A Gaussian beam with $\lambda^{\text{inc}} = 0.1$ mm, $\omega_0 = 2\lambda^{\text{inc}}$ and $x_0 = z_0 = 0$ impinges upon the structure obliquely with $\theta^{\text{inc}} = 45°$.

The region of $-10\lambda^{\text{inc}} < x < 10\lambda^{\text{inc}}$ and $-5\lambda^{\text{inc}} < z < 5\lambda^{\text{inc}}$ is meshed into $N_p = 500 \times 250$ grids to produce a fine resolution. Numerical results for carbon, glass, and metal (perfectly conducting) fibers are given in Fig. 2.20, Fig. 2.21 and Fig. 2.22. Strong scattering is observed in all the three results, fields are scattered into many directions, but two strong beams show up along the direction of reflection and transmission.

For glass-fiber reinforced epoxy slab, fields are observed at the points located in the slab but more than $4\lambda^{\text{inc}}$ away from the center of the beam. These fields might be a result of the fact that the strong interaction between the boundaries of the slab and the fibers produces some modes which can propagate along the direction of the periodicity. But at the same location, no field is observed in the slab reinforced by perfectly conducting fibers.

2.4 Homogenized single-layer slab

The composite structure can be homogenized to produce an anisotropic homogeneous slab. The original periodic structure with different permittivities of the slab and fibers is then replaced by this slab which is characterized by a tensor of effective permittivity. In practice, the calculations corresponding to low-frequency incident waves can then be carried out

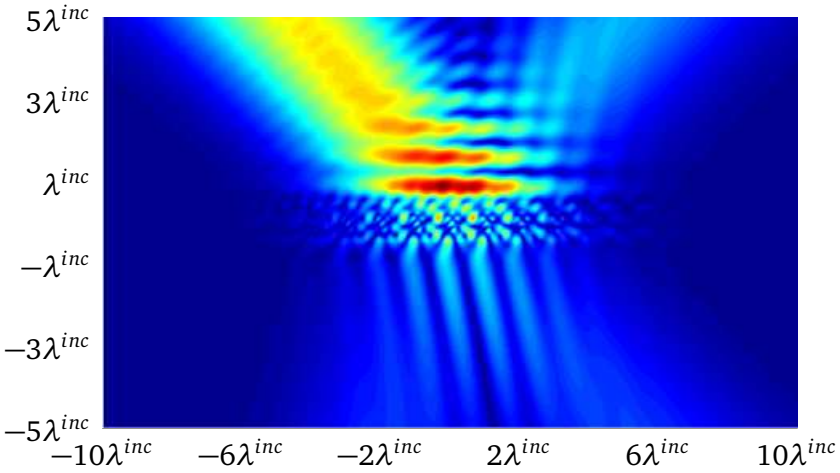

Fig. 2.20 Total field distribution of Gaussian beam scattered by carbon-fiber based slab, $N = 250$, $\lambda = 0.1mm$.

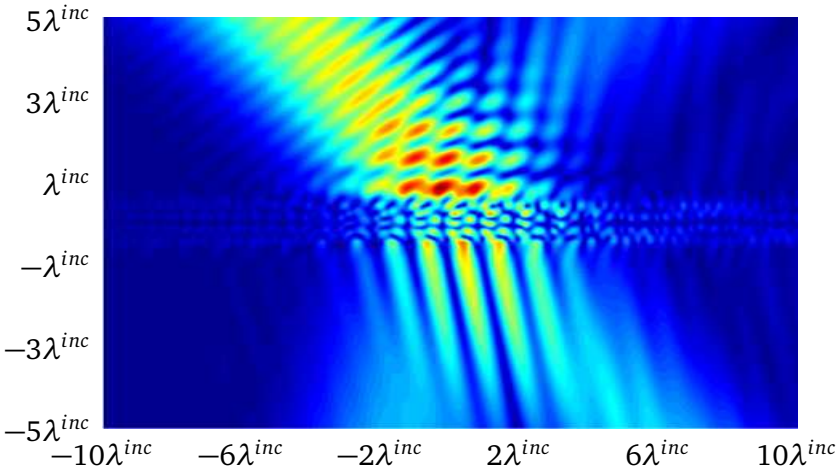

Fig. 2.21 Total field distribution of Gaussian beam scattered by glass-fiber based slab, $N = 250$, $\lambda = 0.1mm$.

approximately with that homogeneous single-layer slab. This homogenization will not help for revealing some details of the structure, but this technique could simplify and accelerate the corresponding calculations without losing accuracy, especially for the structures with defects inside. Combining it with imaging techniques such as MUltiple SIgnal Classification (MUSIC) method, some of the inverse problems can be solved efficiently.

In this thesis, the single-layer periodic composite is homogenized with the approach given in Appendix C, and the corresponding effective permittivities are calculated with the equations (C.17) and (C.25). Several numerical results are proposed to compare with the ones obtained with multipole method and plane wave expansions. The efficacy and accuracy of the method is verified.

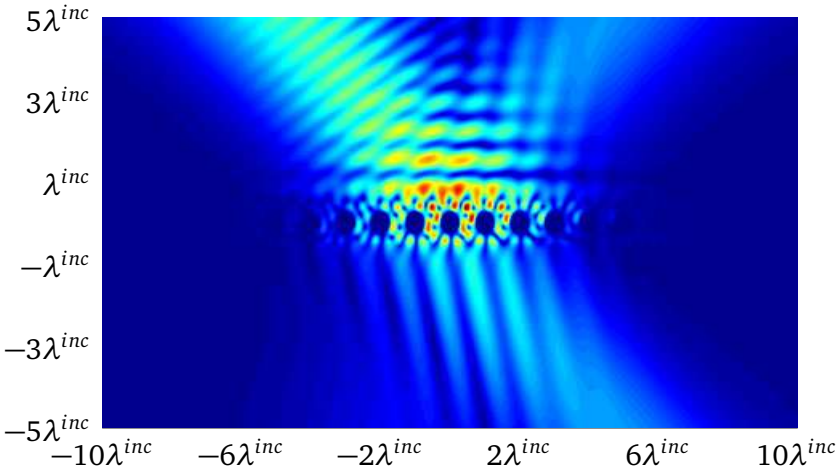

Fig. 2.22 Total field distribution of Gaussian beam scattered by metal-fiber based slab, $N = 250$, $\lambda = 0.1mm$.

A glass-fiber ($\epsilon_r^{(2)} = 6$) reinforced epoxy ($\epsilon_r^{(1)} = 3.6$) slab is first considered for TM (E-polarized) and TE (H-polarized) wave illumination. In the considered 2D cases, the effective permittivities are all scalar and denoted as $\bar{\epsilon}_r^{(tm)}$ and $\bar{\epsilon}_r^{(te)}$ for TM and TE waves, respectively. Since the current structure is lossless, $\bar{\epsilon}_r^{(tm)}$ and $\bar{\epsilon}_r^{(te)}$ are frequency independent. Assuming that the slab is characterized with the parameters $L = d = 0.1$ mm and $c = 0.25d$, then the effective permittivities are given as $\bar{\epsilon}_r^{(tm)} = 4.0712$ and $\bar{\epsilon}_r^{(te)} = 3.9068$.

With the obtained effective permittivity, power reflection coefficients for the considered single-layer glass-fiber-based composite are calculated. The results are then compared with the exact value, as shown in Fig. 2.23 for TM wave and Fig. 2.24 for TE wave. A quite good agreement is obtained for TM wave at the frequency band 10 GHz to 60 GHz, but an obvious deviation is observed between 30 GHz and 60 GHz for the reflection of TE wave. For lower frequency, better agreement can be obtained.

Now, consider a carbon-fiber reinforced epoxy slab with $L = d = 0.1$ mm and $c = 0.25d$. Since the fibers are lossy, the effective permittivity will vary with frequency.

Allow the real and imaginary parts of $\bar{\epsilon}_r^*$ to be $\Re\bar{\epsilon}_r^*$ and $\Im\bar{\epsilon}_r^*$, where $*$ is te or tm in according to TE or TM wave illumination. Fig. 2.25 shows the variance of $\Re\bar{\epsilon}_r^{(tm)}$ and $\Im\bar{\epsilon}_r^{(tm)}$ with frequency. According to equation (C.17), $\Re\bar{\epsilon}_r^{tm}$ will not be influenced by the imaginary part of the permittivity of the materials in slab and fibers, so $\Re\bar{\epsilon}_r^{tm}$ does not change with frequency. $\Im\bar{\epsilon}_r^{tm}$ decreases quickly with the increase of frequency.

For TE wave illumination, the variance of $\Re\bar{\epsilon}_r^{te}$ and $\Im\bar{\epsilon}_r^{te}$ are given in Fig. 2.26 and Fig. 2.27. According to equation (C.25), $\Re\bar{\epsilon}_r^{te}$ is influenced by the imaginary part of the permittivity of the materials in slab and fibers, so $\Re\bar{\epsilon}_r^{te}$ changes for different frequencies. As seen in Fig. 2.27 that $\Im\bar{\epsilon}_r^{te}$ is much smaller than $\Im\bar{\epsilon}_r^{tm}$. For TE wave, the electric components

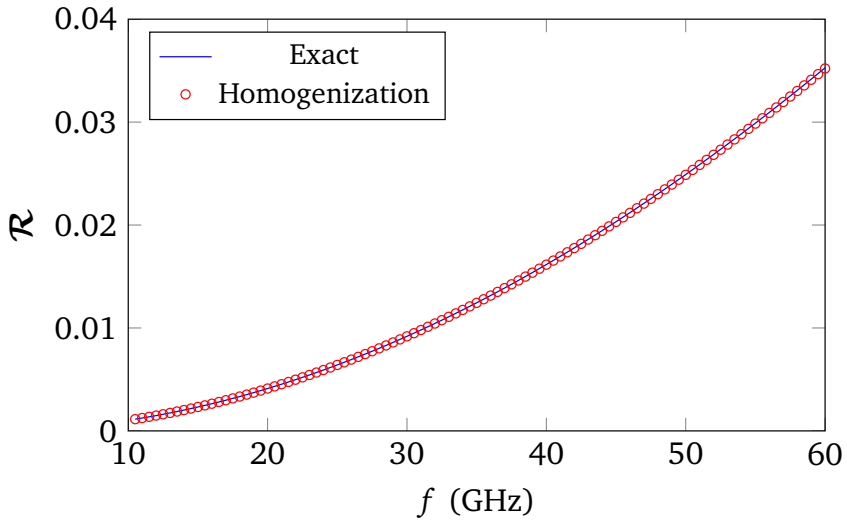

Fig. 2.23 Reflection coefficient of homogenized glass-fiber-based slab for normally incident TM wave, $L = d = 0.1\,\text{mm}$, $c = 0.25d$.

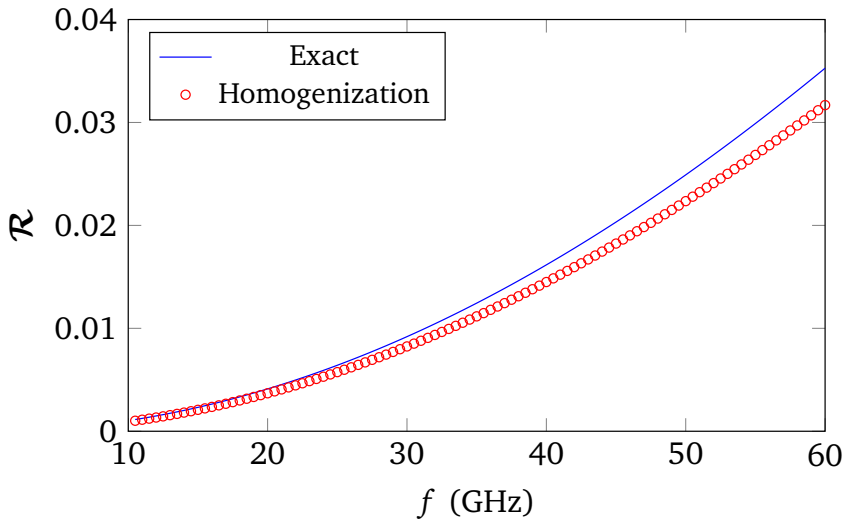

Fig. 2.24 Reflection coefficient of homogenized glass-fiber-based slab for normally incident TE wave, $L = d = 0.1\,\text{mm}$, $c = 0.25d$.

lie in the common cross section of the fibers, where the conductive fibers are isolated by the non-conductive materials in the slab, which in fact leads to a much smaller $\Im\bar{\epsilon}_r^{te}$.

With effective permittivities, power reflection and transmission coefficients are calculated for the homogenized slab. The results are compared with the exact values obtained by using the approach given in this chapter, as shown in Fig. 2.28 for TM wave and Fig. 2.29 for TE wave. The results obtained with the homogenized slab match the exact values quite well for TM wave. The biggest relative error is less than 0.3%. A good approximate results are also obtained for TE wave, with biggest relative error of 4% at high frequency.

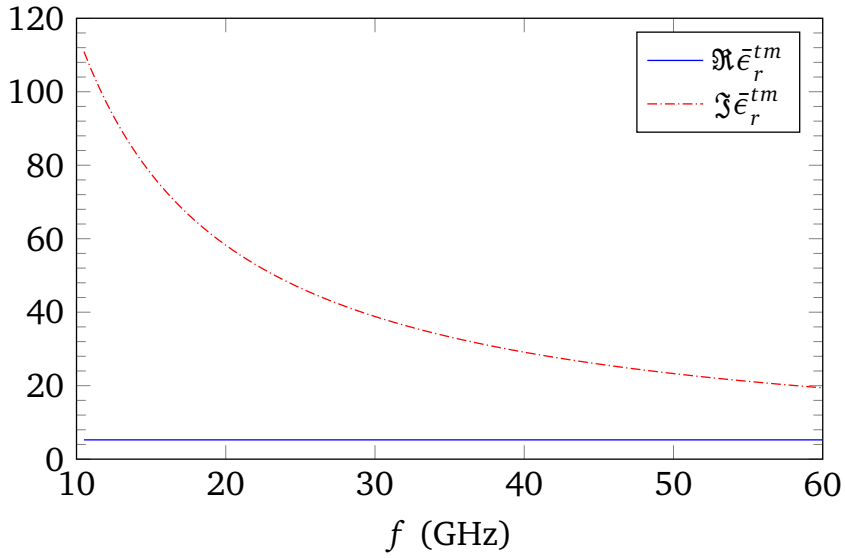

Fig. 2.25 Real and imaginary parts of effective permittivity of a carbon fiber slab varying with frequency, $L = d = 0.1\,\text{mm}$, $c = 0.25d$, TM wave.

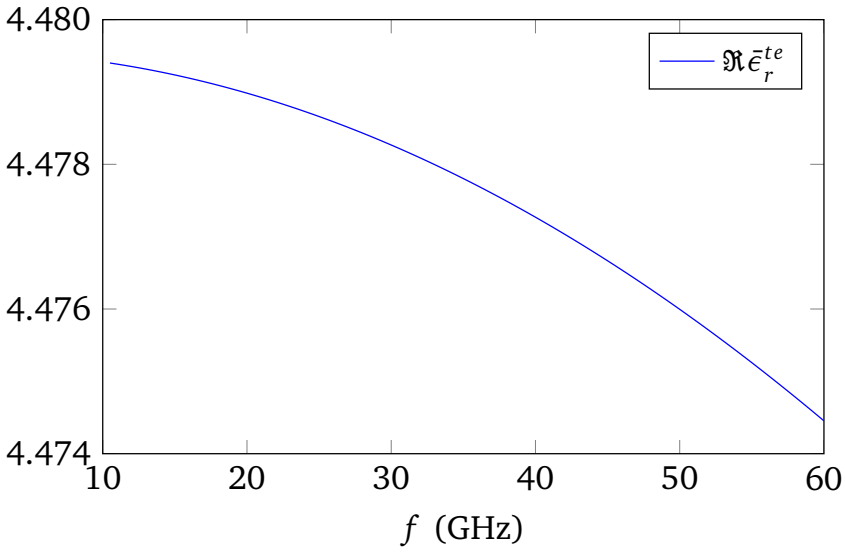

Fig. 2.26 Real part of effective permittivity of a carbon fiber slab varying with frequency, $L = d = 0.1\,\text{mm}$, $c = 0.25d$, TE wave.

For obliquely incident waves, reflection coefficients varying with the angle of incidence are given in Fig. 2.30 and Fig. 2.31 for TM and TE waves impinging upon a glass-fiber reinforced epoxy slab. The frequency of incident wave is 60 GHz. As seen that the exact results and the ones obtained with homogenized slab match well, with the largest relative error of 0.12% and 0.9% for TM and TE waves.

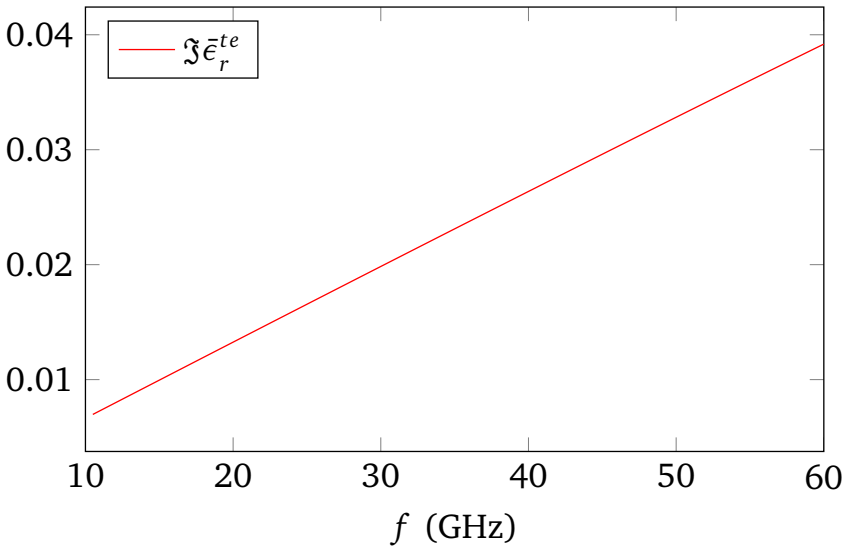

Fig. 2.27 Imaginary parts of effective permittivity of a carbon fiber slab varying with frequency, $L = d = 0.1\,\text{mm}$, $c = 0.25d$, TE wave.

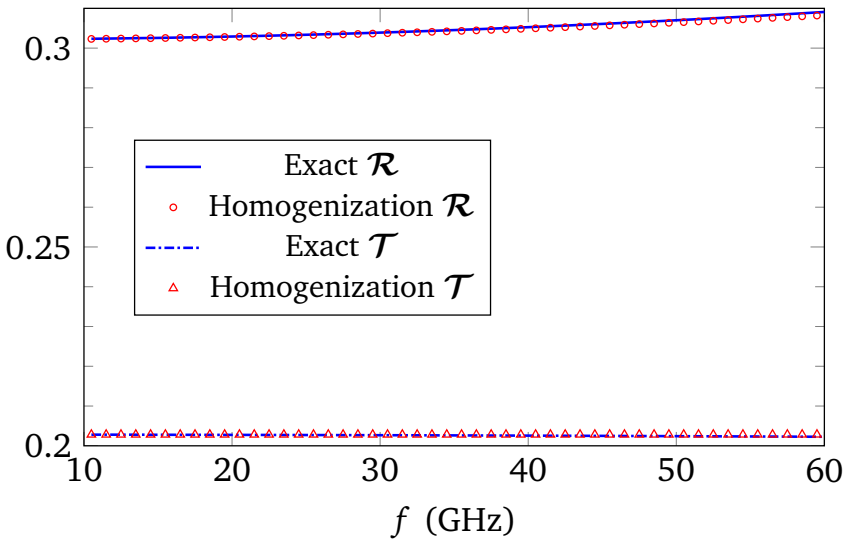

Fig. 2.28 Power reflection and transmission coefficients of a carbon-fiber reinforced slab, $L = d = 0.1\,\text{mm}$, $c = 0.25d$, TM wave normal illumination.

For carbon-fiber reinforced epoxy slab, power reflection and transmission coefficients varying with the angle of incidence are given in Fig. 2.32 and Fig. 2.33 for TM and TE waves. The frequency of incident wave is 60 GHz. As seen that good matches are observed for TM wave. But obvious difference is observed in TE wave case, and the largest relative error is less than 4%. According to Fig. 2.27, $\Im\bar{\epsilon}_r^{te}$ is very small, which leads to the small absorption of TE wave, as seen in Fig. 2.33.

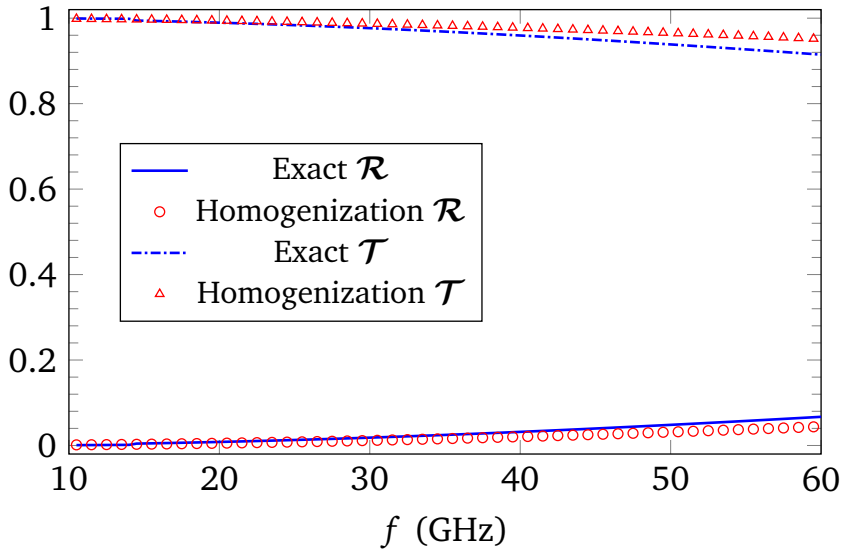

Fig. 2.29 Power reflection and transmission coefficients of a carbon-fiber reinforced slab, $L = d = 0.1\,\text{mm}$, $c = 0.25d$, TE wave normal illumination.

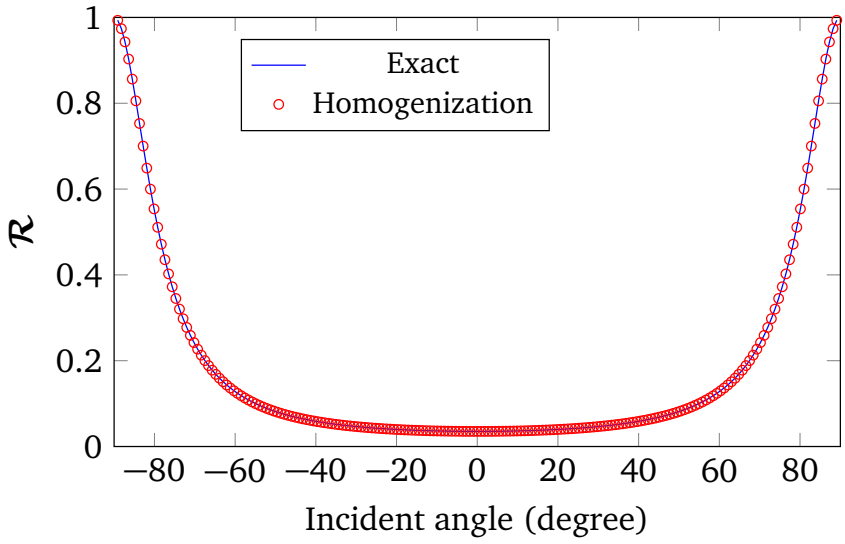

Fig. 2.30 Power reflection coefficients of a glass-fiber reinforced slab, $L = d = 0.1\,\text{mm}$, $c = 0.25d$, $f = 60\,\text{GHz}$, TM wave oblique illumination.

In addition, the scattering of Gaussian beam is also calculated with the effective permittivity of glass-fiber reinforced slab. Considering E-polarized beam wave with $\lambda^{\text{inc}} = 5\,\text{mm}$, the width of the beam is $\omega_0 = 2\lambda^{\text{inc}}$, and the center is located at $x_0 = z_0 = 0$. Field distribution of normally incident beam is given in Fig. 2.34. Exact field is given in Fig. 2.35. As seen, the field matches well, and the largest relative error is less than 0.2%.

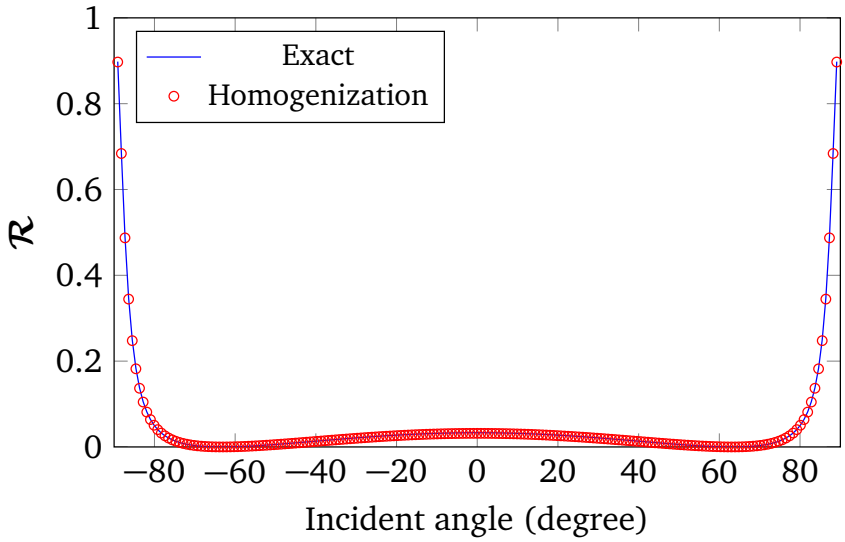

Fig. 2.31 Power reflection coefficients of a glass-fiber reinforced slab, $L = d = 0.1\,\text{mm}$, $c = 0.25d$, $f = 60\,\text{GHz}$, TE wave oblique illumination.

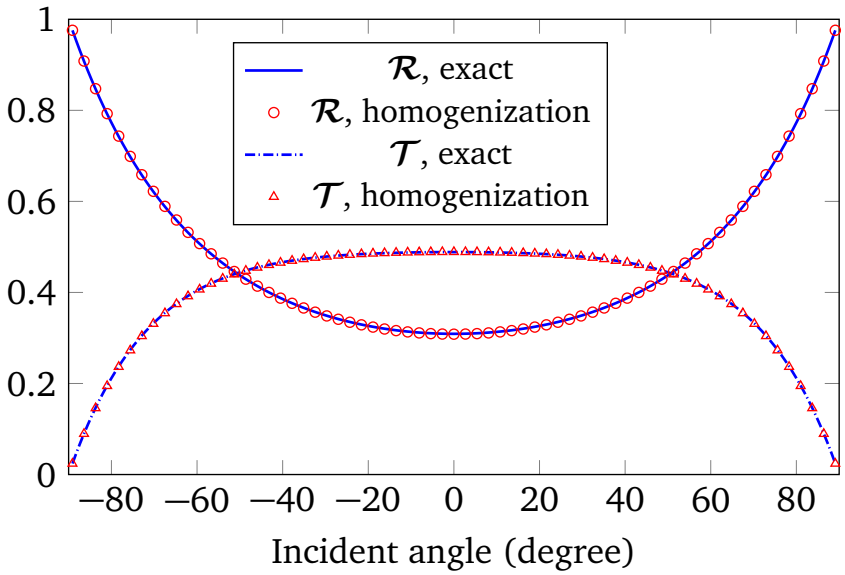

Fig. 2.32 Power reflection and transmission coefficients of a carbon-fiber reinforced slab, $L = d = 0.1\,\text{mm}$, $c = 0.25d$, $f = 60\,\text{GHz}$, TM wave oblique illumination.

2.5 Summary

A theoretical and numerical investigation of the scattering of TM or TE incident wave by a single layer slab reinforced by an periodic array of infinity long circular fibers is carried out in this chapter, and the fundamental principles of the corresponding approaches are introduced.

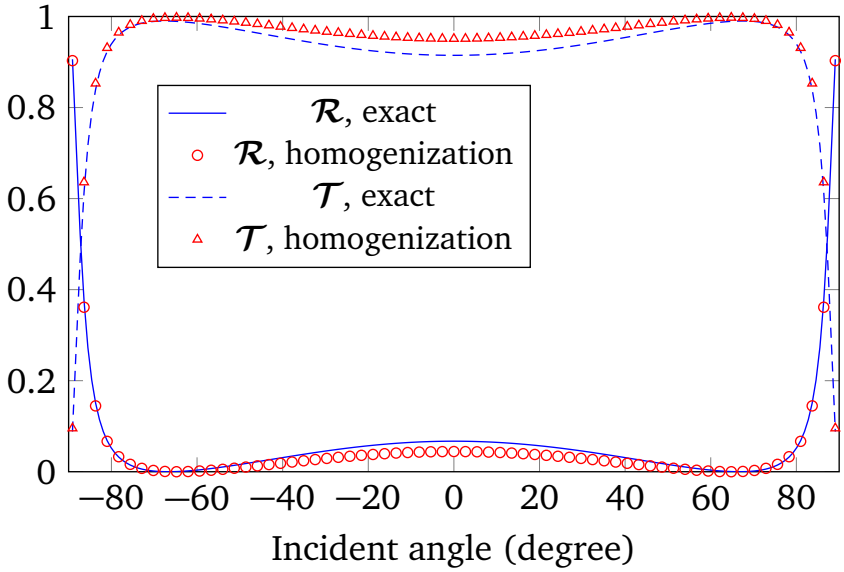

Fig. 2.33 Power reflection and transmission coefficients of a carbon-fiber reinforced slab, $L = d = 0.1\,\text{mm}$, $c = 0.25d$, $f = 60\,\text{GHz}$, TE wave oblique illumination.

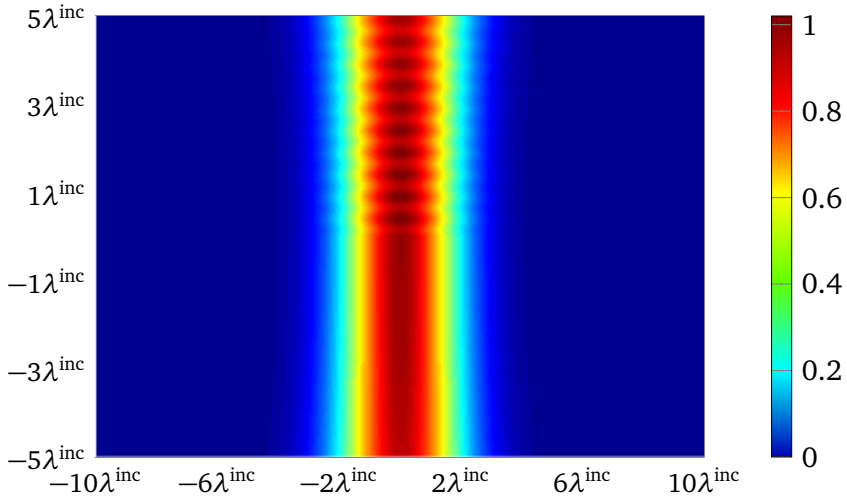

Fig. 2.34 Total field distribution of an E-polarized Gaussian beam normally impinging upon the homogenized slab, $L = d = 0.1\,\text{mm}$, $c = 0.25d$.

The periodic structure in fact divides the whole space into four regions with the boundaries of the fibers and the ones of slab as limits. According to the Floquet theorem, the periodicity of the structure forces the fields in all these regions to be periodic, which then allows these fields to be plane-wave expanded. Then both plane-wave and cylindrical forms of periodic Green's function are applied to evaluate an integration along the boundaries of one unit cell with Green's second identity, which yields the relations of the field expansion coefficients in the slab. Mode-matching at the upper and lower boundaries of the slab

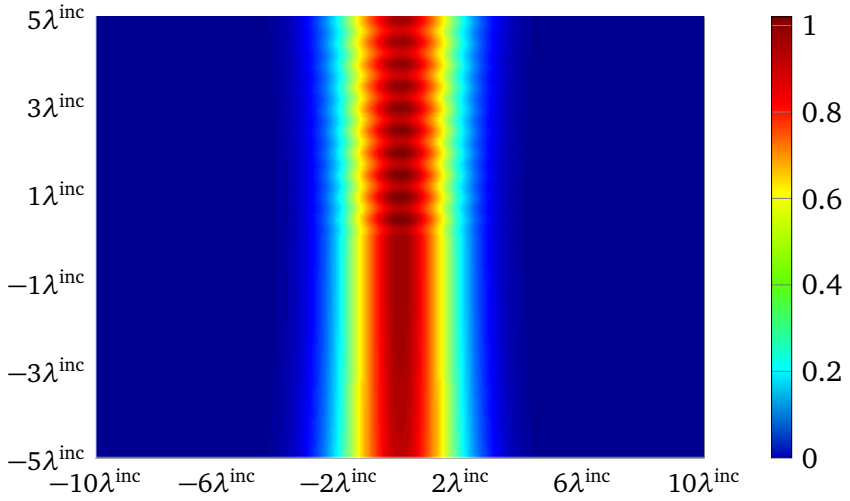

Fig. 2.35 Total field distribution of an E-polarized Gaussian beam normally impinging upon the glass-fiber based slab, $L = d = 0.1\,\text{mm}$, $c = 0.25d$.

produces a linear system which is combined with the relation between the field expansion coefficients inside the slab to produce the final numerical solution of the reflection and transmission coefficients of each mode used in the field expansion. The power reflection and transmission coefficients are then produced by using Poynting theorem. The approach is validated by comparing the present results with those existing in literature.

Since the homogenization technique is practically used for nondestructive testing of defects in composites, the considered single-layer periodic structure is also approximately investigated by replacing it with an homogeneous slab, which is characterized by effective permittivities. Several numerical examples are given for verifying the efficacy and accuracy of the homogenization technique.

Chapter 3

Scattering of conically incident plane wave by a fiber-based slab

Scattering of electromagnetic wave impinging upon the structure conically is important for investigating the response of the structure to an elementary point source. Here, the scattering of a conically incident plane wave is carried out with a similar method as the one used for the 2D case. For the investigation, the fields are first split into transverse and longitudinal components. The longitudinal components are first expanded into a plane-wave or cylindrical harmonic series. The transverse components of the fields are obtained directly with the corresponding relations. The method used for solving the 2D scattering problem is then applied. In fact, the considered 2.5D problem has no much more complexity than the 2D case, which actually makes the calculation cheap and efficient.

As it will be presented, the differences between the approach for 2D and for 2.5D cases are the larger linear systems produced by mode-matching at the boundaries. Because of the longitudinal components of the wave vector, the electric and magnetic field are coupled together, which makes the relation between the transverse and longitudinal components of fields becomes more complicated than the one used in the 2D case, which then leads to a more complicated relation between the field expansion coefficients. But the solution of the large linear system can still be obtained analytically, hence producing explicit mathematical expressions for all the unknowns.

3.1 Preliminary formulation

Here, conically incident plane waves with the defined coordinate system are considered, then the wave vector of the incident wave needs to be defined as $\vec{k}^{\text{inc}} = k_x^{\text{inc}}\hat{x} + k_y^{\text{inc}}\hat{y} -$

$k_z^{\text{inc}}\hat{z}$, the angle between the z-axis and $\vec{k}^{\text{inc}}$ is given as ϑ, and the one between the x-axis and the projection of $\vec{k}^{\text{inc}}$ in the longitudinal x-y plane is defined as φ, see Fig. 3.1a, then $k_x^{\text{inc}} = -k^{\text{inc}}\sin\vartheta\cos\varphi$, $k_y^{\text{inc}} = k^{\text{inc}}\sin\vartheta\sin\varphi$, $k_z^{\text{inc}} = k^{\text{inc}}\cos\vartheta$. $\vec{k}_t^{\text{inc}}$ is defined as the transverse component of $\vec{k}^{\text{inc}}$ within the x-z plane. Thus, the incident fields are defined as $\boldsymbol{\mathcal{E}}(x,y,z) = \mathbf{E}^{\text{inc}} e^{i(k_x^{\text{inc}}x + k_y^{\text{inc}}y - k_z^{\text{inc}}z)}$ and $\boldsymbol{\mathcal{H}}(x,y,z) = \mathbf{H}^{\text{inc}} e^{i(k_x^{\text{inc}}x + k_y^{\text{inc}}y - k_z^{\text{inc}}z)}$ with implicit time-dependence $e^{-i\omega t}$, where $\mathbf{E}^{\text{inc}} = E_x^{\text{inc}}\hat{x} + E_y^{\text{inc}}\hat{y} + E_z^{\text{inc}}\hat{z}$ and $\mathbf{H}^{\text{inc}} = H_x^{\text{inc}}\hat{x} + H_y^{\text{inc}}\hat{y} + H_z^{\text{inc}}\hat{z}$.

Denote the wave vector in the j-th region as $\vec{k}_j = \vec{k}_{tj} + k_{yj}\hat{y}$, where $\vec{k}_{tj} = k_{xj}\hat{x} - k_{zj}\hat{z}$ and $k_{tj}^2 = k_j^2 - k_{yj}^2$. Assuming that $\alpha_j = k_{xj}$ and $\beta_j = k_{zj}$, then $\vec{k}_{tj} = \hat{x}\alpha_j - \hat{z}\beta_j$.

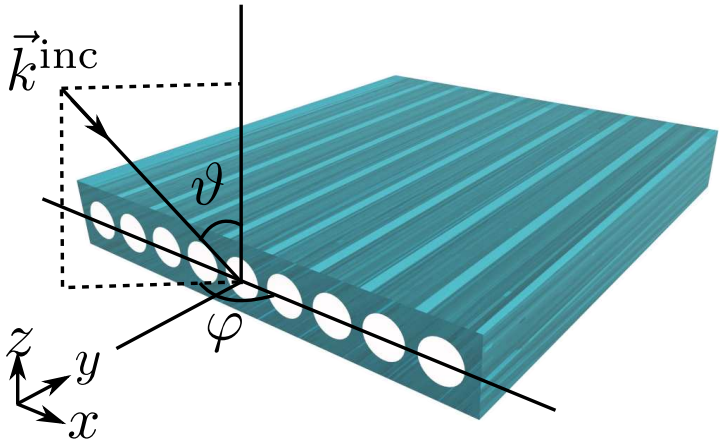

(a) The conically incident electromagnetic plane wave;

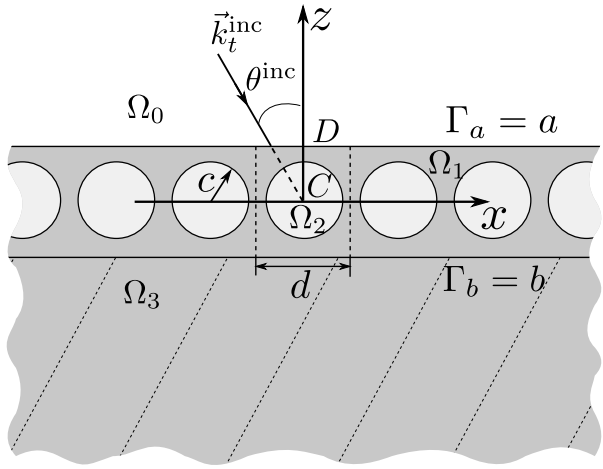

(b) Side view of the structure with transverse components of the incident wave;

Fig. 3.1 A slab including a periodic set of cylindrical fibers under illumination of conically incident electromagnetic plane wave with an angle of ϑ and φ.

In all regions, each field mode is characterized by its propagation constant k_{jy} in the y direction and its transverse dependence of the fields lying in the x-z plane, which means that $\boldsymbol{\mathcal{E}}_j(x,y,z) = \mathbf{E}_j(x,z)e^{ik_{jy}y}$, and $\boldsymbol{\mathcal{H}}_j(x,y,z) = \mathbf{H}_j(x,z)e^{ik_{jy}y}$, where $\boldsymbol{\mathcal{E}}_j$ and $\boldsymbol{\mathcal{H}}_j$ denote

the electric and magnetic fields. Defining the scaled magnetic field as $\mathbf{K}_j(x,z) = Z\mathbf{H}_j(x,z)$, where Z is the impedance of free space, and $Z = \sqrt{\mu_0/\epsilon_0}$. Each such field satisfies the Helmholtz equation

$$(\nabla_t^2 + k_{tj}^2)\mathbf{V}_j = 0, \tag{3.1}$$

where $\mathbf{V}_j$ denotes either $\mathbf{E}_j$ or $\mathbf{K}_j$, and $\nabla_t^2 = \frac{\partial^2}{\partial x^2} + \frac{\partial^2}{\partial z^2}$.

The key feature to exploit here is still the periodicity of the cylinders, which forces the field to be periodic along the direction $\hat{x}$. Allied with the plane wave nature of the field and the Floquet theorem, it yields

$$\mathbf{V}_j(x+d,y,z) = \mathbf{V}_j(x,y,z)e^{i\alpha_0 d}. \tag{3.2}$$

Each x- and y-component of $\mathbf{V}_j$ is continuous across the planar interfaces Γ_a and Γ_b [62]. Decomposing the field $\boldsymbol{\mathcal{E}}_j$ and $\boldsymbol{\mathcal{H}}_j$ into longitudinal and transverse components, parallel to and orthogonal with the cylinder axes, respectively, denoted by subscripts y and t, then

$$\boldsymbol{\mathcal{E}} = (\mathbf{E}_t + E_y\hat{y})e^{ik_{jy}y}, \tag{3.3a}$$

$$\boldsymbol{\mathcal{H}} = (\mathbf{H}_t + H_y\hat{y})e^{ik_{jy}y}. \tag{3.3b}$$

Index j is neglected here since the decomposition is established in all regions. Noticing that $\mathbf{V} = (\mathbf{V}_t + V_y\hat{y})$ and $\mathbf{V}_t = V_x\hat{x} + V_z\hat{z}$, its divergence and curl are read as

$$\nabla\cdot\mathbf{V} = \nabla_t\cdot\mathbf{V}_t + ik_yV_y \tag{3.4}$$

and

$$\nabla\times\mathbf{V} = \nabla_t\times\mathbf{V}_t + ik_y\hat{y}\times\mathbf{V}_t - \hat{y}\times\nabla_tV_y, \tag{3.5}$$

where ∇_t is $\frac{\partial}{\partial x}\hat{x} + \frac{\partial}{\partial z}\hat{z}$ in the Cartesian coordinate system and $\frac{\partial}{\partial r}\hat{r} + \frac{1}{r}\frac{\partial}{\partial\theta}\hat{\theta}$ in the polar coordinate system. The index j is neglected here since the above holds in all regions.

Allowing $k = \omega\sqrt{\mu_0\epsilon_0}$, which is the propagation constant in air, the transverse fields are easily obtained from the longitudinal ones [42, 63]:

$$\mathbf{E}_t = \frac{i}{k_t^2}[k_y\nabla_tE_y - \sqrt{\mu_0/\epsilon_0}k\mu_r\hat{y}\times\nabla_tH_y], \tag{3.6a}$$

$$\mathbf{H}_t = \frac{i}{k_t^2}[k_y\nabla_tH_y + \sqrt{\epsilon_0/\mu_0}k\epsilon_r\hat{y}\times\nabla_tE_y]. \tag{3.6b}$$

In Cartesian coordinates, the tangential components E_x and K_x are obtained directly from the above equations:

$$E_x(x,z) = \frac{i}{k_t^2}\left[k_y \frac{\partial E_y}{\partial x} - k\mu_r \frac{\partial K_y}{\partial z}\right], \tag{3.7a}$$

$$K_x(x,z) = \frac{i}{k_t^2}\left[k_y \frac{\partial K_y}{\partial x} + k\epsilon_r \frac{\partial E_y}{\partial z}\right]. \tag{3.7b}$$

Hence, the appearance of the y dependence of $e^{ik_y y}$ in the electric and magnetic fields makes them coupled together, which complicates the calculation with conically incident wave. In the thesis, the longitudinal components of the field, saying V_y, is always firstly plane-wave expanded, then the field V_x is obtained from V_y with (2.2a) and (2.2c) in the considered 2D case or (3.7) for the 2.5D or 3D cases.

3.1.1 Scattering of conically incident plane wave by single cylinder

Once a conically incident plane wave is under the consideration, the relation between longitudinal fields and the transverse ones in cylindrical coordinates can be obtained from (3.6),

$$\begin{aligned} E_\theta &= \frac{i}{k_t^2}\left[\frac{k_y}{r}\frac{\partial E_y}{\partial \theta} + k\mu_r \frac{\partial K_y}{\partial r}\right], \\ K_\theta &= \frac{i}{k_t^2}\left[\frac{k_y}{r}\frac{\partial K_y}{\partial \theta} - k\epsilon_r \frac{\partial E_y}{\partial r}\right]. \end{aligned} \tag{3.8}$$

Here, k_t is the absolute value of the transverse components of the wave vector.

The longitudinal fields exterior the cylinder are expanded with cylindrical harmonics as

$$E_{1y} = \sum_{n\in\mathbb{Z}} \left[B_n^e H_n^{(1)}(k_{1t}c) + A_n^e J_n(k_{1t}c)\right] e^{in\theta} e^{ik_y y}, \tag{3.9a}$$

$$K_{1y} = \sum_{n\in\mathbb{Z}} \left[B_n^h H_n^{(1)}(k_{1t}c) + A_n^h J_n(k_{1t}c)\right] e^{in\theta} e^{ik_y y}. \tag{3.9b}$$

In the cylinder, the electric and scaled magnetic fields E_{2y} and K_{2y} are expanded in the same way, which gives

$$E_{2y} = \sum_{n\in\mathbb{Z}} C_n^e J_n(k_{2t}r) e^{in\theta} e^{ik_y y}, \tag{3.10a}$$

$$K_{2y} = \sum_{n\in\mathbb{Z}} C_n^h J_n(k_{2t}r) e^{in\theta} e^{ik_y y}. \tag{3.10b}$$

Continuity at the boundary of the cylinder gives

$$\begin{aligned} C_n^e J_n(k_{2t}c) =& B_n^e H_n^{(1)}(k_{1t}c) + A_n^e J_n(k_{1t}c), \\ C_n^h J_n(k_{2t}c) =& B_n^h H_n^{(1)}(k_{1t}c) + A_n^h J_n(k_{1t}c). \end{aligned} \tag{3.11}$$

Substituting (3.9) and (3.10) into (3.8) to get the field expressions for E_θ and K_θ fields exterior and interior of the cylinder, and matching them at the boundary gives

$$\begin{aligned} &\frac{ink_y}{k_{2t}^2 c} C_n^e J_n(k_{2t}c) - \frac{k\mu_{2r}}{k_{2t}} C_n^h J_n'(k_{2t}c) \\ =&\frac{ink_y}{k_{1t}^2 c}[B_n^e H_n^{(1)}(k_{1t}c) + A_n^e J_n(k_{1t}c)] - \frac{k\mu_{1r}}{k_{1t}}[B_n^h H_n'^{(1)}(k_{1t}c) + A_n^h J_n'(k_{1t}c)] \end{aligned} \tag{3.12a}$$

$$\begin{aligned} &\frac{ink_y}{k_{2t}^2 c} C_n^h J_n(k_{2t}c) + \frac{k\epsilon_{2r}}{k_{2t}} C_n^e J_n'(k_{2t}c)] \\ =&\frac{ink_y}{k_{1t}^2 c}[B_n^h H_n^{(1)}(k_{1t}c) + A_n^h J_n(k_{1t}c)] + \frac{k\epsilon_{1r}}{k_{1t}}[B_n^e H_n'^{(1)}(k_{1t}c) + A_n^e J_n'(k_{1t}c)]. \end{aligned} \tag{3.12b}$$

Eliminating C_n^e and C_n^h from (3.11) and (3.12) produces

$$\begin{bmatrix} D_1 & D_2 \\ D_5 & D_6 \end{bmatrix} \begin{bmatrix} A_n^e \\ A_n^h \end{bmatrix} = \begin{bmatrix} D_3 & D_4 \\ D_7 & D_8 \end{bmatrix} \begin{bmatrix} B_n^e \\ B_n^h \end{bmatrix}, \tag{3.13}$$

where the coefficients D_i depend on n and are defined as

$$\begin{aligned} D_1 =& \frac{ink_y}{c}\left(\frac{1}{k_{2t}^2} - \frac{1}{k_{1t}^2}\right) J_n(k_{1t}c), \quad D_2 = \frac{k\mu_{2r}}{k_{2t}} \frac{J_n'(k_{2t}c)}{J_n(k_{2t}c)} J_n(k_{1t}c) - \frac{k\mu_{1r}}{k_{1t}} J_n'(k_{1t}c), \\ D_3 =& \frac{ink_y}{c}\left(\frac{1}{k_{1t}^2} - \frac{1}{k_{2t}^2}\right) H_n^{(1)}(k_{1t}c), \quad D_4 = -\frac{k\mu_{2r}}{k_{2t}} \frac{J_n'(k_{2t}c)}{J_n(k_{2t}c)} H_n^{(1)}(k_{1t}c) + \frac{k\mu_{1r}}{k_{1t}} H_n'^{(1)}(k_{1t}c), \\ D_5 =& -\frac{k\epsilon_{2r}}{k_{2t}} \frac{J_n'(k_{2t}c)}{J_n(k_{2t}c)} J_n(k_{1t}c) + \frac{k\epsilon_{1r}}{k_{1t}} J_n'(k_{1t}c), \quad D_6 = \frac{ink_y}{c}\left(\frac{1}{k_{2t}^2} - \frac{1}{k_{1t}^2}\right) J_n(k_{1t}c), \\ D_7 =& \frac{k\epsilon_{2r}}{k_{2t}} \frac{J_n'(k_{2t}c)}{J_n(k_{2t}c)} H_n^{(1)}(k_{1t}c) - \frac{k\epsilon_{1r}}{k_{1t}} H_n'^{(1)}(k_{1t}c), \quad D_8 = \frac{ink_y}{c}\left(\frac{1}{k_{1t}^2} - \frac{1}{k_{2t}^2}\right) H_n^{(1)}(k_{1t}c), \end{aligned}$$

Transforming (3.13) into matrix form yields

$$\mathbf{B} = \boldsymbol{\mathcal{L}}\mathbf{A}, \tag{3.15}$$

which will be widely used for studying the scattering of multilayered composites. In the calculation the matrix $\boldsymbol{\mathcal{L}}$ is quite important, which is actually the key to build the relation

of the plane-wave expansion coefficients between layers. It is defined as

$$\boldsymbol{\mathcal{L}} = \begin{bmatrix} \mathrm{diag}\left\{L_n^{ee}\right\} & \mathrm{diag}\left\{L_n^{eh}\right\} \\ \mathrm{diag}\left\{L_n^{he}\right\} & \mathrm{diag}\left\{L_n^{hh}\right\} \end{bmatrix}, \tag{3.16}$$

where $\mathrm{diag}\{x_n\}$ represents a diagonal matrix with x_n as its diagonal elements. The coefficients L_n^{ee}, L_n^{eh}, L_n^{he} and L_n^{hh} are defined as

$$\begin{aligned} L_n^{ee} &= \frac{D_8D_1 - D_4D_5}{D_3D_8 - D_4D_7}, \quad L_n^{eh} = \frac{D_8D_2 - D_4D_6}{D_3D_8 - D_4D_7}, \\ L_n^{he} &= \frac{D_3D_5 - D_1D_7}{D_3D_8 - D_4D_7}, \quad L_n^{hh} = \frac{D_3D_6 - D_2D_7}{D_3D_8 - D_4D_7}. \end{aligned} \tag{3.17}$$

3.2 Field representations

The field representations of the longitudinal components in regions Ω_0 and Ω_3 are plane-wave expanded as

$$E_{0y}(x,z) = \sum_{p\in\mathbb{Z}} (E_y^{\mathrm{inc}} e^{-i\beta_{0p}(z-a)}\delta_{p0} + R_p^e e^{i\beta_{0p}(z-a)}) e^{i\alpha_p x}, \tag{3.18a}$$

$$K_{0y}(x,z) = \sum_{p\in\mathbb{Z}} (K_y^{\mathrm{inc}} e^{-i\beta_{0p}(z-a)}\delta_{p0} + R_p^h e^{i\beta_{0p}(z-a)}) e^{i\alpha_p x}, \tag{3.18b}$$

$$E_{3y}(x,z) = \sum_{p\in\mathbb{Z}} T_p^e e^{i\left(\alpha_p x - \beta_{3p}(z-b)\right)}, \tag{3.18c}$$

$$K_{3y}(x,z) = \sum_{p\in\mathbb{Z}} T_p^h e^{i(\alpha_p x - \beta_{3p}(z-b))}. \tag{3.18d}$$

$R_p^{e,h}$ and $T_p^{e,h}$ are the reflection and transmission coefficients of the plane wave indexed by p, superscripts e and h relate to electrical and scaled magnetic field respectively. δ_{p0} the Kronecker symbol, $\alpha_p = \alpha_0 + 2p\pi/d$, $\beta_{jp} = \sqrt{k_{tj}^2 - \alpha_p^2}$. α_p is continuous across Γ_a and Γ_b.

To get the field representation in region Ω_1, the periodic Green's function which satisfies

$$(\nabla_t^2 + k_{t1}^2) G(\mathbf{r}) = \sum_{n=-\infty}^{+\infty} \delta(\mathbf{r} - nd\hat{x}) e^{i\alpha_0 nd} \tag{3.19}$$

is needed. In cylindrical coordinates, $\mathbf{r} = (r,\theta)$, the periodic Green's function is given as

$$G(\mathbf{r}) = -\frac{i}{4} \sum_{n=-\infty}^{+\infty} e^{i\alpha_0 nd} H_0^{(1)}(k_{t1}|\mathbf{r} - nd\hat{\mathbf{x}}|).x \tag{3.20}$$

Applying Graf's addition theorem [47] to the right-hand side of equation (3.20) yields a second form of G:

$$G(\mathbf{r}) = -\frac{i}{4}H_0^{(1)}(k_{t1}r) - \frac{i}{4}\sum_{l=-\infty}^{+\infty}\mathscr{S}_m J_m(k_{t1}r)e^{il\theta}, \tag{3.21}$$

$\mathscr{S}_m$ is lattice sums which are defined as

$$\mathscr{S}_m = \sum_{n=1}^{+\infty}H_m^{(1)}(k_{t1}nd)[e^{i\alpha_0 nd} + (-1)^m e^{-i\alpha_0 nd}]. \tag{3.22}$$

The series and the corresponding approaches of calculation have been widely discussed and introduced in section 2.2.6. The plane wave form of the periodic Green's function [37] (3.20) is also needed here, it is written as

$$G(\mathbf{r}) = \frac{1}{2id}\sum_{p=-\infty}^{+\infty}\frac{1}{\beta_p}e^{i(\alpha_p x + \beta_p|z|)}. \tag{3.23}$$

Allowing field $\mathbf{V}_j$ to stand for either $\mathbf{E}_j$ or $\mathbf{K}_j$ which are defined as $\boldsymbol{\mathcal{E}}_j(x,y,z) = \mathbf{E}_j(x,z)e^{ik_{jy}y}$ and $\boldsymbol{\mathcal{K}}_j(x,y,z) = \mathbf{K}_j(x,z)e^{ik_{jy}y}$. Concentrating on the primary cell given in Fig. 3.1b, the longitudinal fields V_{1y} satisfy

$$V_{1y}(\mathbf{r}) = \oint_{C+D} V_{1y}(\mathbf{r_1})\nabla G(\mathbf{r}-\mathbf{r_1}) - G(\mathbf{r}-\mathbf{r_1})\nabla V_{1y}(\mathbf{r_1})d\mathbf{r_1} \tag{3.24}$$

Following the same treatment given in section 2.2, the field representations for $c < z < a$ and $b < z < -c$ read as

$$E_{1y}^{\pm}(x,z) = \sum_{p\in\mathbb{Z}}(f_{ep}^{+}e^{-i\beta_{1p}z} + g_{ep}^{-}e^{i\beta_{1p}z})e^{i\alpha_p x} + \sum_{p\in\mathbb{Z}}\sum_{m\in\mathbb{Z}}B_m^e Q_{pm}^{\pm}e^{i(\alpha_p x \pm \beta_{1p}z)}, \tag{3.25a}$$

$$K_{1y}^{\pm}(x,z) = \sum_{p\in\mathbb{Z}}(f_{hp}^{+}e^{-i\beta_{1p}z} + g_{hp}^{-}e^{i\beta_{1p}z})e^{i\alpha_p x} + \sum_{p\in\mathbb{Z}}\sum_{m\in\mathbb{Z}}B_m^h Q_{pm}^{\pm}e^{i(\alpha_p x \pm \beta_{1p}z)}, \tag{3.25b}$$

where the plane wave expansions in region Ω_1 are the same as given in (2.38). Obviously, the relation (2.41) also holds true here. The signs + and − correspond to $z > c$ and $z < -c$. B_m^e and B_m^h are the multipole expansion coefficients, $Q_{pm}^{\pm} = \frac{2(-i)^m}{d\beta_{1p}}e^{\pm im\theta_p}$. Transverse fields E_x, E_z, K_x and K_z in both Cartesian and cylindrical coordinates are easily obtained from equations (3.7a) and (3.7b).

Matching the modes at both boundaries Γ_a and Γ_b, the coefficients R_p^e, R_p^h, T_p^e, T_p^h, f_{ep}^{+}, g_{ep}^{-}, f_{hp}^{+} and g_{hp}^{-} are expressed with the unknown coefficients B_m^e and B_m^h, as detailed in

Appendix B. Coefficients B_m^e and B_m^h are obtained by solving the Rayleigh's identity established by matching the fields at the boundary of the fibers [42]. The general idea of the approach is illustrated in Fig. 3.2, which also shows the similarity between the methods used for solving the 2D and 2.5D scattering problems.

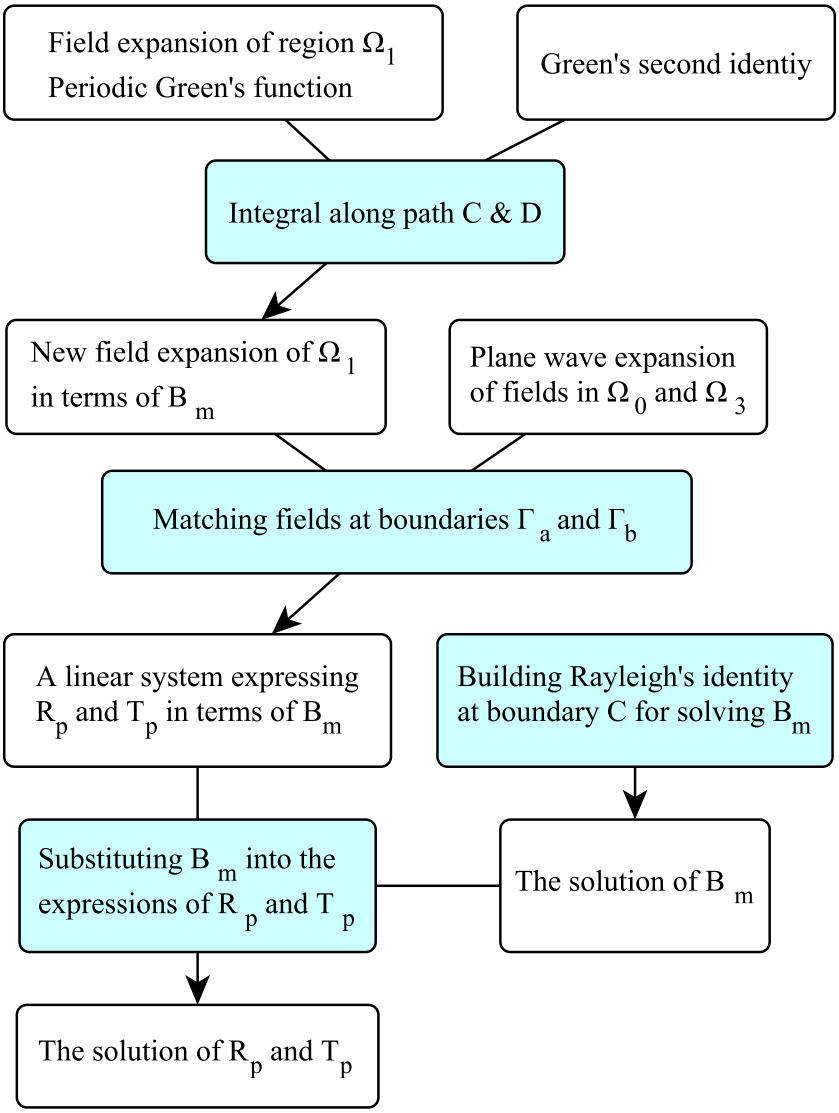

Fig. 3.2 The general idea of the approach which is based on the mode-matching, plane-wave expansion and multipole expansion methods.

3.3 Establishing Rayleigh's identity

The essential feature of multipole methods is a clever field identity involving the non-singular parts of a multipole expansion of the fields and the superposed effect of singular

sources arising from other points in the array [3, 32, 42]. For Rayleigh's identity, the indispensable cylindrical harmonic form of the equation (3.25) is obtained by transforming its Cartesian form by using $x = r\cos\theta$, $z = r\sin\theta$, $\alpha_{1p} = k_{1t}\cos\theta_p$, $\beta_{1p} = k_{1t}\sin\theta_p$ and the identity $e^{ikr\cos\theta} = \sum_{m\in\mathbb{Z}} i^m J_m(kr)e^{im\theta}$. It is written as

$$V_{1y}(x,z) = \sum_{n\in\mathbb{Z}}\sum_{p\in\mathbb{Z}}\left(e^{in\theta_p}f_p^- + e^{-in\theta_p}f_p^+\right)i^n J_n(k_{1t}r)e^{in\theta} + \sum_{n\in\mathbb{Z}} J_n(k_1 r)e^{in\theta}\sum_{m\in\mathbb{Z}}\mathscr{S}_{n-m}B_m + \sum_{n\in\mathbb{Z}} B_n H_n^{(1)}(k_{1t}r)e^{in\theta} \tag{3.26}$$

Substituting the coefficients (B.4) into (3.26) yields

$$E_{1y} = \sum_{n\in\mathbb{Z}}\left[B_n^e H_n^{(1)}(k_{1t}r) + \left(\sum_{m\in\mathbb{Z}}(M_{nm}^e + \mathscr{S}_{nm})B_m^e + \sum_{m\in\mathbb{Z}} N_{nm}^e B_m^h + F_n^e\right)J_n(k_{1t}r)\right]e^{in\theta}, \tag{3.27a}$$

$$K_{1y} = \sum_{n\in\mathbb{Z}}\left[B_n^h H_n^{(1)}(k_{1t}r) + \left(\sum_{m\in\mathbb{Z}}(N_{nm}^h + \mathscr{S}_{nm})B_m^h + \sum_{m\in\mathbb{Z}} M_{nm}^h B_m^e + F_n^h\right)J_n(k_{1t}r)\right]e^{in\theta}, \tag{3.27b}$$

where M_{nm}^e, N_{nm}^e, F_n^e, M_{nm}^h, N_{nm}^h and F_n^h are defined as

$$M_{nm}^e = \sum_{p\in\mathbb{Z}}\frac{i^n}{S_p^eQ_p^e - P_p^eW_p^e}\left[\left(U_{mp}^{ee}Q_p^e - V_{mp}^{ee}W_p^e\right)e^{in\theta_p} - \left(U_{mp}^{ee}P_p^e - V_{mp}^{ee}S_p^e\right)e^{-in\theta_p}\right], \tag{3.28a}$$

$$N_{nm}^e = \sum_{p\in\mathbb{Z}}\frac{i^n}{S_p^eQ_p^e - P_p^eW_p^e}\left[\left(U_{mp}^{eh}Q_p^e - V_{mp}^{eh}W_p^e\right)e^{in\theta_p} - \left(U_{mp}^{eh}P_p^e - V_{mp}^{eh}S_p^e\right)e^{-in\theta_p}\right], \tag{3.28b}$$

$$F_n^e = \sum_{p\in\mathbb{Z}}\frac{i^n}{S_p^eQ_p^e - P_p^eW_p^e}\left[\left(U_p^{ei}Q_p^e - V_p^{ei}W_p^e\right)e^{in\theta_p} - \left(U_p^{ei}P_p^e - V_p^{ei}S_p^e\right)e^{-in\theta_p}\right], \tag{3.28c}$$

$$M_{nm}^h = \sum_{p\in\mathbb{Z}}\frac{i^n}{S_p^hQ_p^h - P_p^hW_p^h}\left[(U_{mp}^{he}Q_p^h - V_{mp}^{he}W_p^h)e^{in\theta_p} - (U_{mp}^{he}P_p^h - V_{mp}^{he}S_p^h)e^{-in\theta_p}\right], \tag{3.28d}$$

$$N_{nm}^h = \sum_{p\in\mathbb{Z}}\frac{i^n}{S_p^hQ_p^h - P_p^hW_p^h}\left[(U_{mp}^{hh}Q_p^e - V_{mp}^{hh}W_p^h)e^{in\theta_p} - (U_{mp}^{hh}P_p^h - V_{mp}^{hh}S_p^h)e^{-in\theta_p}\right], \tag{3.28e}$$

$$F_n^h = \sum_{p\in\mathbb{Z}}\frac{i^n}{S_p^hQ_p^h - P_p^hW_p^h}\left[(U_p^{hi}Q_p^h - V_p^{hi}W_p^h)e^{in\theta_p} - (U_p^{hi}P_p^h - V_p^{hi}S_p^h)e^{-in\theta_p}\right]. \tag{3.28f}$$

The field in the vicinity of the fiber in the primary cell is written as

$$V_{1y}(x,z) = \sum_{n\in\mathbb{Z}}\left[B_n H_n^{(1)}(k_{1t}r) + A_n J_n(k_{1t}r)\right]e^{in\theta}, \tag{3.29}$$

which is the multipole expansion of the longitudinal field around the cylinder. But obviously the y dependence of $e^{ik_y y}$ is neglected since it has no influence on the final results.

Comparing it with (3.27), identities for A_n^e and A_n^h read as

$$A_n^e = \sum_{m\in\mathbb{Z}} \left[\left(M_{nm}^e + \mathscr{S}_{nm} \right) B_m^e + N_{nm}^e B_m^h \right] + F_n^e, \tag{3.30a}$$

$$A_n^h = \sum_{m\in\mathbb{Z}} \left[\left(N_{nm}^h + \mathscr{S}_{nm} \right) B_m^h + M_{nm}^h B_m^e \right] + F_n^h. \tag{3.30b}$$

which can be put for convenience into matrix form as $\mathbf{A} = \mathcal{Q}\mathbf{B} + \mathcal{F}$ where $\mathbf{A}$, $\mathbf{B}$ and $\mathcal{F}$ are all column vectors defined as $\mathbf{A} = [[A_n^e], [A_n^h]]^T$, $\mathbf{B} = [[B_n^e], [B_n^h]]^T$ and $\mathbf{F} = [[F_n^e], [F_n^h]]^T$, where $[x_n]$ is a row vector with x_n as its elements. The superscript T denotes the transpose of the indicated vector. $\mathcal{Q}$ is a $2n \times 2m$ matrix expressed as

$$\mathcal{Q} = \begin{bmatrix} \mathcal{M}^e + \mathcal{S} & \mathcal{N}^e \\ \mathcal{M}^h & \mathcal{N}^h + \mathcal{S}, \end{bmatrix}. \tag{3.31}$$

where $\mathcal{M}^e$, $\mathcal{N}^e$, $\mathcal{M}^h$, $\mathcal{N}^h$ and $\mathcal{S}$ are all $n \times m$ square matrices whose (n,m)-th elements are M_{nm}^e, N_{nm}^e, M_{nm}^h, N_{nm}^h and $\mathscr{S}_{n-m}$ respectively.

Substituting (3.15) into equation (3.30) yields the required Rayleigh's identity

$$\mathbf{B} = \mathcal{L}\mathcal{Q}\mathbf{B} + \mathcal{L}\mathcal{F}. \tag{3.32}$$

With this matrix identity, the value of $\mathbf{B}$ can be computed numerically. $f_{ep}^{\pm}$ and $f_{hp}^{\pm}$ are obtained with (B.4). Then, substituting them into the equations in (B.1), transmission and reflection coefficients R_p^e, R_p^h, T_p^e and T_p^h can be obtained.

Here, it is interesting to point out, as analyzed in [40], the possible influence of modified plate modes that arise from complex interference between the matrix and the fiber array embedded in it. To avoid the complication and without losing the generality, taking the incident wave as TM polarized as an illustrative example, the wave vector of the incident wave being orthogonal to the axis of the fibers, B_n^e and B_n^h decouple, so L_n^{eh} and L_n^{he} in (3.15) vanish, and $B_n^e = L_n^{ee} A_n^e$. Equation (3.30a) becomes $A_n^e = \sum_{m\in\mathbb{Z}} \left(M_{nm}^e + \mathscr{S}_{nm} \right) B_m^e + F_n^e$. Then, B_m^e is such that

$$\left(1 - L_n \left(M_{nn}^e + \mathscr{S}_0 \right)\right) B_n^e = L_n^{ee} \sum_{m\in\mathbb{Z}} \left(M_{nm}^e + \mathscr{S}_{nm} \right) B_m^e (1 - \delta_{mn}) + L_n^{ee} F_n^e. \tag{3.33}$$

This set of equations, as already discussed in the above, can be solved directly with inverse of the coefficient matrix. Here, for the sake of analysis, an iterative solution is given as

$$B_n^{e(0)} = \frac{L_n^{ee} F_n^e}{1 - L_n^{ee} (M_{nn}^e + \mathscr{S}_0)}, \tag{3.34a}$$

$$B_n^{e(q)} = \frac{L_n^{ee}\left(\sum_{m\in\mathbb{Z}}\left(M_{nm}^e + \mathscr{S}_{nm}\right)B_m^e(1-\delta_{mn}) + F_n^e\right)}{1 - L_n^{ee}(M_{nn}^e + \mathscr{S}_0)} \tag{3.34b}$$

for any order of approximation of $B_n^{e(q)}$. Allowing

$$\mathscr{D}_n = 1 - L_n^{ee}(M_{nn}^e + \mathscr{S}_0) \tag{3.35}$$

and combining it with the expression of $\mathscr{M}_{nn}^e$ yields

$$\mathscr{D}_n = 1 - \left[\sum_{p\in\mathbb{Z}} \frac{i^n\left(U_{mp}^{ee}Q_p^e - V_{mp}^{ee}W_p^e\right)e^{in\theta_p} - \left(U_{mp}^{ee}P_p^e - V_{mp}^{ee}S_p^e\right)e^{-in\theta_p}}{S_p^eQ_p^e - P_p^eW_p^e} - \mathscr{S}_0\right] L_n^{ee}. \tag{3.36}$$

It becomes clear that each n-th mode corresponds to an infinite set of (n,p) modified plate modes. As a consequence, for certain couples of (α_p,ω), the coefficients B_n can be large and cause the scattered fields to be large since the values of B_n are closely related to $\mathcal{R}$ and $\mathcal{T}$.A numerical investigation is given in section 3.5.

3.4 Reflection and transmission coefficients

The time-averaged Poynting vector is defined as $\langle\mathbf{S}\rangle = \boldsymbol{\mathcal{E}}\times\boldsymbol{\mathcal{H}}^*$ [62], which indicates the time-averaged power density. So the power reflection transmission coefficients for the p-th mode are defined as

$$\mathscr{R}_p = \Re\left\{\frac{\hat{z}\cdot\langle\mathbf{S}^r\rangle}{-\hat{z}\cdot\langle\mathbf{S}^{\text{inc}}\rangle}\right\} \tag{3.37a}$$

$$\mathscr{T}_p = \Re\left\{\frac{-\hat{z}\cdot\langle\mathbf{S}^t\rangle}{-\hat{z}\cdot\langle\mathbf{S}^{\text{inc}}\rangle}\right\} \tag{3.37b}$$

where $\langle\mathbf{S}^{\text{inc},r,t}\rangle$ is the time-averaged Poynting vectors for the p-th mode of incident, reflected and transmitted electromagnetic waves. Substituting the field expansions shown in (3.18), (3.25) and the corresponding x and z field components into (3.37) produces

$$\mathscr{R}_p = \Re\left\{\frac{R_p^e\xi_p^{r\,*} - R_p^{h^*}\zeta_p^r}{K_y^{\text{inc}*}\xi_p^{\text{inc}} - E_y^{\text{inc}}\zeta_p^{\text{inc}*}}\right\}, \tag{3.38a}$$

$$\mathscr{T}_p = \Re\left\{\frac{T_p^{h*}\xi_p^t - T_p^e\zeta_p^{t\,*}}{K_y^{\text{inc}*}\xi_p^{\text{inc}} - E_y^{\text{inc}}\zeta_p^{\text{inc}*}}\right\}, \tag{3.38b}$$

where the coefficients are

$$\xi_p^{\text{inc}} = \frac{k_y \alpha_0 E_y^{\text{inc}} + k\mu_{0r}\beta_0 K_y^{\text{inc}}}{k_{0t}^2}, \qquad \zeta_p^{\text{inc}} = \frac{k_y \alpha_0 K_y^{\text{inc}} - k\epsilon_{0r}\beta_0 E_y^{\text{inc}}}{k_{0t}^2},$$
$$\xi_p^{r} = \frac{k_y \alpha_p R_p^{h} + k\epsilon_{0r}\beta_{0p} R_p^{e}}{k_{0t}^2}, \qquad \zeta_p^{r} = \frac{k_y \alpha_p R_p^{e} - k\mu_{0r}\beta_{0p} R_p^{h}}{k_{0t}^2},$$
$$\xi_p^{t} = \frac{k_y \alpha_p T_p^{e} + k\mu_{3r}\beta_{3p} T_p^{h}}{k_{3t}^2}, \qquad \zeta_p^{t} = \frac{k_y \alpha_p T_p^{h} - k\epsilon_{3r}\beta_{3p} T_p^{e}}{k_{3t}^2}.$$

The power reflection, transmission and absorption coefficients of the fields are defined as $\boldsymbol{\mathcal{R}} = \sum_{p\in\mathbb{Z}} \mathscr{R}_p$, $\boldsymbol{\mathcal{T}} = \sum_{p\in\mathbb{Z}} \mathscr{T}_p$ and $\boldsymbol{\mathcal{A}} = 1 - \boldsymbol{\mathcal{R}} - \boldsymbol{\mathcal{T}}$.

3.5 Numerical simulations

Before entering into the discussion of the numerical simulations, one item of importance is that infinite sums $\sum_{p\in\mathbb{Z}}$ and $\sum_{m\in\mathbb{Z}}$ are computed as $\sum_{p=-P}^{P}$ and $\sum_{m=-M}^{M}$, letting $P = \text{Int}\,(d/2\pi(3\Re(k_1) - \alpha_0))$, $M = \text{Int}\left(\Re(4.05\times(k_1 c)^{1/3}) + k_1 c\right)$ [40] to achieve an approximation with error $|\boldsymbol{\mathcal{R}}^{n+1} - \boldsymbol{\mathcal{R}}^{n}|$, $n = P, M$, less than 10^{-6}, refer to Chapter 2 for details.

Now, to verify the proposed approach, its results are compared in Fig. 3.3 and Fig. 3.4 with those produced by the COMSOL FEM code with its solver for periodic structure. Power reflection coefficients of the 0-th mode, when TM- and TE -polarized waves are obliquely impinging on carbon-fiber ($\epsilon_{r2} = 12$, $\sigma = 3.3\times10^2\,\text{S}\,\text{m}^{-1}$ [57, 58]) reinforced composites (CFRC) with epoxy ($\epsilon_{r1} = 3.6$) matrices, are displayed in Fig. 3.3, which shows a good match. The wavelength of the incident wave is $\lambda^{\text{inc}} = 0.1\,\text{mm}$, and $\varphi = 0$, while $E_y^{\text{inc}} = 1$, $K_y^{\text{inc}} = 0$ and $E_y^{\text{inc}} = 0$, $K_y^{\text{inc}} = 1$, respectively. The laminated geometry is specified by parameters $d = L = \lambda^{\text{inc}}$, $c = 0.25d$, and the parameters are used in this whole chapter except otherwise specified.

Results given in Fig. 3.4 show the variation of power reflection coefficients with ϑ for TM- and TE-polarized waves obliquely impinging on a periodic array of dielectric fibers ($\epsilon_{r2} = 3.6$), with the wavelength of incident wave $\lambda^{\text{inc}} = 2d$ and $\varphi = 15^{\circ}$. A good match is observed for $-80^{\circ} < \vartheta < 80^{\circ}$.

To simulate the presented 2.5D case with COMSOL, Perfectly Matched Layers (PML) and Floquet periodic boundary condition are required to build a full 3D model which actually produces many unknowns for achieving a good accuracy, hence leading to a time- and resource- consuming computation. The presented approach could be much lighter and faster since it is actually a 2.5D approach which has no much more complexity compared

to the 2D case. Moreover, PML, with an incident angle close to 90°, will reflect respectable amount of waves back to the computation region which increases the reflection of the waves. Hence, when $80° < |\vartheta| < 90°$, results of $\mathcal{R}$ obtained with COMSOL 3D model are larger than that of present approach.

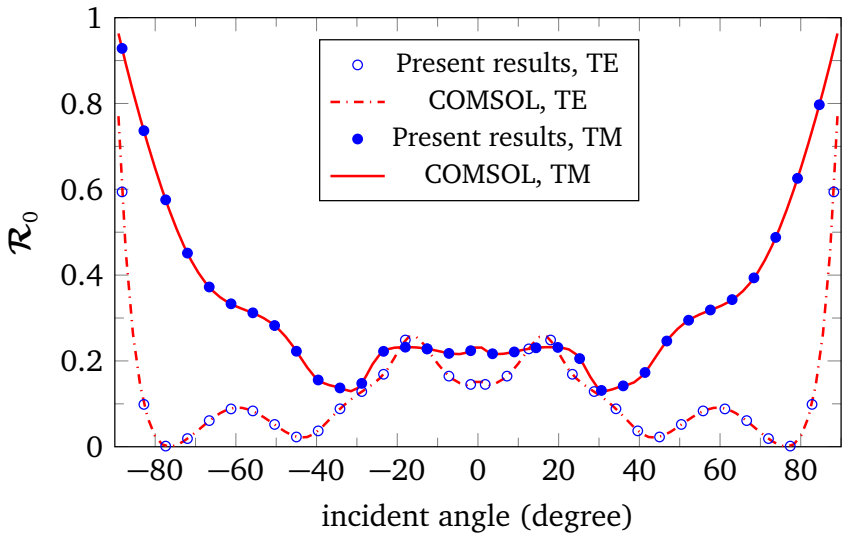

Fig. 3.3 Validating the approach by comparing the results of TE and TM cases with those from COMSOL FEM, $\varphi = 0$.

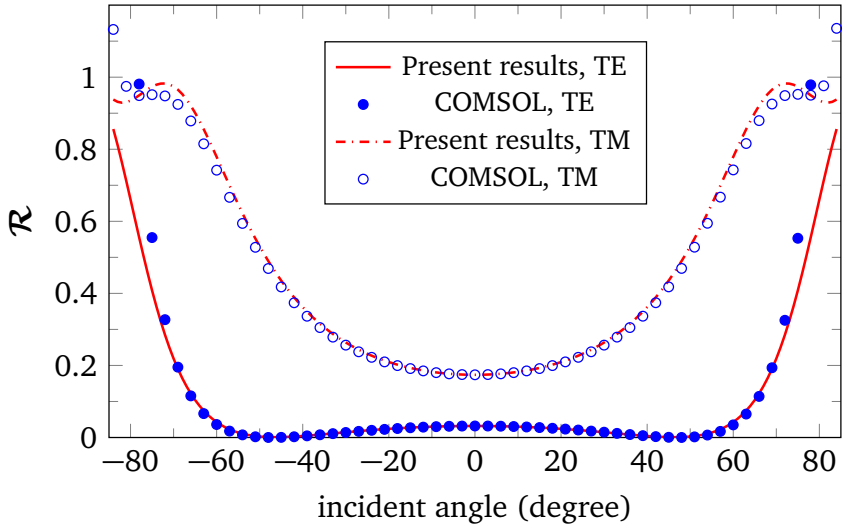

Fig. 3.4 Validating the approach by comparing the results of TE and TM cases with those from COMSOL FEM, $\varphi = 15^o$.

In order to illustrate the broad applicability of the proposed method and possibly provide reference results for testing more brute-force approaches, a number of simulation

results are shown in various cases of interest. The investigation is mainly given in the context of non-destructive testing of fiber-reinforced composites to look at their expected behavior and the consequences thereof.

The results of $\mathcal{R}$ for glass-fiber ($\epsilon_{r2} = 6$) reinforced composites (GFRC) are given in Fig. 3.5 with $L = d = \lambda^{\text{inc}} = 0.1mm$; several peaks appear when ϑ varies from $-90°$ to $90°$ and good symmetry is observed. When $\varphi = 45°$, the reflection is stronger than that of $\varphi = 90°$ except ϑ close to 0.

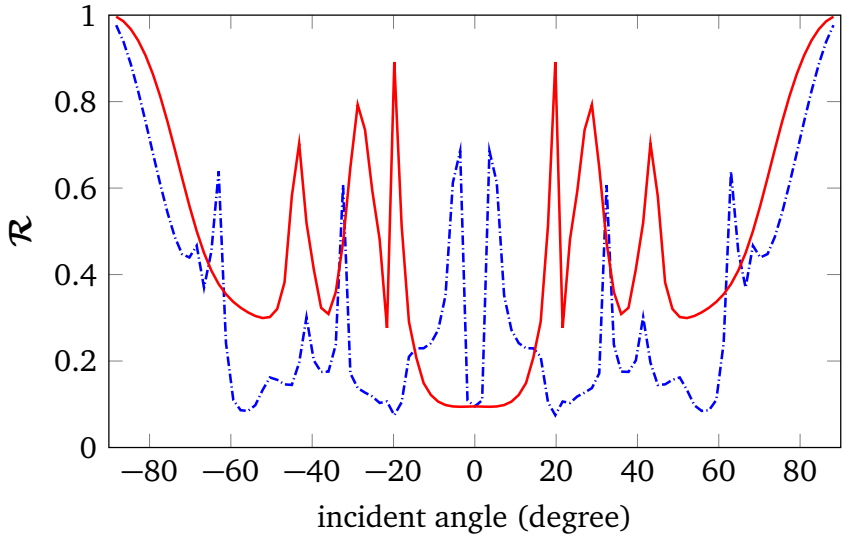

Fig. 3.5 Variation of $\mathcal{R}$ with ϑ for $\varphi = 45°$ (dash-dotted line) and $\varphi = 90°$ (solid line), glass fibers.

The variation of $\mathcal{R}$ with d/λ^{inc} for GFRC is given in Fig. 3.6 for different values of φ with $\vartheta = 60°$, which is also the essential situation for periodic structures used as frequency and polarization selective components in microwave and optical regions. The power reflection coefficient $\mathcal{R}$ approaches zero when d/λ^{inc} is small, as shown in Fig. 3.6, hence, in view of non-destructive testing of GFRC, a frequency band 10 GHz to 60 GHz is expected. Several narrow peaks are observed, some associated to full reflection, all (if one zooms into them via small steps of d/λ^{inc}) vary quite smoothly however. As discussed in section 3.3, this corresponds with the modified plate modes. It can be seen clearly from Fig.3.7 (normal illumination of TM wave) that the peaks on the curve of $\mathcal{R}$ appear when B_n is large. Since B_n closely depends on the mode pair index by (n, p) and each n-th mode is modified by an infinite number of p-th mode, for some pair of (n, p) mode, B_n becomes large and cause large reflected field.

For CFRC, results for $\mathcal{R}$ and $\mathcal{T}$ as a function of d/λ^{inc} are given in Fig. 3.8 for different values of φ, where $\vartheta = 60°$. Strong absorption is observed when d/λ^{inc} approaches to 1, while, for the long wavelength case, strong transmission is obtained. For the usual testing

frequency band of CFRC, from 1 MHz to 1 GHz, $\mathcal{R}$ for $\varphi = 45°$ and $\varphi = 90°$ are about 0.2 and 0.1, and $\mathcal{T}$ in both cases are 0.6 and 0.8, respectively.

Influence of the period d and fibers' radius c is exhibited in Fig. 3.9 and Fig. 3.10. In the low-frequency band, decreasing d or increasing c increases the volume occupied by the lossy carbon fibers, the power transmission coefficient $\mathcal{T}$ decreases and the power reflection coefficient $\mathcal{R}$ increases slightly.

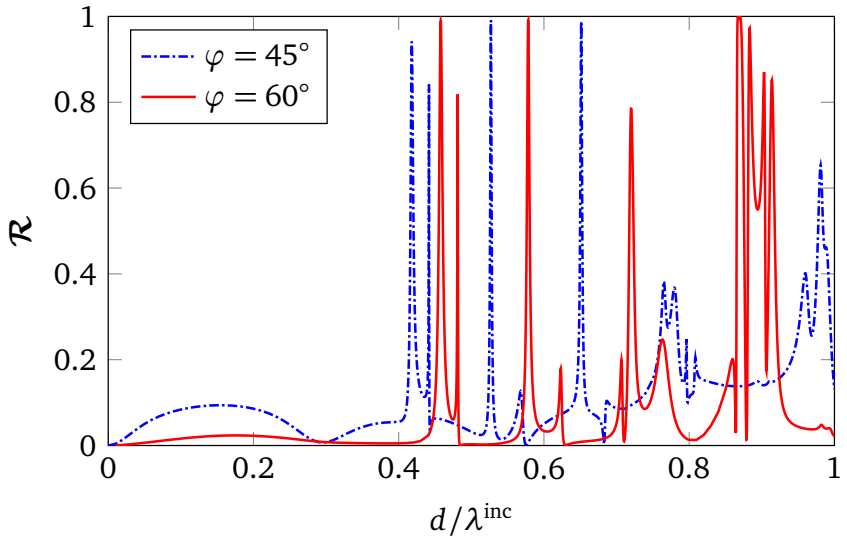

Fig. 3.6 Variation of $\mathcal{R}$ with d/λ^{inc}, glass fibers, $L = d = 0.1mm$, $c = 0.25d$, $\vartheta = 60°$.

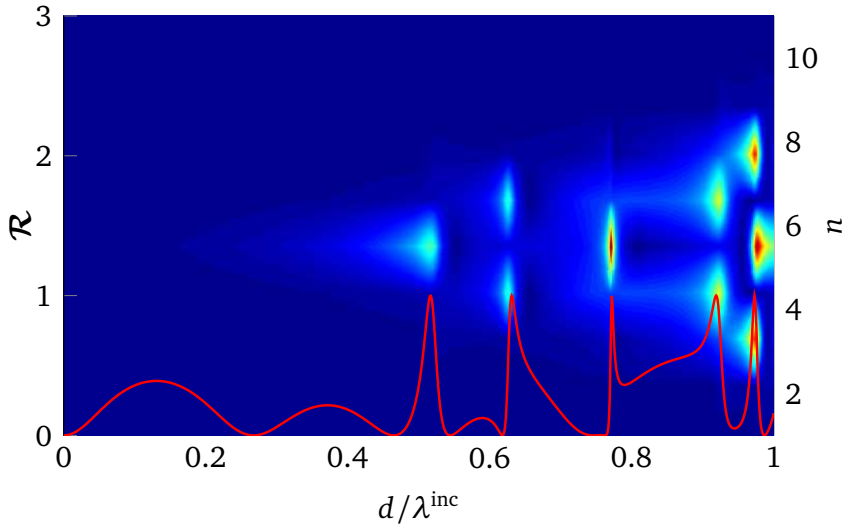

Fig. 3.7 Comparison between the distribution of B_n and $\mathcal{R}$ for TM wave illuminating normally. Strong reflection is observed when B_n is large.

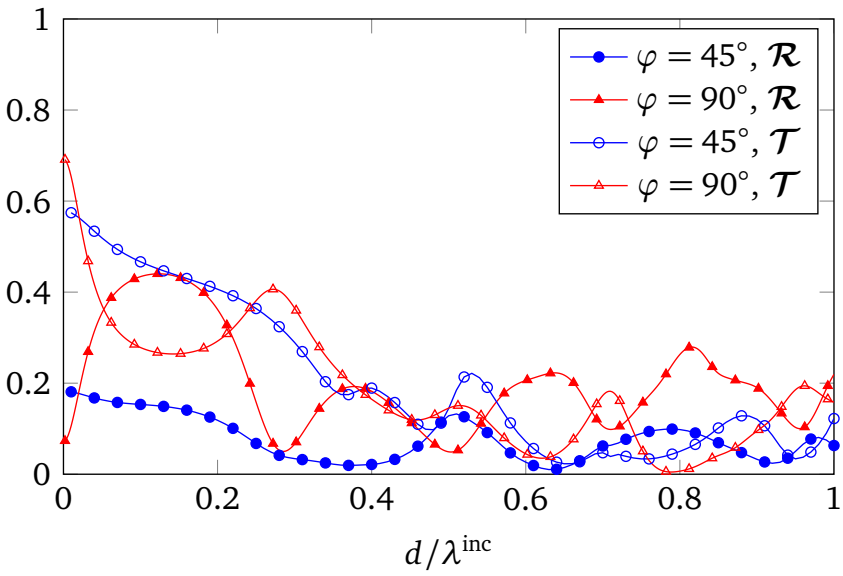

Fig. 3.8 Variation of $\mathcal{R}$ and $\mathcal{T}$ with d/λ^{inc} for $\varphi = 45°$ and $\varphi = 90°$, $\vartheta = 60°$, carbon fibers.

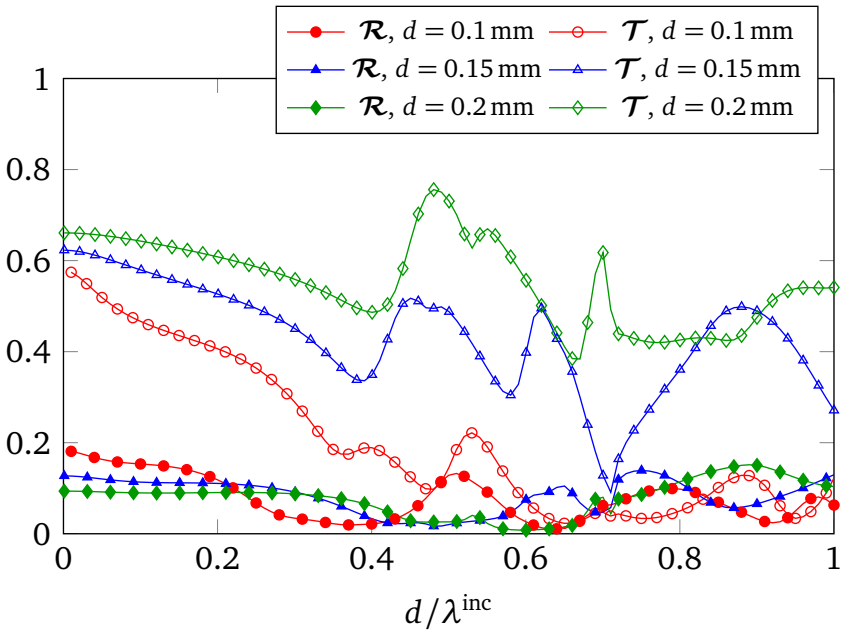

Fig. 3.9 Variation of $\mathcal{R}$ and $\mathcal{T}$ with d/λ^{inc} for different d, $\varphi = 45°$, $\vartheta = 60°$, carbon fibers

3.6 Summary

The approach built in Chapter 2 is extended in this chapter for the scattering of a conically incident plane wave by a single-layer composite panel reinforced by a periodic array of circular fibers. The method is intrinsically frequency-broad-band and valid for any isotropic constitutive material. Its effectiveness and accuracy are illustrated by numerical results

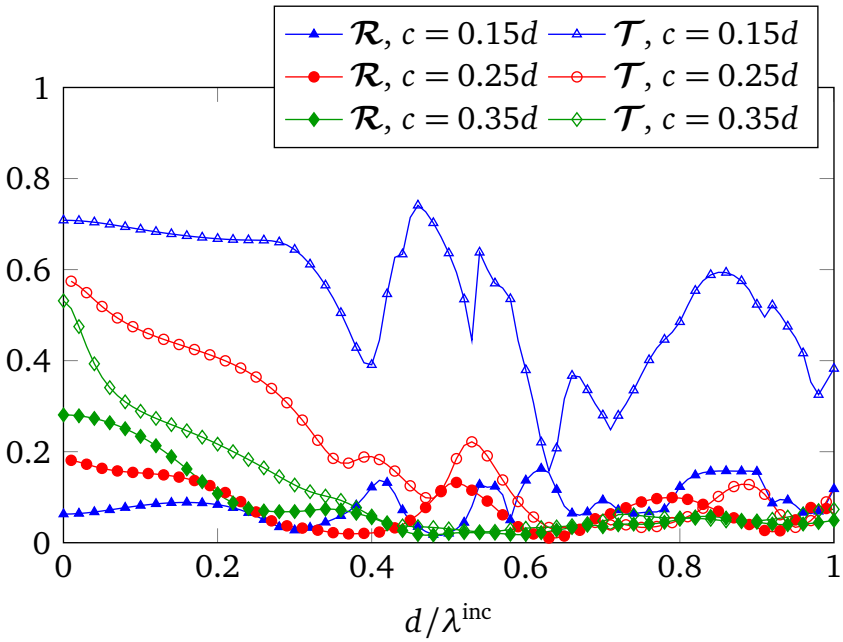

Fig. 3.10 Variation of $\mathcal{R}$ and $\mathcal{T}$ with d/λ^{inc} for different c, $\varphi = 45°$, $\vartheta = 60°$, carbon fibers

for single-layer carbon or glass fiber-reinforced composites as used in aeronautic and automotive parts. One has also validated the approach via the COMSOL software.

The work as summarized is about the 2.5D scattering problems of single-layer composite, but it can be applied to analyze the electromagnetic characters of multilayer periodic composites, which is constructed by stacking up the single-layer composite one over the other. The fibers in different layers are either parallel to each other or orientated into an arbitrary direction. Details are given in the following chapters.

Chapter 4

Scattering by composite laminates with the same orientation of fibers

Following the discussion in [64] on the recursive matrix methods for simple layered structure, a scheme based on S-matrix is further developed here for investigating the considered periodic composite which is more complicated, hence resulting in more complex field behavior. This approach is proved to be stable and also intrinsically broad-band. Though some difficulties are still encountered for directly computing the field distribution inside the structure with obtained reflection and transmission coefficients, they are easily overcome by rearranging the corresponding matrices to relate the field expansion coefficients inside the composite to the incident field.

Comparing to S-matrix based approach, the present problem can also be investigated with another approach based on transfer matrices (T-matrices), which is more straightforward to implement and easier for understanding. But such type of method is known to suffer from intractable numerical instability at high frequency as exemplified by [65, 66]. Some numerical investigations will be presented to further reveal the possible causes of the instability, and referring to [67] for a possible approach to solve this problem.

4.1 Configurations and formulation

The laminate of interest is sketched in Fig. 4.1. A periodic array of homogeneous circular cylinders is embedded inside each constitutive homogeneous planar layer indexed by l, from 1 to n, with thickness h_l, all such cylinders having the same orientation and the same periodicity d (center-to-center distance between two adjacent fibers) throughout the laminate, though the fibers in a given layer can be shifted by a distance s_l along the

direction of periodicity. The cylinder radius c_l is constant in a given layer but can differ between layers. Upper and lower interfaces of the l-th layer are denoted as $z = t_{l-1}$ and $z = t_l$, the laminate itself being sandwiched between two homogeneous half spaces denoted with indexes $l = 0$ and $l = n+1$ for convenience.

A Cartesian coordinate system xyz with $\hat{x}$, $\hat{y}$ and $\hat{z}$ as unit vectors is defined, $\hat{x}$ as direction along the periodicity of the laminate, $\hat{y}$ along the axis of the fibers, $\hat{z} = \hat{x} \times \hat{y}$. Of interest in the analysis is the d-wide primary cell of the l-th layer, which can produce the whole layer by repeating to infinity along positive or negative directions of periodicity.

The upper and lower spaces are filled with air here, but the approach works with any isotropic homogeneous material in the lower space. Their electromagnetic parameters accordingly are ϵ_0 and μ_0. All materials in the layered composite are linear isotropic with layer-dependent complex-valued relative permittivity $\epsilon_l^{(\nu)}$ and relative permeability $\mu_l^{(\nu)}$ which are normalized with ϵ_0 and μ_0, $l = 0, 1, 2, ..., n+1$, and $\nu = 1, 2$ denoting the background material when $\nu = 1$ and the material in the cylinders when $\nu = 2$. One uses an implicit time-harmonic dependence $e^{-i\omega t}$.

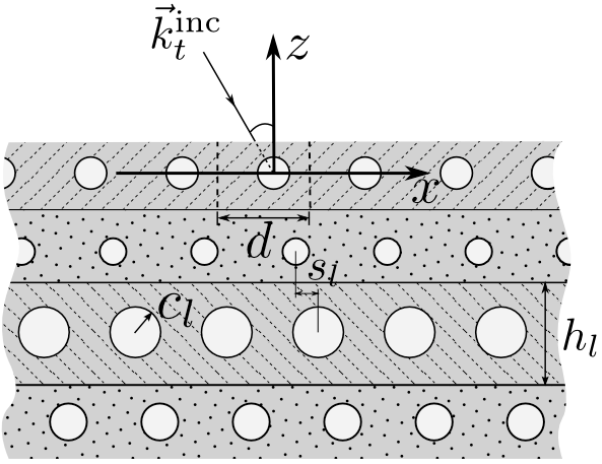

Fig. 4.1 The local coordinate system and the transverse component of incident wave.

A conically incident wave as shown in Fig. 3.1a is considered, and the layers are numbered in the way shown in Fig. 4.2. For the wave within the l-th layer but outside the embedded cylinders if any, the wave vector is $\vec{k}_l$ and its transverse and longitudinal components are $\vec{k}_{lt}$ and $\vec{k}_{ly}$, where $\vec{k}_{lt} = k_{lx}\hat{x} - k_{lz}\hat{z}$, $l = 0, 1, 2, ..., n+1$. Thus, $k_{lt}^2 = k_l^2 - k_{ly}^2$. letting $\alpha_l = k_{lx}$, $\beta_l = k_{lz}$ and $\xi_l = k_{ly}$, then $\vec{k}_{lt} = \hat{x}\alpha_l - \hat{z}\beta_l$. Because of the continuity of α_l and ξ_l across the boundaries, $\alpha_l = \alpha_0$ and $\xi_l = \xi_0$, $l = 1, 2, ..., n$.

Here, the fields $\boldsymbol{\mathcal{E}}_l$ and $\boldsymbol{\mathcal{K}}_l$ are also decomposed into longitudinal and transverse components, parallel with and orthogonal to the common cylinder axis, respectively, denoted by subscripts y and t, where $\boldsymbol{\mathcal{E}}_l = (\mathbf{E}_{lt} + E_{ly}\hat{y})e^{ik_y y}$ and $\boldsymbol{\mathcal{K}}_l = (\mathbf{K}_{lt} + K_y\hat{y})e^{ik_y y}$. The relation

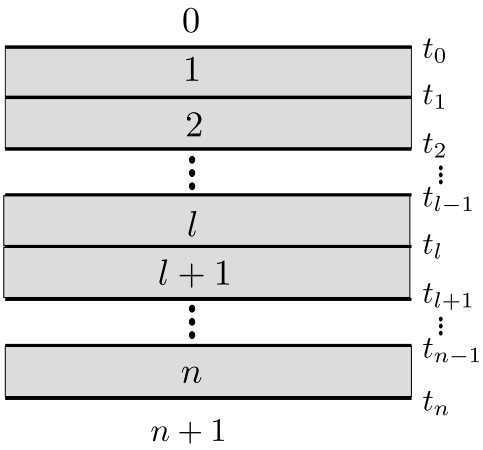

Fig. 4.2 The way of numbering the layers.

between V_{ly} and V_{lx} is similar to (3.7), it reads

$$E_{lx}(x,z) = \frac{i}{k_{lt}^2}\left[k_y \frac{\partial E_{ly}}{\partial x} - k\mu_r \frac{\partial K_{ly}}{\partial z}\right], \tag{4.1a}$$

$$K_{lx}(x,z) = \frac{i}{k_{lt}^2}\left[k_y \frac{\partial K_{ly}}{\partial x} + k\epsilon_r \frac{\partial E_{ly}}{\partial z}\right], \tag{4.1b}$$

where k is the wavenumber in vacuum.

4.2 Field expansion in different layers

Longitudinal components of the fields in both upper and lower half-spaces can be plane-wave expanded as

$$E_{0y}(x,z) = \sum_{p\in\mathbb{Z}} \left(E_y^{inc} e^{-i\beta_{0p}(z-t_0)}\delta_{p0} + R_p^e e^{i\beta_{0p}(z-t_0)}\right) e^{i\alpha_p x}, \tag{4.2a}$$

$$K_{0y}(x,z) = \sum_{p\in\mathbb{Z}} \left(K_y^{inc} e^{-i\beta_{0p}(z-t_0)}\delta_{p0} + R_p^h e^{i\beta_{0p}(z-t_0)}\right) e^{i\alpha_p x}, \tag{4.2b}$$

$$E_{n'y}(x,z) = \sum_{p\in\mathbb{Z}} T_p^e e^{i\left(\alpha_p x - \beta_{n'p}(z-t_n)\right)}, \tag{4.2c}$$

$$K_{n'y}(x,z) = \sum_{p\in\mathbb{Z}} T_p^h e^{i\left(\alpha_p x - \beta_{n'p}(z-t_n)\right)}. \tag{4.2d}$$

$n' = n+1$, $R_p^{e,h}$ and $T_p^{e,h}$ are the reflection and transmission coefficients of the plane wave indexed by p, δ_{p0} the Kronecker symbol, $\alpha_p = \alpha_0 + 2p\pi/d$, $\beta_{lp} = \sqrt{k_{tl}^2 - \alpha_p^2}$.

Define (s_l, e_l) as the coordinates of the center of the primary cell characteristic of the l-th layer, the field within the l-th layer outside the cylinders is plane-wave expanded as

$$V_{ly}^{\pm} = \sum_{p\in\mathbb{Z}} \left(f_{lp}^{\pm} e^{-i\beta_{lp}(z-e_l)} + g_{lp}^{\pm} e^{i\beta_{lp}(z-e_l)} \right) e^{i\alpha_p(x-s_l)}, \tag{4.3}$$

The coefficients $f_{lp}^{\pm}$ and $g_{lp}^{\pm}$ depending on $V_{ly}^{\pm}$ for E_{ly} and K_{ly} fields are common representations of $f_{l\{e,h\}p}^{\pm}$ and $g_{l\{e,h\}p}^{\pm}$. $f_{lp}^{\pm}$ represents the field propagating along the $-z$ direction and $g_{lp}^{\pm}$ the one propagating along the $+z$ direction. $+$ and $-$ indicate the slices of the layer that are above and below the cylinders $c_l < z < a$ and $b < z < c_l$, respectively.

4.3 Mode-matching at the boundaries

Mode-matching at the boundary between two adjacent layers produces a linear system which links the expansion coefficient of the field at the two sides of the corresponding boundary. Both of the T-matrix and S-matrix which relate to the considered boundary are produced from this linear system according to their individual physical meanings. The T-matrices of each boundary can be produced directly from the obtained linear system, but to produce the S-matrices needs to reorganize the linear system to separate the input and output corresponding to the considered boundary. These matrices are part of the building bricks for constructing the T-matrix or the S-matrix of one single layer. The detailed procedures of constructing these matrices are presented in this section.

4.3.1 Mode-matching at boundaries for T-matrix

Allowing $\chi_{lp} = \alpha_p k_y / k_{l1t}^2$, $\eta_{lp} = k\mu_l^{(1)} \beta_{l1p} / k_{l1t}^2$, $\rho_{lp} = k\epsilon_l^{(1)} \beta_{l1p} / k_{l1t}^2$ and matching the fields at the boundary between the l-th layer and the $(l+1)$-th one yields

$$P_{lp} f_{lep}^{-} + U_{lp} g_{lep}^{-} = P_{l'p} f_{l'ep}^{+} + U_{l'p} g_{l'ep}^{+}, \tag{4.4a}$$

$$P_{lp} f_{lhp}^{-} + U_{lp} g_{lhp}^{-} = P_{l'p} f_{l'hp}^{+} + U_{l'p} g_{l'hp}^{+}, \tag{4.4b}$$

$$\begin{aligned} &\chi_{lp} \left(P_{lp} f_{lep}^{-} + U_{lp} g_{lep}^{-} \right) + \eta_{lp} \left(P_{lp} f_{lhp}^{-} - U_{lp} g_{lhp}^{-} \right) \\ &= \chi_{l'p} \left(P_{l'p} f_{l'ep}^{+} + U_{l'p} g_{l'ep}^{+} \right) + \eta_{l'p} \left(P_{l'p} f_{l'hp}^{+} - U_{l'p} g_{l'hp}^{+} \right), \end{aligned} \tag{4.4c}$$

$$\begin{aligned} &\chi_{lp} \left(P_{lp} f_{lhp}^{-} + U_{lp} g_{lhp}^{-} \right) - \rho_{lp} \left(P_{lp} f_{lep}^{-} - U_{lp} g_{lep}^{-} \right) \\ &= \chi_{l'p} \left(P_{l'p} f_{l'hp}^{+} + U_{l'p} g_{l'hp}^{+} \right) - \rho_{l'p} \left(P_{l'p} f_{l'ep}^{+} - U_{l'p} g_{l'ep}^{+} \right), \end{aligned} \tag{4.4d}$$

where $P_{lp} = e^{-i(\alpha_p s_l + \beta_{lp}(t_l - e_l))}$ and $U_{lp} = e^{-i(\alpha_p s_l - \beta_{lp}(t_l - e_l))}$. $P_{l'p}$ and $U_{l'p}$ have similar definition with $t_{l'}$. $l' = l + 1$ for the sake of convenience. This system can be written as

$$\boldsymbol{\mathcal{F}}_l^- = \boldsymbol{\mathcal{M}}_l \boldsymbol{\mathcal{F}}_l^+ \tag{4.5}$$

with column vectors $\boldsymbol{\mathcal{F}}_l^- = \left[[f_{lep}^-], [f_{lhp}^-], [g_{lep}^-], [g_{lhp}^-]\right]^{\mathrm{T}}$, $\boldsymbol{\mathcal{F}}_{l'}^+ = \left[[f_{l'ep}^+], [f_{l'hp}^+], [g_{l'ep}^+], [g_{l'hp}^+]\right]^{\mathrm{T}}$ and with $\boldsymbol{\mathcal{M}}_l$ the matrix of coefficients. Assuming $\mathbf{M}_l^{(i,j)}$ as the block matrix at i-th row and j-th column of $\boldsymbol{\mathcal{M}}_l$ with $i, j = 1, 2, 3, 4$, matrix $\mathbf{M}_l^{(ij)}$ then is a diagonal matrix with p-th element $M_{lp}^{(ij)}$ on the main diagonal, with the definitions given as

$$\begin{aligned}
M_{lp}^{(11)} &= \frac{(\rho_{l'p} + \rho_{lp})P_{l'p}}{2\rho_{lp}P_{lp}}, M_{lp}^{(12)} = \frac{(\chi_{lp} - \chi_{l'p})P_{l'p}}{2\rho_{lp}P_{lp}}, \\
M_{lp}^{(13)} &= \frac{(\rho_{lp} - \rho_{l'p})U_{l'p}}{2\rho_{lp}P_{lp}}, M_{lp}^{(14)} = \frac{(\chi_{lp} - \chi_{l'p})U_{l'p}}{2\rho_{lp}P_{lp}}, \\
M_{lp}^{(21)} &= \frac{(\chi_{l'p} - \chi_{lp})P_{l'p}}{2\eta_{lp}P_{lp}}, M_{lp}^{(22)} = \frac{(\eta_{l'p} + \eta_{lp})P_{l'p}}{2\eta_{lp}P_{lp}}, \\
M_{lp}^{(23)} &= \frac{(\chi_{l'p} - \chi_{lp})U_{l'p}}{2\eta_{lp}P_{lp}}, M_{lp}^{(24)} = \frac{(\eta_{lp} - \eta_{l'p})U_{l'p}}{2\eta_{lp}P_{lp}}, \\
M_{lp}^{(31)} &= \frac{(\rho_{lp} - \rho_{l'p})P_{l'p}}{2\rho_{lp}U_{lp}}, M_{lp}^{(32)} = \frac{(\chi_{l'p} - \chi_{lp})P_{l'p}}{2\rho_{lp}U_{lp}}, \\
M_{lp}^{(33)} &= \frac{(\rho_{lp} + \rho_{l'p})U_{l'p}}{2\rho_{lp}U_{lp}}, M_{lp}^{(34)} = \frac{(\chi_{l'p} - \chi_{lp})U_{l'p}}{2\rho_{lp}U_{lp}}, \\
M_{lp}^{(41)} &= \frac{(\chi_{lp} - \chi_{l'p})P_{l'p}}{2\eta_{lp}U_{lp}}, M_{lp}^{(42)} = \frac{(\eta_{lp} - \eta_{l'p})P_{l'p}}{2\eta_{lp}U_{lp}}, \\
M_{lp}^{(43)} &= \frac{(\chi_{lp} - \chi_{l'p})U_{l'p}}{2\eta_{lp}U_{lp}}, M_{lp}^{(44)} = \frac{(\eta_{lp} + \eta_{l'p})U_{l'p}}{2\eta_{lp}U_{lp}}
\end{aligned}$$

At $z = t_0$, $\boldsymbol{\mathcal{F}}_0^- = [[E_y^{inc}\delta_{0p}], [K_y^{inc}\delta_{0p}], [R_p^e], [R_p^h]]^{\mathrm{T}}$, and at $z = t_n$ $\boldsymbol{\mathcal{F}}_{n'}^+ = \left[0, 0, [T_p^e], [T_p^h]\right]^{\mathrm{T}}$.

4.3.2 Mode-matching at boundaries for S-matrix

Coefficients $\mathbf{f}_l^+$ and $\mathbf{g}_{l'}^-$ represent the waves arriving at the boundary (input), and $\mathbf{f}_{l'}^-$ and $\mathbf{g}_l^+$ those leaving it (output). Reorganizing the linear system (4.4) to link both, one has

$$\begin{bmatrix} \mathbf{f}_{l'}^+ \\ \mathbf{g}_l^- \end{bmatrix} = \begin{bmatrix} \boldsymbol{\mathcal{M}}_{ll'}^{(1)} & \boldsymbol{\mathcal{M}}_{ll'}^{(2)} \\ \boldsymbol{\mathcal{M}}_{ll'}^{(3)} & \boldsymbol{\mathcal{M}}_{ll'}^{(4)} \end{bmatrix} \begin{bmatrix} \mathbf{f}_l^- \\ \mathbf{g}_{l'}^+ \end{bmatrix}; \tag{4.6}$$

$\boldsymbol{\mathcal{M}}_{ll'}^{(1)}$, $\boldsymbol{\mathcal{M}}_{ll'}^{(2)}$, $\boldsymbol{\mathcal{M}}_{ll'}^{(3)}$ and $\boldsymbol{\mathcal{M}}_{ll'}^{(4)}$ are four blocks of $\boldsymbol{\mathcal{M}}_{ll'}$ calculated with $\boldsymbol{\mathcal{M}}_{ll'} = \boldsymbol{\mathcal{M}}_{ll'}^{(a)^{-1}} \boldsymbol{\mathcal{M}}_{ll'}^{(b)}$,

$$\boldsymbol{\mathcal{M}}_{ll'}^{(a)} = \begin{bmatrix} P_{l'p} & 0 & -U_{lp} & 0 \\ 0 & P_{l'p} & 0 & -U_{lp} \\ \chi_{l'p}P_{l'p} & \eta_{l'p}P_{l'p} & -\chi_{lp}U_{lp} & \eta_{lp}U_{lp} \\ -\rho_{l'p}P_{l'p} & \chi_{l'p}P_{l'p} & -\rho_{lp}U_{lp} & -\chi_{lp}U_{lp} \end{bmatrix} \tag{4.7}$$

$$\boldsymbol{\mathcal{M}}_{ll'}^{(b)} = \begin{bmatrix} P_{lp} & 0 & -U_{l'p} & 0 \\ 0 & P_{lp} & 0 & -U_{l'p} \\ \chi_{lp}P_{lp} & \eta_{lp}P_{lp} & -\chi_{l'p}U_{l'p} & \eta_{l'p}U_{l'p} \\ -\rho_{lp}P_{lp} & \chi_{lp}P_{lp} & -\rho_{l'p}U_{l'p} & -\chi_{l'p}U_{l'p} \end{bmatrix} \tag{4.8}$$

Matrices $\boldsymbol{\mathcal{M}}_{ll'}^{*}$ (S-matrix) and $\boldsymbol{\mathcal{M}}_{l}$ (T-matrix) are easily distinguished from their indexing. For $\boldsymbol{\mathcal{M}}_{ll'}^{*}$, index ll' indicates that the matrix relates the field between the l-th and l'-th layers. Index l of $\boldsymbol{\mathcal{M}}_{l}$ means that the field is matched at boundary t_l. At $z = t_0$, $\mathbf{f}_0^- = [[E_y^{inc}\delta_{0p}], [K_y^{inc}\delta_{0p}]]$ and $\mathbf{g}_0^- = [[R_p^e], [R_p^h]]$. At $z = t_n$, $\mathbf{f}_{n'}^+ = [[T_p^e], [T_p^h]]$ and $\mathbf{g}_{n'}^+ = [0, 0]$.

4.4 The relation between $f_{lep}^{\pm}$ and $g_{lep}^{\pm}$

In the l-th layer, following the treatment presented in section 3.3, the field in the vicinity of the circular cylinder is given as

$$\begin{aligned} V_{ly}(x,z) = &\sum_{n\in\mathbb{Z}}\sum_{p\in\mathbb{Z}}\left(f_{lp}^{+}e^{in\theta_{lp}} + g_{lp}^{-}e^{-in\theta_{lp}}\right) i^n \mathrm{J}_n(k_{lt}r)e^{in\theta} \\ &+ \sum_{n\in\mathbb{Z}} \mathrm{J}_n(k_{lt}r)e^{in\theta} \sum_{m\in\mathbb{Z}} \mathscr{S}_{lnm}B_{lm} + \sum_{n\in\mathbb{Z}} B_{ln}\mathrm{H}_n^{(1)}(k_{lt}r)e^{in\theta} \end{aligned} \tag{4.9}$$

Here, B_{ln} indicates either B_{ln}^e or B_{ln}^h as multipole expansion coefficients. $\mathscr{S}_{lnm} = \mathscr{S}_{l,n-m}$, are lattice sums or Schlömilch series. The field in the vicinity of the cylinder can also be expanded as equation (2.8). Comparing equation (4.9) with equation (2.8) yields

$$A_{ln}^e = \sum_{p\in\mathbb{Z}}\left(i^n e^{in\theta_{lp}} f_{lep}^{+} + i^n e^{-in\theta_{lp}} g_{lep}^{-}\right) + \sum_{m\in\mathbb{Z}} \mathscr{S}_{n-m}B_{lm}^e, \tag{4.10a}$$

$$A_{ln}^h = \sum_{p\in\mathbb{Z}}\left(i^n e^{in\theta_{lp}} f_{lhp}^{+} + i^n e^{-in\theta_{lp}} g_{lhp}^{-}\right) + \sum_{m\in\mathbb{Z}} \mathscr{S}_{n-m}B_{lm}^h, \tag{4.10b}$$

which can be written as

$$\boldsymbol{\mathcal{A}}_l = \boldsymbol{\mathcal{O}}_1\mathbf{f}_l^{+} + \boldsymbol{\mathcal{O}}_2\mathbf{g}_l^{-} + \boldsymbol{\mathcal{S}}_l\boldsymbol{\mathcal{B}}_l \tag{4.11}$$

with the vectors defined as $\boldsymbol{\mathcal{A}}_l = \left[\left[A_{ln}^e\right],\left[A_{ln}^h\right]\right]^T$, $\boldsymbol{\mathcal{B}}_l = \left[\left[B_{lm}^e\right],\left[B_{lm}^h\right]\right]^T$, $\mathbf{f}_l^+ = \left[\left[f_{lep}^+\right],\left[f_{lhp}^+\right]\right]^T$ and $\mathbf{g}_l^- = \left[\left[g_{lep}^-\right],\left[g_{lhp}^-\right]\right]^T$. The matrices are defined as

$$\boldsymbol{\mathcal{O}}_1 = \begin{bmatrix} \mathrm{diag}\left\{\left[i^n e^{in\theta_{lp}}\right]\right\} & 0 \\ 0 & \mathrm{diag}\left\{\left[i^n e^{in\theta_{lp}}\right]\right\} \end{bmatrix}, \tag{4.12a}$$

$$\boldsymbol{\mathcal{O}}_2 = \begin{bmatrix} \mathrm{diag}\left\{\left[i^n e^{-in\theta_{lp}}\right]\right\} & 0 \\ 0 & \mathrm{diag}\left\{\left[i^n e^{-in\theta_{lp}}\right]\right\} \end{bmatrix}, \tag{4.12b}$$

$$\boldsymbol{\mathcal{S}}_l = \begin{bmatrix} \left[\mathscr{S}_{lnm}\right]_{nm} & 0 \\ 0 & \left[\mathscr{S}_{lnm}\right]_{nm} \end{bmatrix}. \tag{4.12c}$$

Here, $\left[x_p\right]$ defines a row vector with x_p as its elements, $\left[x_{nm}\right]_{nm}$ stands for a matrix with elements x_{nm}. The relation between $\boldsymbol{\mathcal{A}}_l$ and $\boldsymbol{\mathcal{B}}_l$ is detailed in section 3.1.1, and summarized into $\boldsymbol{\mathcal{B}}_l = \boldsymbol{\mathcal{L}}_l \boldsymbol{\mathcal{A}}_l$. Letting $\boldsymbol{\mathcal{W}}_l = (\boldsymbol{\mathcal{I}} - \boldsymbol{\mathcal{L}}_l \boldsymbol{\mathcal{S}}_l)^{-1}$ and eliminating $\boldsymbol{\mathcal{A}}_l$ from (4.11) yields

$$\boldsymbol{\mathcal{B}}_l = \boldsymbol{\mathcal{W}}_l \boldsymbol{\mathcal{L}}_l \boldsymbol{\mathcal{O}}_1 \mathbf{f}_l^+ + \boldsymbol{\mathcal{W}}_l \boldsymbol{\mathcal{L}}_l \boldsymbol{\mathcal{O}}_2 \mathbf{g}_l^- \tag{4.13}$$

In the l-th layer, the relationship between $\{f,g\}_{lp}^+$ and $\{f,g\}_{lp}^-$ can be obtained by evaluating the Green's second identity along the closed path defined by the boundary of the primary cell and the one of the inside fiber. The procedure is the same as the one detailed in sections 2.2.2 and 3.2. The relation is similar with the one given in equation (2.41), it is

$$f_{lp}^- = f_{lp}^+ + \sum_{m\in\mathbb{Z}} B_{lm} Q_{lpm}^-, \tag{4.14a}$$

$$g_{lp}^+ = g_{lp}^- + \sum_{m\in\mathbb{Z}} B_{lm} Q_{lpm}^+. \tag{4.14b}$$

with $Q_{lpm}^{\pm} = \frac{2(-i)^m e^{\pm im\theta_{lp}}}{d\beta_{lp}}$. Writing it into matrix form yields

$$\mathbf{f}_l^- = \mathbf{f}_l^+ + \boldsymbol{\mathcal{Q}}_l^- \boldsymbol{\mathcal{B}}_l, \tag{4.15a}$$

$$\mathbf{g}_l^+ = \mathbf{g}_l^- + \boldsymbol{\mathcal{Q}}_l^+ \boldsymbol{\mathcal{B}}_l, \tag{4.15b}$$

where $\boldsymbol{\mathcal{Q}}_l^{\pm} = \mathrm{diag}\left\{\left[Q_{lpm}^{\pm}\right]_{pm},\left[Q_{lpm}^{\pm}\right]_{pm}\right\}$, $\mathbf{f}_l^{\pm} = \left[\left[f_{lep}^{\pm}\right],\left[f_{lhp}^{\pm}\right]\right]^T$ and $\mathbf{g}_l^{\pm} = \left[\left[g_{lep}^{\pm}\right],\left[g_{lhp}^{\pm}\right]\right]^T$. Substituting (4.13) into (4.15) and eliminating $\boldsymbol{\mathcal{B}}_l$ produces

$$\mathbf{f}_l^- = \mathbf{f}_l^+ + \boldsymbol{\mathcal{Q}}_l^- \boldsymbol{\mathcal{W}}_l \boldsymbol{\mathcal{L}}_l \boldsymbol{\mathcal{O}}_1 \mathbf{f}_l^+ + \boldsymbol{\mathcal{Q}}_l^- \boldsymbol{\mathcal{W}}_l \boldsymbol{\mathcal{L}}_l \boldsymbol{\mathcal{O}}_2 \mathbf{g}_l^-, \tag{4.16a}$$

$$\mathbf{g}_l^+ = \mathbf{g}_l^- + \mathcal{Q}_l^+ \mathcal{W}_l \mathcal{L}_l \mathcal{O}_1 \mathbf{f}_l^+ + \mathcal{Q}_l^+ \mathcal{W}_l \mathcal{L}_l \mathcal{O}_2 \mathbf{g}_l^-, \tag{4.16b}$$

4.5 T-matrix approach

Letting $\mathcal{F}_l^- = \left[\mathbf{f}_l^-, \mathbf{g}_l^-\right]^{\mathrm{T}}$ and $\mathcal{F}_l^+ = \left[\mathbf{f}_l^+, \mathbf{g}_l^+\right]^{\mathrm{T}}$, the relation between them is obtained by reorganizing (4.16), which is written as

$$\mathcal{F}_l^+ = \mathcal{G}_l \mathcal{F}_l^-. \tag{4.17}$$

The matrix $\mathcal{G}_l$ is calculated by $\mathcal{G}_l = \mathcal{G}_l^{(a)^{-1}} \mathcal{G}_l^{(b)}$ where $\mathcal{G}_l^{(a)}$ and $\mathcal{G}_l^{(b)}$ are defined as

$$\mathcal{G}_l^{(a)} = \begin{bmatrix} \mathcal{I} + \mathcal{Q}_l^- \mathcal{W}_l \mathcal{L}_l \mathcal{O}_1 & \mathbf{0} \\ \mathcal{Q}_l^+ \mathcal{W}_l \mathcal{L}_l \mathcal{O}_1 & -\mathcal{I} \end{bmatrix}, \quad \mathcal{G}_l^{(b)} = \begin{bmatrix} \mathcal{I} & -\mathcal{Q}_l^- \mathcal{W}_l \mathcal{L}_l \mathcal{O}_2 \\ \mathbf{0} & -(\mathcal{I} + \mathcal{Q}_l^+ \mathcal{W}_l \mathcal{L}_l \mathcal{O}_2) \end{bmatrix}. \tag{4.18a}$$

$\mathcal{I}$ denotes the identity matrix here. The relation between $\mathcal{F}_l^-$ and $\mathcal{F}_{l'}^+$ is given in equation (4.5) in section 4.3.1. Combining (4.5) with (4.17) yields

$$\mathcal{F}_l^+ = \mathcal{G}_l \mathcal{M}_l \mathcal{F}_{l'}^+ \tag{4.19}$$

As illustrated in Fig. 4.3, there are two transfer matrices actually, $\mathcal{M}_l$ and $\mathcal{G}_l$. $\mathcal{M}_l$ transfers the field across the t_l boundary and $\mathcal{G}_l$ transfers it across the cylinders in the l-th layer. Combining the two matrices yields the iterative relation (4.19) which is used from the top layer to the bottom one to produce the relation between transmission and reflection coefficients,

$$\mathcal{F}_0^+ = (\mathcal{M}_0 \mathcal{G}_1 \mathcal{M}_1, ..., \mathcal{G}_n) \mathcal{M}_n \mathcal{F}_{n'}^-, \tag{4.20}$$

where $\mathcal{F}_0^+$ and $\mathcal{F}_{n'}^-$ are defined in section 4.3.1. The solution of $\mathcal{R}$ and $\mathcal{T}$ is obtained by solving this equation.

Computationally speaking, the summation $\sum_{m\in\mathbb{Z}}$ related to multipole expansion and the one $\sum_{p\in\mathbb{Z}}$ corresponding to plane-wave expansion are truncated as $\sum_{m=-M}^{M}$ and $\sum_{m=-P_{min}}^{P_{max}}$, respectively. Since some elements in $\mathcal{M}_l$ will be much larger for evanescent modes than the values associated to propagating modes, $\mathcal{M}_l$ is ill-conditioned. So, the values of P_{min} and P_{max} need to be carefully chosen to include all propagating modes but exclude all evanescent modes, leading to potentially poor accuracy at high frequency. When the frequency of the incident wave is low enough, the approach works properly since only one propagating mode exists in this case where the electromagnetic behavior of the laminate is similar to the one of a homogeneous slab. A more thorough discussion of this topic is in section 4.7.

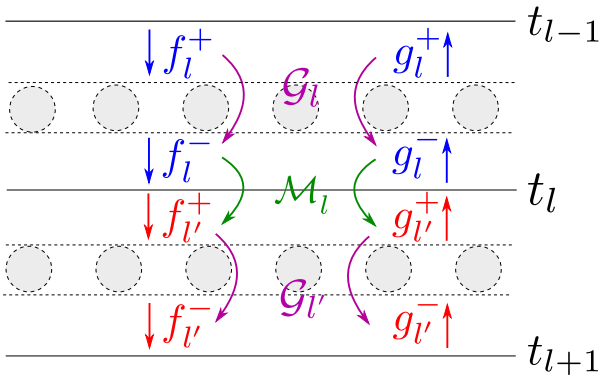

Fig. 4.3 The procedure of calculation from layer to layer with scattering matrices.

4.6 S-matrix approach

In scattering theory, S-matrix which is short for scattering matrix relates the scattered field to the incident field. For the concerned problem, two types of S-matrices exist. One is called interface S-matrix, which relates the field scattered by the interfaces t_l to the field impinging on the interface. The other one is called layer S-matrix, which links the scattered field and the incident field corresponding to the fibers in one single layer. For the considered multilayered structure, all the interface and layer S-matrices are combined in the order of the layers to produce the S-matrix of the whole structure.

In order to avoid the numerical problem above, another approach based on S-matrices [64] is now proposed. Let $\mathcal{G}_l^{(1)}$, $\mathcal{G}_l^{(2)}$, $\mathcal{G}_l^{(3)}$ and $\mathcal{G}_l^{(4)}$ be defined as

$$\mathcal{G}_l^{(1)} = \mathcal{I} + \mathcal{Q}_l^- \mathcal{W}_l \mathcal{L}_l \mathcal{O}_1, \tag{4.21a}$$
$$\mathcal{G}_l^{(2)} = \mathcal{Q}_l^- \mathcal{W}_l \mathcal{L}_l \mathcal{O}_2, \tag{4.21b}$$
$$\mathcal{G}_l^{(3)} = \mathcal{Q}_l^+ \mathcal{W}_l \mathcal{L}_l \mathcal{O}_1, \tag{4.21c}$$
$$\mathcal{G}_l^{(4)} = \mathcal{I} + \mathcal{Q}_l^+ \mathcal{W}_l \mathcal{L}_l \mathcal{O}_2, \tag{4.21d}$$

then the relation (4.16) for $\mathbf{f}_l^\pm$ and $\mathbf{g}_l^\pm$ is written as

$$\begin{bmatrix} \mathbf{f}_l^- \\ \mathbf{g}_l^+ \end{bmatrix} = \begin{bmatrix} \mathcal{G}_l^{(1)} & \mathcal{G}_l^{(2)} \\ \mathcal{G}_l^{(3)} & \mathcal{G}_l^{(4)} \end{bmatrix} \begin{bmatrix} \mathbf{f}_l^+ \\ \mathbf{g}_l^- \end{bmatrix}. \tag{4.22}$$

where, the superscript $(*)$ with $* = 1, 2, 3, 4$ indicates the positions of the block matrices $\mathcal{G}_l^{(*)}$. Applying equation (4.6) on boundary t_{l-1} and combining it with (4.22) produces the

relationship between $\{\mathbf{f},\mathbf{g}\}^-_{l-1}$ and $\{\mathbf{f},\mathbf{g}\}^-_l$,

$$\begin{bmatrix}\mathbf{f}^-_l\\ \mathbf{g}^-_{l-1}\end{bmatrix}=\begin{bmatrix}\mathcal{D}^{(1)}_{l-1,l} & \mathcal{D}^{(2)}_{l-1,l}\\ \mathcal{D}^{(3)}_{l-1,l} & \mathcal{D}^{(4)}_{l-1,l}\end{bmatrix}\begin{bmatrix}\mathbf{f}^-_{l-1}\\ \mathbf{g}^-_l\end{bmatrix} \tag{4.23}$$

with matrices

$$\mathcal{D}^{(1)}_{l-1,l}=\mathcal{G}^{(1)}_l\left(\mathcal{I}-\mathcal{M}^{(2)}_{l-1,l}\mathcal{G}^{(3)}_l\right)^{-1}\mathcal{M}^{(1)}_{l-1,l}, \tag{4.24a}$$

$$\mathcal{D}^{(2)}_{l-1,l}=\mathcal{G}^{(2)}_l+\mathcal{G}^{(1)}_l\left(\mathcal{I}-\mathcal{M}^{(2)}_{l-1,l}\mathcal{G}^{(3)}_l\right)^{-1}\mathcal{M}^{(2)}_{l-1,l}\mathcal{G}^{(4)}_l, \tag{4.24b}$$

$$\mathcal{D}^{(3)}_{l-1,l}=\mathcal{M}^{(3)}_{l-1,l}+\mathcal{M}^{(4)}_{l-1,l}\left(\mathcal{I}-\mathcal{G}^{(3)}_l\mathcal{M}^{(2)}_{l-1,l}\right)^{-1}\mathcal{G}^{(3)}_l\mathcal{M}^{(1)}_{l-1,l}, \tag{4.24c}$$

$$\mathcal{D}^{(4)}_{l-1,l}=\mathcal{M}^{(4)}_{l-1,l}\left(\mathcal{I}-\mathcal{G}^{(3)}_l\mathcal{M}^{(2)}_{l-1,l}\right)^{-1}\mathcal{G}^{(4)}_l \tag{4.24d}$$

As shown in Fig. 4.4, two S-matrices $\mathcal{M}^*_{l-1,l}$ and $\mathcal{G}^*_l$ are used here for relating input and output on the boundary t_{l-1} and the fiber array respectively.

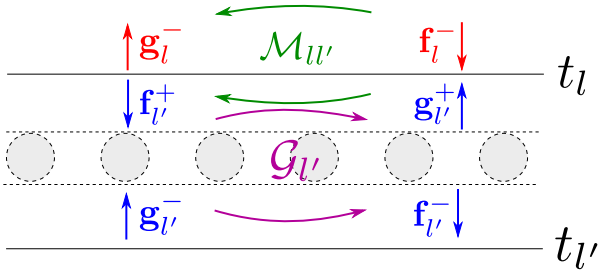

Fig. 4.4 The procedure of calculation from layer to layer with transfer matrices.

Applying (4.23) to all layers above the l-th layer and combining the produced matrices yields the relation between incident field and the fields in the l-th layer, which reads

$$\begin{bmatrix}\mathbf{f}^-_l\\ \mathbf{g}^-_0\end{bmatrix}=\begin{bmatrix}\mathcal{D}^{(1)}_{0,l} & \mathcal{D}^{(2)}_{0,l}\\ \mathcal{D}^{(3)}_{0,l} & \mathcal{D}^{(4)}_{0,l}\end{bmatrix}\begin{bmatrix}\mathbf{f}^-_0\\ \mathbf{g}^-_l\end{bmatrix} \tag{4.25}$$

where $\mathbf{f}^-_0=[[E^{inc}_y\delta_{0p}],[K^{inc}_y\delta_{0p}]]$ and $\mathbf{g}^-_0=[[R^e_p],[R^h_p]]$ at $z=t_0$. Applying (4.23) to the $(l+1)$-th layer and combining it with (4.25) produces the relationship between $\{\mathbf{f},\mathbf{g}\}^-_0$ and $\{\mathbf{f},\mathbf{g}\}^-_{l'}$, which is read as

$$\begin{bmatrix}\mathbf{f}^-_{l'}\\ \mathbf{g}^-_{0,}\end{bmatrix}=\begin{bmatrix}\mathcal{D}^{(1)}_{0,l'} & \mathcal{D}^{(2)}_{0,l'}\\ \mathcal{D}^{(3)}_{0,l'} & \mathcal{D}^{(4)}_{0,l'}\end{bmatrix}\begin{bmatrix}\mathbf{f}^-_0\\ \mathbf{g}^-_{l'}\end{bmatrix} \tag{4.26}$$

within which the matrices are defined as

$$\mathcal{D}_{0,l'}^{(1)} = \mathcal{D}_{ll'}^{(1)}(\mathcal{I} - \mathcal{D}_{0,l}^{(2)}\mathcal{D}_{ll'}^{(3)})^{-1}\mathcal{D}_{0,l}^{(1)} \tag{4.27a}$$

$$\mathcal{D}_{0,l'}^{(2)} = \left[\mathcal{D}_{ll'}^{(1)}(\mathcal{I} - \mathcal{D}_{0,l}^{(2)}\mathcal{D}_{ll'}^{(3)})^{-1}\mathcal{D}_{0,l}^{(2)}\mathcal{D}_{ll'}^{(4)} + \mathcal{D}_{ll'}^{(2)}\right], \tag{4.27b}$$

$$\mathcal{D}_{0,l'}^{(3)} = \left[\mathcal{D}_{0,l}^{(3)} + \mathcal{D}_{0,l}^{(4)}(\mathcal{I} - \mathcal{D}_{ll'}^{(3)}\mathcal{D}_{0,l}^{(2)})^{-1}\mathcal{D}_{ll'}^{(3)}\mathcal{D}_{0,l}^{(1)}\right], \tag{4.27c}$$

$$\mathcal{D}_{0,l'}^{(4)} = \mathcal{D}_{0,l}^{(4)}(\mathcal{I} - \mathcal{D}_{ll'}^{(3)}\mathcal{D}_{0,l}^{(2)})^{-1}\mathcal{D}_{ll'}^{(4)} \tag{4.27d}$$

Notice that equation (4.27) is a recursive relation, and equation (4.25) is actually a result of applying (4.27) on all the layers above the l-th layer (include the l-th layer). Applying the recursive relation (4.27) from the top layer to the bottom one produces

$$\begin{bmatrix} \mathbf{f}_n^- \\ \mathbf{g}_0^- \end{bmatrix} = \begin{bmatrix} \mathcal{D}_{0,n}^{(1)} & \mathcal{D}_{0,n}^{(2)} \\ \mathcal{D}_{0,n}^{(3)} & \mathcal{D}_{0,n}^{(4)} \end{bmatrix} \begin{bmatrix} \mathbf{f}_0^- \\ \mathbf{g}_n^- \end{bmatrix}, \tag{4.28}$$

Applying (4.6) on boundary t_n and combining it with equation (4.28) through equation (4.24) yields

$$\begin{bmatrix} \mathbf{f}_{n'}^+ \\ \mathbf{g}_0^- \end{bmatrix} = \begin{bmatrix} \mathcal{D}_{0,n'}^{(1)} & \mathcal{D}_{0,n'}^{(2)} \\ \mathcal{D}_{0,n'}^{(3)} & \mathcal{D}_{0,n'}^{(4)} \end{bmatrix} \begin{bmatrix} \mathbf{f}_0^- \\ \mathbf{g}_{n'}^+ \end{bmatrix}, \tag{4.29}$$

which is the relation between the incident field and reflection/transmission coefficients with $\mathbf{f}_{n'}^+ = [[T_p^e], [T_p^h]]$ and $\mathbf{g}_{n'}^+ = [0, 0]$ at $z = t_n$. Noticing that the S-matrix at the boundary $z = t_n$ is finally included in (4.29) which is actually the S-matrix for the whole structure and can be used straightforwardly to obtain reflection and transmission coefficients. Once they are obtained, the coefficients $\{\mathbf{f}, \mathbf{g}\}_l^-$ easily follow with (4.25),

$$\mathbf{f}_l^- = \mathcal{D}_{0,l}^{(1)}\mathbf{f}_0^- + \mathcal{D}_{0,l}^{(2)}\mathbf{g}_l^- \tag{4.30a}$$

$$\mathbf{g}_l^- = \mathcal{D}_{0,l}^{(4)^{-1}}\left(\mathbf{g}_0^- - \mathcal{D}_{0,l}^{(3)}\mathbf{f}_0^-\right) \tag{4.30b}$$

Since the inversion of matrix $\mathcal{D}_{0,l}^{(4)}$, which is ill-conditioned, is needed here, (4.30) is not suitable for computing the field distribution inside the structure. Numerical investigation is carried out in section 4.7. Another way for computing the field inside the structure is to use $\mathbf{f}_{n'}^-$, which avoids inverting $\mathcal{D}_{0,l}^{(4)}$ but requires to invert $\mathcal{D}_{0,l}^{(2)}$ which is also ill-conditioned. But with a low-frequency incident wave, (4.30) will be much more stable.

However, a full-wave solution is needed for calculating the field distribution inside the composite. Here, an effective approach is proposed to solve this problem thoroughly by rearranging the corresponding matrices to relate the expansion coefficients in the l-th layer to the incident wave. Then the inversion of any ill-conditioned matrix is avoided naturally.

According to (4.27), the relation between $\{\mathbf{f},\mathbf{g}\}_l^-$ and $\{\mathbf{f},\mathbf{g}\}_{n'}^+$ reads as

$$\mathbf{f}_{n'}^+ = \boldsymbol{\mathcal{D}}_{l,n'}^{(1)}\mathbf{f}_l^- + \boldsymbol{\mathcal{D}}_{l,n'}^{(2)}\mathbf{g}_{n'}^+ \tag{4.31a}$$

$$\mathbf{g}_l^- = \boldsymbol{\mathcal{D}}_{l,n'}^{(3)}\mathbf{f}_l^- + \boldsymbol{\mathcal{D}}_{l,n'}^{(4)}\mathbf{g}_{n'}^+. \tag{4.31b}$$

Since $\mathbf{g}_{n'}^+ = [0,0]^T$, (4.31b) is written as $\mathbf{g}_l^- = \boldsymbol{\mathcal{D}}_{l,n'}^{(3)}\mathbf{f}_l^-$, combining it with (4.30a) produces

$$\mathbf{g}_l^- = \boldsymbol{\mathcal{D}}_{l,n'}^{(3)}\mathbf{f}_l^- \tag{4.32a}$$

$$\mathbf{f}_l^- = \left(\boldsymbol{\mathcal{I}} - \boldsymbol{\mathcal{D}}_{0,l}^{(2)}\boldsymbol{\mathcal{D}}_{l,n'}^{(3)}\right)^{-1}\boldsymbol{\mathcal{D}}_{0,l}^{(1)}\mathbf{f}_0^- \tag{4.32b}$$

which is stable for calculating $\mathbf{f}_l^-$ and $\mathbf{g}_l^-$. $\mathbf{f}_l^+$ and $\mathbf{g}_l^+$ are obtained afterwards with (4.22).

4.7 Numerically investigating the stability of the approaches

As said in the above, some matrices used in the T- and S-matrix approaches become ill-conditioned when the number of layers increases. T-matrices cause serious numerical instability in the approach, which is not easily overcome by reformulating the equations or reducing the thickness of the layers. Ill-conditioned S-matrices are exhibited also but their direct inversion is naturally avoided when formulating the equations for computations.

Considering a laminate with same background layer material (epoxy, $\epsilon_l^{(1)} = 3.6$), matrices $\mathbf{M}_{lp}^{(ij)}$ will all be null matrices save $\mathbf{M}_l^{(11)}$, $\mathbf{M}_l^{(22)}$, $\mathbf{M}_l^{(33)}$, and $\mathbf{M}_l^{(44)}$ the elements of which on the main diagonal are $M_{lp}^{(11)}$, $M_{lp}^{(22)}$, $M_{lp}^{(33)}$, and $M_{lp}^{(44)}$. Notice that $e_{l'} < t_l < e_l$ and $\Im\beta_{lp} > 0$, $P_{l'p}$ and U_{lp} exponentially increase with the order of the evanescent modes, but P_{lp} and $U_{l'p}$, at the denominator in $\mathbf{M}_{lp}^{(ij)}$, exponentially decrease. This means very large values of matrices $\mathbf{M}_l^{(11)}$ and $\mathbf{M}_l^{(22)}$ but very small ones of matrices $\mathbf{M}_l^{(33)}$ and $\mathbf{M}_l^{(44)}$, which renders matrix $\boldsymbol{\mathcal{M}}_l$ ill-conditioned.

Let as an example the period of the fiber arrays be $d = 0.1\,\text{mm}$, with constant layer thickness $h_l = d$ and radius of fibers $c_l = 0.25d$. Let the incident wave be with $\lambda^{\text{inc}} = d$, $\vartheta = 60°$, $E_y^{inc} = 1$ and $K_y^{inc} = 1$. Assuming $\sum_{p\in\mathbb{Z}}$ to be truncated as $\sum_{m=-P}^{P}$ with $P = P_0 + P'$, where only $2P_0 + 1$ propagating modes and $2P'$ evanescent modes are counted and the condition number of $\boldsymbol{\mathcal{M}}_l$ being defined as $C^{(m)}$, the logarithm (base 10) of the condition number of $\boldsymbol{\mathcal{M}}_l$ is computed. Its maximum values are in Table 4.1 for different numbers of evanescent modes and different numbers of layers. As seen, the T-matrix method works fine for a single-layer laminate or a multi-layered laminate with only propagating modes. Once evanescent modes included in the computation for the multilayered laminates, $\boldsymbol{\mathcal{M}}_l$ becomes ill-conditioned. At the same time, matrices $\boldsymbol{\mathcal{M}}_l$ are multiplied together, as given

in (4.20), which may amplify the error and can also cause data overflow, hence producing inaccurate results.

	1 layer	*10 layers*	*20 layers*
$P = P_0$	1.2928	1.2928	1.2928
$P = P_0 + 1$	6.2245	11.7210	18.1831
$P = P_0 + 2$	9.6015	18.3828	27.7389
$P = P_0 + 3$	12.6963	24.4549	35.6067

Table 4.1 $\log_{10} C^{(m)}$ of matrix $\boldsymbol{\mathcal{M}}_l$ for different numbers of layers and evanescent modes associated with P'. $2P_0$ denotes the total number of propagating modes.

In contrast, the S-matrix approach is much more stable for calculating the reflection and transmission coefficients, although matrices $\boldsymbol{\mathcal{D}}_{0,l}^{(1)}$, $\boldsymbol{\mathcal{D}}_{0,l}^{(2)}$, and $\boldsymbol{\mathcal{D}}_{0,l}^{(4)}$ are all ill-conditioned. Since the elements of matrices $\boldsymbol{\mathcal{D}}_{0,l}^{(*)}$, where $* = 1, 2, 3, 4$, represent the contribution of input $\mathbf{f}_0^-$ and $\mathbf{g}_l^-$ to the output $\mathbf{f}_l^-$ and $\mathbf{g}_0^-$, the ill-condition of the matrices might be caused by the exponentially decreasing elements which correspond to evanescent modes. But inversion of these ill-conditioned matrix are avoided naturally in the calculation, which then leads to a stable recursive algorithm for investigating the scattering of multilayered composite structures. The difficulty met during calculating the field distribution in the composite is easily overcome by rearranging the equation to link the field expansion coefficients in the l-th layer to the incident field. Then the relationship given in equation (4.32) is produced, and it can be used to calculate the field distribution stably. It is seen from equation (4.32) that the inversion of the ill-conditioned matrices is avoided naturally.

Considering the same structure used for Table 4.1 with 10 layers, and defining $C_j^{(d)}$ the condition number of $\boldsymbol{\mathcal{D}}_{0,l}^{(j)}$, where $j = 1, 2, 3, 4$, the values of $\log_{10} C_j^{(d)}$ are in Table 4.2, which shows that the matrix $\boldsymbol{\mathcal{D}}_{0,l}^{(2)}$ has a relatively small condition number, and the matrix $\boldsymbol{\mathcal{D}}_{0,l}^{(3)}$ is well conditioned. But the condition numbers of the matrices $\boldsymbol{\mathcal{D}}_{0,l}^{(1)}$ and $\boldsymbol{\mathcal{D}}_{0,l}^{(4)}$ are all large except the one of the matrices in the top layer.

However, elements of matrices $\boldsymbol{\mathcal{D}}_{0,l}^{(2)}\boldsymbol{\mathcal{D}}_{ll'}^{(3)}$ and $\boldsymbol{\mathcal{D}}_{ll'}^{(3)}\boldsymbol{\mathcal{D}}_{0,l}^{(2)}$ used in equation (4.27) are all small, and most of their elements are close to zero. The values of elements in $\boldsymbol{\mathcal{D}}_{0,l}^{(2)}\boldsymbol{\mathcal{D}}_{ll'}^{(3)}$ are displayed in Fig. 4.5 for $l = 5$ and $l = 6$; when $l = 5$, the elements are almost all null. For $l = 6$, most are null as well, save several that are not larger than ten. The elements in the matrices during calculation have values similar to the two sets shown in Fig. 4.5 alternatively with different l. For $\boldsymbol{\mathcal{D}}_{ll'}^{(3)}\boldsymbol{\mathcal{D}}_{0,l}^{(2)}$, a similar behavior is observed. Hence, the identity matrix $\boldsymbol{\mathcal{I}}$ ensures $\boldsymbol{\mathcal{I}} - \boldsymbol{\mathcal{D}}_{ll'}^{(3)}\boldsymbol{\mathcal{D}}_{0,l}^{(2)}$ and $\boldsymbol{\mathcal{I}} - \boldsymbol{\mathcal{D}}_{0,l}^{(2)}\boldsymbol{\mathcal{D}}_{ll'}^{(3)}$ in equation (4.27) be invertible, which renders the algorithm stable. So the performance of the S-matrix based scheme is

much better than the one based on T-matrix, and S-matrix will be built in this chapter to investigate the multilayered composites.

l	$\log_{10} C_1^{(d)}$	$\log_{10} C_2^{(d)}$	$\log_{10} C_3^{(d)}$	$\log_{10} C_4^{(d)}$
1	9.6523	8.7496	1.8641	11.0357
2	18.9713	8.7338	1.8598	19.5416
3	23.8055	8.6902	1.8448	24.3109
4	25.2755	8.7180	1.8464	24.6378
5	24.2842	8.6944	1.8457	24.4984
6	24.3070	8.7183	1.8619	24.9091
7	24.8560	8.6647	1.8616	25.0637
8	24.7776	8.6317	1.8403	24.0852
9	24.5594	8.6771	1.8463	24.4174
10	24.5732	8.6808	1.8466	24.2384

Table 4.2 Values of $\log_{10} C_j^{(d)}$ for matrices $\boldsymbol{\mathcal{D}}_{0,l}^{(j)}$ of the l-th layer in a 10-layer laminate.

4.8 Scattering of the multi-layered laminate

Power reflection and transmission coefficients $\boldsymbol{\mathcal{R}}$ and $\boldsymbol{\mathcal{T}}$ for plane waves are calculated with Poynting's theorem, referring to section 3.4 for more detail. Let $\boldsymbol{\mathcal{R}}(\theta_n)$ and $\boldsymbol{\mathcal{T}}(\theta_n)$ be related to the n-th plane-wave item in the expansion of the Gaussian beam, power reflection/transmission coefficients of the Gaussian beam are

$$\boldsymbol{\mathcal{R}}^{(g)} = \frac{\sum_{n\in\mathbb{Z}}^{N} \boldsymbol{\mathcal{R}}(\theta_n)|A(\theta_n)|^2}{\sum_{n\in\mathbb{Z}}^{N} |A(\theta_n)|^2}, \tag{4.33a}$$

$$\boldsymbol{\mathcal{T}}^{(g)} = \frac{\sum_{n\in\mathbb{Z}}^{N} \boldsymbol{\mathcal{T}}(\theta_n)|A(\theta_n)|^2}{\sum_{n\in\mathbb{Z}}^{N} |A(\theta_n)|^2} \tag{4.33b}$$

where the superscript g means Gaussian, which distinguishes the reflection/transmission coefficients of Gaussian beam from plane-wave ones.

The infinite summation $\sum_{m\in\mathbb{Z}}$ for the multiple expansion is truncated as $\sum_{m=-M}^{M}$, and $\sum_{p\in\mathbb{Z}}$ for the plane-wave expansion is calculated with $\sum_{m=P_{\min}}^{P_{\max}}$. Here, $M = \max\{\mathrm{Int}(\Re(4.05\times(k_{lt}c)^{1/3}) + k_{lt}c)\}$ [40], which shows that the value of M depends on the material of the l-th layer, the radius of the fiber and the frequency of the incident wave. At high frequency, the value of M is around 10, but at low frequency, its value could be smaller. $P_{\min}$ and $P_{\max}$

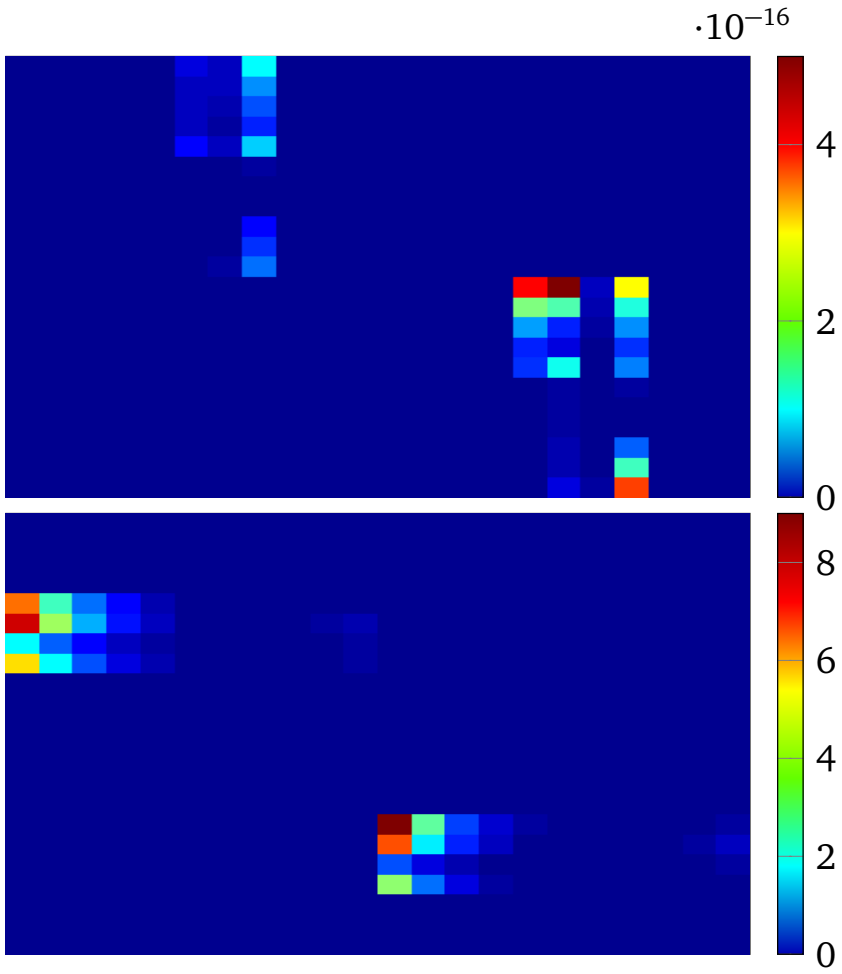

Fig. 4.5 Values in matrix $\mathcal{D}^{(2)}_{0,l}\mathcal{D}^{(3)}_{ll'}$ for (a) $l = 5$ and (b) $l = 6$.

are carefully selected to include all propagating modes ($\beta^2_{lp} > 0$) and at least 6 lowest-order evanescent modes ($\beta^2_{lp} < 0$) for the plane-wave expansion used in the calculation to achieve a relative error less than 10^{-6} for $|\boldsymbol{\mathcal{R}}^{(n+1)} - \boldsymbol{\mathcal{R}}^{(n)}|$, n truncation order P or M.

In the following simulations, the S-matrix approach is used. First, it is validated by comparing its results with those in [3], as shown in Fig. 4.6. A multilayered structure with six layers of periodic arrays of circular fibers standing in air is considered. The entire structure is divided into slabs with in effect air as background material, and all have the same thickness $h = 0.7d$. All fibers are of same radius $c = 0.3d$ and aligned along their axis from left to right and top to bottom. The fiber material has relative permittivity $\epsilon^{(2)}_l = 2.5$. Power reflection coefficients $\boldsymbol{\mathcal{R}}$ of normally incident TM-polarized waves are computed by allowing $E^{inc}_y = 0$ and $K^{inc}_y = 1$. Good match is observed except that the first peak in the present results is much higher than the one of the results in [3], which is likely due to the fact that dense sampling points are needed to catch the sharp peak.

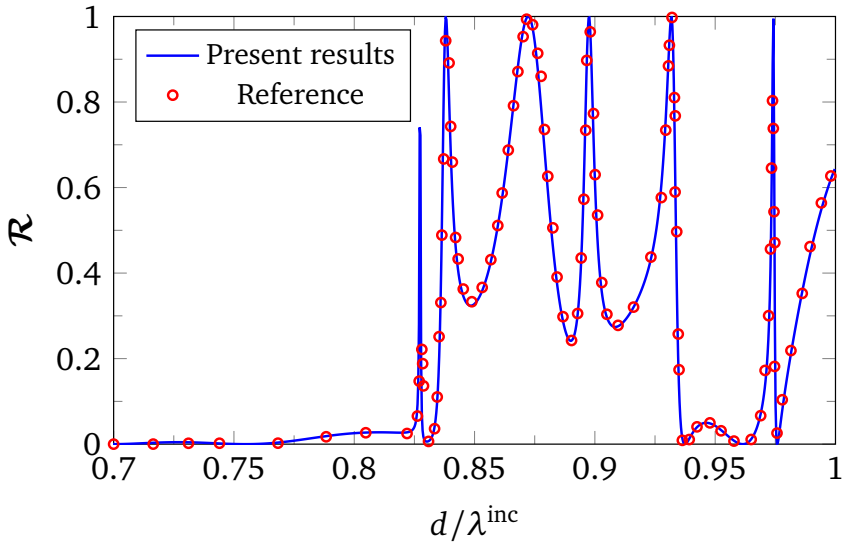

Fig. 4.6 Validating the approach by comparison of the present results (TM polarization) with those of [3]. λ^{inc} is the wavelength of the incident wave.

To validate the approach for out-of-plane incidence, another 6-layer composite is considered here with epoxy ($(\epsilon_l^{(1)} = 3.6)$) matrix and glass fiber with $\epsilon_l^{(2)} = 4.8$. Period $d = 0.1mm$, height $h_l = d$ and radius of all fibers $c_l = 0.25d$. A plane wave with $E_y^{\text{inc}} = K_y^{\text{inc}} = 1$ and $d/\lambda^{\text{inc}} = 1$ obliquely impinges on the composite with $\varphi = 45°$ and ϑ varying from $-90°$ to $90°$. Reflection coefficients are given in Fig. 4.7, and energy conservation is checked. It shows that the energy conservation law is satisfied for any incident angle, and a good symmetry is observed.

Next, one considers an 8-layer glass-fiber ($\epsilon_l^{(2)} = 4.8$) laminate involving two background materials, epoxy ($\epsilon_l^{(1)} = 3.6$) and polyester ($\epsilon_l^{(1)} = 2.8$). Glass-fiber reinforced epoxy and polyester slabs are piled up alternatively, the epoxy slab being top layer. The period of the fiber arrays is $d = 0.1\,\text{mm}$ and the layer thicknesses are the same, $h_l = d$. The fibers in a given layer are of same radius, but it is increased from $c_1 = 0.1d$ for the top layer to $c_8 = 0.45d$ for the bottom one, with $0.05d$ step. Within each even-numbered layer, the fibers are shifted to the right by $0.5d$. A broad frequency band, d/λ^{inc} varying from 0 to 1, is considered with 1500 samples taken. Normal and oblique incident waves are considered, with $\vartheta = 60°$ and $\varphi = 45°$ for obliquely incident ones, $E_y^{inc} = 1$, $K_y^{inc} = 1$.

Numerical results are displayed in Fig. 4.8, where quite smooth curves are observed at low frequency, in accord with the fact that only one propagating mode exists, and the behavior of the laminate appears similar with the one of a homogeneous slab structure. Rapid oscillations appear at high frequency with strong interaction as expected between

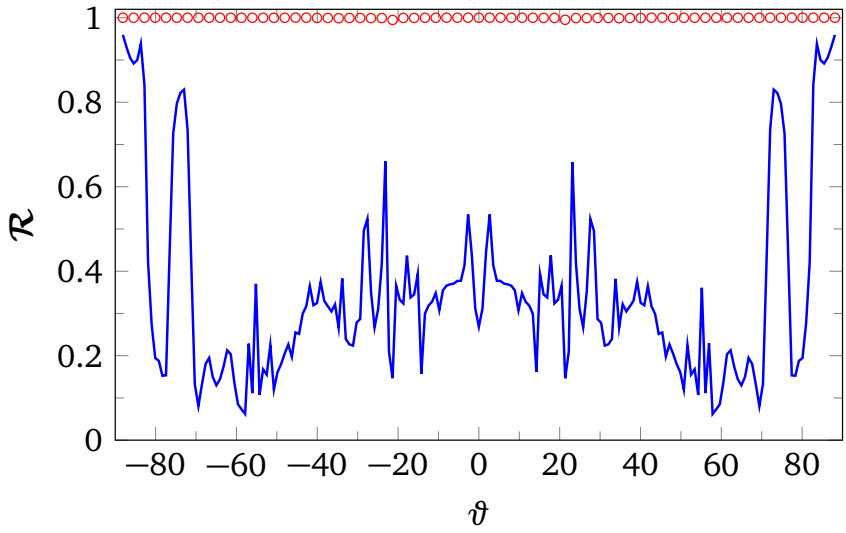

Fig. 4.7 Validating the approach with energy conservation $\mathcal{R} + \mathcal{T} = 1$ for epoxy matrix with glass fibers. λ^{inc} is the wavelength of the incident wave, and $d/\lambda^{\text{inc}} = 1$. Energy conservation is checked, and results are shown as red circles.

multiple propagating modes and the laminate. The energy conservation law is also checked for oblique incidence, which is satisfied well.

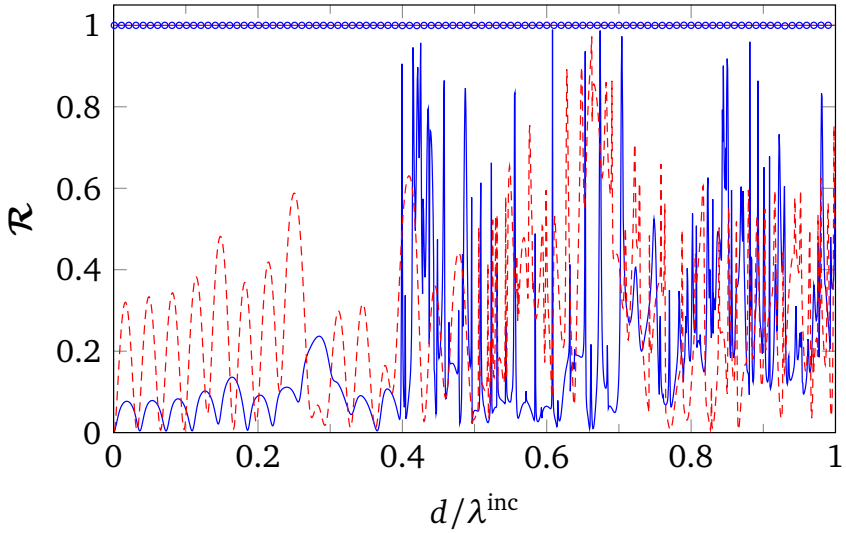

Fig. 4.8 Scattering of an 8-layer composite with alternative background materials and different radius of fibers in different layers, for normally (dashed red curve, $\vartheta = 0°$, $\varphi = 0°$) and obliquely (solid blue, $\vartheta = 60°$, $\varphi = 45°$) incident plane waves. Energy conservation is checked, and results are shown as straight line (red) for normal incidence while the circles (blue) for oblique case.

Another example in the same realm is the one of a 50-layer laminate with epoxy matrix and glass fibers ($\epsilon_l^{(2)} = 4.8$), with period $d = 0.1mm$, radius $c_l = 0.25d$, and constant thicknesses $h_l = d$. Fibers in the even-numbered layers are right shifted by $d/2$. A plane wave with $E_y^{inc} = 1$ and $K_y^{inc} = 1$ impinges on the structure normally or obliquely, then with $\vartheta = 60°$ and $\varphi = 45°$. Numerical results are displayed in Fig. 4.9. Reflection and transmission coefficients appear very sensitive to the variation of frequency. Some total reflection peaks or gaps are exhibited in both normal and oblique incidence case. The energy conservation law is satisfied well, too.

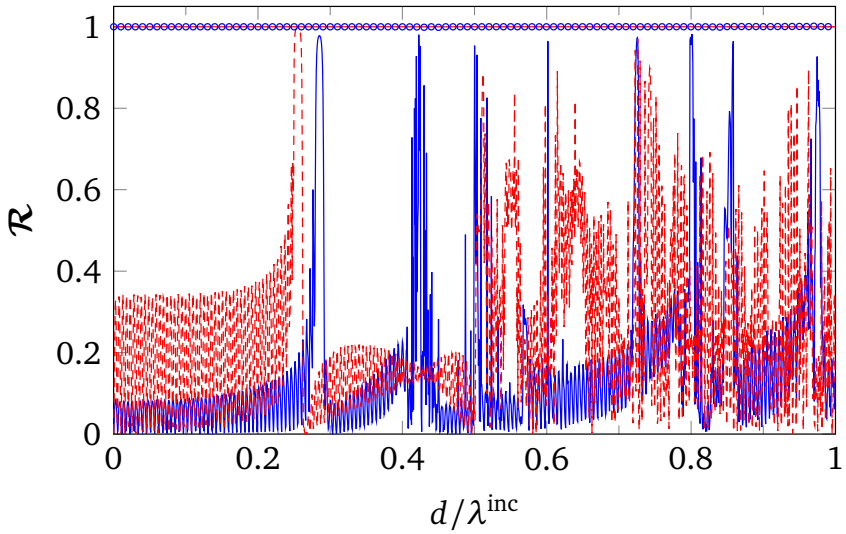

Fig. 4.9 Scattering of a 50-layer composite with epoxy background material. Plane wave incident normally (dashed, red) or obliquely (solid) with $\vartheta = 60°$ and $\varphi = 45°$. Energy conservation is checked and results are shown as straight line (red) for normal incidence and circles (blue) for oblique case.

Increasing the number of layers of the 50-layer composite to 100 constructs a 100-layer composite, in which the horizontal shift is removed to align the fibers along their axes from top to bottom. The reflection coefficients of the structure is given in Fig. 4.10 with the incident wave being the same as the one for the 50-layer model. Very fast oscillation is observed, and some total reflection gaps appear in both normal and oblique incident cases. But at high frequency, gaps only show up for normal incidence. The energy conservation is checked again, and it is satisfied well, except a slight difference at $d/\lambda^{\text{inc}} = 0.84$ and $d/\lambda^{\text{inc}} = 0.96$ for oblique incidence. The accuracy is mainly influenced by the calculation of lattice sums while the numerical errors are accumulated and amplified by cascading the S-matrix through layers.

Now, let us consider Gaussian beam scattering. Convergence of its expansion is appraised in section 2.3.2; here, θ_n varies from $-90°$ to $90°$, and 500 plane waves are used

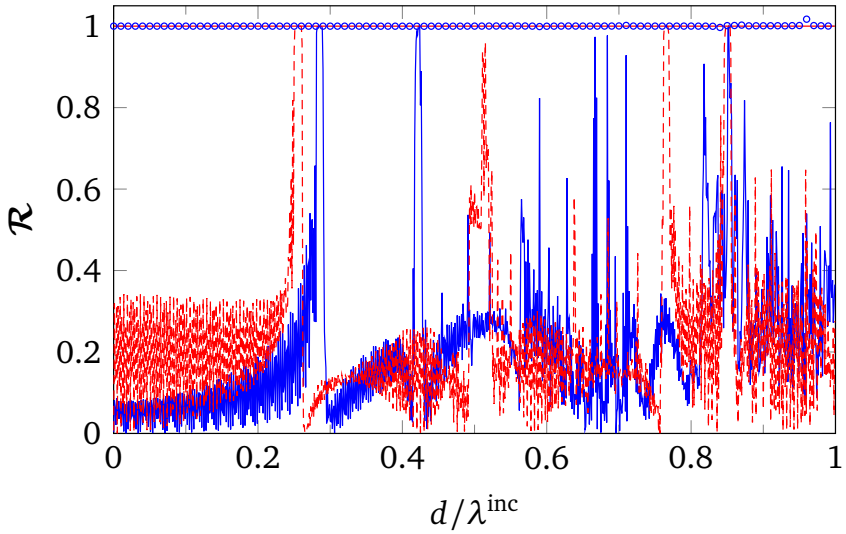

Fig. 4.10 Scattering of a 100-layer composite with epoxy matrix and glass fibers. Plane wave incident normally (dashed, red) or obliquely (solid) with $\vartheta = 60°$ and $\varphi = 45°$. Energy conservation is checked, and results are shown as straight line (red) for normal incidence and the circles (blue) for oblique case.

for the computation. First, a low-frequency incident wave with wavelength $\lambda^{\text{inc}} = 10d$ is obliquely impinging ($\vartheta = 60°$, $\varphi = 0$) upon an 8-layer glass-fiber laminate with center of the beam at $(x_0, z_0) = (0, 0)$, where $w_0 = 2\lambda^{\text{inc}}$. Only one propagating mode exists, and the behavior of the laminate is close to the one of a homogeneous slab. In Fig. 4.11 the total field is displayed. Here, the power reflection coefficient $\boldsymbol{\mathcal{R}}^{(g)} = 0.1880$, so most of the power is transmitted.

Replacing glass fibers with carbon fibers ($\epsilon_l^{(2)} = 12$, $\sigma = 3.3 \times 10^2\,\mathrm{S\,m^{-1}}$ [57, 58]) produces a laminate which, though its total thickness is only 0.8 mm, exhibits strong absorption of incident waves with long wavelength $\lambda^{\text{inc}} = 10d$, as shown in Fig. 4.12. Very little is transmitted, and the power reflection coefficients is 0.1276, so the absorption coefficient of the material is 0.8724, offering electromagnetic shieldness already.

A high-frequency incident beam ($\lambda^{\text{inc}} = d$) is also considered here for the 8-layer model with glass-fibers aligned from top layer to the bottom one, and the radii of the fibers are all the same, $c_l = 0.25d$. The total field distribution in the upper and lower half-spaces is shown in Fig. 4.13, illustrating a strong interaction between the wave and the structure, the wave being scattered in many directions even though two stronger beams along the reflection and transmission directions show up, and negative reflection phenomenon is observed. Here, power reflection and transmission are $\boldsymbol{\mathcal{R}}^{(g)} = 0.2270$ and $\boldsymbol{\mathcal{T}}^{(g)} = 0.7730$.

In Fig. 4.14, the total field for a Gaussian beam normally impinging on a 100-layer glass-fiber laminate with epoxy matrix is displayed. The laminate is of period $d = 0.1\,\mathrm{mm}$

and the thickness of each slab is $h = d$. Fibers have same radius $c_l = 0.25d$, and no shift along the x direction. The wavelength of the incident wave is $\lambda^{\text{inc}} = 10d$. Reflection and transmission are $\mathcal{R}^{(g)} = 0.2893$ and $\mathcal{T}^{(g)} = 0.7107$.

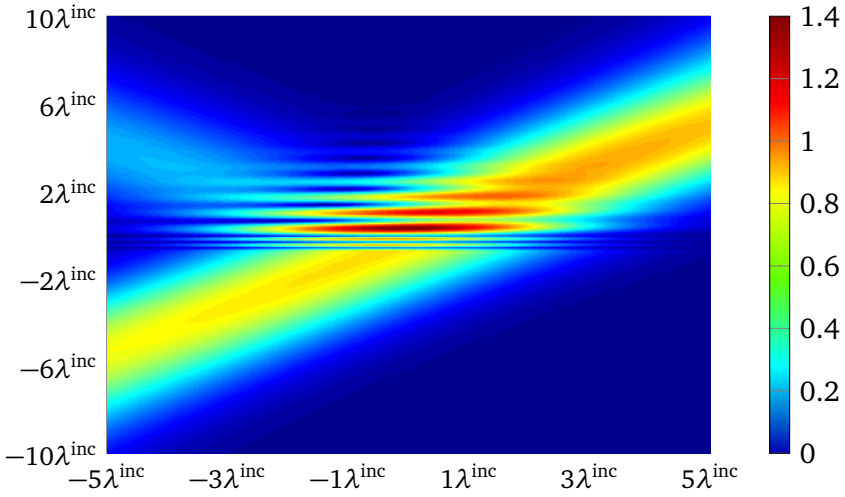

Fig. 4.11 Total field distribution for a Gaussian beam obliquely impinging onto an 8-layer glass-fiber laminate, with $(0,0)$ beam center and $\phi^{inc} = 45°$. $\lambda^{\text{inc}} = 10d$.

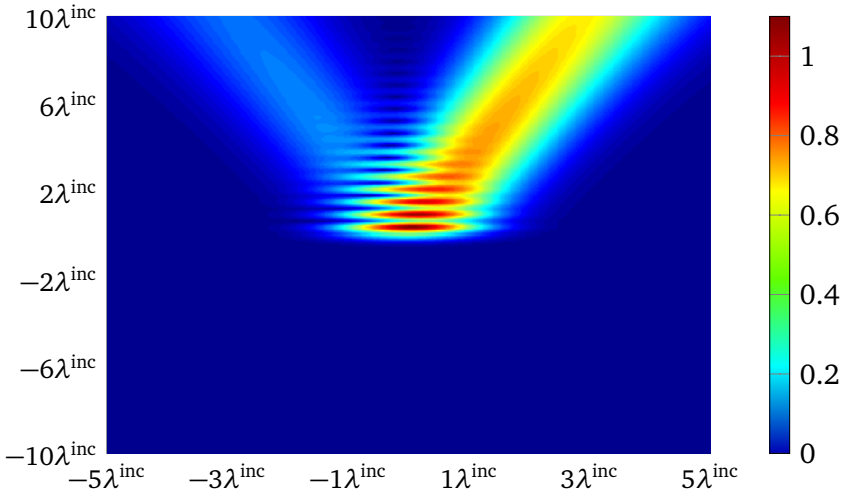

Fig. 4.12 Total field distribution for a Gaussian beam obliquely impinging onto an 8-layer carbon-fiber laminate, with $(0,0)$ beam center and $\phi^{inc} = 30°$. $\lambda^{\text{inc}} = 10d$.

At low enough frequency, the considered multilayered structure can be treated as a homogeneous structure with an effective permittivity which is calculated by the wave given in Appendix C. Some numerical results and discussions on single-layer structure have been given in section 2.4. Following all these works, the focus here is given to multilayered structures. Two sets of numerical results are proposed to verify efficacy and accuracy of

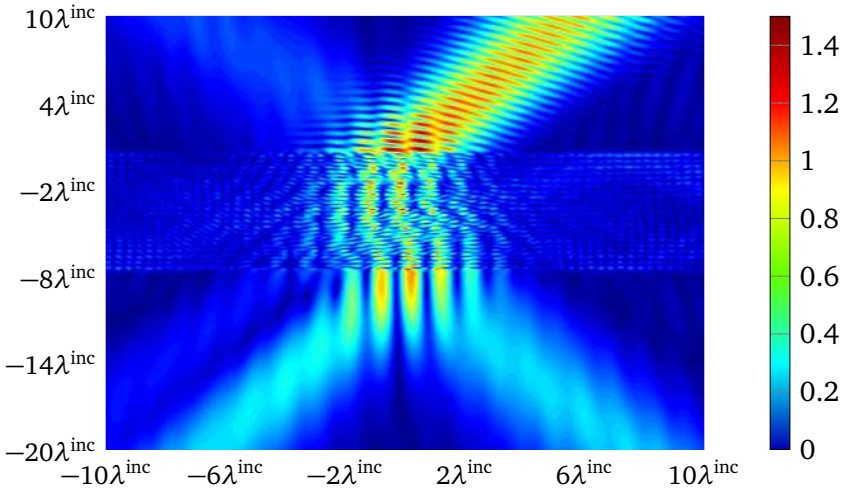

Fig. 4.13 Total field distribution for a Gaussian beam obliquely impinging onto an 8-layer glass-fiber laminate with $(0,0)$ beam center, $\phi^{inc} = 30°$, $\lambda^{inc} = d$. $w_0 = 2\lambda^{inc}$.

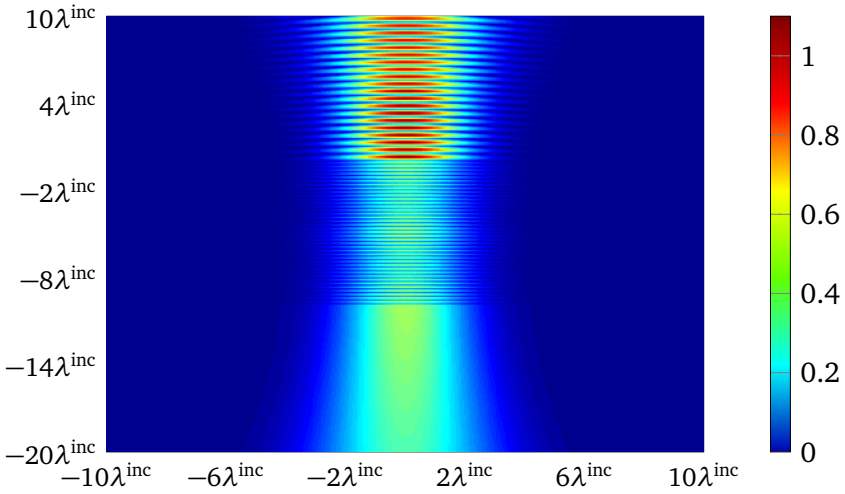

Fig. 4.14 Total field distribution of a Gaussian beam impinging onto a 100-layer model normally, with $(0,0)$ beam center and $\phi^{inc} = 30°$. $\lambda^{inc} = 10d$. $w_0 = 2\lambda^{inc}$.

approximately investigating the scattering of multilayered structure with the homogenized model. In the calculation, each of the layer is first homogenized, then the whole multilayered periodic structure is considered as a stack of homogenized layers.

For glass-fiber reinforced composites, the effective permittivity $\bar{\epsilon}_r$ is independent of the incident wave frequency. Consider a 100-layer glass-fiber ($\epsilon_r^{(2)} = 4.8$) composite with epoxy as background material ($\epsilon_r^{(1)} = 3.6$), the effective permittivity is $\bar{\epsilon}_r = 3.8356$ for TM wave and $\bar{\epsilon}_r = 3.7858$ for TE wave. With the effective permittivities, power reflection coefficients of the homogenized multilayered structure are calculated and compared with the exact values in a low frequency band. Results are given in Fig. 4.15 for TM wave and

Fig. 4.16 for TE waves. As seen, good matches are observed between the exact results and the one obtained with homogenized structure at low frequency. For TM wave illumination, the scattering of the multilayered structure can be well approximated with the homogenized structure as long as $d/\lambda^{\text{inc}} < 0.15$. But for TE wave illumination, the good approximation can be only achieved for $d/\lambda^{\text{inc}} < 0.1$. Even though, in microwave band $10\,\text{GHz} < f < 60\,\text{GHz}$, the homogenized model works well for both cases, as relative error less than 0.1% can be achieved. For TM case, the homogenized model works better than for the case of TE wave illumination.

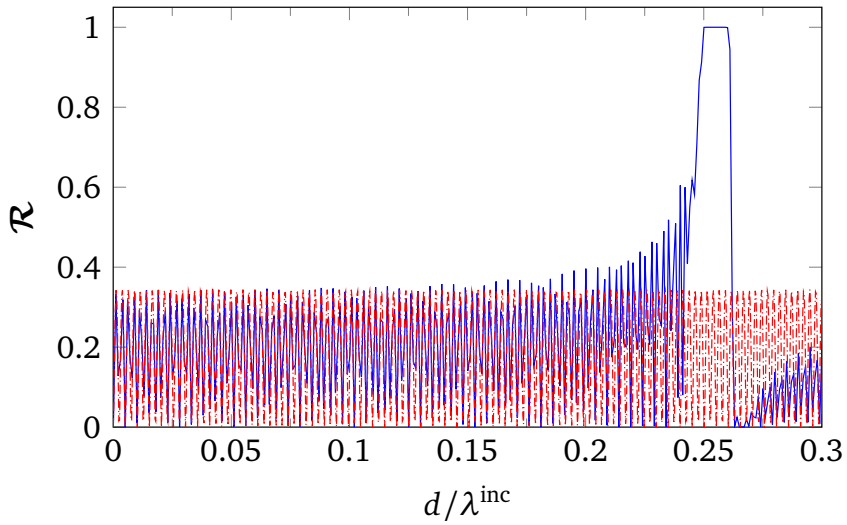

Fig. 4.15 Comparison of the results obtained with homogenized model and exact periodic model under TM wave illumination, normal incidence. Glass-fiber with epoxy background material. $\lambda^{\text{inc}} = d = 0.1\,\text{mm}$, $c = 0.25d$.

4.9 Summary

Recursive matrix schemes for modeling electromagnetic scattering of composites involving periodic arrays of fibers has been investigated. Though the approach with transfer matrix is more straightforward to put together and apply, the existence of exponentially increasing elements in the matrices entails that it is not suitable at high frequency (it works well at low frequency). In contrast, the more complicated scattering matrix method is far more stable and intrinsically broad-band. However, calculating the field distributions within the laminate at high frequency suffers from ill-conditioned matrices; one approach is proposed to solve this problem thoroughly by rearranging the corresponding matrices to relate field expansion coefficients in the structure to the incident wave.

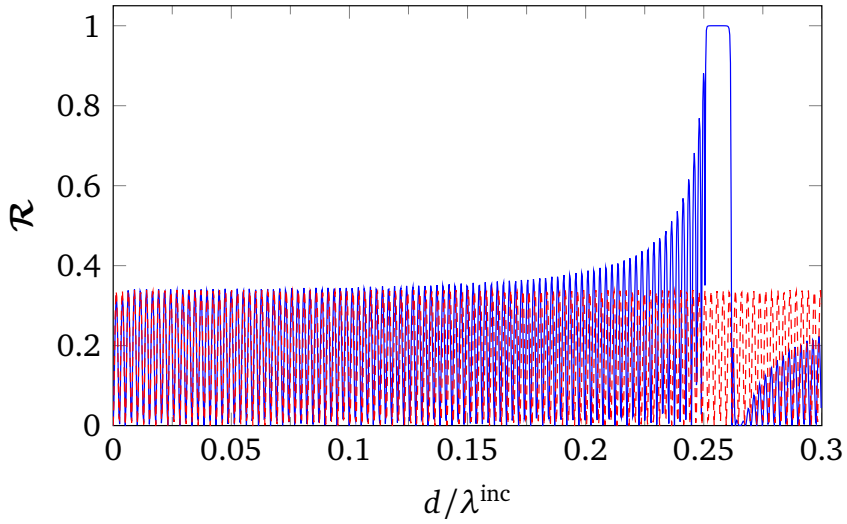

Fig. 4.16 Comparison of the results obtained with homogenized model and exact periodic model under TE wave illumination, normal incidence. Glass-fiber with epoxy background material. $\lambda^{\text{inc}} = d = 0.1\,\text{mm}$, $c = 0.25d$.

The main focus of the numerical experimentation has been on carbon- and glass-fiber-reinforced epoxy and polyester composites, for obliquely incident plane waves and Gaussian beams. Effectiveness and accuracy are exhibited for different composite models, with different degree of complexities. One has also validated the approach by sucessfully comparing the present results with those in the literature on optical crystals. Numerical results are also compared with the ones obtained with homogenized model of multilayered glass-fiber reinforced epoxy composite, and good efficacy and accuracy is achieved by homogenization technique.

Chapter 5

Scattering by laminates with arbitrary orientation of fibers in different layers

Scattering by laminated composites with fibers in all layers parallel to each other has been studied in the preceding chapters. These investigations provide the basic techniques which are extended in this chapter for scattering by laminates in which the fibers in different layers have arbitrary orientations. Two types of stratified organization are under consideration, assuming two kinds of elementary building blocks. The first type is composed from 2-layer fiber-reinforced blocks in which each layer is a single-layer composite. The fibers in different layers could be orientated into different directions. Stacking up a number of 2-layer blocks produces the multilayered structure. The second type is constructed in the same way, but the elementary building block has four layers in which the fibers are orientated into different directions.

5.1 Scattering by the composite with 2-layer stack

For the 2-layer stack, a periodic array of circular fibers is embedded in each layer. The fibers in the upper layer are arranged parallelly with their axes orientated into the same direction. The second layer is constructed in the same way, but the fibers in this layer are orientated into an arbitrary direction that can be different from the one of the fibers in the upper layer. The way of arranging the fibers for the stack is sketched in Fig. 5.1. The period and thickness of the l-th layer are d_l and h_l. The radii of the fibers are c_l. The cross-section of the primary cell is orthogonal to the axes of fibers in the l-th layer.

The materials used for the fibers and the backgrounds could be different from one to the other, but the upper and lower spaces are filled with air. The notations for distinguish-

ing different materials are defined in the same fashion as in section 4.1. The layers are numbered as shown in Fig. 5.2 with the boundaries $z = t_l$, $l = 0, 1, 2$.

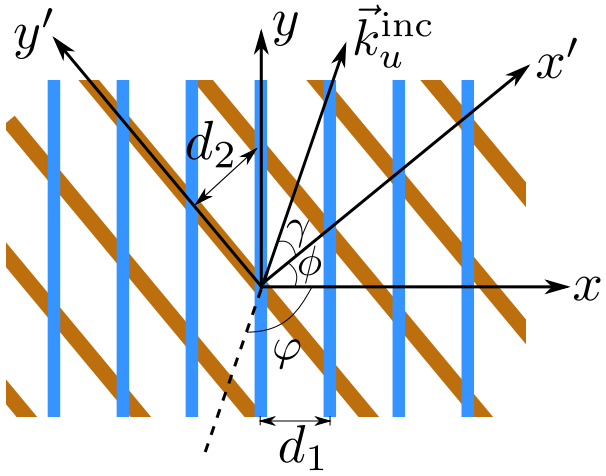

Fig. 5.1 Arranging the fibers for the 2-layer stack and coordinate systems with parameters of the structure

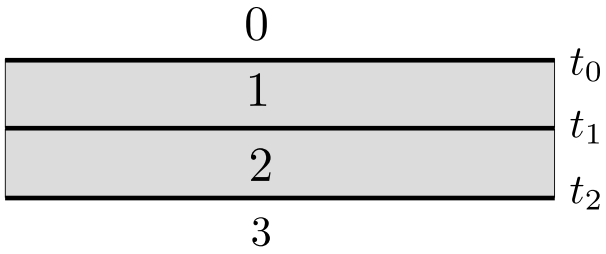

Fig. 5.2 Numbering of the considered laminate and the upper and lower half-spaces;.

To describe the stack mathematically, two Cartesian coordinate systems xyz and $x'y'z'$ are defined as shown in Fig. 5.1. Assigning the system xyz to the upper layer by setting the x axis along the direction of fibers' periodicity and the y axis along their orientation, then the other coordinate system $x'y'z'$ can be obtained by rotating the xyz system along the z axis by an angle ϕ so as to align the y' axis with the axis of the fibers in the second layer, noticing that there is no displacement along the z direction. Here, the xyz coordinate system is taken as the global one.

Considering time-harmonic field with $e^{-i\omega t}$, ω as the angular frequency, the incident fields are defined as $\boldsymbol{\mathcal{E}}(x,y,z) = \boldsymbol{\mathcal{E}}^{\text{inc}} e^{i(k_x^{\text{inc}} x + k_y^{\text{inc}} y - k_z^{\text{inc}} z)}$ and $\boldsymbol{\mathcal{H}}(x,y,z) = \boldsymbol{\mathcal{H}}^{\text{inc}} e^{i(k_x^{\text{inc}} x + k_y^{\text{inc}} y - k_z^{\text{inc}} z)}$. The wave vector of the incident plane wave is defined as $\vec{k}^{\text{inc}} = (\alpha_0, \xi_0, -\beta_0)$ in the global coordinate system with $\alpha_0 = k_x^{\text{inc}} = -k^{\text{inc}} \sin\vartheta \cos\varphi$, $\xi_0 = k_y^{\text{inc}} = k^{\text{inc}} \sin\vartheta \sin\varphi$, and $\beta_0 = k_z^{\text{inc}} = k^{\text{inc}} \cos\vartheta$, where the wavenumber is $k^{\text{inc}} = \omega/c = \sqrt{\alpha_0^2 + \beta_0^2 + \xi_0^2}$, c as speed of light

in vacuum, ϑ the angle between the z-axis and $\vec{k}^{\text{inc}}$, φ the one between the x-axis and the projection of $\vec{k}^{\text{inc}}$ in the x-y plane. Allowing $\vec{k}_u^{\text{inc}}$ to be the projection of $\vec{k}^{\text{inc}}$ in the x-y plane, and $\vec{k}_t^{\text{inc}}$ be the one in the x-z plane, then the wave vector of the incident wave can be decomposed as shown in Fig. 5.3, with $\vec{k}_u^{\text{inc}} = \alpha_0\hat{x} + \xi_0\hat{y}$, and $\vec{k}_t^{\text{inc}} = \alpha_0\hat{x} - \beta_0\hat{z}$.

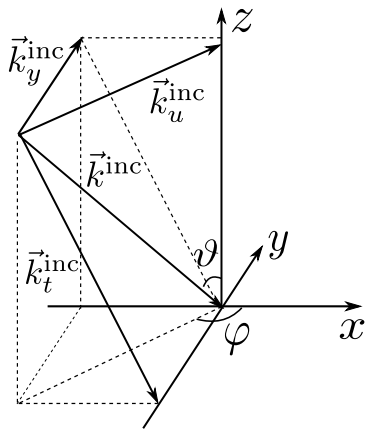

Fig. 5.3 Decomposition of incident wave vector $\vec{k}^{\text{inc}}$.

Denote the wave vector in the l-th layer and j-th region as $\vec{k}_{lj} = \vec{k}_{tlj} + k_{ylj}\hat{y}$, where $\vec{k}_{tlj} = k_{xlj}\hat{x} - k_{zlj}\hat{z}$ and $k_{tlj}^2 = k_{lj}^2 - k_{ylj}^2$. Allow $\vec{k}_{ulj} = k_{xlj}\hat{x} + k_{ylj}\hat{y}$, then $\vec{k}_{ulj} = \vec{k}_u^{\text{inc}}$ since it is continuous across all boundaries; here $\vec{k}_u$ is used instead of $\vec{k}_{ulj}$ in all layers ($l = 0, 1, 2, 3$) for convenience. In the following discussion, k_l, k_{tl}, α_l and β_l are used to replace k_{l1}, k_{tl1}, α_{l1} and β_{l1} in order to avoid possible confusion.

5.2 Field representations

Dispersion introduced by the top layer is characterized by $e^{i\alpha_p x}$, with $\alpha_p = 2\pi p/d_1$, and the one introduced by the bottom layer is characterized by $e^{i\alpha_q x'}$ in the coordinate system $x'y'z'$, with $\alpha_q = 2\pi q/d_2$. In the global coordinate system, the dependence of $e^{i\alpha_q x'}$ is rewritten as $e^{i\alpha_q \cos\phi x + i\alpha_q \sin\phi y}$. Therefore, the dispersion in the x direction is given as $\alpha_s = \alpha_0 + \alpha_p + \alpha_q \cos\phi$, and the one in the y direction is $\xi_q = \xi_0 + \alpha_q \sin\phi$, then the z dependence of the fields in the l-th layer is given as $e^{\pm i\beta_{ls} z}$ with $\beta_{ls} = \sqrt{k_l^2 - \alpha_s^2 - \xi_q^2}$, where s is a pair of p and q, denoted as $s = (p, q)$. The values of β_{ls} correspond to propagating modes satisfying $\beta_{ls}^2 > 0$, and the ones satisfying $\beta_{ls}^2 < 0$ are for evanescent modes.

Since there is an incident plane wave as down-going wave and a reflected one as up-going wave in the upper half-space, the longitudinal field can be plane-wave expanded as

$$E_{0y}(x,z)=\sum_{p\in\mathbb{Z}}\sum_{q\in\mathbb{Z}}(E_y^{\mathrm{inc}}e^{-i\beta_{0s}(z-t_0)}\delta_{s0}+R_s^e e^{i\beta_{0s}(z-t_0)})e^{i\alpha_s x}e^{i\xi_q y}, \tag{5.1a}$$

$$K_{0y}(x,z)=\sum_{p\in\mathbb{Z}}\sum_{q\in\mathbb{Z}}(K_y^{\mathrm{inc}}e^{-i\beta_{0s}(z-t_0)}\delta_{s0}+R_s^h e^{i\beta_{0s}(z-t_0)})e^{i\alpha_s x}e^{i\xi_q y}, \tag{5.1b}$$

Here, K_* is used to denote the scaled magnetic field, $K_*=\sqrt{\mu_0/\epsilon_0}H_*$. δ_{s0} is the Kronecker symbol helping to form a matrix in the calculation. $\delta_{s0}=1$ when $p=q=0$, otherwise $\delta_{s0}=0$. R_s^e and R_s^h are the reflection coefficients of the plane wave indexed by $s=(p,q)$.

In the lower half-space, only down-going transmitted waves exists, which is written as

$$E_{3y}(x,z)=\sum_{p\in\mathbb{Z}}\sum_{q\in\mathbb{Z}}T_s^e e^{i(\alpha_s x-\beta_{3s}(z-t_2)+\xi_q y)}, \tag{5.2a}$$

$$K_{3y}(x,z)=\sum_{p\in\mathbb{Z}}\sum_{q\in\mathbb{Z}}T_s^h e^{i(\alpha_s x-\beta_{3s}(z-t_2)+\xi_q y)}, \tag{5.2b}$$

where T_s^e and T_s^h are transmission coefficients of the plane wave indexed by $s=(p,q)$.

Assuming the center of fiber in the primary cell of the l-th layer to be located at $z=e_l$ in the global coordinate system, then the field between $e_l+c_l<z<t_{l-1}$ and $t_l<z<e_l-c_l$ is plane-wave expanded as

$$V_{ly}^{\pm}=\sum_{p\in\mathbb{Z}}\sum_{q\in\mathbb{Z}}\left(f_{ls}^{\pm}e^{-i\beta_{ls}(z-e_l)}+g_{ls}^{\pm}e^{i\beta_{ls}(z-e_l)}\right)e^{i\alpha_s x}e^{i\xi_q y}, \tag{5.3}$$

where V_{ly} denotes either E_{ly} or K_{ly}. The coefficients $f_{ls}^{\pm}$ and $g_{ls}^{\pm}$ are the expansion coefficients, where $f_{ls}^{\pm}$ represents the scattered fields propagating along the $-z$ direction, which are down-going waves, and $f_{ls}^{\pm}$ represents the ones propagating along the $+z$ direction, which are up-going waves. $+$ and $-$ indicate regions $e_l+c_l<z<t_{l-1}$ and $t_l<z<e_l-c_l$.

For conical diffraction of fields with a specified y dependence of $e^{i\xi_q y}$, the relations between the x and y components of the electric and the scaled magnetic fields are given as

$$E_{lxq}(x,z)=\frac{i}{k_{ltq}^2}\left[\xi_q\frac{\partial E_{lyq}}{\partial x}-k\mu_{lr}\frac{\partial K_{lyq}}{\partial z}\right], \tag{5.4a}$$

$$K_{lxq}(x,z)=\frac{i}{k_{ltq}^2}\left[\xi_q\frac{\partial K_{lyq}}{\partial x}+k\epsilon_{lr}\frac{\partial E_{lyq}}{\partial z}\right], \tag{5.4b}$$

where E_{lxq} and K_{lxq} are the fields with a specified ξ_q, and k_{ltq} are the transverse components of the wave vector related to the q-th mode. Allowing k_l be the wavenumber corresponding to the background material of the l-th layer, then $k_{ltq} = \sqrt{k_l^2 - \xi_q^2}$. k is the wavenumber in the vacuum.

5.3 Mode-matching at the boundary between two layers

Without lost of any generality, the field matching at boundary t_l is discussed here. In the global coordinate system, considering the fields with a specific y dependence of $e^{i\xi_q y}$, the x components of the fields in the l-th and $(l+1)$-th layers are obtained by substituting equation (5.3) into (5.4). Matching the fields at boundary t_l produces

$$f^-_{les}e^{-i\beta_{ls}(t_l-e_l)} + g^-_{les}e^{i\beta_{ls}(t_l-e_l)} = f^+_{l'es}e^{-i\beta_{l's}(t_l-e_{l'})} + g^+_{l'es}e^{i\beta_{l's}(t_l-e_{l'})}, \tag{5.5a}$$

$$f^-_{lhs}e^{-i\beta_{ls}(t_l-e_l)} + g^-_{lhs}e^{i\beta_{ls}(t_l-e_l)} = f^+_{l'hs}e^{-i\beta_{l's}(t_l-e_{l'})} + g^+_{l'hs}e^{i\beta_{l's}(t_l-e_{l'})}, \tag{5.5b}$$

$$\begin{aligned}&\chi_{ls}\left(f^-_{les}e^{-i\beta_{ls}(t_l-e_l)} + g^-_{les}e^{i\beta_{ls}(t_l-e_l)}\right) + \eta_{ls}\left(f^-_{lhs}e^{-i\beta_{ls}(t_l-e_l)} - g^-_{lhs}e^{i\beta_{ls}(t_l-e_l)}\right)\\ =&\chi_{l's}\left(f^+_{l'es}e^{-i\beta_{l's}(t_l-e_{l'})} + g^+_{l'es}e^{i\beta_{l's}(t_l-e_{l'})}\right) + \eta_{l's}\left(f^+_{l'hs}e^{-i\beta_{l'p}(t_l-e_{l'})} - g^+_{l'hs}e^{i\beta_{l's}(t_l-e_{l'})}\right),\end{aligned} \tag{5.5c}$$

$$\begin{aligned}&\chi_{ls}\left(f^-_{lhs}e^{-i\beta_{ls}(t_l-e_l)} + g^-_{lhs}e^{i\beta_{ls}(t_l-e_l)}\right) - \rho_{ls}\left(f^-_{les}e^{-i\beta_{ls}(t_l-e_l)} - g^-_{les}e^{i\beta_{ls}(t_l-e_l)}\right)\\ =&\chi_{l's}\left(f^+_{l'hs}e^{-i\beta_{l's}(t_l-e_{l'})} + g^+_{l'hs}e^{i\beta_{l's}(t_l-e_{l'})}\right) - \rho_{l's}\left(f^+_{l'es}e^{-i\beta_{l's}(t_l-e_{l'})} - g^+_{l'es}e^{i\beta_{l's}(t_l-e_{l'})}\right),\end{aligned} \tag{5.5d}$$

where $l' = l+1$, $\chi_{ls} = \frac{\alpha_s \xi_q}{k^2_{ltq}}$, $\eta_{ls} = \frac{k\mu_{lr}\beta_{ls}}{k^2_{ltq}}$, and $\rho_{ls} = \frac{k\epsilon_{lr}\beta_{ls}}{k^2_{ltq}}$. Noticing that coefficients $f^-_{l\{e,h\}s}$ and $g^+_{l'\{e,h\}s}$ represent the field impinging on the boundary t_l, $f^-_{l\{e,h\}s}$ and $g^+_{l'\{e,h\}s}$ represent the one scattered from t_l, arranging the terms in equation (5.5) and moving the incident and scattered fields to the right and left sides of the equations yields a linear system which can be written as

$$\begin{bmatrix}\mathbf{f}^+_{l'q}\\ \mathbf{g}^-_{lq}\end{bmatrix} = \begin{bmatrix}\boldsymbol{\mathcal{M}}^{(1)}_{ll',q} & \boldsymbol{\mathcal{M}}^{(2)}_{ll',q}\\ \boldsymbol{\mathcal{M}}^{(3)}_{ll',q} & \boldsymbol{\mathcal{M}}^{(4)}_{ll',q}\end{bmatrix}\begin{bmatrix}\mathbf{f}^-_{lq}\\ \mathbf{g}^+_{l'q}\end{bmatrix} \tag{5.6}$$

where $\boldsymbol{\mathcal{M}}^{(1)}_{ll',q}$, $\boldsymbol{\mathcal{M}}^{(2)}_{ll',q}$, $\boldsymbol{\mathcal{M}}^{(3)}_{ll',q}$ and $\boldsymbol{\mathcal{M}}^{(4)}_{ll',q}$ are four block matrices of the interface S-matrix $\boldsymbol{\mathcal{M}}_{ll',q}$ which is calculated by $\boldsymbol{\mathcal{M}}_{ll',q} = {\boldsymbol{\mathcal{M}}^{(a)}_{ll',q}}^{-1}\boldsymbol{\mathcal{M}}^{(b)}_{ll',q}$, where the matrices $\boldsymbol{\mathcal{M}}^{(a)}_{ll'}$ and $\boldsymbol{\mathcal{M}}^{(b)}_{ll'}$ are defined as

$$\boldsymbol{\mathcal{M}}^{(a)}_{ll',q} = \begin{bmatrix}P_{l's} & 0 & -U_{ls} & 0\\ 0 & P_{l's} & 0 & -U_{ls}\\ \chi_{l's}P_{l's} & \eta_{l's}P_{l's} & -\chi_{ls}U_{ls} & \eta_{ls}U_{ls}\\ -\rho_{l's}P_{l's} & \chi_{l's}P_{l's} & -\rho_{ls}U_{ls} & -\chi_{ls}U_{ls}\end{bmatrix} \tag{5.7}$$

$$\mathcal{M}^{(b)}_{ll',q} = \begin{bmatrix} P_{ls} & 0 & -U_{l's} & 0 \\ 0 & P_{ls} & 0 & -U_{l's} \\ \chi_{ls}P_{ls} & \eta_{ls}P_{ls} & -\chi_{l's}U_{l's} & \eta_{l's}U_{l's} \\ -\rho_{ls}P_{ls} & \chi_{ls}P_{ls} & -\rho_{l's}U_{l's} & -\chi_{l's}U_{l's} \end{bmatrix} \tag{5.8}$$

where coefficients $P_{ls} = e^{-i\beta_{ls}(t_l - e_l)}$ and $U_{lp} = e^{i\beta_{ls}(t_l - e_l)}$. $P_{l'p}$ and $U_{l'p}$ have the similar definition except keeping t_l instead of $t_{l'}$. At boundary $z = t_0$, $e_0 = t_0$, $\mathbf{f}^-_{0q} = [[E^{\text{inc}}_y \delta_{0s}], [K^{\text{inc}}_y \delta_{0s}]]$ and $\mathbf{g}^-_{0q} = [[R^e_s], [R^h_s]]^{\mathrm{T}}$. At boundary $z = t_n$, $e_n = t_n$, $\mathbf{f}^+_{n'q} = [[T^e_s], [T^h_s]]^{\mathrm{T}}$ and $\mathbf{g}^+_{n'q} = [0, 0]$.

5.4 Relations for $f^{\pm}_{1s}$ and $g^{\pm}_{1s}$

The coefficients of $f^{\pm}_{1s}$ and $g^{\pm}_{1s}$ account for the scattered field inside the first layer. Their relations are established by building Rayleigh's identity in the corresponding layer, in the global coordinate system. Focusing on a specific y dependence of $e^{i\xi_q y}$ again, the q-th mode of the field (5.3) is expressed as

$$V^{\pm}_{1yq} = \sum_{p\in\mathbb{Z}} \left(f^{\pm}_{1s} e^{-i\beta_{1s}z} + g^{\pm}_{1s} e^{i\beta_{1s}z} \right) e^{i\alpha_s x} e^{i\xi_q y} \tag{5.9}$$

where the relations between $\{f, g\}^+_{1s}$ and $\{f, g\}^-_{1s}$ are

$$\begin{aligned} f^-_{1s} &= f^+_{1s} + \sum_{m\in\mathbb{Z}} Q^-_{1sm} B_{1mq}, \\ g^+_{1s} &= g^-_{1s} + \sum_{m\in\mathbb{Z}} Q^+_{1sm} B_{1mq}, \end{aligned} \tag{5.10}$$

with a specific value for q. $Q^{\pm}_{1sm} = \frac{2(-i)^m e^{\pm im\theta_{1s}}}{d\beta_{1s}}$, the angle θ_{1s} is such as $k_{1tq}\theta_{1s} = \alpha_{1s} + i\beta_{1s}$, where $k^2_{1tq} = \sqrt{k^2_1 - \xi^2_q}$. Writing equation (5.10) into a matrix form,

$$\begin{aligned} \mathbf{f}^-_{1q} &= \mathbf{f}^+_{1q} + \boldsymbol{\mathcal{Q}}^-_{lq} \boldsymbol{\mathcal{B}}_{1q}, \\ \mathbf{g}^+_{1q} &= \mathbf{g}^-_{1q} + \boldsymbol{\mathcal{Q}}^+_{1q} \boldsymbol{\mathcal{B}}_{1q}, \end{aligned} \tag{5.11}$$

where $\boldsymbol{\mathcal{B}}_{1q} = [[B^e_{1mq}], [B^h_{1mq}]]^{\mathrm{T}}$, $\mathbf{f}^{\pm}_{1q} = \left[[f^{\pm}_{1es}], [f^{\pm}_{1hs}]\right]^{\mathrm{T}}$, $\mathbf{g}^{\pm}_{1q} = \left[[g^{\pm}_{1es}], [g^{\pm}_{1hs}]\right]^{\mathrm{T}}$, and $\boldsymbol{\mathcal{Q}}^{\pm}_{1q} = \mathrm{diag}\{[Q^{\pm}_{1sm}]_{pm}, [Q^{\pm}_{lsm}]_{pm}\}$. Following the same procedure as in section 4.4, one has

$$\boldsymbol{\mathcal{A}}_{1q} = \boldsymbol{\mathcal{O}}^{(1)}_{1q} \mathbf{f}^+_{1q} + \boldsymbol{\mathcal{O}}^{(2)}_{1q} \mathbf{g}^-_{1q} + \boldsymbol{\mathcal{S}}_{1q} \boldsymbol{\mathcal{B}}_{1q}, \tag{5.12}$$

where $\boldsymbol{\mathcal{A}}_{1q} = [[A^e_{1nq}], [A^h_{1nq}]]^T$, $\boldsymbol{\mathcal{B}}_{1q} = [[B^e_{1nq}], [B^h_{1nq}]]^T$. The other matrices are given as

$$\boldsymbol{\mathcal{O}}^{(1)}_{1q} = \begin{bmatrix} \mathrm{diag}\{\left[i^n e^{in\theta_{ls}}\right]\} & 0 \\ 0 & \mathrm{diag}\{\left[i^n e^{in\theta_{ls}}\right]\} \end{bmatrix}, \tag{5.13a}$$

$$\boldsymbol{\mathcal{O}}^{(2)}_{1q} = \begin{bmatrix} \mathrm{diag}\{\left[i^n e^{-in\theta_{ls}}\right]\} & 0 \\ 0 & \mathrm{diag}\{\left[i^n e^{-in\theta_{ls}}\right]\} \end{bmatrix}, \tag{5.13b}$$

$$\boldsymbol{\mathcal{S}}_{1q} = \begin{bmatrix} \left[\mathcal{S}_{1nm,q}\right]_{nm} & 0 \\ 0 & \left[\mathcal{S}_{1nm,q}\right]_{nm} \end{bmatrix}, \tag{5.13c}$$

with lattice sums defined as $\mathcal{S}_{m,q} = \sum_{n=1}^{+\infty} H^{(1)}_m(k_{1tq} nd)[e^{i\alpha_0 nd_1} + (-1)^m e^{-i\alpha_0 nd_1}]$.

The relation between $\boldsymbol{\mathcal{A}}_{1q}$ and $\boldsymbol{\mathcal{B}}_{1q}$ is written as $\boldsymbol{\mathcal{B}}_{1q} = \boldsymbol{\mathcal{L}}_{1q}\boldsymbol{\mathcal{A}}_{1q}$, where $\boldsymbol{\mathcal{L}}_{1q}$ is easily obtained by following the same derivation as in section 3.1.1. So eliminating $\boldsymbol{\mathcal{A}}_{1q}$ from equation (5.12) yields

$$\boldsymbol{\mathcal{B}}_{1q} = \boldsymbol{\mathcal{W}}\boldsymbol{\mathcal{L}}_{1q}\boldsymbol{\mathcal{O}}^{(1)}_{1q}\mathbf{f}^+_{1q} + \boldsymbol{\mathcal{W}}\boldsymbol{\mathcal{L}}_{1q}\boldsymbol{\mathcal{O}}^{(2)}_{1q}\mathbf{g}^-_{1q}, \tag{5.14}$$

where $\boldsymbol{\mathcal{W}} = (\boldsymbol{\mathcal{I}} - \boldsymbol{\mathcal{L}}_{1q}\boldsymbol{\mathcal{S}}_{1q})^{-1}$, and $\boldsymbol{\mathcal{I}}$ is the identity matrix. Substituting (5.14) into (5.11) and eliminating $\boldsymbol{\mathcal{B}}_{1q}$ yields

$$\begin{aligned} \mathbf{f}^-_{1q} =& \mathbf{f}^+_{1q} + \boldsymbol{\mathcal{Q}}^-_{1q}\boldsymbol{\mathcal{W}}\boldsymbol{\mathcal{L}}_{1q}\boldsymbol{\mathcal{O}}^{(1)}_{1q}\mathbf{f}^+_{1q} + \boldsymbol{\mathcal{Q}}^-_{1q}\boldsymbol{\mathcal{W}}\boldsymbol{\mathcal{L}}_{1q}\boldsymbol{\mathcal{O}}^{(2)}_{1q}\mathbf{g}^-_{1q}, \\ \mathbf{g}^+_{1q} =& \mathbf{g}^-_{1q} + \boldsymbol{\mathcal{Q}}^+_{1q}\boldsymbol{\mathcal{W}}\boldsymbol{\mathcal{L}}_{1q}\boldsymbol{\mathcal{O}}^{(1)}_{1q}\mathbf{f}^+_{1q} + \boldsymbol{\mathcal{Q}}^+_{1q}\boldsymbol{\mathcal{W}}\boldsymbol{\mathcal{L}}_{1q}\boldsymbol{\mathcal{O}}^{(2)}_{1q}\mathbf{g}^-_{1q}, \end{aligned} \tag{5.15}$$

5.5 S-matrix for the top and bottom layers

The relations between incident and scattered fields at boundary t_l and the fiber array in the l'-th layer are shown in Fig. 5.4, where $\boldsymbol{\mathcal{M}}_{ll'}$ is the interface S-matrix, and $\boldsymbol{\mathcal{G}}_{l'}$ is the layer S-matrix for the l'-th layer.

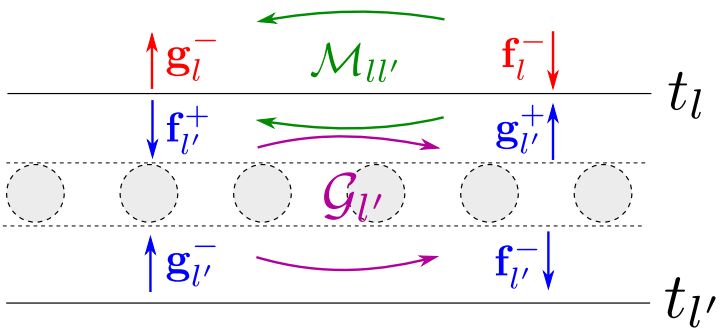

Fig. 5.4 Illustration of interface and layer S-matrix

Once the matrices $\boldsymbol{\mathcal{M}}_{ll'}$ and $\boldsymbol{\mathcal{G}}_{l'}$ are known, the relation for $\{\mathbf{f},\mathbf{g}\}_l^-$ and $\{\mathbf{f},\mathbf{g}\}_{l'}^-$ can be obtained easily, in which the S-matrix of the l'-th layers is produced and named as $\boldsymbol{\mathcal{D}}_{ll'}$. Cascading $\boldsymbol{\mathcal{D}}_{ll'}$ from the top layer of the stack to the bottom one and then combining with the interface S-matrix of the boundary at the bottom produce the S-matrix which links the reflected and transmitted fields to the incident field on the stack.

A multilayered composite laminate is usually fabricated by piling up the stacks one over the other. The S-matrix for the n-th stack will be the same as the one of the first stack, hence cascading the S-matrix of all stacks produces the S-matrix for the whole laminate, then the reflection and transmission coefficients can be easily computed. Here, the method for calculating the S-matrix of one 2-layer stack is illustrated in detail.

5.5.1 S-matrix for the upper layer

In the global coordinate system, the interface S-matrix at boundary t_0 for a specified y dependence of $e^{i\xi_q y}$, which is produced by matching the field at the boundary, is written as

$$\begin{bmatrix}\mathbf{f}_{1q}^+\\ \mathbf{g}_{0q}^-\end{bmatrix}=\begin{bmatrix}\boldsymbol{\mathcal{M}}_{01,q}^{(1)} & \boldsymbol{\mathcal{M}}_{01,q}^{(2)}\\ \boldsymbol{\mathcal{M}}_{01,q}^{(3)} & \boldsymbol{\mathcal{M}}_{01,q}^{(4)}\end{bmatrix}\begin{bmatrix}\mathbf{f}_{0q}^-\\ \mathbf{g}_{1q}^+\end{bmatrix}. \tag{5.16}$$

According to (5.15), the relation for $\mathbf{f}_{1b}^{\pm}$ and $\mathbf{g}_{1b}^{\pm}$ can be written as

$$\begin{bmatrix}\mathbf{f}_{1q}^-\\ \mathbf{g}_{1q}^+\end{bmatrix}=\begin{bmatrix}\boldsymbol{\mathcal{G}}_{1q}^{(1)} & \boldsymbol{\mathcal{G}}_{1q}^{(2)}\\ \boldsymbol{\mathcal{G}}_{1q}^{(3)} & \boldsymbol{\mathcal{G}}_{1q}^{(4)}\end{bmatrix}\begin{bmatrix}\mathbf{f}_{1q}^+\\ \mathbf{g}_{1q}^-\end{bmatrix}, \tag{5.17}$$

with matrices $\boldsymbol{\mathcal{G}}_{1q}^{(1)}$, $\boldsymbol{\mathcal{G}}_{1q}^{(2)}$, $\boldsymbol{\mathcal{G}}_{1q}^{(3)}$ and $\boldsymbol{\mathcal{G}}_{1q}^{(4)}$ defined as

$$\boldsymbol{\mathcal{G}}_{1q}^{(1)}=\boldsymbol{\mathcal{I}}+\boldsymbol{\mathcal{Q}}_{1q}^-\boldsymbol{\mathcal{W}}_{1q}\boldsymbol{\mathcal{L}}_{1q}\boldsymbol{\mathcal{O}}_{1q}^{(1)}, \tag{5.18a}$$

$$\boldsymbol{\mathcal{G}}_{1q}^{(2)}=\boldsymbol{\mathcal{Q}}_{1q}^-\boldsymbol{\mathcal{W}}_{1q}\boldsymbol{\mathcal{L}}_{1q}\boldsymbol{\mathcal{O}}_{1q}^{(2)}, \tag{5.18b}$$

$$\boldsymbol{\mathcal{G}}_{1q}^{(3)}=\boldsymbol{\mathcal{Q}}_{1q}^+\boldsymbol{\mathcal{W}}_{1q}\boldsymbol{\mathcal{L}}_{1q}\boldsymbol{\mathcal{O}}_{1q}^{(1)}, \tag{5.18c}$$

$$\boldsymbol{\mathcal{G}}_{1q}^{(4)}=\boldsymbol{\mathcal{I}}+\boldsymbol{\mathcal{Q}}_{1q}^+\boldsymbol{\mathcal{W}}_{1q}\boldsymbol{\mathcal{L}}_{1q}\boldsymbol{\mathcal{O}}_{1q}^{(2)}. \tag{5.18d}$$

Combining equations (5.16) and (5.17) to eliminate $\mathbf{f}_{1q}^+$ and $\mathbf{g}_{1q}^+$ produces

$$\begin{bmatrix}\mathbf{f}_{1q}^-\\ \mathbf{g}_{0q}^-\end{bmatrix}=\begin{bmatrix}\boldsymbol{\mathcal{D}}_{01,q}^{(1)} & \boldsymbol{\mathcal{D}}_{01,q}^{(2)}\\ \boldsymbol{\mathcal{D}}_{01,q}^{(3)} & \boldsymbol{\mathcal{D}}_{01,q}^{(4)}\end{bmatrix}\begin{bmatrix}\mathbf{f}_{0q}^-\\ \mathbf{g}_{1q}^-\end{bmatrix}. \tag{5.19}$$

Here, $\boldsymbol{\mathcal{D}}^{(1)}_{01,q}$, $\boldsymbol{\mathcal{D}}^{(2)}_{01,q}$, $\boldsymbol{\mathcal{D}}^{(3)}_{01,q}$ and $\boldsymbol{\mathcal{D}}^{(4)}_{01,q}$ are defined as

$$\boldsymbol{\mathcal{D}}^{(1)}_{01,q} = \boldsymbol{\mathcal{G}}^{(1)}_{1q}\left(\boldsymbol{\mathcal{I}} - \boldsymbol{\mathcal{M}}^{(2)}_{01,q}\boldsymbol{\mathcal{G}}^{(3)}_{1q}\right)^{-1}\boldsymbol{\mathcal{M}}^{(1)}_{01,q}, \tag{5.20a}$$

$$\boldsymbol{\mathcal{D}}^{(2)}_{01,q} = \boldsymbol{\mathcal{G}}^{(2)}_{1q} + \boldsymbol{\mathcal{G}}^{(1)}_{1q}\left(\boldsymbol{\mathcal{I}} - \boldsymbol{\mathcal{M}}^{(2)}_{01,q}\boldsymbol{\mathcal{G}}^{(3)}_{1q}\right)^{-1}\boldsymbol{\mathcal{M}}^{(2)}_{01,q}\boldsymbol{\mathcal{G}}^{(4)}_{1q}, \tag{5.20b}$$

$$\boldsymbol{\mathcal{D}}^{(3)}_{01,q} = \boldsymbol{\mathcal{M}}^{(3)}_{01,q} + \boldsymbol{\mathcal{M}}^{(4)}_{01,q}\left(\boldsymbol{\mathcal{I}} - \boldsymbol{\mathcal{G}}^{(3)}_{1q}\boldsymbol{\mathcal{M}}^{(2)}_{01,q}\right)^{-1}\boldsymbol{\mathcal{G}}^{(3)}_{1q}\boldsymbol{\mathcal{M}}^{(1)}_{01,q}, \tag{5.20c}$$

$$\boldsymbol{\mathcal{D}}^{(4)}_{01,q} = \boldsymbol{\mathcal{M}}^{(4)}_{01,q}\left(\boldsymbol{\mathcal{I}} - \boldsymbol{\mathcal{G}}^{(3)}_{1q}\boldsymbol{\mathcal{M}}^{(2)}_{01,q}\right)^{-1}\boldsymbol{\mathcal{G}}^{(4)}_{1q}. \tag{5.20d}$$

Assuming that $P_{\min} < p < P_{\max}$, then $\mathbf{f}^{\pm}_{lq}$ and $\mathbf{g}^{\pm}_{lq}$ are vectors with $P_{\max} - P_{\min} + 1$ elements. Truncating $q \in \mathbb{Z}$ as $Q_{\min} < q < Q_{\max}$ and putting the unknown coefficients into a vector as

$$\mathbf{f}^{\pm}_{l} = \left[\mathbf{f}^{\pm}_{l,Q_{\min}}, \cdots, \mathbf{f}^{\pm}_{l,0}, \cdots, \mathbf{f}^{\pm}_{l,Q_{\max}}\right]^{\mathrm{T}}, \tag{5.21a}$$

$$\mathbf{g}^{\pm}_{l} = \left[\mathbf{g}^{\pm}_{l,Q_{\min}}, \cdots, \mathbf{g}^{\pm}_{l,0}, \cdots, \mathbf{g}^{\pm}_{l,Q_{\max}}\right]^{\mathrm{T}}, \tag{5.21b}$$

then $\mathbf{f}^{\pm}_{l}$ and $\mathbf{g}^{\pm}_{l}$ are vectors with $(P_{\max}-P_{\min}+1)\times(Q_{\max}-Q_{\min}+1)$ elements. With equation (5.19), the relation between $\mathbf{f}^{\pm}_{l}$ and $\mathbf{g}^{\pm}_{l}$ can be finally written as

$$\begin{bmatrix}\mathbf{f}^{-}_{1}\\ \mathbf{g}^{-}_{0}\end{bmatrix} = \begin{bmatrix}\boldsymbol{\mathcal{D}}^{(1)}_{01} & \boldsymbol{\mathcal{D}}^{(2)}_{01}\\ \boldsymbol{\mathcal{D}}^{(3)}_{01} & \boldsymbol{\mathcal{D}}^{(4)}_{01}\end{bmatrix}\begin{bmatrix}\mathbf{f}^{-}_{0}\\ \mathbf{g}^{-}_{1}\end{bmatrix}, \tag{5.22}$$

where matrices $\boldsymbol{\mathcal{D}}^{(1)}_{01}$, $\boldsymbol{\mathcal{D}}^{(2)}_{01}$, $\boldsymbol{\mathcal{D}}^{(3)}_{01}$ and $\boldsymbol{\mathcal{D}}^{(4)}_{01}$ are defined as

$$\boldsymbol{\mathcal{D}}^{(*)}_{01} = \begin{bmatrix}\boldsymbol{\mathcal{D}}^{(*)}_{01,Q_{\min}} & & & & \\ & \ddots & & & \\ & & \boldsymbol{\mathcal{D}}^{(*)}_{01,0} & & \\ & & & \ddots & \\ & & & & \boldsymbol{\mathcal{D}}^{(*)}_{01,Q_{\max}}\end{bmatrix} \tag{5.23}$$

with $* = 1, 2, 3, 4$.

5.5.2 S-matrix for the lower layer

In the coordinate system $x'y'z'$, the projection of the incident wave onto the x'-y' plane is read as $\vec{k}^{\mathrm{inc}}_{u} = (\alpha'_0, \xi'_0)$ with $\alpha'_0 = k^{\mathrm{inc}}\sin\vartheta\cos\gamma$, $\xi'_0 = k^{\mathrm{inc}}\sin\vartheta\sin\gamma$, where γ is the angle between $\vec{k}^{\mathrm{inc}}_{u}$ and the x' direction, which is calculated with $\gamma = \pi - \varphi - \phi$, as shown in Fig. 5.1. Allow $\alpha'_s = \alpha'_0 + \alpha_q + \alpha_p\cos\phi$ and $\xi'_p = \xi'_0 - \alpha_p\sin\phi$ for the components of

wavenumbers of the s-th mode along x' and y' directions. In a general way, the field representation in the l-th layer is

$$\widetilde{V}_{ly'} = \sum_{p\in\mathbb{Z}}\sum_{q\in\mathbb{Z}} \left(\tilde{f}_{ls}^{\pm} e^{-i\beta'_{ls}(z'-e_l)} + \tilde{g}_{ls}^{\pm} e^{i\beta'_{ls}(z'-e_l)}\right) e^{i\alpha'_s x'} e^{i\xi'_p y'} \tag{5.24}$$

where $\widetilde{V}_{ly'}$ denotes either $\widetilde{E}_{ly'}$ or $\widetilde{K}_{ly'}$, which are the fields in $x'y'z'$ coordinate system. The coefficients $\tilde{f}_{ls}^{\pm}$ and $\tilde{g}_{ls}^{\pm}$ are the expansion coefficients and have the same physical meanings as $f_{ls}^{\pm}$ and $g_{ls}^{\pm}$. $\beta'_{ls} = \sqrt{k_l^2 - \alpha_s'^2}$. The transverse components of the fields are calculated with equation (5.4) by defining $\tilde{k}_{ltp}^2 = k_l^2 - \xi_p'^2$.

The field representation (5.24) is transformed into the global coordinate system with

$$V_{ly}^{\pm} = \sin\phi\, \tilde{V}_{lx'}^{\pm} + \cos\phi\, \tilde{V}_{ly'}^{\pm}. \tag{5.25}$$

Here, $\tilde{V}_{lx'}^{\pm}$ is obtained by substituting (5.24) into (5.4). Comparing the field expression of $V_{ly}^{\pm}$ obtained from equation (5.25) with (5.9) yields

$$\bar{f}_{les}^{\pm} = (\cos\phi - \chi'_{ls}\sin\phi)\tilde{f}_{les}^{\pm} - \eta'_{ls}\sin\phi\,\tilde{f}_{lhs}^{\pm}, \tag{5.26a}$$
$$\bar{f}_{lhs}^{\pm} = \rho'_{ls}\sin\phi\,\tilde{f}_{les'}^{\pm} + (\cos\phi - \chi'_{ls}\sin\phi)\tilde{f}_{lhs'}^{\pm}, \tag{5.26b}$$
$$\bar{g}_{les}^{\pm} = (\cos\phi - \chi'_{ls}\sin\phi)\tilde{g}_{les'}^{\pm} + \eta'_{ls}\sin\phi\,\tilde{g}_{lhs'}^{\pm}, \tag{5.26c}$$
$$\bar{g}_{lhs}^{\pm} = (\cos\phi - \chi'_{ls}\sin\phi)\tilde{g}_{lhs'}^{\pm} - \rho'_{ls}\sin\phi\,\tilde{g}_{les'}^{\pm}, \tag{5.26d}$$

with which the transformation matrices are defined as

$$\boldsymbol{\mathcal{V}}_{1p}^{f} = \begin{bmatrix} \cos\phi - \chi_{2s'}\sin\phi & -\eta_{2s'}\sin\phi \\ \rho_{2s'}\sin\phi & \cos\phi - \chi_{2s'}\sin\phi \end{bmatrix}, \tag{5.27a}$$
$$\boldsymbol{\mathcal{V}}_{1p}^{g} = \begin{bmatrix} \cos\phi - \chi_{2s'}\sin\phi & \eta_{2s'}\sin\phi \\ -\rho_{2s'}\sin\phi & \cos\phi - \chi_{2s'}\sin\phi \end{bmatrix}. \tag{5.27b}$$

Allowing $\tilde{\mathbf{f}}_{lp}^{\pm} = \left[\tilde{f}_{les}^{\pm}, \tilde{f}_{lhs}^{\pm}\right]$ and $\tilde{\mathbf{g}}_{lp}^{\pm} = \left[\tilde{g}_{les}^{\pm}, \tilde{g}_{lhs}^{\pm}\right]$, then the transforming relation reads

$$\bar{\mathbf{f}}_{lp}^{\pm} = \boldsymbol{\mathcal{V}}_{lp}^{f}\tilde{\mathbf{f}}_{lp}^{\pm}, \tag{5.28a}$$
$$\bar{\mathbf{g}}_{lp}^{\pm} = \boldsymbol{\mathcal{V}}_{lp}^{g}\tilde{\mathbf{g}}_{lp}^{\pm}, \tag{5.28b}$$

where $\bar{\mathbf{f}}_{lp}^{\pm}$ and $\bar{\mathbf{g}}_{lp}^{\pm}$ are counterparts of $\tilde{\mathbf{f}}_{lp}^{\pm}$ and $\tilde{\mathbf{g}}_{lp}^{\pm}$ in the global coordinate system. Field-matching at t_l with expansion (5.24) produces the same relation given in section 5.3, but P_{ls} and U_{lp} in equation (5.7) and (5.8) are replaced by $\widetilde{P}_{ls} = e^{-i\beta'_{ls}(t_l - e_l)}$ and $\widetilde{U}_{lp} = e^{i\beta'_{ls}(t_l - e_l)}$.

Others are defined as $\chi'_{ls} = \frac{\alpha'_s \xi'_p}{\tilde{k}^2_{ltp}}$, $\eta'_{ls} = \frac{k\mu_{lr}\beta'_{ls}}{\tilde{k}^2_{ltp}}$, and $\rho'_{ls} = \frac{k\epsilon_{lr}\beta'_{ls}}{\tilde{k}^2_{ltp}}$. At boundary t_1 one has

$$\begin{bmatrix} \tilde{\mathbf{f}}^{+}_{2p} \\ \tilde{\mathbf{g}}^{-}_{1p} \end{bmatrix} = \begin{bmatrix} \widetilde{\mathcal{M}}^{(1)}_{12,p} & \widetilde{\mathcal{M}}^{(2)}_{12,p} \\ \widetilde{\mathcal{M}}^{(3)}_{12',p} & \widetilde{\mathcal{M}}^{(4)}_{12,p} \end{bmatrix} \begin{bmatrix} \tilde{\mathbf{f}}^{-}_{1p} \\ \tilde{\mathbf{g}}^{+}_{2p} \end{bmatrix}. \tag{5.29}$$

Applying the procedure given in section 5.4 to the bottom layer yields

$$\begin{bmatrix} \tilde{\mathbf{f}}^{-}_{2p} \\ \tilde{\mathbf{g}}^{+}_{2p} \end{bmatrix} = \begin{bmatrix} \widetilde{\mathcal{G}}^{(1)}_{2p} & \widetilde{\mathcal{G}}^{(2)}_{2p} \\ \widetilde{\mathcal{G}}^{(3)}_{2p} & \widetilde{\mathcal{G}}^{(4)}_{2p} \end{bmatrix} \begin{bmatrix} \tilde{\mathbf{f}}^{+}_{2p} \\ \tilde{\mathbf{g}}^{-}_{2p} \end{bmatrix}. \tag{5.30}$$

Combining (5.29) and (5.30) with the recursive relation given in equation (5.20) yields

$$\begin{bmatrix} \tilde{\mathbf{f}}^{-}_{2p} \\ \tilde{\mathbf{g}}^{-}_{1p} \end{bmatrix} = \begin{bmatrix} \widetilde{\mathcal{D}}^{(1)}_{12,p} & \widetilde{\mathcal{D}}^{(2)}_{12,p} \\ \widetilde{\mathcal{D}}^{(3)}_{12,p} & \widetilde{\mathcal{D}}^{(4)}_{12,p} \end{bmatrix} \begin{bmatrix} \tilde{\mathbf{f}}^{-}_{1p} \\ \tilde{\mathbf{g}}^{-}_{2p} \end{bmatrix}. \tag{5.31}$$

Applying (5.27) to (5.31) produces

$$\begin{bmatrix} \bar{\mathbf{f}}^{-}_{2p} \\ \bar{\mathbf{g}}^{-}_{1p} \end{bmatrix} = \begin{bmatrix} \bar{\mathcal{D}}^{(1)}_{12,p} & \bar{\mathcal{D}}^{(2)}_{12,p} \\ \bar{\mathcal{D}}^{(3)}_{12,p} & \bar{\mathcal{D}}^{(4)}_{12,p} \end{bmatrix} \begin{bmatrix} \bar{\mathbf{f}}^{-}_{1p} \\ \bar{\mathbf{g}}^{-}_{2p} \end{bmatrix}. \tag{5.32}$$

The matrices $\bar{\mathcal{D}}^{(1)}_{12,p}$, $\bar{\mathcal{D}}^{(2)}_{12,p}$, $\bar{\mathcal{D}}^{(3)}_{12,p}$ and $\bar{\mathcal{D}}^{(4)}_{12,p}$ are given as

$$\bar{\mathcal{D}}^{(1)}_{12,p} = \mathcal{V}^{f}_{2p} \widetilde{\mathcal{D}}^{(1)}_{12,p} {\mathcal{V}^{f}_{1p}}^{-1}, \quad \bar{\mathcal{D}}^{(1)}_{12,p} = \mathcal{V}^{f}_{2p} \widetilde{\mathcal{D}}^{(1)}_{12,p} {\mathcal{V}^{g}_{2p}}^{-1}, \tag{5.33a}$$

$$\bar{\mathcal{D}}^{(1)}_{12,p} = \mathcal{V}^{g}_{1p} \widetilde{\mathcal{D}}^{(1)}_{12,p} {\mathcal{V}^{f}_{1p}}^{-1}, \quad \bar{\mathcal{D}}^{(1)}_{12,p} = \mathcal{V}^{g}_{1p} \widetilde{\mathcal{D}}^{(1)}_{12,p} {\mathcal{V}^{g}_{2p}}^{-1}. \tag{5.33b}$$

Allowing

$$\bar{\mathbf{f}}^{\pm}_{l} = \left[\bar{\mathbf{f}}^{\pm}_{l,P_{\min}}, \cdots, \bar{\mathbf{f}}^{\pm}_{l,0}, \cdots, \bar{\mathbf{f}}^{\pm}_{l,P_{\max}} \right]^{\mathrm{T}}, \tag{5.34a}$$

$$\bar{\mathbf{g}}^{\pm}_{l} = \left[\bar{\mathbf{g}}^{\pm}_{l,P_{\min}}, \cdots, \bar{\mathbf{g}}^{\pm}_{l,0}, \cdots, \bar{\mathbf{g}}^{\pm}_{l,P_{\max}} \right]^{\mathrm{T}}, \tag{5.34b}$$

then the field relation for $\bar{\mathbf{f}}^{\pm}_{l}$ and $\bar{\mathbf{g}}^{\pm}_{l}$ is given as

$$\begin{bmatrix} \bar{\mathbf{f}}^{-}_{2} \\ \bar{\mathbf{g}}^{-}_{1} \end{bmatrix} = \begin{bmatrix} \bar{\mathcal{D}}^{(1)}_{12} & \bar{\mathcal{D}}^{(2)}_{12} \\ \bar{\mathcal{D}}^{(3)}_{12} & \bar{\mathcal{D}}^{(4)}_{12} \end{bmatrix} \begin{bmatrix} \bar{\mathbf{f}}^{-}_{1} \\ \bar{\mathbf{g}}^{-}_{2} \end{bmatrix}, \tag{5.35}$$

with matrices $\bar{\boldsymbol{\mathcal{D}}}_{12}^{(1)}$, $\bar{\boldsymbol{\mathcal{D}}}_{12}^{(2)}$, $\bar{\boldsymbol{\mathcal{D}}}_{12}^{(3)}$ and $\bar{\boldsymbol{\mathcal{D}}}_{12}^{(4)}$ defined as

$$\bar{\boldsymbol{\mathcal{D}}}_{12}^{(*)} = \begin{bmatrix} \bar{\boldsymbol{\mathcal{D}}}_{12,P_{\min}}^{(*)} & & & & \\ & \ddots & & & \\ & & \bar{\boldsymbol{\mathcal{D}}}_{12,0}^{(*)} & & \\ & & & \ddots & \\ & & & & \bar{\boldsymbol{\mathcal{D}}}_{12,P_{\max}}^{(*)} \end{bmatrix}. \tag{5.36}$$

Notice that the order of elements in vectors $\bar{\mathbf{f}}_l^{\pm}$ and $\bar{\mathbf{g}}_l^{\pm}$ is different from the one of $\mathbf{f}_l^{\pm}$ and $\mathbf{g}_l^{\pm}$. For the calculation, the elements in $\bar{\mathbf{f}}_l^{\pm}$ and $\bar{\mathbf{g}}_l^{\pm}$ need to be reordered to have the same order as the one of $\mathbf{f}_l^{\pm}$ and $\mathbf{g}_l^{\pm}$. The matrix for reordering these elements is defined as $\boldsymbol{\mathcal{U}}$, which is obtained as detailed in Appendix D. With matrix $\boldsymbol{\mathcal{U}}$, the equation (5.35) is re-written as

$$\begin{bmatrix} \mathbf{f}_2^- \\ \mathbf{g}_1^- \end{bmatrix} = \begin{bmatrix} \boldsymbol{\mathcal{D}}_{12}^{(1)} & \boldsymbol{\mathcal{D}}_{12}^{(2)} \\ \boldsymbol{\mathcal{D}}_{12}^{(3)} & \boldsymbol{\mathcal{D}}_{12}^{(4)} \end{bmatrix} \begin{bmatrix} \mathbf{f}_1^- \\ \mathbf{g}_2^- \end{bmatrix}, \tag{5.37}$$

with $\boldsymbol{\mathcal{D}}_{12}^{(*)} = \boldsymbol{\mathcal{U}} \bar{\boldsymbol{\mathcal{D}}}_{12}^{(*)} \boldsymbol{\mathcal{U}}^{-1}$.

In brief, the interface S-matrix at t_0 and the layer S-matrix of the first layer are combined to produce the equation (5.22) which involves the S-matrix of the first layer. The interface S-matrix at t_1 and the layer S-matrix of the second layer are combined to produce (5.37) which involves the S-matrix of the second layer. Combining them yields

$$\begin{bmatrix} \mathbf{f}_2^- \\ \mathbf{g}_0^- \end{bmatrix} = \begin{bmatrix} \boldsymbol{\mathcal{D}}_{02}^{(1)} & \boldsymbol{\mathcal{D}}_{02}^{(2)} \\ \boldsymbol{\mathcal{D}}_{02}^{(3)} & \boldsymbol{\mathcal{D}}_{02}^{(4)} \end{bmatrix} \begin{bmatrix} \mathbf{f}_0^- \\ \mathbf{g}_2^- \end{bmatrix}. \tag{5.38}$$

Assuming that the interface S-matrix at t_2 is given as

$$\begin{bmatrix} \mathbf{f}_3^+ \\ \mathbf{g}_2^- \end{bmatrix} = \begin{bmatrix} \boldsymbol{\mathcal{M}}_{23}^{(1)} & \boldsymbol{\mathcal{M}}_{23}^{(2)} \\ \boldsymbol{\mathcal{M}}_{23}^{(3)} & \boldsymbol{\mathcal{M}}_{23}^{(4)} \end{bmatrix} \begin{bmatrix} \mathbf{f}_2^- \\ \mathbf{g}_3^+ \end{bmatrix}, \tag{5.39}$$

then $\mathbf{f}_2^-$ and $\mathbf{g}_2^-$ can be eliminated from equation (5.38) and (5.39) to produce the S-matrix of the whole 2-layer stack

$$\begin{bmatrix} \mathbf{f}_3^+ \\ \mathbf{g}_0^- \end{bmatrix} = \begin{bmatrix} \boldsymbol{\mathcal{D}}_{03}^{(1)} & \boldsymbol{\mathcal{D}}_{03}^{(2)} \\ \boldsymbol{\mathcal{D}}_{03}^{(3)} & \boldsymbol{\mathcal{D}}_{03}^{(4)} \end{bmatrix} \begin{bmatrix} \mathbf{f}_0^- \\ \mathbf{g}_3^+ \end{bmatrix}. \tag{5.40}$$

This is a linear system which relates the reflected field $\mathbf{g}_0^-$ and the transmitted field $\mathbf{f}_3^+$ to the incident fields $\mathbf{f}_0^-$ and $\mathbf{g}_3^+$. Since no wave is incident from the bottom of the stack, $\mathbf{g}_3^+ = [0,0]^T$. The reflection and transmission coefficient are easily obtained by solving this linear system. For a composite laminate constructed with the 2-layer stack, the S-matrix

of each stack can be obtained in a similar way. Cascading all S-matrices from the top stack to the bottom one produces the S-matrix for the whole structure, then the reflection and transmission coefficients easily follow.

5.6 Extension of the approach to 4-layer stack

The laminates constructed with the 2-layer stack can only provide the strength and stiffness along two directions which cannot satisfy practical requirements, so the 4-layer stack as shown in Fig. 5.5 is always used in practice to produce the laminated composites.

Here, the approach for the 2-layer stack is extended for investigating this practically used multilayered composite. Yet the discussion will focus on a more general case in which the fibers in different layers are orientated into an arbitrary direction instead of the directions given in Fig. 5.5.

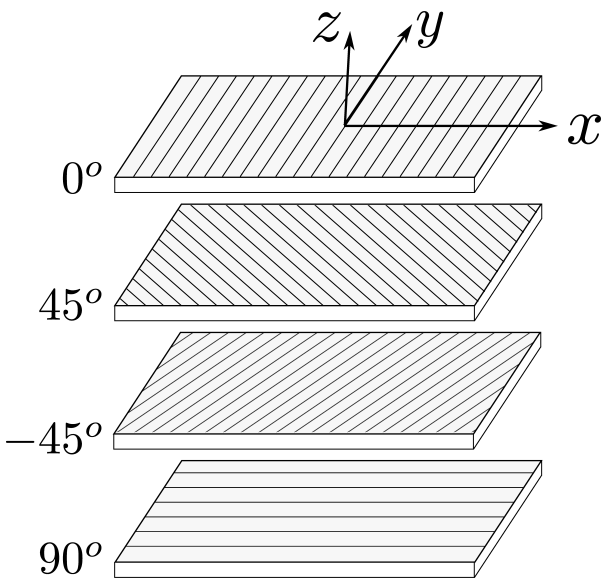

Fig. 5.5 A practical way of fabricating the stack for multilayered composites

The extension of the approach described above for the 2-layer stack is straightforwardly made to investigate scattering by a structure composed of a 4-layer stack. Here, the directions of the periodicity of the fibers in each layer are denoted with vectors $\vec{v}_l$, where $l = 1, 2, 3, 4$ is the layer-number. A global coordinate system xyz located at the center of the primary cell of the first layer is chosen, with its x axis directed to $\vec{v}_1$ and y-axis along the axes of the fibers. Then the orientations of the fibers in other layers are defined by the angle between the x axis and $\vec{v}_l$, as shown in Fig. 5.6. Accordingly, another three local co-

ordinate systems $x'y'z'$, $x''y''z''$ and $x'''y'''z'''$ are defined with their origin located at the one of the xyz system but the axis x', x'' and x''' directing into $\vec{v}_2$, $\vec{v}_3$ and $\vec{v}_4$ respectively.

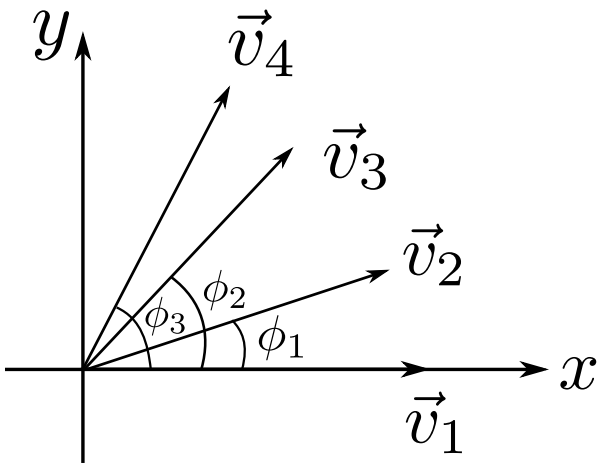

Fig. 5.6 Fibers embedded in the 4-layer stack with fibers in different layers orientated to different directions.

The dispersion introduced by different layers is signified with $e^{i\alpha_p x}$, $e^{i\alpha_q x'}$, $e^{i\alpha_u x''}$ and $e^{i\alpha_v x'''}$, where $\alpha_p = 2\pi p/d_1$, $\alpha_q = 2\pi q/d_2$, $\alpha_u = 2\pi u/d_3$ and $\alpha_v = 2\pi v/d_4$. Defining an index s as a set of p, q, u and v, $s = (p,q,u,v)$, then the x and y components of the s-th mode are given in the global coordinate system,

$$\alpha_s = \alpha_0 + \alpha_p + \alpha_q \cos\phi_1 + \alpha_u \cos\phi_2 + \alpha_v \cos\phi_3, \tag{5.41a}$$

$$\xi_s = \xi_0 + \alpha_q \sin\phi_1 + \alpha_u \sin\phi_2 + \alpha_v \sin\phi_3. \tag{5.41b}$$

Accordingly, the components projected on the direction of the periodicity and the one along the axis of the fibers in other layers easily follow. Hence the field representations in different layers are easily obtained by following the procedure shown in 5.2, and the scattering problem corresponding to the 4-layer stack can easily be solved by following the approach described above for the 2-layer stack.

Notice that the S-matrices for every layer are first built in their local coordinate system and then transformed into the global coordinate system. The transformation matrix can be obtained in the same way as discussed in section 5.5.2. Accordingly, the expansion coefficients of the fields also need to be rearranged before cascading the corresponding S-matrices. In the calculation, one assumes that $P_{\min} < p < P_{\max}$, $Q_{\min} < q < Q_{\max}$, $U_{\min} < u < U_{\max}$, and $V_{\min} < v < V_{\max}$, where $V_{\min}$ and $V_{\max}$ can be easily distinguished from the field variable V_{l_y} with their indices. In the local coordinate system of each layer, the expansion coefficients of the layers from top to bottom are indexed with the sequences

$s_1 = (p,q,u,v)$, $s_2 = (q,p,u,v)$, $s_3 = (u,q,p,v)$ and $s_4 = (v,q,u,p)$, respectively. The sequences s_2, s_3 and s_4 need to be all reordered to have the same order of the sequence s_1 before cascading the S-matrices. In s_*, $* = 1,2,3,4$, the index in the left always varies faster than the right one. The matrices for reordering the sequences used to index the expansion coefficients of the second, third and fourth layers are all different from each other. The algorithms of producing the reordering matrices are given in Appendix D.

5.7 Power reflection and transmission coefficients

Power reflection and transmission coefficients are defined with the time-averaged Poynting vector, and the same procedure as in section 3.4 is applied. Here, the power reflection and transmission coefficients are given directly as

$$R_s = \Re\left\{\frac{R_s^e \xi_s^{r*} - R_s^{h*}\zeta_s^r}{K_y^{\text{inc}*}\xi_s^{\text{inc}} - E_y^{\text{inc}}\zeta_s^{\text{inc}*}}\right\}, \quad T_s = \Re\left\{\frac{T_s^{h*}\xi_s^t - T_s^e\zeta_s^{t*}}{K_y^{\text{inc}*}\xi_s^{\text{inc}} - E_y^{\text{inc}}\zeta_s^{\text{inc}*}}\right\}, \tag{5.42a}$$

with the necessary coefficients

$$\xi_s^{\text{inc}} = \frac{k_y\alpha_0 E_{inc} + k\mu_{0r}\beta_0 K_{inc}}{k_{0t}^2}, \quad \zeta_s^{\text{inc}} = \frac{k_y\alpha_0 K_{inc} - k\epsilon_{0r}\beta_0 E_{inc}}{k_{0t}^2}, \tag{5.43}$$

$$\xi_s^r = \frac{\xi_q\alpha_s R_s^h + k\epsilon_{0r}\beta_{0s}R_s^e}{k_{0tq}^2}, \quad \zeta_s^r = \frac{\xi_q\alpha_s R_s^e - k\mu_{0r}\beta_{0s}R_s^h}{k_{0tq}^2}, \tag{5.44}$$

$$\xi_s^t = \frac{\xi_q\alpha_s T_s^e + k\mu_{3r}\beta_{3s}T_s^h}{k_{3tq}^2}, \quad \zeta_s^t = \frac{\xi_q\alpha_s T_s^h - k\epsilon_{3r}\beta_{3s}T_s^e}{k_{3tq}^2}. \tag{5.45}$$

The definition given here is suitable for different stacks. For the 2-layer stack and the corresponding multilayered composite, the power reflection, transmission and absorption coefficients of the fields are defined as $\boldsymbol{\mathcal{R}} = \sum_{p\in\mathbb{Z}}\sum_{q\in\mathbb{Z}} R_s$, $\boldsymbol{\mathcal{T}} = \sum_{p\in\mathbb{Z}}\sum_{q\in\mathbb{Z}} T_s$ and $\boldsymbol{\mathcal{A}} = 1 - \boldsymbol{\mathcal{R}} - \boldsymbol{\mathcal{T}}$. The ones for the 4-layer stack and the related multilayered composite easily follow.

5.8 Numerical investigations

In the numerical investigations, the infinite sums appearing in the plane-wave and multipole expansions need to be truncated. A 2-layer stack with $d_1 = d_2 = d = 0.1\,\text{mm}$, $h_1 = h_2 = h = 0.1\,\text{mm}$, and $c_l = 0.25d$ is first considered. The wavelength of the incident wave $\lambda^{\text{inc}} = d$, the number of propagating modes for different rotation angles ϕ and

different values of d/λ^{inc} are given in table 5.1, which shows that the larger the rotation angle ϕ, the smaller the number of propagating modes. Meanwhile, a high frequency corresponds with more propagating modes than a small one. Allowing $\phi = 30°$, then the distribution of the modes for plane wave illuminating the stack normally and obliquely is given in Fig. 5.7 and Fig. 5.8, respectively. It is observed that the distribution for different incident angles is different, and an obliquely incident wave produces more propagating modes. In what follows, the sums $\sum_{p\in\mathbb{Z}}$ and $\sum_{q\in\mathbb{Z}}$ are truncated to $\sum_{p=P_{\min}}^{P_{\max}}$ and $\sum_{q=Q_{\min}}^{Q_{\max}}$, where a square area defined by $P_{\min} < p < P_{\max}$ and $Q_{\min} < p < Q_{\max}$ is chosen to count all the propagating modes ($\beta_{ls}^2 > 0$) in the calculation. At the same time, enough evanescent modes ($\beta_{ls}^2 < 0$) should be also included for ensuring the convergence of the computation. The sum $\sum_{m\in\mathbb{Z}}$, which is related to the multipole expansion, is truncated as $\sum_{m=-M}^{M}$ with a proper M for good convergence.

Table 5.1 The number of propagating modes.

$\frac{d}{\lambda^{\text{inc}}}$	$\phi = 15°$	$\phi = 30°$	$\phi = 45°$	$\phi = 60°$	$\phi = 90°$
0.2	3	1	1	1	1
0.4	5	3	1	1	1
0.6	17	9	7	7	5
0.8	27	13	11	7	9
1.0	39	19	15	13	9

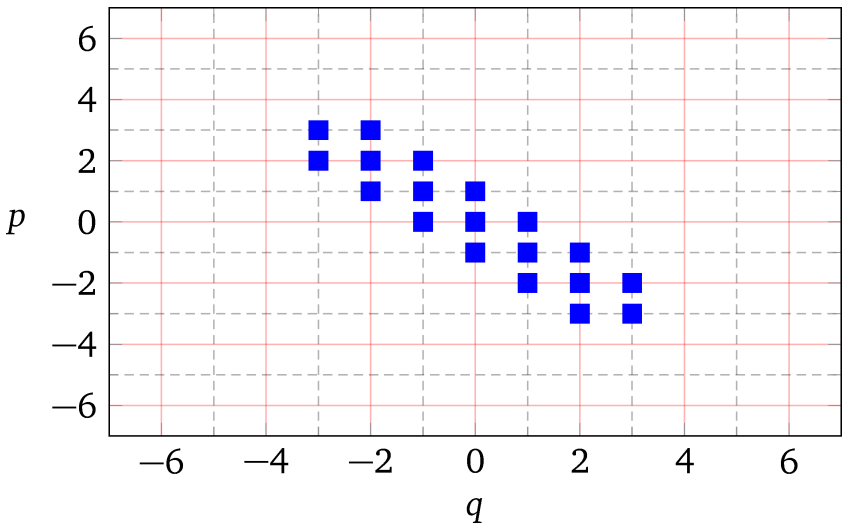

Fig. 5.7 Distribution of the propagating modes (red blocks) for the 2-layer stack with $\phi = 30°$ and $\vartheta = \varphi = 0°$. $\lambda^{\text{inc}} = d$.

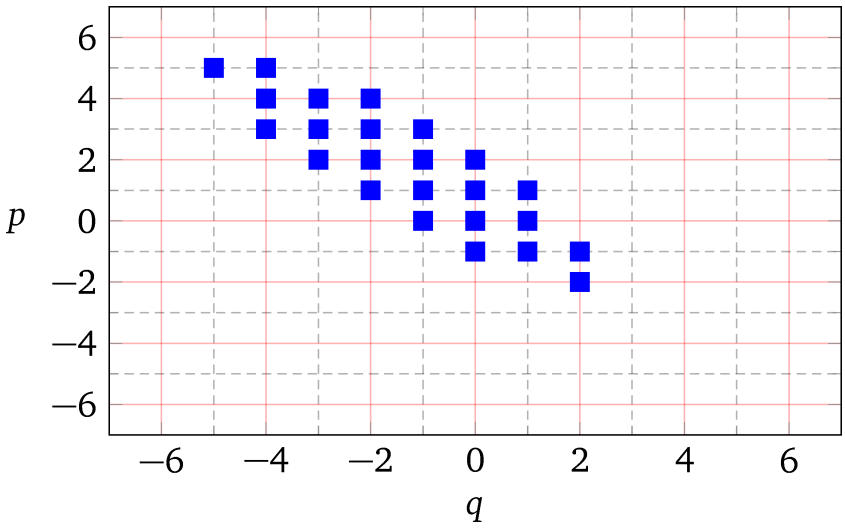

Fig. 5.8 Distribution of the propagating modes (red blocks) for the 2-layer stack with $\phi = 30°$, $\vartheta = 60°$ and $\varphi = 45°$. $\lambda^{\text{inc}} = d$.

To validate the approach, a woodpile structure, originally investigated in [68], the same results being also reproduced in [4] and [39], is considered. The multilayered woodpile is composed of 32 layers which is equivalent to 16 stacks. In each stack, there are two layers with orientation of the fibers in the top layer orthogonal to the one of the fibers in the bottom layer. The whole stack is placed in air. One has $\epsilon_{r12} = \epsilon_{r22} = 5$, $d_1 = d_2 = 0.1\,\text{mm}$ and $h_1 = h_2 = d$. All fibers have the same radius $c = 0.25d$. An E-polarized (TM) incident plane wave is considered, allowing $E_y^{\text{inc}} = 1$ and $K_y^{\text{inc}} = 0$ in the calculation. 2000 points are used for sampling the frequency band $0 < d/\lambda^{\text{inc}} < 1$, where λ^{inc} is the wavelength of the incident wave. Numerical results are given in Fig. 5.9, which show a good agreement between the present results and the ones of [4]. The sudden drop appearing near $d/\lambda^{\text{inc}} = 0.97$ in the results of [4] is not seen in the present results, which is likely caused by the different sampling of the frequency band considered.

Furthermore, consider a 64-layer woodpile structure with epoxy ($\epsilon_r^{(1)} = 3.6$) and glass fibers ($\epsilon_r^{(2)} = 4.8$). Periods of the fibers in different layers are all the same, $d_l = d = 0.1\,\text{mm}$, and one has the same thickness $h_l = d$. The radii of fibers are $c = 0.25d$. The variation of reflection coefficients with the incident angle ϑ is given in Fig. 5.10 for $d/\lambda^{\text{inc}} = 0.5$ and $d/\lambda^{\text{inc}} = 1$, an E-polarized wave being assumed. It is observed that the variation is quite smooth with good symmetry. The energy conservation law is also checked, and it is generally satisfied very well except some small notches at some specific frequencies with a specific incident angle. This numerical error appears to be mainly caused by the bad convergence of the 0-th order lattice sum $\mathscr{S}_0$ at high frequency as well as the strong interactions between the fibers and the slab, and it is also influenced by the condition

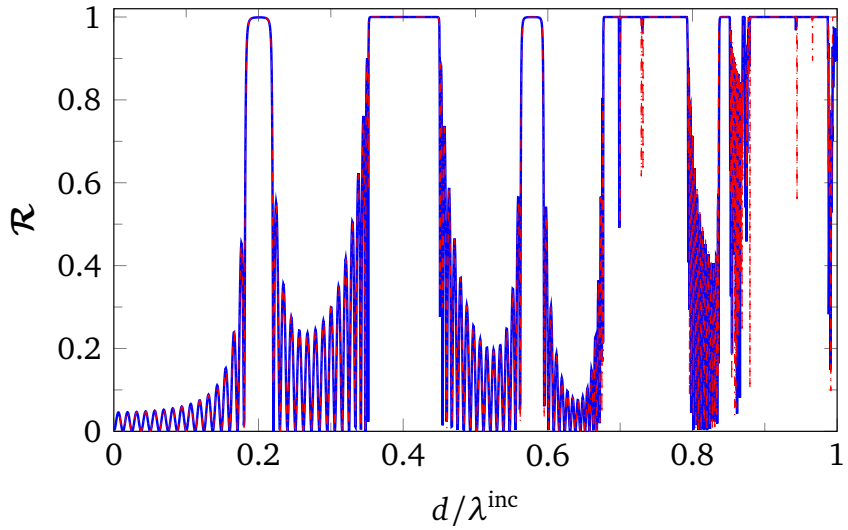

Fig. 5.9 Validating the approach by comparing the present results (blue solid line) of woodpile structure illuminated by a TM wave with those (red dashed line) given in [4] (curves are easily identified with colors).

number of the matrices. Generally speaking, these errors are tolerable for a woodpile structure, and the calculations are accurate enough when the relative error of the lattice sums is smaller than 1×10^{-6}. Increasing the layers will not affect this error much. For the composites constructed by stacks with $0° < \phi < 90°$, more modes are involved in the calculation, related to stronger interactions between fibers and slab, then the numerical error worsens at some specific high frequency with a specific incident angle, as shown in Fig. 5.11 for a 4-layer composite at high frequency. This could become even worse with an increasing number of layers since the errors are accumulated. This error become smaller when the relative error of the lattice sums is decreased, but much more calculation time is needed to achieve the required convergence.

Even though, the approach is always very stable at low frequency ($d/\lambda^{\text{inc}} < 0.5$), as shown in Fig. 5.11 for a 32-layer composite, since less modes are involved in the calculation, meanwhile lattice sums converge very well and quite fast.

Consider the scattering by one 2-layer stack for $\phi = 30°$ and $\phi = 60°$, illuminated by a normally($\vartheta = 0°$, $\varphi = 0°$) incident E-polarized ($E_y^{\text{inc}} = 1$, $K_y^{\text{inc}} = 0$) plane wave. Numerical results are shown in Fig. 5.12. The energy conservation law is very well satisfied since there are only 2 layers. When the wave illuminates the structure normally, it is observed that the reflection coefficients for $\phi = 30°$ and $\phi = 60°$ are almost the same at low frequency, but difference shows up with the increase of the frequency. Significant difference is observed at high frequency. The reason of this phenomenon is that when only one or a few propagating modes exist for low frequency, as shown in table 5.1, the $(0,0)$-th mode

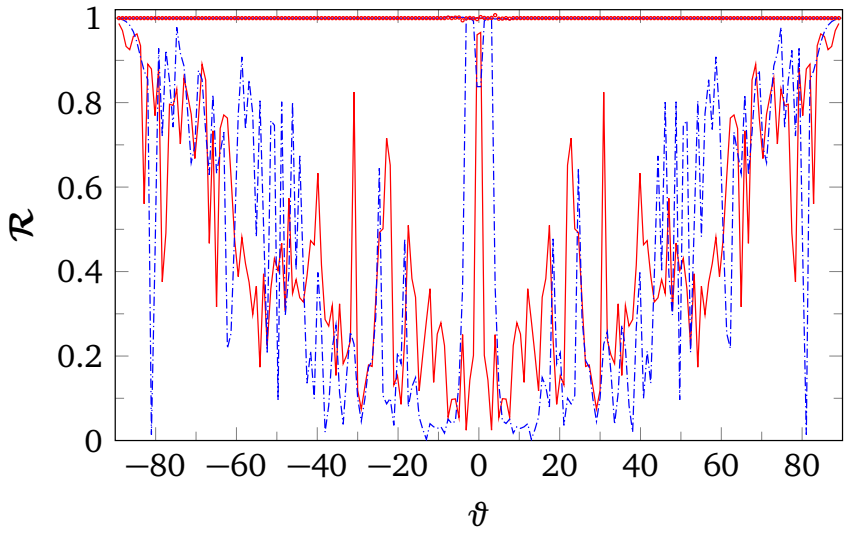

Fig. 5.10 Validating the approach by checking energy conservative law for composite woodpile with $d/\lambda^{\text{inc}} = 0.5$ (blue, dashed line) and $d/\lambda^{\text{inc}} = 1$ (red, solid line or circles).

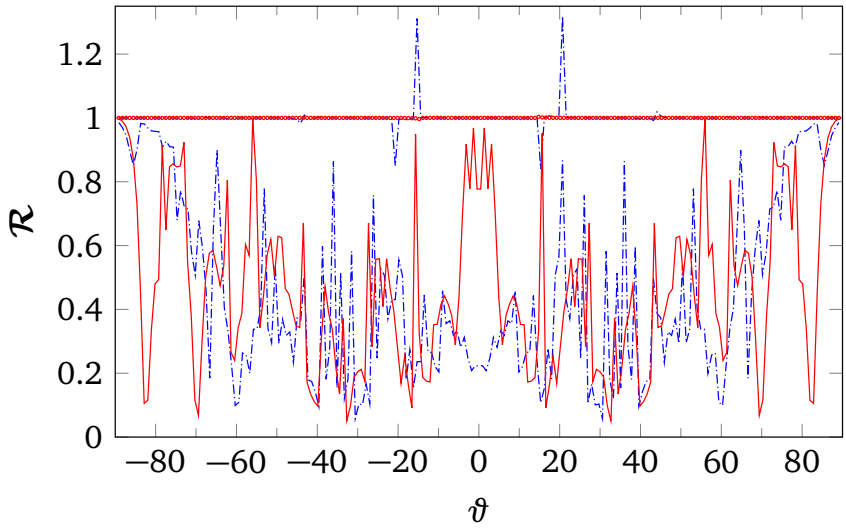

Fig. 5.11 Power reflection coefficients vary with different incident angle for composites constructed with 2 stacks (blue, dashdotted) and 16 stacks (red, solid or circles). $d/\lambda^{\text{inc}} = 1$ for 2-stack composite, and $d/\lambda^{\text{inc}} = 0.5$ for the one with 16 stacks. Each stack has two layers, $\phi = 60°$

plays a dominant role for the response of the incident plane wave. The whole structure behaves like a homogeneous plate. But at high frequency tens of propagating modes are involved, and strong interaction between the wave scattered by plate and cylinders arises. And obviously the rotation of the fibers will affect this interaction and then influence the reflection and transmission of the wave.

A normally and an obliquely ($\vartheta = 60°$, $\varphi = 45°$) incident wave is also considered for a 2-layer stack with the same rotation angle $\phi = 60°$, as shown in Fig. 5.13, the reflection of the normally incident wave is as expected lower than that for the oblique illumination, but the oscillation at high frequency for normal incidence is faster than that of oblique incidence, which means stronger interactions of the fields inside the slab for normal incidence.

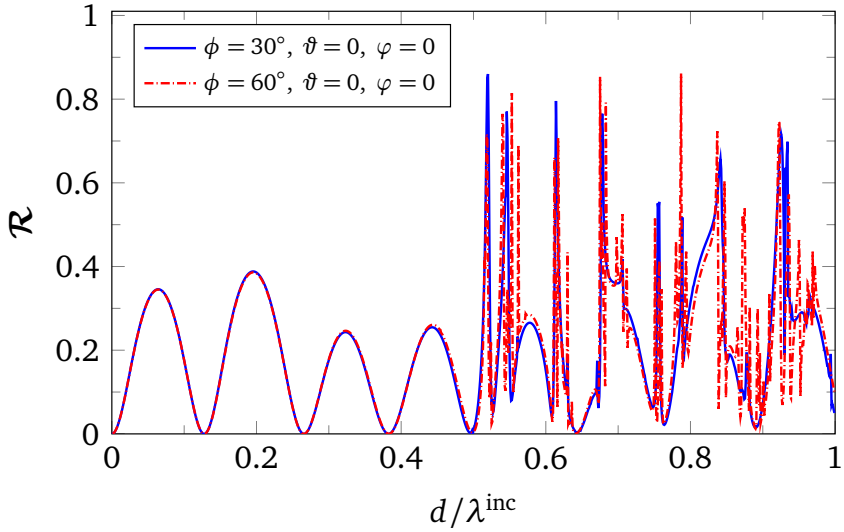

Fig. 5.12 Comparison of results of 2-layer stack with rotation angle of $\phi = 30°$ and $\phi = 60°$, for normal incident plane wave. Obliquely incident plane is also considered for $\vartheta = 60°$, $\varphi = 45°$. $d_1 = d_2 = d = 0.1\,\text{mm}$, $h_1 = h_2 = d$ and $c_1 = c_2 = 0.25d$.

Consider a 32-layer laminated composite constructed with 16 2-layer stacks. The periods are $d_1 = d_2 = d = 0.1\,\text{mm}$, thicknesses are $h_1 = h_2 = h = d$, and $c_l = 0.25d$. The power reflection coefficients of normally and obliquely ($\vartheta = 60°$, $\varphi = 45°$) incident E-polarized plane waves impinging on the composite are given in Fig. 5.14. Strong reflection is observed at some frequency band, and strong oscillations happen. A slight shift of the strong reflection interval is also observed.

As observed from Fig. 5.12, Fig. 5.13 and Fig. 5.14, fast oscillations show up when the frequency is high ($d/\lambda^{\text{inc}} \to 1$). These oscillations will become stronger and faster when the composite material has more layers or higher contrast between the background material and the material of the embedded fibers. But these fast oscillations always happens at frequencies out of the frequency band of non-destructive testing, and what is exhibited by them is not very useful information.

Conclude the above discussions, the following calculation is carried out at low frequency ($d/\lambda^{\text{inc}} < 0.5$) for a 100-layer composite with glass fibers and epoxy background material. The frequency band is in harmony with the frequency band used in the non-

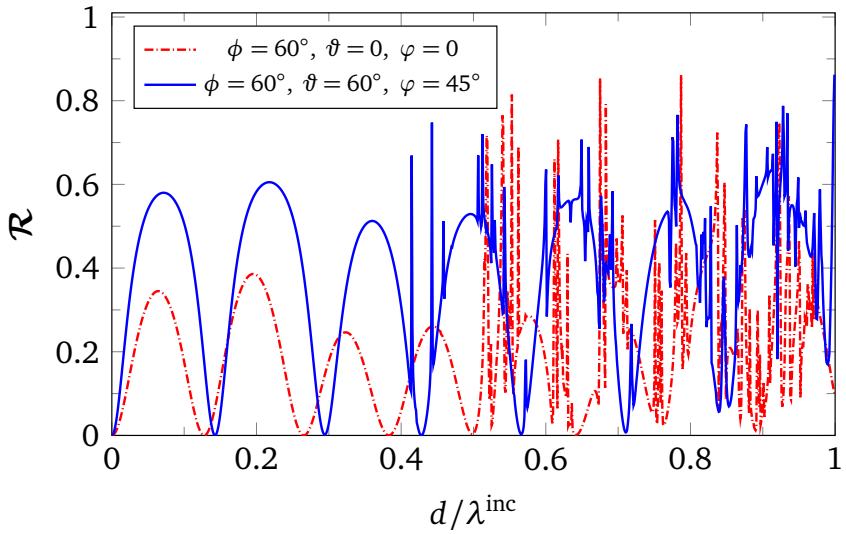

Fig. 5.13 Comparison of results of 2-layer stack with rotation angle of $\phi = 60°$, for normally and obliquely ($\vartheta = 60°,\ \varphi = 45°$) incident plane wave. $d_1 = d_2 = d = 0.1\,\text{mm}$, $h_1 = h_2 = d$ and $c_1 = c_2 = 0.25d$.

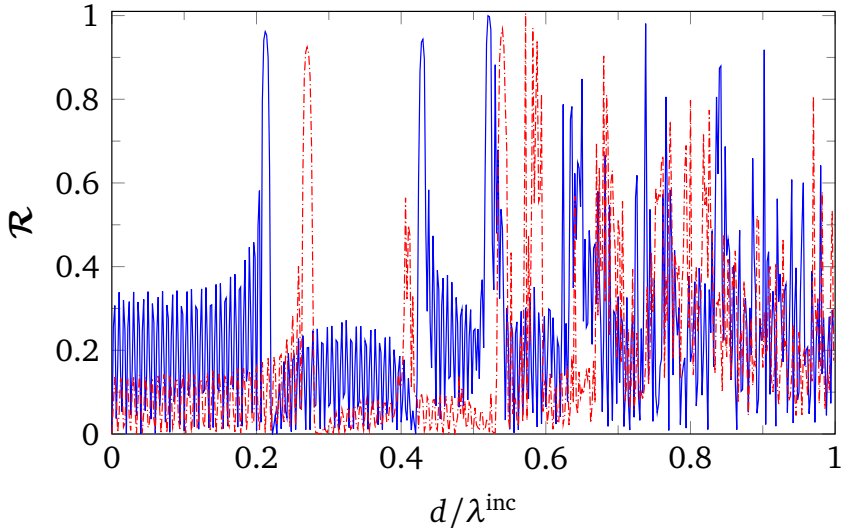

Fig. 5.14 Reflection coefficients of a 32-layer composite consisted of layered 2-layer stacks is given with $\phi = 60°$ for a normally (blue, solid) and obliquely (red, dash dotted, $\vartheta = 60°,\ \varphi = 45°$) incident E-polarized plane wave. $d_1 = d_2 = d = 0.1\,\text{mm}$, $h_1 = h_2 = d$ and $c_1 = c_2 = 0.25d$.

destructive testing. One has $d_1 = d_2 = d = 0.1\,\text{mm}$, $h_1 = h_2 = d$ and $c_1 = c_2 = 0.25d$. Variations of power reflection coefficients with different incident angles ϑ ($\varphi = 45°$) are first given in Fig. 5.15 for $d/\lambda^{\text{inc}} = 0.5$ and $f = 60\,\text{GHz}$ ($d/\lambda^{\text{inc}} = 0.02$, in microwave band). As seen, the energy conservation is well satisfied for both frequencies, and the curve corresponding to $f = 60\,\text{GHz}$ is quite smooth, which means that the interaction

between the fibers and the one between the fiber and slab become quite weak, and correspondingly, less modes are involved in the calculation.

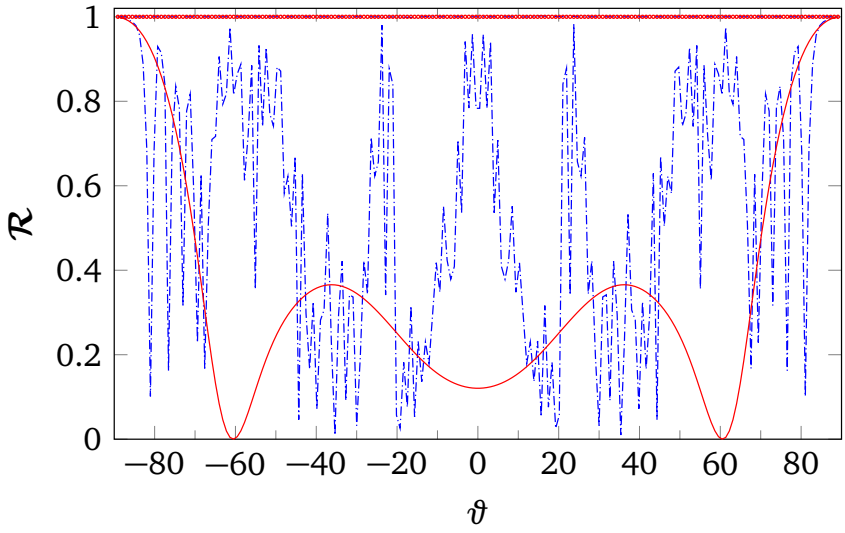

Fig. 5.15 Reflection coefficients of a 100-layer composite made of 2-layer stacks with $\phi = 60°$ for different incident angles, with $d/\lambda^{\text{inc}} = 0.5$ (blue dashed line) and $f = 60\,\text{GHz}$ (red solid line), E-polarized plane wave. $d_1 = d_2 = d = 0.1\,\text{mm}$, $h_1 = h_2 = d$ and $c_1 = c_2 = 0.25d$.

The power reflection coefficients of E- and H-polarized incident wave are compared. The waves impinge the structure conically with $\vartheta = 60°$ and $\varphi = 45°$, with $d/\lambda^{\text{inc}} = 0.5$. The behaviors for the two polarized waves are quite different, especially in the region $-30° < \vartheta < 30°$. At normal incidence, the reflection of the E-polarized wave is much stronger than the one of the H-polarized wave. Energy conservation is also checked, and it is very well satisfied in both cases.

The reflection coefficients varying with different values of d/λ^{inc} are presented in Fig. 5.17. Strong oscillations are observed, and a total reflection interval shows up.

In practice, laminated composites are usually constructed with a 4-layer stack with $\phi_1 = 45°$, $\phi_2 = -45°$ and $\phi_3 = 90°$, as shown in Fig. 5.5. Allowing that $P = P_{\text{max}} - P_{\text{min}} + 1$, $Q = Q_{\text{max}} - Q_{\text{min}} + 1$, $U = U_{\text{max}} - U_{\text{min}} + 1$ and $V = V_{\text{max}} - V_{\text{min}} + 1$, then $P \times Q \times U \times V$ modes are needed to be considered in the calculation. If $P_{\text{min}} = Q_{\text{min}} = U_{\text{min}} = V_{\text{min}} = -1$ and $P_{\text{max}} = Q_{\text{max}} = U_{\text{max}} = V_{\text{max}} = 1$, then 3^4 modes are needed in the calculation, which cost in average about 20 minutes for the calculation at each frequency point. But if $P_{\text{min}} = Q_{\text{min}} = U_{\text{min}} = V_{\text{min}} = -2$ and $P_{\text{max}} = Q_{\text{max}} = U_{\text{max}} = V_{\text{max}} = 2$, the total number of modes calculated is 5^4, which makes the average time cost at each frequency point increasing to hours. In a practical calculation, more modes are needed at high frequency for a good convergence. The efficiency of the calculation is mainly influenced by the un-

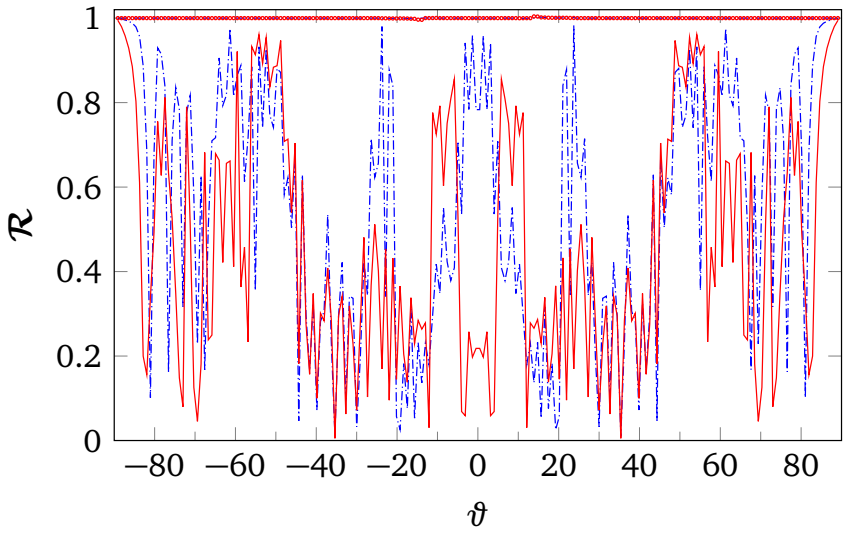

Fig. 5.16 Reflection coefficients of a 100-layer composite consisting of 2-layer stacks with $\phi = 60°$ for E-polarized (dashed, blue) and H-polarized (solid line, red) plane wave. Energy conservation is checked, blue dashed line for E-polarized wave, and red circles for H-polarized one. $d_1 = d_2 = d = 0.1\,\text{mm}$, $h_1 = h_2 = d$ and $c_1 = c_2 = 0.25d$.

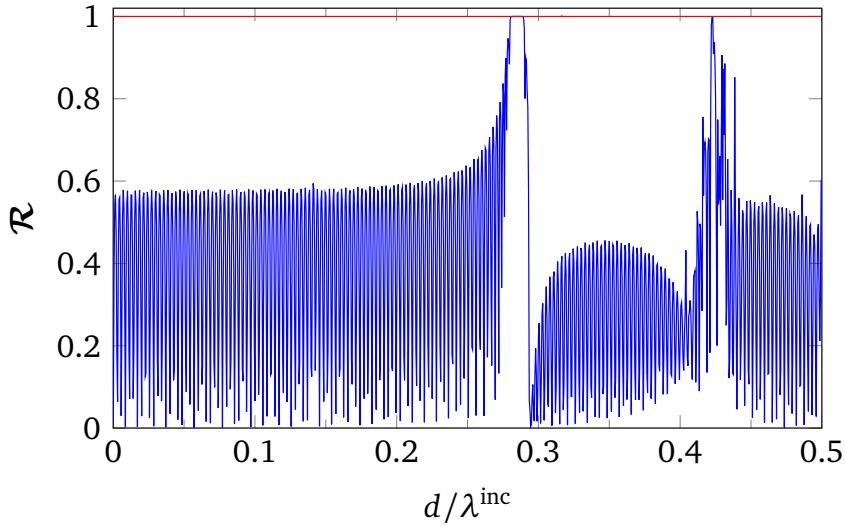

Fig. 5.17 Reflection coefficients of a 100-layer composite consisting of 2-layer stacks with $\phi = 60°$ for E-polarized plane wave with different frequencies. Energy conservation is checked (red solid line). $d_1 = d_2 = d = 0.1\,\text{mm}$, $h_1 = h_2 = d$ and $c_1 = c_2 = 0.25d$. $\vartheta = 60°$, and $\varphi = 45°$.

avoidable lattice sums and the increase of the number of propagating modes with the increase of frequency. Accelerating the calculation is necessary for investigating reflection and transmission of the structure at high frequency, which can be achieved by using a faster

convergent approach for lattice sums or by applying parallel computing on a workstation or cluster.

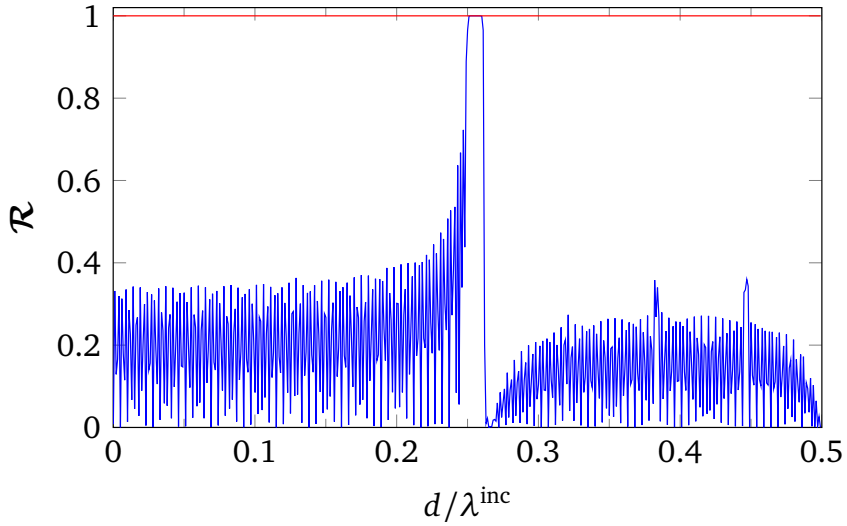

Fig. 5.18 Reflection coefficients of a 100-layer composite constructed with 4-layer stacks is given with $\phi_1 = 45°$, $\phi_2 = -45°$ and $\phi_3 = 90°$ for a normally incident E-polarized plane wave. Energy conservation law is checked (red solid line). All layers have the same period $d_l = d = 0.1\,\text{mm}$, thickness $h_l = d$ and radius $c_l = 0.25d$.

But for non-destructive testing, the wavelength is generally much larger than the period of the structures, hence the calculation for composites constructed by 4-layer stacks are carried out here with $0 < d/\lambda^{\text{inc}} < 0.5$, where the mode of $s = (0,0,0,0)$ dominates the electromagnetic behavior of the structure. The reflection coefficients of a 100-layer composite constructed with 4-layer stacks are shown in Fig. 5.18 with $\phi_1 = 45°$, $\phi_2 = -45°$ and $\phi_3 = 90°$ for a normally incident E-polarized plane wave. All layers have the same period $d_l = d = 0.1\,\text{mm}$, height $h_l = d$ and radius $c_l = 0.25d$. It is observed that the reflection coefficients are very sensitive to the variation of frequency, and fast oscillations being observed in the concerned frequency band. Meanwhile, a total reflection interval appears around $d/\lambda^{\text{inc}} = 0.25$. Comparing these results with the ones given in Fig. 5.17 for a 100-layer composite constructed with 2-layer stacks, a similar behavior is observed.

5.9 Summary

Currently, the approach combining plane-wave expansion and multipole method is successfully extended for investigation of multilayered composite with the fibers orientated into different directions. Based on the work presented in Chapter 4, the approach is applied for the composites constructed with two kinds of stacks. For the frequency band concerned for

non-destructive testing, the approach works stably and efficiently. Numerical experiments are also carried out for various cases concerning glass-fiber reinforced composites, and the accuracy and efficiency are also discussed.

Chapter 6

Conclusion and Perspectives

Conclusion

In the present work, one has built an efficient computational model of multilayered composite materials reinforced by periodically arranged fibers, such as carbon-/glass-fiber reinforced composites used in aerospace, naval and automotive industries. Good understanding of the electromagnetic behavior of the composites has been acquired, which should serve for non-destructive testing and imaging of disorganized periodic structures in particular so as to exhibit the location of possibly damaged zones and provide some quantification of these zones.

The work started by considering a single-layer composite constructed by embedding a periodic array of infinitely long circular cylindrical fibers into a dielectric slab. This first step helped to understand the basic principles and related philosophy of the used approach, which is a combination of multipole method and plane-wave expansion. Thus a solid basis was made available for further investigating the scattering of multilayered structures as a pile of many single-layer composites.

Two cases have been under consideration for a plane wave illuminating the single-layer composite. The first one (2D case) concerned the E- or H-polarized incident wave with the plane of incidence parallel to the plane of the cross-section of the fibers. The problems corresponding to E- or H-polarized incident waves have been studied in an unified way, which allows to carry out an unified program for the calculation. Then the scattering of Gaussian beam was investigated by expanding the Gaussian beam properly into a plane-wave distribution. The scattered field obtained for each plane wave was then overlapped to produce the scattered field of the beam. Lattice sums have naturally arisen for suitably combining the contribution of other circular fibers to the field in the region around the considered one, so as to satisfy the required periodic boundary conditions.

Based on the solution of this 2D case, a plane wave conically illuminating the single-layer composite has then been considered. The plane of incidence was out of the plane orthogonal with the axes of fibers. This considered problem is denoted as 2.5D case. The solution for the 2D case was then applied straightforwardly to investigate this 2.5D case. It actually has no many more complexities than the 2D case except some complicated relations between longitudinal and transverse field components, since the longitudinal electric and magnetic fields are coupled when the wave is impinging the structure conically.

Once the reflection and transmission coefficients of each modes has been obtained in all considered cases, Poynting's theorem has been applied to produce the power reflection and transmission coefficients.

Investigation of the 2D and 2.5D cases provided the basic knowledge for producing the Green's functions of the single-layer structure by calculating the response of line or dipole sources. The techniques introduced in detail in the above works has been extended to solve the scattering problem of complex composites.

The first considered multilayered structure was constructed by piling up the single-layer composite with the fibers in all layers parallel to each other. T-matrix and S-matrix based recursive schemes have been proposed for making the calculation, but it was shown that the S-matrix based approach is more stable. Instability of the T-matrix based approach is caused by the exponentially decreasing or increasing elements corresponding to the evanescent modes. This problem cannot be easily overcome since a proper number of evanescent modes is needed in the calculation for obtaining a good convergence of the field expansions.

Meanwhile, the S-matrix based approach naturally obviates the need of inverting the ill-conditioned matrices in the calculation. Some difficulties met for directly calculating the field distribution inside the structure were easily overcome by rearranging the matrices to link the expansion coefficients to the incident field.

The stable recursive scheme based on S-matrices was then extended for investigating multilayered composite with arbitrary orientations of the fibers in different layers. Attention was on two kinds of structures constructed with two kinds of stacks. The first was a 2-layer stack with the fibers in different layers orientated into an arbitrary direction. The second was a more practical one where 4 layers are included in the stack with different orientations of the fibers in different layers. The two kinds of multilayered structures have been constructed by piling up the two kinds of stacks individually.

The S-matrix for one stack was established by cascading the S-matrices of all layers. Then the S-matrices for all the stacks were combined to produce the S-matrix for the whole

structure, which actually linked the reflection and transmission coefficients to the incident field, which can then be used to get reflection and transmission coefficients.

Main focus of the numerical investigations was mainly on reflection and transmission properties of the glass/carbon-fiber reinforced composites. Notice that in the case of fiber-reinforced composites, the adequate frequency bands have been chosen for carrying out the numerical experiments in harmony with those usually considered during non-destructive testing of such composites.

Effectiveness and accuracy have been exhibited for different composite models, with different degree of complexities. All the approaches proposed in the thesis were widely validated by comparing the present results with those existing in the literature on photonic crystals. One has also compared some results of the presented approach with those produced by the COMSOL software, and one successfully retrieved the same results.

So, the electromagnetic behaviors of multilayered composites, with fibers inside orientated into arbitrary directions, have been investigated by combining the multipole method and plane-wave expansion. The way of generalizing the approach and the difficulties met during the procedure as well as the challenges faced were all presented in detail. In parallel, approximate models, replacing each layer by its homogenized counterpart, has also been given in 2D case, for single- or multi-layer structures.

Perspectives

The present work mainly paid attention to well-organized structures. But there might be one or several fibers missing or displaced inside a composites. Local damages might occur also, leading to changes in shape or electromagnetic properties of one or more cylinders in one or more layers. Randomness in the distribution of the inclusions might account for uncertainties of positioning with respect to assumed geometries. Properly illuminating the structures and collecting the resulting fields in the near-field hopefully and possibly in the far-field should allow their imaging and concur to their diagnostics. So, a periodic structure under interrogation is disorganized. One wishes to successfully image the structure while taking care at best of prior information on periodicity and disorganization, on sensing systems, and obviously of needs and limitations of the testing.

The coming contributions should focus on the disorganized structure, and the work falls into two steps, accurate scattering modeling (forward problem) and high-resolution imaging (inverse problem). With the work presented in this thesis, the response of the well-organized periodic structure to an inner or outer elementary line or dipole sources could be obtained through plane-wave expansion of the elementary sources, which then lead to the dyadic Green's function. At low frequency, the scattered field of the dis-organized

structure could be easily obtained with Born approximation. High order approximation techniques could also be applied if necessary.

To avoid the calculation of Green's function and accurately compute the response of dis-organized structure to electromagnetic waves, several analytic models could be built for several different cases of disorganized structures. In the most simple case, a single-layer disorganized periodic structure with one missing fiber should be considered. Multiple scattering theory, "supercell" method and periodic Fourier transform should be the possible useful strategies. Well establishing this electromagnetic model allows one to explore the possible techniques and build a good basis. Finite Element Method and Finite-Difference Time-Domain method could provide results for validations. Simple extension of the single-layer model should allows one to investigate the periodic array with several missing fibers cases. For more complicated disorganized structures, such as the one with defects and with changes in shape or electromagnetic properties, the approach based on "supercell" or periodic Fourier transform might also be useful. All these approaches could be further developed to study multilayered disorganized periodic structure.

The equivalent layer model should be a good approximate solution to the above problems for low frequency incident wave, and it should be more applicable for the complicated structures. In this model, the array of fibers is homogenized and replaced by an uniaxially anisotropic layer. Then the response of the structure to a line source is calculated to produce the dyadic Green's function, where the magnetic-electric Green's function may be better.

For imaging, one-shot or iterative imaging may be proposed, which is fully relevant to the field of time-reversal (TR) seen "at large". Full transient data might end up in being time-harmonic frequency-diverse data, and carefully tailored back-propagation algorithms might substitute to TR mirrors as usually thought of. These algorithms starting from first-order models of electromagnetic phenomena, but increasing in complexity as/if necessary;

In brief, the work presented in this thesis gave the perspectives of building the forward electromagnetic model of both well-organized and disorganized periodic structures. By using these forward models, dyadic Green's functions can be obtained via calculating the response of an elementary dipole source. Then non-destructive testing and imaging of the composite material could follow with multiple approaches.

Appendix A

Graf's addition theory

Addition theorems [47] arise in a number of solutions of multiple scattering problem by cylinders, where the linear transformation of cylindrical wave functions from one coordinate system to another one is needed. Here, the addition theorem in cylindrical coordinates is given as

$$H_0^{(1)}(k_\rho|\vec{\rho}-\vec{\rho}'|) = \sum_{n=-\infty}^{\infty} H_n^{(1)}(k_\rho\rho_>)J_n(k_\rho\rho_<)e^{in(\phi-\phi')}, \tag{A.1}$$

where $\rho_<$ is the smaller one of ρ and ρ', and $\rho_>$ is the larger one of ρ and ρ', see Fig. A.1.

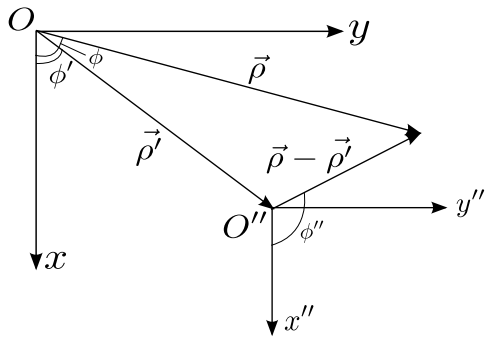

Fig. A.1 Translation in the cylindrical coordinate system.

Equation (A.1) can also be written as

$$H_m^{(1)}(k_\rho|\vec{\rho}-\vec{\rho}'|)e^{im\phi''} = \begin{cases} \sum_{n=-\infty}^{\infty} J_{n-m}(k_\rho\rho')H_n^{(1)}(k_\rho\rho)e^{in\phi-i(n-m)\phi'}, & \rho>\rho', \\ \sum_{n=-\infty}^{\infty} H_n^{(1)}(k_\rho\rho')J_{n-m}(k_\rho\rho)e^{in\phi-i(n-m)\phi'}, & \rho<\rho', \end{cases} \tag{A.2}$$

Moreover, taking the regular part of (A.2) on both sides of the equation produces

$$J_m(k_\rho|\vec{\rho}-\vec{\rho}'|)e^{im\phi''} = \sum_{n=-\infty}^{\infty} J_{n-m}(k_\rho\rho')J_n(k_\rho\rho)e^{in\phi-i(n-m)\phi'}, \tag{A.3}$$

which establishes the addition theorem for Bessel functions. It can be rewritten as

$$\begin{aligned} J_{-m}(k_\rho|\vec{\rho}-\vec{\rho}'|)e^{-im\phi''} &= \sum_{n=-\infty}^{\infty} J_{n+m}(k_\rho\rho')J_n(k_\rho\rho)e^{in\phi-i(n+m)\phi'} \\ &= \sum_{n=-\infty}^{\infty} J_n(k_\rho\rho')J_{n-m}(k_\rho\rho)e^{i(n-m)\phi-in\phi'} \end{aligned} \tag{A.4}$$

Another useful identity is written as

$$J_m(k_\rho|\vec{\rho}-\vec{\rho}'|)e^{im\phi''} = \sum_{n=-\infty}^{\infty} J_n(k_\rho\rho')J_{n+m}(k_\rho\rho)e^{i(n+m)\phi-in\phi'}, \tag{A.5}$$

Appendix B

Mode-matching at boundaries Γ_a and Γ_b

Matching the fields represented by (3.18) and (3.25) on the boundaries Γ_a and Γ_b and applying the property $\int_{-d/2}^{d/2} e^{i(\alpha_m-\alpha_n)x}dx = d\delta_{mn}$, $m,n\in\mathbb{Z}$, to the obtained four equations

$$E_{inc}\delta_{0p}+R_p^e-(f_{ep}^+e^{-i\beta_{1p}a}+g_{ep}^-e^{i\beta_{1p}a}+\sum_{m\in\mathbb{Z}}B_m^eG_{pm}^+e^{i\beta_{1p}a})=0, \tag{B.1a}$$

$$T_p^e-(f_{ep}^+e^{-i\beta_{1p}b}+g_{ep}^-e^{i\beta_{1p}b}+\sum_{m\in\mathbb{Z}}B_m^eG_{pm}^-e^{-i\beta_{1p}b})=0, \tag{B.1b}$$

$$K_{inc}\delta_{0p}+R_p^h-(f_{hp}^+e^{-i\beta_{1p}a}+g_{hp}^-e^{i\beta_{1p}a}+\sum_{m\in\mathbb{Z}}B_m^hG_{pm}^+e^{i\beta_{1p}a})=0, \tag{B.1c}$$

$$T_p^h-(f_{hp}^+e^{-i\beta_{1p}b}+g_{hp}^-e^{i\beta_{1p}b}+\sum_{m\in\mathbb{Z}}B_m^hG_{pm}^-e^{-i\beta_{1p}b})=0. \tag{B.1d}$$

With the x components of the fields obtained by substituting (3.18) and (3.25) into equations (3.7a) and (3.7b), the following four equations can be easily obtained in the same way

$$\begin{aligned}&\frac{k_{1t}^2}{k_{0t}^2}[\alpha_pk_y(E_{inc}\delta_{0p}+R_p^e)+k\mu_{0r}\beta_{0p}(K_{inc}\delta_{0p}-R_p^h)]\\=&\alpha_pk_y(f_{ep}^+e^{-i\beta_{1p}a}+g_{ep}^-e^{i\beta_{1p}a}+\sum_{m\in\mathbb{Z}}B_m^eG_{pm}^+e^{i\beta_{1p}a})\\&+k\mu_{1r}\beta_{1p}(f_{hp}^+e^{-i\beta_{1p}a}-g_{hp}^-e^{i\beta_{1p}a}-\sum_{m\in\mathbb{Z}}B_m^hG_{pm}^+e^{i\beta_{1p}a}),\end{aligned} \tag{B.2a}$$

$$\begin{aligned}&\frac{k_{1t}^2}{k_{3t}^2}(\alpha_pk_yT_p^e+k\mu_{3r}\beta_{3p}T_p^h)\\=&\alpha_pk_y(f_{ep}^+e^{-i\beta_{1p}b}+g_{ep}^-e^{i\beta_{1p}b}+\sum_{m\in\mathbb{Z}}B_m^eG_{pm}^-e^{-i\beta_{1p}b})\\&+k\mu_{1r}\beta_{1p}(f_{hp}^+e^{-i\beta_{1p}b}-g_{hp}^-e^{i\beta_{1p}b}+\sum_{m\in\mathbb{Z}}B_m^hG_{pm}^-e^{-i\beta_{1p}b}),\end{aligned} \tag{B.2b}$$

$$\begin{aligned}
&\frac{k_{1t}^2}{k_{0t}^2}[\alpha_p k_y(K_{inc}\delta_{0p}+R_p^h)-k\epsilon_{0r}\beta_{0p}(E_{inc}\delta_{0p}-R_p^e)]\\
=&\alpha_p k_y(f_{hp}^+e^{-i\beta_{1p}a}+g_{hp}^-e^{i\beta_{1p}a}+\sum_{m\in\mathbb{Z}}B_m^hG_{pm}^+e^{i\beta_{1p}a})\\
&-k\epsilon_{1r}\beta_{1p}(f_{ep}^+e^{-i\beta_{1p}a}-g_{ep}^-e^{i\beta_{1p}a}-\sum_{m\in\mathbb{Z}}B_m^eG_{pm}^+e^{i\beta_{1p}a}),
\end{aligned}\tag{B.2c}$$

$$\begin{aligned}
&\frac{k_{1t}^2}{k_{3t}^2}[k_y\alpha_pT_p^h-k\epsilon_{3r}\beta_{3p}T_p^e]\\
=&\alpha_p k_y(f_{hp}^+e^{-i\beta_{1p}b}+g_{hp}^-e^{i\beta_{1p}b}+\sum_{m\in\mathbb{Z}}B_m^hG_{pm}^-e^{-i\beta_{1p}b})\\
&-k\epsilon_{1r}\beta_{1p}(f_{ep}^+e^{-i\beta_{1p}b}-g_{ep}^-e^{i\beta_{1p}}+\sum_{m\in\mathbb{Z}}B_m^eG_{pm}^-e^{-i\beta_{1p}b}),
\end{aligned}\tag{B.2d}$$

Eliminating R_p^e, T_p^e, R_p^h and T_p^h from (B.1) and (B.2) yields

$$\begin{aligned}
&\alpha_pk_yf_{ep}^+e^{-i\beta_{1p}a}+\alpha_pk_yg_{ep}^-e^{i\beta_{1p}a}-\frac{\tau_0\rho_0+\rho_1}{\tau_0-1}f_{hp}^+e^{-i\beta_{1p}a}-\frac{\tau_0\rho_0-\rho_1}{\tau_0-1}g_{hp}^-e^{i\beta_{1p}a}\\
=&-\alpha_pk_y\sum_{m\in\mathbb{Z}}B_m^eG_{pm}^+e^{i\beta_{1p}a}-\frac{2\tau_0\rho_0}{\tau_0-1}K_{inc}\delta_{0p}+\frac{\tau_0\rho_0-\rho_1}{\tau_0-1}\sum_{m\in\mathbb{Z}}B_m^hG_{pm}^+e^{i\beta_{1p}a},
\end{aligned}\tag{B.3a}$$

$$\begin{aligned}
&\alpha_pk_yf_{ep}^+e^{-i\beta_{1p}b}+\alpha_pk_yg_{ep}^-e^{i\beta_{1p}b}+\frac{\tau_3\rho_3-\rho_1}{\tau_3-1}f_{hp}^+e^{-i\beta_{1p}b}+\frac{\tau_3\rho_3+\rho_1}{\tau_3-1}g_{hp}^-e^{i\beta_{1p}b}\\
=&-\alpha_pk_y\sum_{m\in\mathbb{Z}}B_m^eG_{pm}^-e^{-i\beta_{1p}b}-\frac{\tau_3\rho_3-\rho_1}{\tau_3-1}\sum_{m\in\mathbb{Z}}B_m^hG_{pm}^-e^{-i\beta_{1p}b},
\end{aligned}\tag{B.3b}$$

$$\begin{aligned}
&\alpha_pk_yf_{hp}^+e^{-i\beta_{1p}a}+\alpha_pk_yg_{hp}^-e^{i\beta_{1p}a}+\frac{\tau_0\eta_0+\eta_1}{\tau_0-1}f_{ep}^+e^{-i\beta_{1p}a}+\frac{\tau_0\eta_0-\eta_1}{\tau_0-1}g_{ep}^-e^{i\beta_{1p}a}\\
=&-\alpha_pk_y\sum_{m\in\mathbb{Z}}B_m^hG_{pm}^+e^{i\beta_{1p}a}+\frac{2\tau_0\eta_0}{\tau_0-1}E_{inc}\delta_{0p}-\frac{\tau_0\eta_0-\eta_1}{\tau_0-1}\sum_{m\in\mathbb{Z}}B_m^eG_{pm}^+e^{i\beta_{1p}a},
\end{aligned}\tag{B.3c}$$

$$\begin{aligned}
&\alpha_pk_yf_{hp}^+e^{-i\beta_{1p}b}+\alpha_pk_yg_{hp}^-e^{i\beta_{1p}b}-\frac{\tau_3\eta_3-\eta_1}{\tau_3-1}f_{ep}^+e^{-i\beta_{1p}b}-\frac{\tau_3\eta_3+\eta_1}{\tau_3-1}g_{ep}^-e^{i\beta_{1p}b}\\
=&-\alpha_pk_y\sum_{m\in\mathbb{Z}}B_m^hG_{pm}^-e^{-i\beta_{1p}b}+\frac{\tau_3\eta_3-\eta_1}{\tau_3-1}\sum_{m\in\mathbb{Z}}B_m^eG_{pm}^-e^{-i\beta_{1p}b}.
\end{aligned}\tag{B.3d}$$

In the above, $\tau_j=\frac{k_{1t}^2}{k_{jt}^2}$, $\rho_j=k\mu_{jr}\beta_{jp}$ and $\eta_j=k\epsilon_{jr}\beta_{jp}$. Solving the linear system yields

$$f_{ep}^+=\frac{M_p^eQ_p^e-N_p^eW_p^e}{S_p^eQ_p^e-P_p^eW_p^e},\quad g_{ep}^-=\frac{M_p^eP_p^e-N_p^eS_p^e}{W_p^eP_p^e-Q_p^eS_p^e},\tag{B.4a}$$

$$f_{hp}^+=\frac{M_p^hQ_p^h-N_p^hW_p^h}{S_p^hQ_p^h-P_p^hW_p^h},\quad g_{hp}^-=\frac{M_p^hP_p^h-N_p^hS_p^h}{W_p^hP_p^h-Q_p^hS_p^h},\tag{B.4b}$$

where f_{ep}^{+}, g_{ep}^{-}, f_{hp}^{+} and g_{hp}^{-} are expressed in terms of B_m^h and B_m^e with coefficients M_p^h, N_p^h, M_p^e and N_p^e defined as

$$M_p^e = \sum_{m\in\mathbb{Z}} B_m^e U_{mp}^{ee} + \sum_{m\in\mathbb{Z}} B_m^h U_{mp}^{eh} + U_p^{ei}, \quad N_p^e = \sum_{m\in\mathbb{Z}} B_m^e V_{mp}^{ee} + \sum_{m\in\mathbb{Z}} B_m^h V_{mp}^{eh} + V_p^{ei}, \tag{B.5a}$$

$$M_p^h = \sum_{m\in\mathbb{Z}} B_m^e U_{mp}^{he} + \sum_{m\in\mathbb{Z}} B_m^h U_{mp}^{hh} + U_p^{hi}, \quad N_p^h = \sum_{m\in\mathbb{Z}} B_m^e V_{mp}^{he} + \sum_{m\in\mathbb{Z}} B_m^h V_{mp}^{hh} + V_p^{hi}, \tag{B.5b}$$

Coefficients $S_p^{e,h}$, $W_p^{e,h}$, $P_p^{e,h}$ and $Q_p^{e,h}$ are given as

$$S_p^e = \Upsilon^- - \Xi_0^+ e^{-i\beta_{1p}(2a-b)} + \Lambda_3^- e^{-i\beta_{1p}b},\ W_p^e = \Upsilon^+ + \Xi_0^- e^{i\beta_{1p}(2a-b)} - \Lambda_3^+ e^{i\beta_{1p}b}, \tag{B.6}$$

$$P_p^e = \Upsilon^- + \Xi_3^- e^{-i\beta_{1p}(a-2b)} - \Lambda_0^+ e^{-i\beta_{1p}a},\ Q_p^e = \Upsilon^+ - \Xi_3^+ e^{-i\beta_{1p}(a-2b)} + \Lambda_0^- e^{i\beta_{1p}a}, \tag{B.7}$$

$$S_p^h = \Upsilon^- - \Xi_0^+ e^{-i\beta_{1p}(2a-b)} + \Theta_3^- e^{-i\beta_{1p}b},\ W_p^h = \Upsilon^+ + \Xi_0^- e^{i\beta_{1p}(2a-b)} - \Theta_3^+ e^{i\beta_{1p}b}, \tag{B.8}$$

$$P_p^h = \Upsilon^- + \Xi_3^- e^{i\beta_{1p}(a-2b)} - \Theta_0^+ e^{-i\beta_{1p}a},\ Q_p^h = \Upsilon^+ - \Xi_3^+ e^{-i\beta_{1p}(a-2b)} + \Theta_0^+ e^{i\beta_{1p}a}, \tag{B.9}$$

where

$$\Upsilon^{\pm} = e^{\pm i\beta_{1p}a}(\alpha_p k_y)^2(\tau_0-1)^2(\tau_3-1)^2, \tag{B.10a}$$

$$\Xi_{\{0,3\}}^{\pm} = \frac{\tau_{\{3,0\}}-1}{2i\sin(\beta_{1p}L)}\Big[(\tau_{\{0,3\}}\rho_{\{0,3\}}+\rho_1)\times(\tau_{\{0,3\}}\eta_{\{0,3\}}+\eta_1)(\tau_{\{3,0\}}-1)\Big], \tag{B.10b}$$

$$\begin{aligned}\Lambda_{\{0,3\}}^{\pm} = \frac{\tau_{\{0,3\}}-1}{2i\sin(\beta_{1p}L)}\Big[&2\rho_1(\tau_{\{0,3\}}\eta_{\{0,3\}}\pm\eta_1)(\tau_{\{3,0\}}-1)\\ &\pm(\tau_{\{3,0\}}\rho_{\{3,0\}}\pm\rho_1)(\tau_{\{3,0\}}\eta_{\{3,0\}}\mp\eta_1)(\tau_{\{0,3\}}-1)\Big],\end{aligned} \tag{B.10c}$$

$$\begin{aligned}\Theta_{\{0,3\}}^{\pm} = \frac{\tau_{\{0,3\}}-1}{2i\sin(\beta_{1p}L)}\Big[&2\eta_1(\tau_{\{0,3\}}\rho_{\{0,3\}}\pm\eta_1)(\tau_{\{3,0\}}-1)\\ &\pm(\tau_{\{3,0\}}\eta_{\{3,0\}}\pm\eta_1)(\tau_{\{3,0\}}\rho_{\{3,0\}}\mp\rho_1)(\tau_{\{0,3\}}-1)\Big].\end{aligned} \tag{B.10d}$$

The others are defined as

$$\begin{aligned}U_{mp}^{eh} =&(\alpha_p k_y)(\tau_3-1)^2(\tau_0-1)\Big[(\tau_0\rho_0-\rho_1)G_{pm}^{+}e^{i\beta_{1p}a}\\ &-\frac{1}{2i\sin(\beta_{1p}L)}\Big(2\rho_1 G_{pm}^{-}e^{-i\beta_{1p}b}-(\tau_0\rho_0+\rho_1)\\ &\times G_{pm}^{+}e^{i\beta_{1p}b}+(\tau_0\rho_0-\rho_1)G_{pm}^{+}e^{i\beta_{1p}(2a-b)}\Big)\Big],\end{aligned} \tag{B.11}$$

$$V_p^{ei} = \frac{-2\tau_0\eta_0\rho_1(\tau_3-1)(\tau_0-1)E_y^{\mathrm{inc}}\delta_{p0}}{i\sin(\beta_{1p}L)}, \tag{B.12}$$

$$
\begin{aligned}
U_{mp}^{ee} =&(\tau_3-1)\Big[-G_{pm}^{+}e^{i\beta_{1p}a}(\alpha_p k_y)^2(\tau_0-1)^2(\tau_3-1)\\
&+\frac{1}{2i\sin(\beta_{1p}L)}\Big((\tau_0\rho_0+\rho_1)(\tau_0\eta_0-\eta_1)(\tau_3-1)\\
&\times G_{pm}^{+}e^{i\beta_{1p}b}+2\rho_1(\tau_3\eta_3-\eta_1)(\tau_0-1)G_{pm}^{-}e^{-i\beta_{1p}b}\\
&-(\tau_0\rho_0-\rho_1)(\tau_0\eta_0-\eta_1)(\tau_3-1)G_{pm}^{+}e^{i\beta_{1p}(2a-b)}\Big)\Big],
\end{aligned}
\tag{B.13}
$$

$$
\begin{aligned}
U_{p}^{ei} =&(\tau_3-1)^2\Big[-2\tau_0\rho_0(\alpha_p k_y)(\tau_0-1)K_y^{\mathrm{inc}}\delta_{0p}\\
&+\frac{2\tau_0\eta_0\left(i\tau_0\rho_0\sin(\beta_{1p}L)-\rho_1\cos(\beta_{1p}L)\right)E_y^{\mathrm{inc}}\delta_{0p}}{i\sin(\beta_{1p}L)}\Big],
\end{aligned}
\tag{B.14}
$$

$$
\begin{aligned}
V_{mp}^{eh} =&(\alpha_p k_y)(\tau_0-1)^2(\tau_3-1)\Big[-(\tau_3\rho_3-\rho_1)G_{pm}^{-}e^{-i\beta_{1p}b}\\
&+\frac{1}{2i\sin(\beta_{1p}L)}\Big(2\rho_1 G_{pm}^{+}e^{i\beta_{1p}a}+(\tau_3\rho_3-\rho_1)\\
&\times G_{pm}^{-}e^{i\beta_{1p}(a-2b)}-(\tau_3\rho_3+\rho_1)G_{pm}^{-}e^{-i\beta_{1p}a}\Big)\Big],
\end{aligned}
\tag{B.15}
$$

$$
\begin{aligned}
V_{mp}^{ee} =&(\tau_0-1)\Big[-(\tau_0-1)(\tau_3-1)^2(\alpha_p k_y)^2G_{pm}^{-}e^{-i\beta_{1p}b}\\
&+\frac{1}{2i\sin(\beta_{1p}L)}\Big((\tau_3\rho_3+\rho_1)(\tau_3\eta_3-\eta_1)(\tau_0-1)\\
&\times G_{pm}^{-}e^{-i\beta_{1p}a}+2\rho_1(\tau_0\eta_0-\eta_1)(\tau_3-1)G_{pm}^{+}e^{i\beta_{1p}a}\\
&-(\tau_3\rho_3-\rho_1)(\tau_3\eta_3-\eta_1)(\tau_0-1)G_{pm}^{-}e^{i\beta_{1p}(a-2b)}\Big)\Big],
\end{aligned}
\tag{B.16}
$$

$$
\begin{aligned}
U_{mp}^{hh} =&(\tau_3-1)\Big[-(\tau_0-1)^2(\tau_3-1)(\alpha_p k_y)^2G_{pm}^{+}e^{i\beta_{1p}a}\\
&+\frac{1}{2i\sin(\beta_{1p}L)}\Big((\tau_0\rho_0-\rho_1)(\tau_0\eta_0+\eta_1)(\tau_3-1)\\
&\times G_{pm}^{+}e^{i\beta_{1p}b}+2\eta_1(\tau_3\rho_3-\rho_1)(\tau_0-1)G_{pm}^{-}e^{-i\beta_{1p}b}\\
&-(\tau_0\eta_0-\eta_1)(\tau_0\rho_0-\rho_1)(\tau_3-1)G_{pm}^{+}e^{i\beta_{1p}(2a-b)}\Big)\Big],
\end{aligned}
\tag{B.17}
$$

$$
\begin{aligned}
U_{mp}^{he} =&(\alpha_p k_y)(\tau_3-1)^2(\tau_0-1)\Big[-(\tau_0\eta_0-\eta_1)G_{pm}^{+}e^{i\beta_{1p}a}\\
&+\frac{1}{2i\sin(\beta_{1p}L)}\Big(2\eta_1 G_{pm}^{-}e^{-i\beta_{1p}b}-(\tau_0\eta_0+\eta_1)\\
&\times G_{pm}^{+}e^{i\beta_{1p}b}+(\tau_0\eta_0-\eta_1)G_{pm}^{+}e^{i\beta_{1p}(2a-b)}\Big)\Big],
\end{aligned}
\tag{B.18}
$$

$$
\begin{aligned}
U_{p}^{hi} =&(\tau_3-1)^2\Big[2\tau_0\eta_0(\tau_0-1)\alpha_p k_y E_y^{\mathrm{inc}}\delta_{0p}\\
&+\frac{2\tau_0\rho_0\left(i\tau_0\eta_0\sin(\beta_{1p}L)-\eta_1\cos(\beta_{1p}L)\right)}{i\sin(\beta_{1p}L)}K_y^{\mathrm{inc}}\delta_{0p}\Big],
\end{aligned}
\tag{B.19}
$$

$$
\begin{aligned}
V_{mp}^{hh} =&(\tau_0-1)\Big[-G_{pm}^{-}e^{-i\beta_{1p}b}(\alpha_p k_y)^2(\tau_3-1)^2(\tau_0-1)\\
&+\frac{1}{2i\sin(\beta_{1p}L)}\Big((\tau_3\eta_3+\eta_1)(\tau_3\rho_3-\rho_1)(\tau_0-1)\\
&\times G_{pm}^{-}e^{-i\beta_{1p}a}+2\eta_1(\tau_0\rho_0-\rho_1)(\tau_3-1)G_{pm}^{+}e^{i\beta_{1p}a}\\
&-(\tau_3\eta_3-\eta_1)(\tau_3\rho_3-\rho_1)(\tau_0-1)G_{pm}^{-}e^{i\beta_{1p}(a-2b)}\Big)\Big], \qquad \text{(B.20)}\\
V_{mp}^{he} =&\alpha_p k_y(\tau_0-1)^2(\tau_3-1)\Big[(\tau_3\eta_3-\eta_1)G_{pm}^{-}e^{-i\beta_{1p}b}\\
&+\frac{1}{2i\sin(\beta_{1p}L)}\Big((\tau_3\eta_3+\eta_1)G_{pm}^{-}e^{-i\beta_{1p}a}\\
&-(\tau_3\eta_3-\eta_1)G_{pm}^{-}e^{i\beta_{1p}(a-2b)}-2\eta_1 G_{pm}^{+}e^{i\beta_{1p}a}\Big)\Big], \qquad \text{(B.21)}\\
V_{p}^{hi} =&-\frac{2\tau_0\rho_0\eta_1(\tau_3-1)(\tau_0-1)K_y^{\mathrm{inc}}\delta_{0p}}{i\sin(\beta_{1p}(a-b))}. \qquad \text{(B.22)}
\end{aligned}
$$

Once the $B_m^{\{e,h\}}$ are obtained with the Rayleigh identity, $f_{\{e,h\},p}^{+}$ and $g_{\{e,h\},p}^{-}$ can be calculated with equations (B.4), then $R_p^{\{e,h\}}$ and $T_p^{\{e,h\}}$ follow from equation (B.1).

Appendix C

Homogenization of a single layer fiber-based composite

The analytical model of one single-layer composite reinforced by a periodic array of circular fibers has been given in Chapter 2 and Chapter 3. Here, an approximate model will be presented, in which the fiber-reinforced slab will be replaced by its uniaxially anisotropic counterpart with an effective permittivity tensor. But under illumination of a TE or TM wave, only a scalar effective permittivity is needed. The tensor of effective permittivity for the slab illuminated by conically incident plane wave is produced by properly combining the scalar effective permittivity for the TM and TE cases. In order to verify the efficacy and accuracy of the homogenized model, several numerical results have been given in section 2.4 for single-layer composite and section 4.8 for multilayered composite.

Preliminary formulation

In anisotropic homogeneous media, Maxwell equations for time-harmonic fields are

$$\nabla \times \boldsymbol{\mathcal{E}} = i\omega\mu\boldsymbol{\mathcal{H}}, \tag{C.1a}$$

$$\nabla \times \boldsymbol{\mathcal{H}} = -i\omega\epsilon\boldsymbol{\mathcal{E}}, \tag{C.1b}$$

where $\boldsymbol{\mathcal{E}}$ and $\boldsymbol{\mathcal{H}}$ are electric and magnetic fields. $\boldsymbol{\mathcal{E}} = E_x\vec{x} + E_y\vec{y} + E_z\vec{z}$, and $\boldsymbol{\mathcal{H}} = H_x\vec{x} + H_y\vec{y} + H_z\vec{z}$. μ is permeability where $\mu = \mu_0$, μ_0 the permeability of free space. ϵ is the permittivity of the material, $\epsilon = \epsilon_r\epsilon_0$. In our case, ϵ_r varies with x and z, writing as $\epsilon_r(x,z)$. Assuming the plane of incidence to be parallel with the x-z plane and letting $k_0 = \omega\sqrt{\epsilon_0\mu_0}$, the Maxwell equations are written into

$$(\nabla^2 + k_0^2\epsilon_r)E_y = 0, \tag{C.2a}$$

$$\frac{\partial}{\partial x}(\frac{1}{\epsilon_r}\frac{\partial H_y}{\partial x})+\frac{\partial}{\partial z}(\frac{1}{\epsilon_r}\frac{\partial H_y}{\partial z})+k_0^2 H_y=0. \tag{C.2b}$$

With these two wave equations, the periodic composite can be homogenized at a low enough frequency, meaning that the composite is replaced by a homogeneous slab which has an effective permittivity $\bar{\epsilon}_r$ for the E-polarized incident wave (TM) case and the H-polarized incident wave (TE) case. TE and TM cases can be investigated individually with equation (C.2a) and (C.2b).

Assuming that the frequency ω of the incident wave is such that $\lambda=\frac{2\pi c_0}{\omega}\gg d$ with c_0 the speed of light, the wavenumber of the incident wave defined as $k_0=\omega/c_0$ should satisfy $k_0\ll 1$. In order to obtain the effective permittivities for TE and TM waves, one takes $E_y(x,z)=\tilde{E}_y(x,z,\tilde{x},\tilde{z})$ and $H_y(x,z)=\tilde{H}_y(x,z,\tilde{x},\tilde{z})$, where $\tilde{x}=k_0x$ and $\tilde{z}=k_0z$. Then, operations ∇ and ∇^2 become

$$\nabla=\nabla_{x,z}+k_0\nabla_{\tilde{x},\tilde{z}}, \tag{C.3a}$$

$$\nabla^2=\nabla^2_{x,z}+k_0^2\nabla^2_{\tilde{x},\tilde{z}}+k_0(\nabla_{x,z}\cdot\nabla_{\tilde{x},\tilde{z}}+\nabla_{\tilde{x},\tilde{z}}\cdot\nabla_{x,z}). \tag{C.3b}$$

Here, $\nabla_{x,z}=\frac{\partial}{\partial x}\vec{x}+\frac{\partial}{\partial z}\vec{z}$, and $\nabla^2_{x,z}=\frac{\partial^2}{\partial x^2}+\frac{\partial^2}{\partial z^2}$. $\nabla_{\tilde{x},\tilde{z}}$ and $\nabla^2_{\tilde{x},\tilde{z}}$ have similar definitions but the operations are on variables $\tilde{x}$ and $\tilde{z}$. The decomposition of the two operators is then reformed to rewrite equations (C.2) for both TM and TE waves.

Homogenization for incident TM wave

Considering an E-polarized wave and applying (C.3b) to equation (C.2a) produces

$$\frac{1}{k_0^2}\nabla^2_{x,z}\tilde{E}_y+\frac{1}{k_0}(\nabla_{x,z}\cdot\nabla_{\tilde{x},\tilde{z}}+\nabla_{\tilde{x},\tilde{z}}\cdot\nabla_{x,z})\tilde{E}_y+\nabla^2_{\tilde{x},\tilde{z}}\tilde{E}_y+\epsilon_r\tilde{E}_y=0. \tag{C.4}$$

The electric field $\tilde{E}_y$ is then expanded as

$$\tilde{E}_y=\tilde{E}_{0y}+k_0\tilde{E}_{1y}+k_0^2\tilde{E}_{2y}+\cdots. \tag{C.5}$$

Since k_0 has been assumed small enough, the higher the order the terms, the less influence expected on $\tilde{E}_y$. Here, the first three terms are considered and the resulting expansion is substituted into equation (C.4). Then collecting the terms in which k_0 is of the same integer

power yields

$$\begin{aligned}&\frac{1}{k_0^2}\nabla_{x,z}^2\tilde{E}_{0y}+\frac{1}{k_0}\left[\nabla_{x,z}^2\tilde{E}_{1y}+(\nabla_{x,z}\cdot\nabla_{\tilde{x},\tilde{z}}+\nabla_{\tilde{x},\tilde{z}}\cdot\nabla_{x,z})\tilde{E}_{0y}\right]\\&+\nabla_{x,z}^2\tilde{E}_{2y}+(\nabla_{x,z}\cdot\nabla_{\tilde{x},\tilde{z}}+\nabla_{\tilde{x},\tilde{z}}\cdot\nabla_{x,z})\tilde{E}_{1y}+\nabla_{\tilde{x},\tilde{z}}^2\tilde{E}_{0y}+\epsilon_r\tilde{E}_{0y}=0\end{aligned}\tag{C.6}$$

Setting the terms at each integer power of k_0 equal to zero produces

$$\nabla_{x,z}^2\tilde{E}_{0y}=0,\tag{C.7a}$$

$$\nabla_{x,z}^2\tilde{E}_{1y}+(\nabla_{x,z}\cdot\nabla_{\tilde{x},\tilde{z}}+\nabla_{\tilde{x},\tilde{z}}\cdot\nabla_{x,z})\tilde{E}_{0y}=0,\tag{C.7b}$$

$$\nabla_{x,z}^2\tilde{E}_{2y}+(\nabla_{x,z}\cdot\nabla_{\tilde{x},\tilde{z}}+\nabla_{\tilde{x},\tilde{z}}\cdot\nabla_{x,z})\tilde{E}_{1y}+\nabla_{\tilde{x},\tilde{z}}^2\tilde{E}_{0y}+\epsilon_r\tilde{E}_{0y}=0\tag{C.7c}$$

Because of the periodicity of the structure, the field $\tilde{E}_{0y}$ can be expanded as

$$\tilde{E}_{0y}=\sum_{p\in\mathbb{Z}}C_p(z)e^{i\alpha_p x}\tag{C.8}$$

where $\alpha_p=k_0\sin\theta_i+2\pi p/d$. Substituting equation (C.8) into (C.7a) produces

$$\frac{d^2C_p}{dz^2}-\alpha_p^2C_p=0\tag{C.9}$$

If $p\neq 0$, $C_p(z)=a_1e^{\alpha_p z}+a_2$ where a_1 and a_2 are all constant. If $a_1\neq 0$, there are only outgoing waves existing in both regions $z>0$ and $z<0$, which is not true, so $C_p=a_2$. Substituting it into equation (C.9), one gets that $a_2=0$, so $C_p=0$. If $p=0$, C_0 is constant. So equation (C.7b) becomes

$$\nabla_{x,z}^2\tilde{E}_{1y}=0,\tag{C.10}$$

which has the same solution as (C.7a). Simplifying the equation (C.7c) produces

$$\nabla_{x,z}^2\tilde{E}_{2y}+\nabla_{\tilde{x},\tilde{z}}^2\tilde{E}_{0y}+\epsilon_r\tilde{E}_{0y}=0.\tag{C.11}$$

Expanding the field $\tilde{E}_{2y}$ as

$$\tilde{E}_{2y}=\sum_{p\in\mathbb{Z}}C_p(z)e^{i\alpha_p x},\tag{C.12}$$

with which equation (C.11) is written as

$$\frac{d^2C_p}{dz^2}-\alpha_p^2C_p+\nabla_{\tilde{x},\tilde{z}}^2\tilde{E}_{0y}+\epsilon_r(x,z)\tilde{E}_{0y}=0.\tag{C.13}$$

If $p \neq 0$, this equation has a solution $C_p = a_1 e^{\alpha_p z} + f$, where f is a particular solution of (C.13). If $a_1 \neq 0$, the field in space $z > 0$ is infinite and in $z < 0$ is evanescent. If $p = 0$, (C.13) becomes

$$\frac{d^2 C_0}{dz^2} + \nabla^2_{\tilde{x},\tilde{z}} \tilde{E}_{0y} + \epsilon_r(x,z)\tilde{E}_{0y} = 0. \tag{C.14}$$

Here, we have a solution of $C_0 = a_1 z^2 + a_2 z + a_3$. If $a_1 \neq 0$ and $a_2 \neq 0$, the field is infinite when $z = \infty$, so C_0 is constant. Then equation (C.14) becomes

$$\nabla^2_{\tilde{x},\tilde{z}} \tilde{E}_{0y} + \epsilon_r(x,z)\tilde{E}_{0y} = 0. \tag{C.15}$$

Integrating on both sides of (C.15), the left-hand side can be written as

$$\begin{aligned} &\int_{-d/2}^{d/2} \int_b^a (\nabla^2_{\tilde{x},\tilde{z}} \tilde{E}_{0y} + \epsilon_r(x,z)\tilde{E}_{0y}) dx dz \\ =&\nabla^2_{\tilde{x},\tilde{z}} \tilde{E}_{0y} + \int_{-d/2}^{d/2} \int_b^a \epsilon_r(x,z) dx dz \tilde{E}_{0y} \\ =&\nabla^2_{\tilde{x},\tilde{z}} \tilde{E}_{0y} + \bar{\epsilon}_r \tilde{E}_{0y} \end{aligned} \tag{C.16}$$

Here, $\bar{\epsilon}_r$ is

$$\bar{\epsilon}_r = \int_{-d/2}^{d/2} \int_b^a \epsilon_r(x,z) dx dz = \frac{\epsilon_{r1} S_1 + \epsilon_{r2} S_2}{S_1 + S_2}. \tag{C.17}$$

Finally, a Helmholtz wave equation follows as

$$\nabla^2_{\tilde{x},\tilde{z}} \tilde{E}_{0y} + \bar{\epsilon}_r \tilde{E}_{0y} = 0. \tag{C.18}$$

Since $\frac{\partial \tilde{E}_{0y}}{\partial \tilde{x}} = \frac{1}{k_0} \frac{\partial \tilde{E}_{0y}}{\partial x}$, equation (C.18) can be written as

$$\nabla^2_{x,z} \tilde{E}_{0y} + \bar{\epsilon}_r k_0^2 \tilde{E}_{0y} = 0,$$

which indicates that $\bar{\epsilon}_r$ is the effective permittivity with which the scattering of a low frequency TM wave by the periodic composite is assimilated with the one of a homogeneous plate with permittivity $\bar{\epsilon}_r$.

Homogenization for incident TE wave

For the homogenization of the structure with an H-polarized incident wave, equation (C.2b) is needed. Allowing $\epsilon_r^{-1}(x,z) = 1/\epsilon_r(x,z)$, equation (C.2b) is expressed as

$$\frac{\partial}{\partial x}\left(\epsilon_r^{-1}(x,z)\frac{\partial H_y}{\partial x}\right) + \frac{\partial}{\partial z}\left(\epsilon_r^{-1}(x,z)\frac{\partial H_y}{\partial z}\right) + k_0^2 H_y = 0. \tag{C.19}$$

It can be expanded as

$$\epsilon_r^{-1}\frac{\partial^2 H_y}{\partial x^2} + \epsilon_r^{-1}\frac{\partial^2 H_y}{\partial z^2} + \frac{\partial H_y}{\partial x}\frac{\partial \epsilon_r^{-1}}{\partial x} + \frac{\partial H_y}{\partial z}\frac{\partial \epsilon_r^{-1}}{\partial z} + k_0^2 H_y = 0. \tag{C.20}$$

Noticing that $\epsilon_r^{-1}(x,z)$ in region R_1 and R_2 are all constant, so the derivative of $\epsilon_r^{-1}(x,z)$ with respect to x or z equals zero. Now, equation (C.20) can be simplified as

$$\epsilon_r^{-1}\nabla^2 H_y + k_0^2 H_y = 0. \tag{C.21}$$

Letting $H_y(x,z) = \tilde{H}_y(x,z,\tilde{x},\tilde{z})$, and expanding the magnetic field as

$$\tilde{H}_y = \tilde{H}_{0y} + k_0\tilde{H}_{1y} + k_0^2\tilde{H}_{2y} + \cdots. \tag{C.22}$$

Then, following the same treatment for TM wave, it can be proven that

$$\epsilon_r^{-1}\nabla^2_{\tilde{x},\tilde{z}}\tilde{H}_{0y} + \tilde{H}_{0y} = 0. \tag{C.23}$$

Integrating on both sides yields

$$\frac{1}{\bar{\epsilon}_r} = \frac{S_1/\epsilon_{r1} + S_2/\epsilon_{r2}}{S_1 + S_2} \tag{C.24}$$

So the effective permittivity for the TE case is defined as

$$\bar{\epsilon}_r = \frac{S_1 + S_2}{S_1/\epsilon_{r1} + S_2/\epsilon_{r2}} \tag{C.25}$$

Appendix D

Reordering matrix $\mathcal{U}$

D.1 Reordering matrix for 2-layer stack

Assuming that $Q_{total} = Q_{\max} - Q_{\min} + 1$ and $P_{total} = P_{\max} - P_{\min} + 1$, where $P_{\max}$, $P_{\min}$, $Q_{\max}$ and $Q_{\min}$ are defined in section 5.8. Q_{total} and P_{total} are the total number of the modes for truncating the infinite sums corresponding to q and p, then the elements of $\bar{\mathbf{f}}_l^{\pm}$ and $\bar{\mathbf{g}}_l^{\pm}$ can be reordered with a reordering matrix $\mathcal{U}$ which can be produced according to the following algorithm, vec is a zero vector with $P_{total} \times Q_{total}$ elements. Matrix mat is initially empty.

Algorithm 1 Producing matrix for reordering $\bar{\mathbf{f}}_l^{\pm}$ and $\bar{\mathbf{g}}_l^{\pm}$

for $q = 1$ **to** Q_{total} **do**
  $counter\_q \leftarrow q$
  $indicator\_var \leftarrow 1$
  while $indicator\_var \leq 2$ **do**
    $position \leftarrow counter\_q$
    while $position \leq 2 \times P_{total} \times Q_{total}$ **do**
      $tmp\_vec(position) \leftarrow vec$
      $mat \leftarrow vertically\_concatenate(mat, tmp\_vec)$
      $position \leftarrow position + 2 \times Q_{total}$
    end while
    $counter\_q \leftarrow counter\_q + Q_{total}$
    $indicator\_var \leftarrow indicator\_var + 1$
  end while
end for

D.2 Reordering matrix for 4-layer stack

The sequence which is used to indicate the order of the field expansion coefficients of the second layer is defined as $s_2 = (q, p, u, v)$. Hence, for every pair of (u, v), there is a complete set of combinations of (q, p). Here, the complete set indicates the combinations produced with different values of q and p, and q varies faster than p. Hence, for a specific pair of (u, v), the complete set of (q, p) is the same as the one for the second layer of the 2-layer stack. The expansion coefficients indexed by this set of combinations need to be rearranged into the order defined by (p, q). Hence, the reordering matrix for the second layer of the 4-layer stack is calculated with the following procedure: 1) calculating the reordering matrix for a complete set of (q, p) with the algorithm 1; 2) treat the obtained matrix as a block and put $U_{total} \times V_{total}$ of them into one larger matrix with all the blocks standing along the diagonal line. The produced larger matrix is then the needed reordering matrix for the second layer of the structure.

For the third layer, the sequence is defined as $s_3 = (u, q, p, v)$ which shows that the order of the coefficients indexed by (u, q, p) needs to be changed into the order defined by (p, q, u), for each value of v. Hence, a matrix for ordering the coefficients indexed by (u, q, p) is calculated first, then the matrix is treated as a block, and V_{total} of them are put into a larger matrix within which these blocks stand on the diagonal line. The algorithm for reordering (u, q, p) is given in Algorithm 2. $U_{total} = U_{max} - U_{min} + 1$, and $V_{total} = V_{max} - V_{min} + 1$. tmp_vec is a vector with $2 \times P_{total} \times Q_{total} \times U_{total} \times V_{total}$ elements equal to zero.

For the fourth layer, the coefficients indexed by $s_4 = (v, q, u, p)$ need to be reordered into the order defined by $s_1 = (p, q, u, v)$. The reordering matrix is produced with the algorithm shown in 3.

These algorithms can be easily implemented. To verify them, a simple code is written to produce the sequences of $s_1 = (p, q, u, v)$, $s_2 = (q, p, u, v)$, $s_3 = (u, q, p, v)$ and $s_4 = (v, q, u, p)$. Then the sequences s_2, s_3 and s_4 are transformed with the corresponding reordering matrices. The resulting sequences should have the same order of s_1.

Algorithm 2 Reordering matrix for the coefficients of the third layer

for $u = 1$ **to** U_{total} **do**
  $position = u$
  for $q = 1$ **to** Q_{total} **do**
    $position = position + (q-1) \times U_{total} \times 2$
    $indicator\_var \leftarrow 1$
    while $indicator\_var \leq 2$ **do**
      $current\_position \leftarrow position$
      while $current\_position \leq 2 \times P_{total} \times Q_{total} \times U_{total}$ **do**
        $vec(current\_position) \leftarrow 1$
        $reorder\_matrix \leftarrow vertically\_concatenate(reorder\_matrix, vec)$
        $current\_position \leftarrow current\_position + 2 \times Q_{total} \times U_{total}$
        $vec \leftarrow tmp\_vec$
      end while
      $position \leftarrow position + U_{total}$
      $indicator\_var \leftarrow indicator\_var + 1$
    end while
  end for
end for

Algorithm 3 Reordering matrix for the coefficients of the fourth layer

for $v = 1$ **to** V_{total} **do**
  $position = v$
  for $u = 1$ **to** U_{total} **do**
    $position = position + (u-1) \times Q_{total} \times V_{total} \times 2$
    for $q = 1$ **to** Q_{total} **do**
      $position = position + (q-1) \times V_{total} \times 2$
      $indicator\_var \leftarrow 1$
      while $indicator\_var \leq 2$ **do**
        $current\_position \leftarrow position$
        while $current\_position \leq 2 \times P_{total} \times Q_{total} \times U_{total}$ **do**
          $vec(current\_position) \leftarrow 1$
          $reorder\_matrix \leftarrow vertically\_concatenate(reorder\_matrix, vec)$
          $current\_position \leftarrow current\_position + 2 \times Q_{total} \times U_{total} \times V_{total}$
          $vec \leftarrow tmp\_vec$
        end while
        $position \leftarrow position + V_{total}$
        $indicator\_var \leftarrow indicator\_var + 1$
      end while
    end for
  end for
end for

References

[1] C. M. Linton, "Schlömilch series that arise in diffraction theory and their efficient computation," *Journal of Physics A: Mathematical and General*, vol. 39, pp. 25 – 33, 2006.

[2] H. Roussel, W. Chew, F. Jouvie, and W. Tabbara, "Electromagnetic scattering from dielectric and magnetic gratings of fibers - a T-matrix solution," *Journal of Electromagnetic Waves and Applications*, vol. 10, pp. 109–127, 1996.

[3] K. Yasumoto and H. Jia, Modeling of Photonic Crystals by Multilayered Periodic Arrays of Circular Cylinders, Chapter 3 of *Electromagnetic Theory and Applications for Photonic Crystals*. Optical Science and Engineering, Taylor & Francis, 2010.

[4] K. B. Dossou and L. C. Botten, "A combined three-dimensional finite element and scattering matrix method for the analysis of plane wave diffraction by bi-periodic, multilayered structures," *Journal of Computational Physics*, vol. 231, pp. 6969 – 6989, 2012.

[5] C. Alexander, C. Key, and S. Schumacher, "Dynamic response and modeling of a carbon fiber-epoxy composite subject to shock loading," *Journal of Applied Physics*, vol. 114, pp. 1 – 10, 2013.

[6] A. Lukyanov, "Modeling the effect of orientation on the shock response of a damageable composite material," *Journal of Applied Physics*, vol. 112, pp. 9081–9087, 2012.

[7] E. Nesvijski, "Some aspects of ultrasonic testing of composites," *Composite Structures*, vol. 48, pp. 151 – 155, 2000.

[8] S. Mechraoui, A. Laksimi, and S. Benmedakhene, "Reliability of damage mechanism localisation by acoustic emission on glass/epoxy composite material plate," *Composite Structures*, vol. 94, pp. 1483 – 1494, 2012.

[9] L. Taupin, A. Lhémery, and G. Inquiété, "A detailed study of guided wave propagation in a viscoelastic multilayered anisotropic plate," *Journal of Physics: Conference Series*, vol. 269, pp. 1 – 14, 2011.

[10] V. Vavilov, "Modeling and characterizing impact damage in carbon fiber composites by thermal/infrared non-destructive testing," *Composites Part B: Engineering*, vol. 61, pp. 1 – 10, 2014.

[11] H. Heuer, M. Schulze, M. Pooch, S. Gäbler, A. Nocke, G. Bardl, C. Cherif, M. Klein, R. Kupke, R. Vetter, F. Lenz, M. Kliem, C. Bülow, J. Goyvaerts, T. Mayer, and S. Petrenz, "Review on quality assurance along the CFRP value chain – non-destructive testing of fabrics, preforms and CFRP by HF radio wave techniques," *Composites Part B: Engineering*, vol. 77, pp. 494 – 501, 2015.

[12] G. Angelis, M. Meo, D. Almond, S. Pickering, and S. Angioni, "A new technique to detect defect size and depth in composite structures using digital shearography and unconstrained optimization," *NDT-E International*, vol. 45, pp. 91 – 96, 2012.

[13] X. Yin and D. Hutchins, "Non-destructive evaluation of composite materials using a capacitive imaging technique," *Composites Part B: Engineering*, vol. 43, pp. 1282 – 1292, 2012.

[14] L. Cheng and G. Y. Tian, "Pulsed electromagnetic NDE for defect detection and characterisation in composites," in *2012 IEEE International Instrumentation and Measurement Technology Conference (I2MTC)*, pp. 1902 – 1907, 2012.

[15] A. S. B. Sediq and N. Qaddoumi, "Near-field microwave image formation of defective composites utilizing open-ended waveguides with arbitrary cross sections," *Composite Structures*, vol. 71, pp. 343 – 348, 2005.

[16] Y.-H. Teo, X. Wang, and W.-K. Chiu, "Simulations of microwave propagation in delaminated unidirectional glass–epoxy laminate," *Composite Structures*, vol. 75, pp. 422 – 427, 2006.

[17] S. Datta, C. T. Chan, K. M. Ho, and C. M. Soukoulis, "Effective dielectric constant of periodic composite structures," *Physical Review B*, vol. 48, pp. 14936 – 14943, 1993.

[18] M.-S. Lin and C. H. Chen, "Plane-wave shielding characteristics of anisotropic laminated composites," *IEEE Transactions on Electromagnetic Compatibility*, vol. 35, pp. 21 – 27, Feb 1993.

[19] C. Holloway, M. Sarto, and M. Johansson, "Analyzing carbon-fiber composite materials with equivalent-layer models," *IEEE Transactions on Electromagnetic Compatibility*, vol. 47, pp. 833 – 844, 2005.

[20] A. Kader, M. Klingler, T. Dubois, G. Duchamp, G. Ruffie, and F. Bonnaudin, "Surface equivalent modeling of layered composite material," in *2013 International Symposium on Electromagnetic Compatibility (EMC EUROPE)*, pp. 573–578, 2013.

[21] Y. Zhong, M. Lambert, D. Lesselier, and X. Chen, "Electromagnetic response of anisotropic laminates to distributed sources," *IEEE Transactions on Antennas and Propagation*, vol. 62, pp. 247–256, 2014.

[22] B. Delourme, H. Haddar, and P. Joly, "On the well-posedness , stability and accuracy of an asymptotic model for thin periodic interfaces in electromagnetic scattering problems," *Mathematical Models and Methods in Applied Sciences*, vol. 23, p. 2433, 2013.

[23] S. Fliss and P. Joly, "Solutions of the time-harmonic wave equation in periodic waveguides : asymptotic behaviour and radiation condition," *Archive for Rational Mechanics and Analysis,* early access, 2015.

[24] H.-C. Chu, S.-K. Jeng, and C. H. Chen, "Reflection and transmission characteristics of lossy periodic composite structures," *IEEE Transactions on Antennas and Propagation*, vol. 44, pp. 580 – 587, 1996.

[25] C. Chu, S. Jeng, and C. Chen, "Reflection and transmission characteristics of single-layer periodic composite structures for TE case," *IEEE Transactions on Antennas and Propagation*, vol. 45, pp. 1065 – 1070, 1997.

[26] Z. Peng, K.-H. Lim, and J.-F. Lee, "Computations of electromagnetic wave scattering from penetrable composite targets using a surface integral equation method with multiple traces," *IEEE Transactions on Antennas and Propagation*, vol. 61, pp. 256–270, 2013.

[27] F. I. Baida and A. Belkhir, Finite Difference Time Domain Method for Grating Structures*, Chapter 9 of Gratings: Theory and Numeric Applications*. AMU (PUP): Marseille, 2012.

[28] G. Demésy, F. Zolla, A. Nicolet, and B. Vial, Finite Element Method*, Chapter 5 of Gratings: Theory and Numeric Applications*. AMU (PUP): Marseille, 2012.

[29] J. Wang, B. Zhou, B. Chen, and L. Shi, "3D weakly conditionally stable FDTD method for analyzing periodic structures," *IEEE Transactions on Antennas and Propagation*, vol. 61, pp. 3917–3921, 2013.

[30] J. Wang, B. Zhou, L. Shi, and B. Chen, "Efficiency-improved LOD-FDTD method for solving periodic structures at oblique incidence," *IEEE Microwave and Wireless Components Letters*, vol. 23, pp. 521–523, 2013.

[31] D. C. Dobson, J. Gopalakrishnan, and J. E. Pasciak, "An efficient method for band structure calculations in 3D photonic crystals," *Journal of Computational Physics*, vol. 161, pp. 668 – 679, 2000.

[32] S. Guenneau, A. Nicolet, and C. Geuzaine, "Comparisons of finite element and Rayleigh methods for the study of conical Bloch waves in arrays of metallic cylinders," *The International Journal for Computation and Mathematics in Electrical and Electronic Engineering (COMPEL)*, vol. 23, pp. 932 – 949, 2004.

[33] J. Rayleigh, *The Theory of Sound*. New York: MacMillan, 1877.

[34] B. Munk and G. Burrell, "Plane-wave expansion for arrays of arbitrarily oriented piecewise linear elements and its application in determining the impedance of a single linear antenna in a lossy half-space," *IEEE Transactions on Antennas and Propagation*, vol. 27, pp. 331–343, 1979.

[35] J.-J. Greffet, "Scattering of electromagnetic waves by rough dielectric surfaces," *Physical Review B*, vol. 37, pp. 6436–6441, 1988.

[36] L. C. Botten, N.-A. P. Nicorovici, A. A. Asatryan, R. C. McPhedran, C. M. de Sterke, and P. A. Robinson, "Formulation for electromagnetic scattering and propagation through grating stacks of metallic and dielectric cylinders for photonic crystal calculations. Part I. Method," *Journal of the Optical Society of America A*, vol. 17, pp. 2165 – 2176, 2000.

[37] S. Wilcox, L. C. Botten, and R. C. McPhedran, "Modeling of defect modes in photonic crystals using the fictitious source superposition method," *Physical Review E*, vol. 71, pp. 056606–1 – 056606–11, 2005.

[38] G. H. Smith, L. C. Botten, R. C. McPhedran, and N. A. Nicorovici, "Cylinder gratings in conical incidence with applications to woodpile structures," *Physical Review E*, vol. 67, p. 056620, May 2003.

[39] Y. Wu and Y. Y. Lu, "Dirichlet-to-Neumann map method for analyzing crossed arrays of circular cylinders," *Journal of the Optical Society of America B*, vol. 26, pp. 1984–1993, Nov 2009.

[40] J.-P. Groby, A. Wirgin, L. Ryck, W. Lauriks, R. Gilbert, and Y. Xu, "Acoustic response of a rigid-frame porous medium plate with a periodic set of inclusions," *The Journal of the Acoustical Society of America*, vol. 126, pp. 685 – 693, 2009.

[41] V. Romero-García, C. Lagarrigue, J.-P. Groby, O. Richoux, and V. Tournat, "Tunable acoustic waveguides in periodic arrays made of rigid square-rod scatterers: theory and experimental realization," *Journal of Physics D: Applied Physics*, vol. 46, p. 305108, 2013.

[42] S. Guenneau, C. Poulton, and A. Movchan, "Oblique propagation of electromagnetic and elastic waves for an array of cylindrical fibres," *Proceedings of the Royal Society A.*, vol. 459, pp. 2215 – 2263, 2003.

[43] J.-P. Groby and D. Lesselier, "Localization and characterization of simple defects in finite-sized photonic crystals," *Journal of the Optical Society of America A*, vol. 25, pp. 146 – 152, 2008.

[44] V. Twersky, "Elementary function representations of Schlömilch series," *Archive for Rational Mechanics and Analysis*, vol. 8, pp. 323–332, 1961.

[45] V. Twersky, "On scattering of waves by the infinite grating of circular cylinders," *IRE Transactions on Antennas and Propagation*, vol. 10, pp. 737 – 765, 1962.

[46] C. A. Balanis, *Advanced Engineering Electromagnetics*. Wiley: New York, 2nd ed., 2012.

[47] W. C. Chew, *Waves and Fields in Inhomogenous Media*. Wiley: New York, 1999.

[48] K. Yasumoto and K. Yoshitomi, "Efficient calculation of lattice sums for free-space periodic green's function," *IEEE Transactions on Antennas and Propagation*, vol. 47, pp. 1050 – 1055, 1999.

[49] N. A. Nicorovici and R. C. McPhedran, "Lattice sums for off-axis electromagnetic scattering by gratings," *Physical Review E*, vol. 50, pp. 3143 – 3160, 1994.

[50] A. Moroz, "Exponentially convergent lattice sums," *Optics Letters*, vol. 26, pp. 1119 – 1121, 2001.

[51] O. Kavaklioglu, "On Schlömilch series representation for the transverse electric multiple scattering by an infinite grating of insulating dielectric circular cylinders at oblique incidence," *Journal of Physics A: Mathematical and General*, vol. 35, pp. 22 – 29, 2002.

[52] C. Linton, "The Green's function for the two-dimensional Helmholtz equation in periodic domains," *Journal of Engineering Mathematics*, vol. 33, pp. 377 – 401, 1998.

[53] T. Kushta and K. Yasumoto, "Electromagnetic scattering from periodic array of two circular cylinders per unit cell," *Progress in Electromagnetics Research*, vol. 29, pp. 69 – 85, 2000.

[54] M. Antunes, M. Mudarra, and J. I. Velasco, "Broad-band electrical conductivity of carbon nanofibre-reinforced polypropylene foams," *Carbon*, vol. 49, pp. 708 – 717, 2011.

[55] M. Hotta, M. Hayashi, M. T. Lanagan, D. K. Agrawal, and K. Nagata, "Complex permittivity of graphite, carbon black and coal powders in the ranges of X-band frequencies (8.2 to 12.4 GHz) and between 1 and 10 GHz," *ISIJ International*, vol. 51, pp. 1766 – 1772, 2011.

[56] A. Galehdar, K. Nicholson, W. S. T. Rowe, and K. Ghorbani, "The conductivity of unidirectional and quasi isotropic carbon fiber composites," in *Microwave Conference (EuMC), 2010 European*, pp. 882–885, 2010.

[57] X. Luo and D. Chung, "Carbon-fiber/polymer-matrix composites as capacitors," *Composites Science and Technology*, vol. 61, pp. 885 – 888, 2001.

[58] Y. J. Kim, T. S. Shin, H. D. Choi, J. H. Kwon, Y.-C. Chung, and H. G. Yoon, "Electrical conductivity of chemically modified multiwalled carbon nanotube/epoxy composites," *Carbon*, vol. 43, pp. 23 – 30, 2005.

[59] J. W. Goodman, *Introduction to Fourier Optics*. McGraw-Hill: New York, 1968.

[60] E. E. Kriezis, P. K. Pandelakis, and A. G. Papagiannakis, "Diffraction of a gaussian beam from a periodic planar screen," *Journal of the Optical Society of America A*, vol. 11, no. 2, pp. 630 – 636, 1994.

[61] J. Yang, L.-W. Li, K. Yasumoto, and C.-H. Liang, "Two-dimensional scattering of a gaussian beam by a periodic array of circular cylinders," *IEEE Transactions on Geoscience and Remote Sensing*, vol. 43, pp. 280–285, 2005.

[62] J. Kong, *Electromagnetic Wave Theory*. EMW Pub: Chicago, 2000.

[63] A. Snyder and J. Love, *Optical Waveguide Theory*. London: Chapman & Hall, 1996.

[64] L. Li, "Formulation and comparison of two recursive matrix algorithms for modeling layered diffraction gratings," *Journal of the Optical Society of America A*, vol. 13, pp. 1024–1035, 1996.

[65] L. Li, "Multilayer modal method for diffraction gratings of arbitrary profile, depth, and permittivity," *Journal of the Optical Society of America A*, vol. 10, pp. 2581–2591, 1993.

[66] G. H. Smith, L. C. Botten, R. C. McPhedran, and N. A. Nicorovici, "Cylinder gratings in conical incidence with applications to modes of air-cored photonic crystal fibers," *Physical Review E*, vol. 66, p. 056604, Nov 2002.

[67] O. Dazel, J.-P. Groby, B. Brouard, and C. Potel, "A stable method to model the acoustic response of multilayered structures," *Journal of Applied Physics*, vol. 113, p. 083506, 2013.

[68] K. Yasumoto and H. Jia, "Electromagnetic scattering from multilayered crossed-arrays of circular cylinders," in *Proc. SPIE 5445, Microwave and Optical Technology 2003*, vol. 5445, pp. 200–205, 2004.

Résumé et introduction en Français

Résumé

La thèse porte sur la modélisation électromagnétique et la simulation de composites stratifiés plans (laminés), renforcés par des fibres organisées périodiquement. L'objectif est d'acquérir une bonne compréhension du comportement électromagnétique de telles structures, en première étape de ce que pourrait ultérieurement être la production d'images mettant en évidence la localisation de zones éventuellement endommagées, et fournissant une certaine quantification de celles-ci.

La thèse proprement dite se concentre donc sur la construction et l'évaluation de modèles de la diffraction électromagnétique par des composites multicouches tels que chaque couche est renforcée par des fibres disposées périodiquement. Est d'abord investiguée la diffraction par une plaque diélectrique (mono-couche) au sein de laquelle des fibres cylindriques de section circulaire de même rayon sont incorporées périodiquement, ces fibres ayant la même orientation de leurs axes et la même distance de centre à centre.

Un cas bidimensionnel impliquant des ondes planes E ou H-polarisées, ainsi que des faisceaux gaussiens, normalement ou obliquement incidents, est d'abord pris en considération afin de mieux comprendre principes et philosophies des méthodes de choix, le couplage de mode et l'expansion multipolaire. Puis le travail est étendu, la diffraction de la plaque sous un éclairement tridimensionnel (conique) étant alors traitée en détail, ce qui montre aussi le potentiel de la méthodologie mise en œuvre si l'on souhaite obtenir la réponse électromagnétique de la structure à une source ponctuelle.

Un composite multicouche, plus courant, mais plus complexe, qui est fait d'un empilement de plaques l'une sur l'autre, est alors étudié. Deux différentes espèces de composites sont ici prises en compte. Pour étudier la première, dont les fibres dans les différentes couches possèdent les mêmes orientations, des méthodes à base de matrices dites S ou dites T sont introduites, impliquant entre autre de s'intéresser à une résolution convenable du système linéaire produit selon le couplage de mode à la transition entre deux couches adjacentes. Une investigation de la deuxième espèce de composites suit alors, pour lequel

les fibres au sein des différentes couches sont orientées dans des directions différentes quelconques, ce que permet une extension précautionneuse des approches précédentes.

Une certaine attention est également portée au problème de l'homogénéisation des composites, de manière à lier les démarches à petite échelle telles que développées dans la thèse à celles à grande échelle souvent les seules prises en compte dans le contrôle non destructif et l'imagerie des composites stratifiés.

De nombreux résultats de simulations numériques sont proposés et validés autant que possible par des résultats de référence de la littérature (notamment dans le cas de cristaux photoniques) et l'utilisation de solveurs «brute-force». L'accent est aussi mis sur des cas particuliers de matériaux composites (ceux à base de fibres de verre et ceux à base de fibres de carbone) qui sont le plus souvent rencontrés dans les applications pratiques, avec des bandes de fréquences appropriées choisies en accord avec le comportement des fibres, principalement diélectrique ou principalement conducteur.

Introduction et contexte de recherche

Les matériaux composites stratifiés sont de plus en plus utilisés dans l'aérospatiale et l'industrie automobile en remplacement de matériaux métalliques traditionnels en raison de leur légèreté, rigidité élevée et de bonnes propriétés de résistance à la corrosion, etc. Pour la fabrication, deux ou plusieurs constituants des matériaux sont toujours combinés ensemble pour produire les caractéristiques souhaitées qui ne peuvent être facilement fournis par l'un des matériaux particuliers.

Un exemple de matériau composite stratifié est constitué de deux parties, la matrice et le renfort. Les renforts sont incrustés périodiquement à l'intérieur de la matrice pour fournir résistance et la rigidité tandis que la matrice est utilisée pour attacher les renforts ensemble. Prenant, en tant que bloc de construction, une résine époxy ou polyester plaque renforcée par l'incorporation d'un réseau périodique de fibres de verre ou de carbone orientées dans la même direction, une pile peut être fabriquée en empilant des plaques l'une sur l'autre avec les fibres dans les différentes plaques orientées dans des directions différentes, offrant ainsi la résistance de la pile et la rigidité dans toutes les directions. Un composite est produit en empilant des piles [5, 6].

Pour les stratifiés composites précités, les dommages causés par l'impact, la rupture de la fibre et des fissures, etc., peuvent apparaître lors de la fabrication et/ou du temps de service, ce qui affecte les propriétés mécaniques ou raccourcit la durée de vie. En particulier dans le domaine aérospatial, des défauts sous la surface pourraient avoir des conséquences catastrophiques. Les dommages tels que des microfissures et des petits dé-

collements cachés dans les composites sont généralement invisibles lors d'une inspection visuelle. Par conséquent, les méthodes de contrôle non destructif (CND) sont nécessaires pour une inspection efficace.

Les méthodes ultrasonores sont les méthodes de contrôle non destructif le plus largement utilisées dans l'industrie, mais surtout pour la caractérisation des métaux et alliages, et il reste difficile de les appliquer à ce type de composite structuré complexe avec une bonne résolution [7]. Cependant, les ondes ultrasonores sont sensiblement atténuées lorsque la mesure est effectuée en champ proche [8] ou à haute fréquence relative [9], ce qui peut provoquer une détection erronée de la zone endommagée. La thermographie infrarouge est une autre méthode, mais la détection peut être affectée par une faible conductivité des fibres [10]. L'utilisation d'autres méthodes traditionnelles de CND pour détecter ces dommages reste difficile ou de coût trop élevé. Toutes les méthodes non destructives traditionnelles mentionnées ont aussi quelques autres difficultés d'application aux composants renforcés par fibres [11], d'où le développement de méthodes de CND nouvelles devient important [12, 13]. Tester avec des ondes électromagnétiques est l'une des méthodes alternatives, qui montre déjà un bon potentiel pour inspecter les dommages d'impact à faible énergie [14] à des fréquences courants de Foucault [11] et micro-ondes [15, 16] pour les fibres diélectriques et conductrices. Mais une imagerie efficace demande une bonne compréhension du comportement électromagnétique, avec des stratifiés en bon état dans la première étape. Pour une gamme basse fréquence avec prise en charge de l'inspection en régime harmonique, lorsque la distance de centre à centre entre les fibres est beaucoup plus petite que la longueur d'onde électrique pour les cas diélectriques ou de profondeur de pénétration pour les cas conducteurs, les couches homogènes anisotropes uniaxiales sont généralement traitées avec l'hypothèse de couche équivalente [17], impliquant tenseurs effective de permittivité ou de conductivité, le stratifié étant simplement une superposition de ces couches [18–20]. Les coefficients de réflexion et de transmission du stratifié peuvent être calculés avec les approches classiques pour les milieux multicouches planes, des situations générales de diffraction pouvant nécessiter des approches plus sophistiquées [21]. Un modèle asymptotique a également été proposé pour les structures périodiques [22, 23].

Pour une gamme haute fréquence, lorsque la distance entre les fibres est de l'ordre de la longueur d'onde ou de l'épaisseur de peau, l'homogénéisation ci-dessus échoue souvent. L'étude peut être réalisée avec une formulation d'intégrale surface périodique [24, 25] qui représente les champs électriques et magnétiques inconnus avec des courants équivalents apparentés sur les interfaces aux limites et gère la fonction de Green nécessaire en appliquant la formule de sommation de Poisson et la périodicité de la structure. L'équation

intégrale de surface est formulée sur une cellule de l'unité et résolue avec la méthode des moments [26].

Cependant, l'investigation actuelle semble être limitée au cas de deux dimensions (2D) de diffraction impliquant des ondes planes TE ou TM-polarisées ou des faisceaux gaussiens et une périodicité unidimensionnel (1D). Pour le cas plus pratique 2.5D, dans lequel l'onde incidente frappe coniquement sur la structure avec un azimut non nul, ou le cas plus compliqué 3D, avec ondes incidentes coniques sur un composite avec plusieurs directions de périodicité des fibres, le champ d'investigation est grand ouvert. Bien que FDTD [27] ou FEM [28] pourraient traiter des composites avec un profil complexe de section transversale des fibres, mais ces méthodes "force-brutes" ne pourraient que gérer la situation de diffraction 3D avec un niveau limité de complexités structurelles, telles que la structure tas de bois [4, 29–31] construite avec une pile 2-couche dans laquelle les fibres dans les deux couches sont orientées dans deux directions orthogonales [32]. Mais ces méthodes numériques devrait échouer à modéliser des stratifiés complexes avec orientations arbitraires des fibres dans les différentes couches. Par ailleurs, la plupart des algorithmes d'imagerie nécessitent la pleine disponibilité des fonctions de Green dyadique associées à la structure étudiée, les méthodes numériques ou analytiques-numériques mentionées ne fournissent pas facilement.

Au cours des dernières décennies, de nombreuses méthodes théoriques efficaces et précises ont été effectivement appliquées pour la modélisation des cristaux photoniques avec des fibres arrangées de façon similaire que celle à l'intérieur des matériaux composites. Dans les études, une grande attention a été accordée aux méthodes de Rayleigh [33] et développements en ondes planes [34, 35] pour leur efficacité de calcul et la précision ainsi que leur traçabilité analytique. Une investigation typique de cristaux photoniques a été réalisée par Yasumoto *et al.* [3]. Leur procédé d'expansion harmonique cylindrique amène à une formulation simple et souple avec la matrice de transfert pour la modélisation de la diffraction électromagnétique de cylindres diélectriques disposés périodiquement dans l'air. La façon d'arranger les cylindres est similaire à l'un des cas étudiés dans cette thèse, donc ce travail a fourni quelques bons exemples pour valider l'approche. La méthode multipôle et le développements en ondes planes sont combinés par Botten et ses collègues [36–38] pour étudier les dispositifs photoniques. L'accent a été principalement mis sur la diffraction de fibres optiques microstructurées ou l'analyse de mode de Bloch de dispositifs optiques, donc un peu différente que des problèmes considérés ici. Mais la façon de combiner le développements en ondes planes et la méthode multipôle est très intéressante pour étudier la diffraction de composites stratifiés. La plupart des travaux rapportés se concentrent sur la structure de tas de bois qui a été largement étudiée [3, 38, 39] pour des fibres

dans l'air pour leurs lacunes optiques attrayantes. Mais ce genre de structure, même si structurellement similaire aux composites stratifiés, n'existe pas pour les vrais matériaux composites puisque, avec seulement deux orientations des fibres, elle ne peut pas assurer robuste et rigide le long de toutes les directions pour répondre aux demandes pratiques.

En outre, la présence de la plaque remplie par du matériau homogène isotrope résulte en de fortes interactions entre les ondes réfléchies par les réseaux de fibres et les interfaces de la plaque, donc conduisant à un comportement électromagnétique beaucoup plus compliqué. Cette interaction devient forte lorsque un grand contraste de permittivité est consideré. Les orientations arbitraires des fibres dans différentes couches apportent un autre degré de complexité, en particulier dans les composites impliquant des dizaines voire centaines de couches. La dispersion introduite à le système par des fibres orientées différemment doit être considérée soigneusement avec une bonne décomposition des modes. Certains des modes se propagent, mais certains deviennent évanescents. Dans le calcul, tous les modes de propagation et un nombre limité de modes évanescents doivent être considérés pour parvenir à une bonne convergence du champ. Trop de modes évanescents va ralentir la vitesse du calcul. Arbitrairement orienter les fibres complique aussi la procédure de séparation de modes de propagation de ceux évanescents, donc un bon nombre de modes évanescents doit être choisi pour équilibrer l'efficacité du calcul et de la vitesse de convergence. Cette procédure est pénible lorsque il y a plus que trois orientations de fibres dans la structure. Dans le même temps, le mode assortiment à la limite entre deux couches adjacentes est nécessaire pour produire un système linéaire à obtenir les coefficients de réflexion et de transmission, ce qui doit être fait dans le même système de référence. Ainsi, le développement de champ ou des matrices correspondantes aux modes dans les couches où les fibres sont orientées dans des directions différentes doivent être soigneusement disposées et transformées en le même système de coordonnées avant l'application des condition aux limites aux interfaces. La combinaison de ces complexités avec les ondes incidentes conique produit un problème de diffraction électromagnétique complexe qui doit être résolu pour l'obtention de la fonction de Green dyadique en examinant la réponse électromagnétique de la structure aux des sources élémentaires.

Les études dans cette thèse fournissent les principes fondamentaux de l'investigation de la réponse électromagnétique de matériaux composites complexes. Ces études fournissent aussi quelques bonnes techniques qui peuvent être appliquées à étudier des structures périodiques désorganisées. Cette désorganisation peut être causée soit par manque ou déplacement des fibres dans les composites ou par changer leurs paramètres physiques et de forme. Toutes ces contributions sont nécessaires pour de plus amples recherches correspondantes au contrôle non destructif des dommages avec des ondes électromagnétiques.

L'accent de cette thèse est cependant le problème électromagnétique mentionné ci-dessus correspondant à plusieurs types de matériaux composites. L'objectif final est de développer un modèle d'onde plane pour des composites multicouches de calcul efficace.

Comme première étape, la méthode multipôle et le développement en ondes planes, en empruntant des analyses antérieures [2, 40–42] et de celles photoniques [43], sont appliquées ensemble pour étudier la structure composite la plus simple, qui est produite par l'insertion d'un réseau périodique de fibres cylindriques circulaires infiniment longues dans une plaque diélectrique. L'accent est mis principalement sur les plaques époxy renforcées par des fibres carbone ou fibres de verre illuminées par ondes planes. Des ondes incidentes E- (TM) et H-polarisée (TE) sont considérées avec le plan d'incidence dans le plan de la section transversale des fibres. Dans cette thèse, ce cas est appelé cas 2D. Le champ au voisinage du cylindre est naturellement développé avec des fonctions de Bessel. Puis les fonctions cylindriques sont combinées avec la série de Schlömilch (lattice sums) [44, 45] à fin de satisfaire les conditions périodiques aux limites le long de la direction de la périodicité. L'intégration le long de la frontière d'une cellule périodique et d'un des cylindres inclus à l'intérieur concerne le domaine au voisinage du cylindre central, où le développement en ondes planes est impliqué pour calculer le champ dans le demi-espace supérieur ou inférieur.

Dans le même temps, l'accord de modes aux limites des cylindres circulaires révèle les détails fins de la structure et permet en outre le calcul de la distribution de champ en leur sein. L'investigation sur ce sujet permet de comprendre les préliminaires et les principes de base des approches, ainsi que de construire de solides fondamentaux pour la suite des études. Le faisceau gaussien est également considéré en décomposant le faisceau en ondes planes. Le champ diffracté du faisceau est obtenu en sommant toutes les ondes planes. Par ailleurs, la théorie de l'homogénéisation est également examinée et développée comme un lien entre le modèle en onde complete actuel et celui des investigations à basse fréquence.

En gardant la même structure 2D, les approches appliquées au cas 2D sont ensuite étendues pour la diffraction d'une onde incidente de manière conique où le plan d'incidence est hors du plan de la section transversale des fibres. Ce cas est appelé cas 2.5D. Puisque le vecteur d'onde de l'onde incidente a des composantes longitudinales, les champs électriques et magnétiques sont couplés. Ceci complique les relations entre les composantes longitudinale et transversale de champ, ce qui conduit alors à une représentation plus complexe des composantes transversales des champs, et donc à une relation plus complexe entre les coefficients des développements. En raison de la simplicité de la structure 2D, les coefficients des développements des champs peuvent encore être obtenus de manière explicite pour éviter les inversions de matrice.

Une fois, basée sur une seule couche que l'approche pour les problèmes de 2D et 2.5D est bien développée et comprise, l'extension de la méthode est effectuée pour étudier la diffraction d'un composite multicouche. Il est construit par empilements des couches l'une sur l'autre, tous les réseaux de fibres circulaires de différentes couches ayant la même direction. Les fibres de carbone et de verre sont étudées avec leurs rayons étant le même dans la même couche mais peut-être différents d'une couche à l'autre, en gardant les mêmes distances de centre à centre des fibres dans la même couche. Les matériaux de référence et les épaisseurs des différentes couches peuvent également varier d'une à l'autre.

Les méthodes fondées sur la S-matrice et T-matrice sont appliquées. L'instabilité numérique est ensuite exposée dans les deux cas à des niveaux différents en raison de mauvais conditionnements des matrices. Cette propriété introduit quelques difficultés à inverser les matrices correspondantes. En raison de cette limitation, la méthode T-matrice ne peut qu'être appliquée à étudier les caractéristiques des modes de propagation. Une fois les modes évanescents impliqués dans le calcul, la méthode devient très instable. Cette instabilité de la T-matrice est fortement influencée par les éléments qui augmentent exponentiellement avec l'ordre des modes evanescents. Comparativement, la solution à base de la S-matrice est beaucoup plus stable. Elle présente une instabilité pour le calcul de la distribution de champ à l'intérieur de la structure, qui peut être surmontée en réorganisant les matrices de façon à relier les coefficients des développements des champs dans toutes les couches au champ incident.

Au ce niveau, toutes les techniques fondamentales pour la caractérisation des structures composites ont été mises à disposition. Donc un composite multicouche pratique peut être pris en compte. Un empilement de 4 couches est tout d'abord construit avec des fibres dans les différentes couches orientées en des directions différentes. Ensuite, des dizaines de piles se chevauchent pour produire le composite multicouche. Avant la modélisation de la pile 4-couche, une pile 2-couche est utilisée pour expliquer les idées de base. L'approche fondée sur la S-matrice est ensuite développée pour étudier la diffraction de ce type de matériaux composites. Un modèle électromagnétique pour le calcul des composites stratifiés tels que pratiquement utilisés est finalement fourni.

Publications

JOURNAL PAPERS

In Preparation

C. Y. Li, D. Lesselier, and Y. Zhong, "Electromagnetic scattering of laminated composite composed of slabs reinforced by a periodic array of fibers parallelly orientating to an arbitrary direction", *IEEE Transactions on Antennas and Propagation*, in preparation.

Published and Accepted

C. Y. Li, D. Lesselier, and Y. Zhong, "Recursive matrix schemes for multilayered composite with periodically arranged fibers under plane wave or Gaussian beam illumination", *Journal of the Optical Society of America B*, *32*, 1532 - 1549, 2015.

C. Y. Li, D. Lesselier, and Y. Zhong, "Full-wave model and numerical study of 3D electromagnetic plane-wave scattered by multilayered fiber-based periodic composites", *Radio Science*, Accepted, May 12, 2015.

C. Y. Li, D. Lesselier, and Y. Zhong, "Scattering of obliquely incident electromagnetic plane waves by composite panel involving periodic arrays of circular fibers," *IEEE Transactions on Antennas and Propagation*, Accepted, Apr. 30, 2015.

C. Y. Li, D. Lesselier, and Y. Zhong, "Electromagnetic small-scale modeling of composite panels involving periodic arrays of circular fibers," *Applied Physics A*, *117*, 567 - 572, 2014.

CONFERENCE PAPERS

Oral Presentations

C. Y. Li, D. Lesselier, and Y. Zhong, "Full-wave model and numerical study of 3D electromagnetic plane-wave scattered by multilayered fiber-based periodic composites", 1st URSI Atlantic Radio Science Conference (URSI AT-RASC), Gran Canaria, May 2015 **(Third prize at the best student paper competition)**.

C. Y. Li, D. Lesselier, and Y. Zhong, "Scattering of obliquely incident electromagnetic waves by composite panels involving periodic arrays of circular fibers", URSI General Assembly and Scientific Symposium, 2014 XXXIth URSI, Beijing, August 2014.

C. Y. Li, D. Lesselier, and Y. Zhong, "Electromagnetic small-scale modeling of composite panels involving periodic arrays of circular fibers," 5th International Conference on Metamaterials, Photonic Crystals and Plasmonics, META'2014, Singapore, May 2014.

Poster Presentations

C. Y. Li, D. Lesselier, and Y. Zhong, "Modélisation électromagnétique à petite échelle d'un panneau composite", Les Journées Cofrend 2014, Bordeaux, France, May 2014.

C. Y. Li, D. Lesselier, Y. Zhong, and M. Lambert, "Electromagnetic small-scale modeling of composite panels," Assemblée générale biannuelle du GDR Ondes - Interférences d'Ondes, Dijon, France, Oct. 2013.

C. Y. Li and D. Lesselier, "Sur une analyse préliminaire de la modélisation à petite échelle de panneaux composites : arrangement périodique de fibres cylindriques circulaires," URSI-France - Journées scientifiques, Paris, France, March 2013.